Dissertation
submitted to the
Combined Faculties for the Natural Sciences and for Mathematics
of the Ruperto-Carola University of Heidelberg, Germany
for the degree of
Doctor of Natural Sciences

Put forward by
Dipl.-Phys. David Josef Walter
born in Oberkirch, Baden

Oral examination: 26 July 2013

DOAS spectroscopy onboard the CARIBIC passenger aircraft – trace gas concentration, and flux measurement of localized sources

Referees: Prof. Dr. Ulrich Platt
Prof. Dr. Thomas Wagner

Zusammenfassung

Diese Arbeit beschäftigt sich mit der Fernerkundung und Flussbestimmung von atmosphärischen Spurengasen mit Hilfe der Differentiellen Optischen Absorptionsspektroskopie (DOAS). Im Rahmen des CARIBIC-Projektes (Civil Aircraft for the Regular Investigation of the atmosphere Based on an Instrument Container) wird seit 2010 ein neues DOAS-Gerät einmal pro Monat als Bestandteil eines vollautomatischen Messcontainers im Frachtraum eines Passagierflugzeuges installiert. Mit diesem Instrument werden Stickstoffdioxid (NO_2), Schwefeldioxid (SO_2), Brommonoxid (BrO), salpetrige Säure (HONO), Formaldehyd (HCHO) und Ozon (O_3) gemessen. Die Resultate dieser Messungen werden mit Schwerpunkt auf SO_2 und NO_2 vorgestellt, welche in den Abluftfahnen von großen industriellen Anlagen und Städten gemessen wurden. Mit Hilfe von Flussberechnungen werden die SO_2-Emissionen einer Nickelschmelze in Norilsk (Siberien) und die NO_2-Emissionen der Stadt Paris abgeschätzt. Dabei werden die Unsicherheitsfaktoren diskutiert und Vergleiche mit Satellitendaten angestellt. Es wird der Frage nachgegangen, ob sich mit Hilfe ähnlicher Geräte auf weiteren Passagierflugzeugen solche Berechnungen zur Quantifizierung weiterer Quellen nutzen lassen.

Abstract

This thesis deals with the remote sensing and the flux calculation of atmospheric trace gases, using Differential Optical Absorption Spectroscopy (DOAS). Since 2010, within the CARIBIC project (Civil Aircraft for the Regular Investigation of the atmosphere Based on an Instrument Container), a new DOAS instrument is installed in the cargo compartment of a passenger aircraft once per month as part of a fully automated measurement container. With this instrument, nitrogen dioxide (NO_2), sulfphur dioxide (SO_2), bromine oxide (BrO), nitrous acid (HONO), formaldehyde (HCHO) and ozone (O_3) are measured. The results of these measurements are presented with focus on SO_2 and NO_2, which were observed in the downwind plumes of large industrial plants and cities. Using flux calculations, the emission of SO_2 from a nickel smelter in Norilsk (Siberia) and the NO_2 emission of the city of Paris are estimated. Thereby, the uncertainty factors are discussed and comparison with satellite data are performed. The question is dealt with, whether such calculations can be used to quantify further emission sources using similar instruments onboard additional passenger aircraft.

Contents

1. Introduction

With about $5 \cdot 10^{18}$ kg, the atmosphere contributes less than on millionth to the earth's mass, but it is essential for life on our planet. Its composition has strongly changed during its existence due to many factors, including volcanic eruptions and biologic activity. Although only three gases – namely nitrogen, oxygen and argon – constitute more than 99 % of today's atmosphere, certain trace gases influence climate, some of them directly due to absorption of solar or thermal radiation (e.g. water, CO_2, ozone), others indirectly due to chemical reactions (e.g. CFCs, OH, NO_x, SO_2, BrO).

For thousands of years, mankind has been altering the planet's vegetation. While these impacts initially had a more indirect and moderate influence on climate, in the last centuries, the atmospheric composition has been changed directly by high emissions of many species, amongst them aerosols and trace gases. Because of the impact of human activities, the term *Anthropocene*, introduced by Eugene F. Stoermer and propagated by Paul J. Crutzen (*Steffen et al.*, 2011), has been more and more established for a new geological era following the holocene. Between their first assessment in 1990 and the most recent one in 2007, the Panel on Climate Change (IPCC, "www.ipcc.ch"), the awareness grew that the anthropogenic emissions cause a climate warming. However, the degree and the spatial distribution of the temperature increase as well as many details of the changes in precipitation and atmospheric circulation are unclear yet, not to mention the consequences for plants, animals and humans.

Numerical models are used to anticipate changes to the climate based on the current knowledge of the physical and chemical processes in the atmosphere and the impact of trace gases. Wide-ranging observational data are necessary to be able to validate model predictions, to discover new relations and mechanisms and to quantify them. Therefore, measurements have to be designed and campaigns to be performed on various scales – in spacial as well as in temporal respect. Stationary ground stations can be equipped with large equipment and therefore generally yield precise measurements, but they only measure at one point. To increase their representativeness, networks of ground stations have been established. Research ships like the icebreaker 'Polarstern' offer measurements in remote oceanic regions and high latitudes. Precise vertical profiles are obtained by radiosondes; but only for a limited number of places are such probes taken regularly. A largely global coverage is provided by satellites, but typically with a lower spatial resolution and lower accuracy. Research aircraft like *HALO* ('High Altitude and Long Range Research Aircraft') allow detailed measurements with a high spatial

resolution and a high flexibility for specific investigation of features involving transport and chemistry. However, such flights are too expensive for performing regular flights on a long-term basis.

Passenger aircraft can offer a regularly flying platform in the UTLS region ('Upper Troposphere, Lower Stratosphere'). With the *NOXAR* project ('Measurements of Nitrogen Oxides and Ozone Along Air Routes') onboard a Boeing 747 aircraft, the first dataset for nitrogen oxides was created during more than 600 passenger flights in 1995 and 1996 (*Brunner et al.*, 2001). A large dataset of CO_2 and other trace gases based on thousands of flights between Japan and Europe, Australia, Asia and North America, has been established by *CONTRAIL* ('Comprehensive Observation Network for TRace gases by AIrLiner') and precursor projects, cf. JAL Foundation and Japan Airlines (*Niwa et al.*, 2012). In 1994, the European Project *MOZAIC* ('Measurements of OZone, water vapour, carbon monoxide and nitrogen oxides by in-service AIrbus airCraft') took off. With measurement packages installed on several airlines, around 30 000 flights have been performed. Presently, MOZAIC is part of the *IAGOS* project ('In-service Aircraft for a Global Observing System').

A project with less flights but a large variety of analyzed species is *CARIBIC*, standing for 'Civil Aircraft for the Regular Investigation of the atmosphere Based on an Instrument Container'. In phase 1, lasting from 1997 to 2002, an aircraft of LTU International Airways was used. Since 2005, phase 2 is operational. A special airfreight measurement container is installed once a month onboard an Airbus 340-600 of Lufthansa, typically for four consecutive flights. The container contains in-situ instruments and equipment that samples air for detailed past-flight analyses. Besides gases and water content, aerosol particles and their elemental composition are studied. Therefore, CARIBIC provides the largest long-term dataset of the UTLS region in respect to the variety of measured species. This allows detailed analysis of the chemical and physical processes taking place in the UTLS itself or in the 'history' of the probed air masses. With increasing computational power, atmospheric chemistry models are being improved in respect to their spatial and temporal resolution, but also in respect to the variety of chemical processes included. Here, the CARIBIC dataset offers the important possibility of evaluation.

Besides the in-situ instruments and air and particle samplers, the CARIBIC container includes an instrument for remote sensing, based on *DOAS* ('Differential Optical Absorption Spectroscopy'). DOAS instruments are widely used for ground-based measurements as well as in satellites. Also some research aircraft are equipped with DOAS instruments. However, CARIBIC is the first and only system with DOAS onboard a passenger aircraft. A first instrument installed from 2004 to 2009 showed the suitability of such instruments, containing three spectrographs in the visible range, cf. *Dix* (2007).

This thesis deals with the measurements of the successor instrument, which has been in operation since 2010. Like the precursor, it contains three spectrographs; the chosen

wavelength range of 286–413 nm allows the detection of NO_2, O_3, O_4, BrO, HONO, HCHO and SO_2. With three viewing directions (two close to the horizon, one nadir), constraints about the vertical distribution of observed events can be obtained. During the descent, industrial plumes have been observed. With the help of the nadir direction, strong sources (large cities) were measured at standard flight altitude of around 11 km. Nitrogen oxide (NO_2) could be observed above several large cities and over biomass burning regions. Furthermore, BrO was observed over Canada. Also SO_2 was detected several times. Besides the eruption of the Eyjafjallajökull volcano in 2010, the strongest SO_2 source observed by this DOAS instrument is a Siberian Nickel smelter. Here, a flux calculation was performed for estimating the emission source strength of that facility. The same approach was applied for the city of Paris – in that case for NO_2. This leads to the question if a network of DOAS onboard passenger aircraft might allow to monitor several pollution point sources on a regular basis.

Structure of this thesis

This thesis starts with a summary of atmospheric dynamics, chemistry and radiative transfer processes (Chap. 2 and 3). Based on the latter one, the DOAS method used within this thesis is described in Chap. 4, including a section about its application for the determination of trace gas fluxes. These chapters are based on common knowledge (e.g. *Roedel and Wagner* (2011), *Seinfeld and Pandis* (2006), *Platt and Stutz* (2008)), therefore they contain some similarities to previous works in that field (e.g. *Walter*, 2008).

After a brief overview over the CARIBIC project (Chap. 5), the new DOAS instrument and the evaluation of its data are described in Chap. 6. The results are presented and discussed in Chap. 7, with focus on flux calculations for quantifying large emission sources. The idea of installing similar instruments on further passenger aircraft is discussed in Chap. 8; Chap. 9 gives a summary and a outlook.

Overview graphs over the flights (from June 2010 to February 2013) are given in Appendix A. Symbols and conventions about variables, acronyms and other terms used within this thesis are listed in Appendix B.

2. Atmospheric Dynamics and Chemistry

In this chapter, a short overview of thermodynamical basics needed for understanding the vertical temperature and pressure profile of the atmosphere and the processes of atmospheric circulation is given. Afterwards some components of the atmosphere are presented, including major chemical reactions of those compounds being measured by the DOAS instrument. This overview is based on general knowledge of the atmosphere which can be found in various literature, e.g. *Roedel and Wagner* (2011).

2.1. Vertical structure of the Atmosphere

The standard atmospheric ground pressure at sea level is 101 325 Pa; the surface temperature is about 288 K on global and seasonal average. Typical flight altitudes of passenger aircraft like the Airbus A340-600 used for the CARIBIC platform are between 10 and 12 km a.s.l. There, the pressure is reduced to only ≈200 hPa, i.e. one fifth of the surface pressure. Also the temperature at that altitude is much lower, namely ≈220 K. Because pressure and temperature directly influence the density of the atmosphere, they have to be considered when converting gas concentrations into mixing ratios. Also chemical reactions are temperature and pressure dependent. Therefore, the vertical profile of these quantities and the physical background are described in the following.

2.1.1. Pressure Profile

The air pressure in the atmosphere is a result of the temperature and the earth's gravity. It decreases with height nearly exponentially. This can be easily derived from the ideal gas law when visualizing a cuboid of air in the atmosphere with a base area A and an infinitesimal height $\mathrm{d}z$. According to Archimedes' principle, the gravitational force $F_\mathrm{B} = -A \cdot \mathrm{d}z \cdot \rho \cdot g$ exerted on the cuboid is equal to the buoyancy $F_\mathrm{B} = A \cdot \mathrm{d}p$, which is exerted by the surrounding air due to the pressure difference $\mathrm{d}p$ between the upper and the lower base of the cuboid. The surface A cancels out, and the pressure decrease rate is given by $\mathrm{d}p = -\rho \cdot g \cdot \mathrm{d}z$ with the mass density ρ of the cuboid (and the surrounding air) and the gravitational acceleration g. For an ideal gas, the pressure p, the molar volume V_mol and the absolute temperature T are related by the ideal gas equation

$$p \cdot V_\mathrm{mol} = R_\mathrm{gas} \cdot T = N_\mathrm{A} \cdot \mathrm{k_B} \cdot T \tag{2.1}$$

with the general gas constant R_{gas} and the Boltzmann constant k_B.[1] Therewith, the mass density can be described by

$$\rho = \frac{M_{\text{mol}}}{V_{\text{mol}}} = \frac{M_{\text{mol}} \cdot p}{R_{\text{gas}} \cdot T} \tag{2.2}$$

with the molar mass M_{mol}. This leaves to

$$\mathrm{d}p = -p \cdot \frac{M_{\text{mol}} \cdot g}{R_{\text{gas}} \cdot T} \cdot \mathrm{d}z = -p \cdot \frac{m_{\text{molec}} \cdot g}{\text{k}_\text{B} \cdot T} \cdot \mathrm{d}z \tag{2.3}$$

Here, m_{molec} is the mass of one gas molecule.

The pressure at a given altitude z can be calculated by integrating this equation along z, starting with a ground pressure p_0. When the height dependency of the temperature T and the gravitational acceleration g is neglected, the *Barometric formula* can be written as an exponential function

$$p(z) = p_0 \cdot \exp\Big(-\frac{M_{\text{mol}} \cdot g}{R_{\text{gas}} \cdot T} \cdot z\Big) = p_0 \cdot \exp\Big(-\frac{m_{\text{molec}} \cdot g}{\text{k}_\text{B} \cdot T} \cdot z\Big) = p_0 \cdot \mathrm{e}^{-z/z_0} \tag{2.4}$$

The term z_0 with

$$z_0 = \frac{R_{\text{gas}} \cdot T}{M_{\text{mol}} \cdot g} = \frac{\text{k}_\text{B} \cdot T}{m_{\text{molec}} \cdot g} \tag{2.5}$$

is called *scale height* and amounts to roughly 8 km (e.g. *Bohren and Albrecht*, 1998, p. 55). In that height, the pressure amounts to 1/e of the ground pressure. More intuitively spoken, the scale height z_0 describes the height, which the atmosphere would have, if the pressure profile would be box-shaped with a constant pressure p_0 (ground pressure) up to z_0, and no molecules above. Therefore, a more general definition of the scale height is given by $z_0 := \frac{1}{c_{i,0}} \cdot \int_0^{Z_{\text{TOA}}} c_i(z) \cdot \mathrm{d}z$ with concentration $c_k(z)$ of species k and 'top of the atmosphere height' Z_{TOA} (see below); cf. *Roedel* (2000, p. 61) for details.

Due to the different molecular mass of the different species, this scale height should be species dependent. But in the lowermost 80 km, turbulent mixing and large scale circulation dominate, so this process can not be observed. Therefore, long-lived species without strong sinks or sources are quite well-mixed in that part of the atmosphere, the so-called *homosphere*. Instead, the differences in the vertical profiles of different gases are predominantly caused by different sources, sinks and (photo)-chemical reactions.

As the pressure profile has an approximately exponential profile shape, there is no clear upper boundary of the atmosphere. Nevertheless, sometimes the term *top of the atmosphere* (TOA) is used, especially in the context of vertical ranges, e.g. in integral boundaries: $\int_0^{Z_{\text{TOA}}} \mathrm{d}z$ means an integral over the hole atmosphere. In that sense, 'TOA' is used in Sect. 4 when introducing the vertical column density (VCD). For concrete applications, Z_{TOA} might be set to 100 km or lower.

[1] The relationship between the Boltzmann constant k_B and the gas constant R_{gas} is given by $\text{k}_\text{B} = R_{\text{gas}}/N_\text{A}$ with the Avogadro number $N_\text{A} \approx 6 \cdot 10^{23}\,\text{mol}^{-1}$

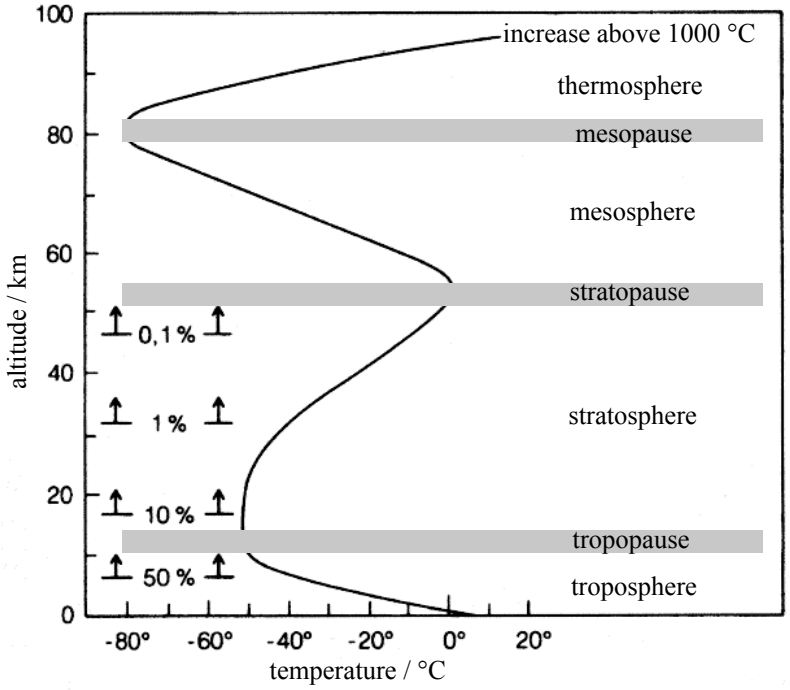

Figure 2.1.: Temperature profile of the Atmosphere. The black curve shows the temporal average of the temperature for temperate latitudes. The numbers in the left part denote the fraction of the atmosphere's mass above the marks – for a flight altitude of 11 km, this fraction is less than 25 %. (Adapted from *Roedel and Wagner*, 2011, p. 85)

2.1.2. Temperature

The temperature of the atmosphere is mainly caused by the solar insolation, its absorption within the atmosphere and the ground, thermal radiation and transport processes. The result is a temperature profile with two minima, so the atmosphere is typically subdivided into the following layers, which are depicted in Fig. 2.1.

Troposphere

The *troposphere* is the lowermost part of the atmosphere, reaching from the ground until the *tropopause*. The troposphere is characterized by a strong negative temperature gradient between ground temperatures of ∼288 K and tropopause temperatures in the order of 220 K (−50 °C). The temperature maximum at the surface is caused by the solar insolation absorbed by the ground, depending on the surface albedo. The heated ground emits infrared radiation into the atmosphere and warms the adjacent air by conductive heat transfer. The energy is transported upwards by radiation and the transport of sensible and latent heat.

An upward moving parcel expands due to the pressure decrease. In the simplest case, this expansion is nearly adiabatic (no heat exchange or mixing with surrounding air),

leading to a cooling of the parcel with the *lapse rate* Γ, which is defined as the negative temperature gradient: $\Gamma = -\mathrm{d}T/\mathrm{d}z$. For a dry, ideal gas, this adiabatic lapse rate is given by

$$\Gamma_{\mathrm{dry}} = -\left.\frac{\mathrm{d}T}{\mathrm{d}z}\right|_{\mathrm{dry}} = \frac{M_{\mathrm{mol}} \cdot g}{c_{\mathrm{p}}} \approx 9.8\,\mathrm{K/km} \tag{2.6}$$

(cf. *Bohren and Albrecht*, 1998, p. 109). c_{p} is the specific heat of the air for a temperature change at constant pressure and amounts to about 29 $\frac{\mathrm{J}}{\mathrm{mol \cdot K}}$. If the parcel contains water vapour, this value slightly changes. If condensation starts, condensation energy ('latent heat') is released, which leads to a smaller lapse rate, typically $\Gamma_{\mathrm{wet}} \approx 0.5\,\mathrm{K/km}$, cf. *Roedel* (2000).

In reality, the assumption of an adiabatic process is only a good approximation inside large convective clouds. Otherwise entrainment (mixing of air masses) plays an important role. Furthermore, aerosols and clouds can absorb a significant fraction of the solar insolation, reducing the light reaching the ground. In such cases, the actual temperature profile can strongly differ from the standard profile, even a positive temperature gradient (negative lapse rate Γ) is possible close to the ground (inversion layer). The troposphere itself can be divided into several layers cf. Sect. 2.2.

Tropopause and Stratosphere

While the convection and the associated cooling of ascending air masses leads to a negative temperature gradient in the troposphere, the temperature increases again in altitudes above ∼15 km up to ∼50 km, in the *stratosphere*. The air in the stratosphere is dry and the convection is weak compared to the troposphere. Therefore, the balance of absorbed and emitted radiation becomes the dominant process. For the molecules in the upper stratosphere, nearly the full solar spectrum is available for absorption. The lower the altitude is, the smaller is the part of the non-absorbed light, especially in the ultraviolet wavelength range. As consequence, the upper stratosphere is warmer than the lower stratosphere.

The transition zone between the troposphere and the stratosphere is called *tropopause*. There are several definitions for the tropopause height which not always are in good coincidence with each other. An approach set up by the World Meteorological Organization (WMO) based on the temperature defines the tropopause as the lowest height where the lapse rate Γ falls below a threshold of $\Gamma < 2\,\mathrm{K/km}$ and remains below that value for a depth of 2 km or more (*Bethan et al.*, 1996). Another definition is based on the potential vorticity (PV). The PV is a measure for the shear in fluids or gases. Under certain conditions, it is a conserved quantity. While the PV in the troposphere is typically below 2 Potential Vorticity Units (PVU), it rapidly increases with height in the tropopause regions and reaches 10 and more PVU in the stratosphere. Therefore, the PV can be used for defining the troposphere. Typical threshold values are around 2 PVU. The definition of the PV and further details about this quantity are given e.g.

in *Clough et al.* (1985), *Bleck* (1973) and *Ertel* (1942). The PV based definition of the tropopause height places emphasis on the property of the tropopause being "the boundary between the turbulently mixed troposphere and the stably stratified stratosphere above" (*Bethan et al.*, 1996).

Another tropopause definition is based on the chemical composition which differs between the troposphere and stratosphere. A widely used tracer is ozone which has low mixing ratios in the troposphere and high mixing ratios in the stratosphere, cf. Sect. 2.3.6. In contrast to the PV, the ozone concentrations or mixing ratios can be directly measured by ozone sondes with a good height resolution. Also CO is sometimes taken as a tracer for defining the tropopause height, cf. *Pan et al.* (2004), *Zahn et al.* (2004), *Assonov et al.* (2010).

The tropopause height does not only depend on the definition but also on the latitude, the season, and, to a lesser extend, on the longitude, cf. Sect. 2.2. The region of the **u**pper **t**roposphere, the tropopause and the **l**ower **s**tratosphere is often referred to as 'UTLS'. Typical values for the tropopause height are around 17 to 18 km in the tropics and 9 to 13 km in higher latitudes (*Roedel and Wagner*, 2011, p. 82). Passenger aircraft flying in such altitudes offer a suitable platform to study this region, which is done in the CARIBIC project (Chap. 5).

Mesosphere and Thermosphere

The stratosphere ends at an altitude of roughly 50 km with the stratopause, followed by the *mesosphere*, which reaches till ∼80 km. In the mesosphere, the temperature decreases with height. A reason for this decrease is the low amount of ozone which absorbs the UV radiation from the sun. The *mesopause* at ∼80 km altitude is the coldest region of the atmosphere. The *thermosphere* above the mesopause is characterized by a strong temperature increase to more than 1000 K, caused by the absorption of high energy ultraviolet and x-ray radiation, mainly by oxygen. Above 500 km altitude, temperatures can reach 500 to 2000 K (*Brasseur and Solomon*, 2005).

Ionosphere, Homosphere and Heterosphere

Because the highly energetic photons found above ∼75 km can ionise molecules, this region is called the *ionosphere* (*Glickman*, 2000).

Furthermore, the atmosphere can be divided into the *homosphere* below 80–100 km and the *heterosphere* above, because the long-lived atmospheric compounds (especially the predominant oxygen and nitrogen) are quite well mixed in the homosphere, while above the species start to separate according to their mass, cf. mass dependency of the scale height in the Barometric formula, (2.4) and (2.5). Therefore virtually only hydrogen is present in altitudes above 1000 km.

Potential Temperature

A commonly used quantity in meteorology is the *potential temperature* T_{pot}. For the dry adiabatic expansion of an air parcel, it is a conserved quantity. By definition, the potential temperature T_{pot} of a dry air parcel somewhere at altitude z with pressure p is equal to the temperature T_0 the air parcel would reach when shifting down the air parcel to the ground (with pressure p_0) in an adiabatic manner (contraction of its volume due to the higher pressure at ground level but without exchange of mass or heat with the surrounding air). From the ideal gas law, cf. (6.2), the following equation can be derived for the potential temperature of the air parcel:

$$T_{\mathrm{pot}} = T \cdot \left(\frac{p_0}{p}\right)^{\frac{\kappa-1}{\kappa}} \tag{2.7}$$

The unitless coefficient $\kappa = c_{\mathrm{p}}/c_{\mathrm{v}}$ is defined as quotient of the specific heat at constant pressure and the specific heat at constant volume. For air, it amounts to $\sim$1.4, thus $\frac{\kappa-1}{\kappa} \approx 0.29$, cf. *Glickman* (2000). Because the tropospheric convection of dry air masses represents such adiabatic process in good approximation, the potential temperature is nearly constant in the lower part of the troposphere and increases strongly in higher altitudes. In the stratosphere it exceeds 1000 K.

The increase in potential temperature is the reason why the temperature in aircraft would be too high if the aircraft would be thermally isolated too much: The ambient air has to be compressed (more or less adiabatically) to reach a cabin pressure not too far below the standard pressure, which is connected with a strong temperature increase. For example, for an ambient temperature $T = 220$ K, an ambient pressure $p = 200$ hPa and a cabin pressure $p_0 = 800$ hPa, the temperature inside the cabin would be around 330 K for the case of an adiabatic compression without energy loss.

2.2. Circulation

For the interpretation of the CARIBIC measurements, information about the origin of the probed air masses are needed, e.g. calculated by atmospheric circulation models yielding forward and backward trajectories. Therefore, a brief overview over the basic transport mechanism is given; afterwards, global circulation pattern are mentioned.

2.2.1. Mechanism

Molecular Diffusion

Even without any convection, the molecules of an air parcel spread due to molecular diffusion. The average distance covered by a molecule in this stochastic process is not linear with time but with the square root of time. If there is a concentration gradient of a gaseous species, a net flux of the molecules of that species occurs proportional to the gradient, as described by Fick's laws, cf. *Fick* (1855), *von Smoluchowski* (1906).

Convection

Convection means the net flux of air in terms of the movement of an air parcel. It occurs if there is a pressure gradient, or if the air parcel has a lower or larger density than the ambient air (cf. 'buoyancy', 2.1.1). In the atmosphere, such pressure and density variations are mainly caused by temperature differences ('thermal convection'). Prominent equations for describing the movement are the Navier-Stokes equation and the Euler equation (cf. *Roedel*, 2000, p. 99). In an Lagrangian view, the acceleration $\frac{\mathrm{d}\vec{v}}{\mathrm{d}t}$ of the air parcel can be written as

$$\frac{\mathrm{d}\vec{v}}{\mathrm{d}t} = -\frac{\mathrm{grad}(p)}{\rho} - \vec{g} + 2 \cdot (\vec{v} \times \vec{\Omega}) + \frac{\vec{F}_\mathrm{R}}{\rho} \tag{2.8}$$

Here, ρ stands for the mass density of the parcel, p for the ambient air pressure, $\vec{g}$ for the gravitational acceleration, $\vec{v}$ for the speed of the air parcel relative to the earth, $\vec{\Omega}$ for the earth rotation[2] and $\vec{F}_\mathrm{R}$ for frictional forces.

As mentioned in Sect. 2.1.2, convection in the lower troposphere is driven by the solar insolation, heating the ground and therefore the lowest air masses. During the ascend, a heated air parcel expands and therefore cools down until its temperature is equal to the temperature of the ambient air.[3] The occurrence of convection depends on the prevailing meteorological situation, which is denoted as 'stable' (if $-\mathrm{d}T/\mathrm{d}z < \Gamma$), 'neutral' or 'unstable' ($-\mathrm{d}T/\mathrm{d}z > \Gamma$).[4] While in a stable atmosphere convection is suppressed (inversion layer), strong convection can occur in unstable atmospheric conditions; cf. literature for details, e.g. *Bohren and Albrecht* (1998, p. 111ff). Moist air parcels contain latent heat. When the temperature of such an ascending parcel falls below the dew point temperature and the water vapour condenses, condensation energy is released, allowing the air parcel to further ascend. This can lead to deep convective clouds.

Coriolis Force, Geostrophic Winds

The cross product $2 \cdot (\vec{v} \times \vec{\Omega})$ in (2.8) is the so-called *Coriolis acceleration*, named after the French scientist Gaspard-Gustave de Coriolis.

$$\vec{a}_\mathrm{Coriolis} = 2 \cdot (\vec{v} \times \vec{\Omega}) \tag{2.9}$$

While not existing in an inertial system, this fictitious acceleration (or the corresponding *Coriolis force*) occurs for a body moving with velocity $\vec{v}$ in respect to a rotating coordinate systems like the earth system. When neglecting the vertical wind compo-

[2] Vector $\vec{\Omega}$ is directing from the south to north pole with an absolute value of $\frac{2\pi}{24\,\mathrm{hours}}$.

[3] Due to its inertia, the parcel can overshoot to some extend, leading to so-called 'Brunt-Väisälä waves'.

[4] Here, $-\mathrm{d}T/\mathrm{d}z$ is the actual (real) lapse rate, Γ the (theoretical) dry or wet adiabatic lapse rate, cf. (2.6).

nent,[5] the absolute value of the horizontal component[6] of the Coriolis acceleration can be written as

$$a_{\text{Coriolis,h}} = 2 \cdot v \cdot \Omega \cdot \sin(\phi) \tag{2.10}$$

with latitude ϕ, showing the highest Coriolis acceleration close to the poles and no (horizontal) Coriolis acceleration at the equator. In the northern hemisphere, a moving air mass is accelerated to the right (seen from above); in the southern hemisphere, it is accelerated to the left.

The driving force for the horizontal movement of the air are horizontal pressure differences. Without the Coriolis acceleration, air would flow from higher pressure to lower pressure, leading to an equalisation of the pressure difference. But the Coriolis force acts orthogonal to this direction. In a dynamic equilibrium state, the Coriolis force and the hydrostatic force compensate each other. This is the case, if the velocity $\vec{v}$ is perpendicular to the pressure gradient. Such winds are called *geostrophic winds*. As a consequence, in the northern hemisphere, high pressure regions are surrounded by *anticyclones* (air moving around clockwise when seen from above) and low pressure regions by *cyclones*. In the southern hemisphere, it is the other way round. This geostrophic behaviour hinders the pressure equalisation efficiently, making low-pressure and high-pressure areas quite stable. In lower altitudes, however, where friction due to the surface occurs, the wind speed and therefore the Coriolis force is too low, so the air follows the negative pressure gradient. Therefore, the wind direction typically changes between the surface and the free atmosphere by roughly 90°, a phenomenon called *Ekman spiral* (*Glickman*, 2000).

Turbulence

In the soil and very close to the surface, molecular diffusion is the dominating transport process, while convection is dominant in the free atmosphere. In between, a mixture of both processes takes place, depending on the speed and the surface, *laminar flow* and *turbulence* occur. While molecular diffusion is described by microscopic or statistical approaches, convection is a macroscopic phenomenon based on classical (fluid) mechanics. Equations like the Stoke's law for the frictional force help to deal with laminar motions. Turbulence is quite difficult to handle, as it is characterized by irregular fluctuations which can not be predicted in detail (*Glickman*, 2000). Therefore statistical or parametrical approaches are used for describing turbulent processes like 'Large Eddy Simulations', cf. *Smagorinsky* (1963). Turbulence leads to an efficient mixing of air masses. The large scale kinetic energy is transfered to smaller scales until it is converted to thermal (undirected) energy.

[5] Because being by magnitudes higher than the vertical wind speed, only the horizontal speed is relevant for the Coriolis force.

[6] Only the horizontal component of the Coriolis force is important, because the vertical component is superimposed by the much higher gravitational force.

Vertical Transport, Vertical Structure

Molecules traveling from the surface up to the stratosphere pass through several layers, being transported by the above-mentioned processes. Within the soil and air directly above (up to millimeters above the ground), molecular diffusion takes place. Above, turbulent convection dominates. In the first meters, shear forces are important ('Prandtl layer', 'surface boundary layer'). While they loose importance with height, larger scaled but still more or less turbulent convection occurs ('Ekman layer'). As mentioned before, the horizontal wind direction changes towards the geostrophic wind direction (Ekman spiral).

Those lower atmospheric layers are summarized as *atmospheric boundary layer* (ABL), also called *planetary boundary layer* or just *boundary layer*. The ABL is characterized by an effective mixing and therefore reacts within an hour or less to changes in the surface pressure and temperature (*Stull*, 1988). It is normally capped by a layer of temperature inversion – the *inversion layer* – hindering the exchange with higher air masses.[7] Because of that, the ABL above large cities contains a significantly higher pollution of emitted gases and aerosol particles than the air above, therefore the top height of the ABL is sometimes visible to the naked eye. The height of the boundary layer varies with daytime and the meteorological condition. It can range from less than 100 m in calm nights to several kilometers in hot summer days or stormy conditions (*Glickman*, 2000). At the top of the ABL, cumulus clouds can often be observed.

The region above the ABL is called *free atmosphere*. Here, the effect of the earth's surface friction is negligible. Vertical transport is mainly caused by convection until the tropopause, which acts as mixing barrier. The exchange between the troposphere and the stratosphere mainly takes place in *Inner Tropical Convergence Zone* (ITCZ). In that region, the maximal mean solar radiation occurs, leading to strong convections. Especially over the ocean, the uplifting moist air masses contain large amounts of latent heat, so the air masses reach far above 10 km altitude – as mentioned in Sect. 2.1.2, the tropical tropopause height is around 17 to 18 km. After the uplift, the air distributes to the north or to the south, now being in the stratosphere (see Sect. 2.2.2). Because the insolation has an annual cycle, the latitude of the ITCZ over the ocean changes between ∼10° N, in the northern summer and ∼0° S, in the southern summer. Over land, there is a stronger cycle of the ITCZ (up to ±25° around the mean latitude of ∼5° N), cf. *Roedel* (2000, p. 154ff).

Also in higher latitudes, stratosphere-troposphere exchange (STE) takes place to some extend due to deep convective clouds breaking through the tropopause, tropopause folds, subtropical jets and turbulent processes, cf. *Holton et al.* (1995), *Fischer et al.* (2000). A quite recent term is the *Extratropical Transition Layer* (ExTL), which is

[7] Depending on the literature, the inversion layer is on top of the ABL or the topmost part of the ABL. In latter case, the lower part of the ABL is called 'mixing layer'.

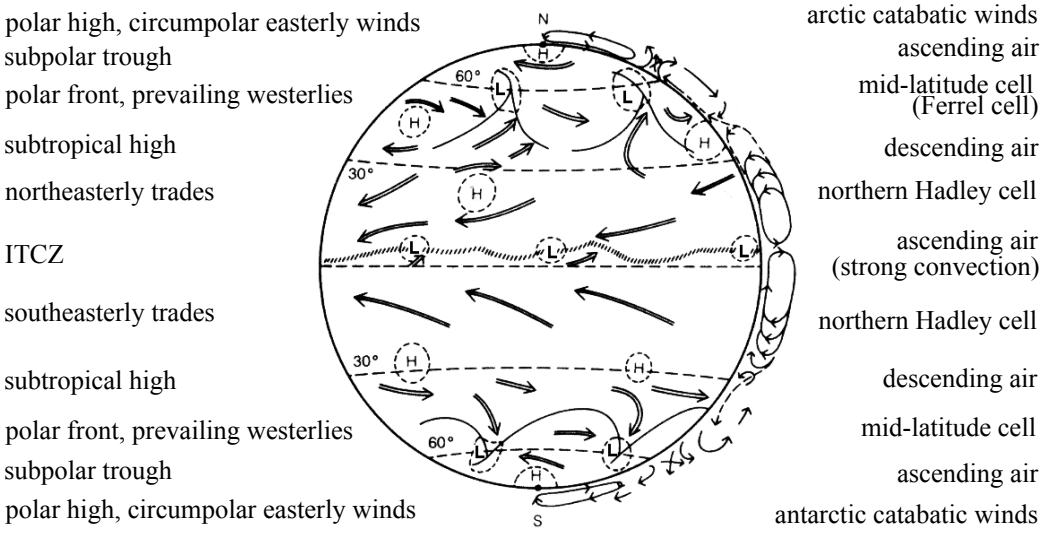

Figure 2.2.: Schematic of the global circulation. On the left side, the most important horizontal winds are stated; the right side contains terms concerning the meridional circulation. (Adapted from *Roedel and Wagner*, 2011, p. 144)

used to describe the extratropical layer around the tropopause, where air masses have been observed with mixed stratospheric and tropospheric characteristics (*Gettelman et al.*, 2011). Enhanced transport into the stratosphere occurs due to the very deep summer monsoon convection over Southeast Asia (*Lelieveld et al.*, 2007), indicated by enhanced mixing ratios of tracers like methane, CO, N_2O and SF_6 found in the lowermost stratosphere, cf. *Schuck et al.* (2010).

2.2.2. Global Circulation Patterns

Atmospheric circulation is very complex, containing variations on different spatial and temporal scales, therefore the following brief summary, mainly focusing on the tropospheric circulation, is only a very broad description of some, regularly observed, features. For a concrete position and time, the reality can strongly differ.

Air having been lifted upwards in the ITCZ flows polewards in the upper troposphere and lower stratosphere (UTLS). Because of the Coriolis force (Sect. 2.2.1), it is deflected more and more eastwards (in both, the northern hemisphere as well as in the southern hemisphere). As consequence, the air does not (directly) reach the poles, but moves eastwards in latitudes around 30–35° N, cf. Fig. 2.2. There it sinks down into the lower troposphere where it flows back to the equator (however, a part of the air moves further polewards, see below). Again, the Coriolis force deflects the air, leading to the *trade winds* in the tropics – northeasterly winds in the northern tropics and southeasterly winds in the southern tropics. This circulation pattern between about 30° S and 30° N is called *Hadley cell* after George Hadley for his studies on the explanation of the trade

winds (*Hadley*, 1735).

In higher latitudes, the *Ferrel cell* (after William Ferrel) follows, reaching until ∼60° N or 60° S. Its meridional cycle has an opposite direction. Here, the lower air masses move polewards, typically with a wind component from the west. However, the *west wind drift* is less regular than the trade winds in the tropics. Instead, winds from different directions are superposed, and large weather fronts, cyclones (in low pressure areas on the northern hemisphere) and anticyclones (high pressure, northern hemisphere) are observed. In principle, the west wind drift can be interpreted as thermal wind caused by the temperature difference between the tropics and the polar region (*Roedel*, 2000, p. 128).

The poles are surrounded by circumpolar eastern winds, predominantly in the lower altitudes (below 3 km). These winds are *fall winds* (also *katabatic winds*) – the air descends near the poles, than moves southwestwards until it mets the air from the west wind drift in the *subpolar low pressure belt* (also 'subpolar trough') between 50° and 70° latitude.

2.3. Chemistry

In this section, an overview of the atmospheric composition is given, followed by a brief description of chemical processes of those compounds measured by our DOAS system.

2.3.1. Atmospheric Composition

Species		**Volume Mixing Ratio**
Nitrogen	N_2	78 %
Oxygen	O_2	21 %
Argon	Ar	0.93 %
Carbon dioxide	CO_2	390 ppm
Neon	Ne	18 ppm
Helium	He	5.2 ppm
Methane	CH_4	1.8 ppm
Krypton	Kr	1.1 ppm
Hydrogen	H_2	550 ppb
Nitrous oxide	N_2O	330 ppb
Xenon	Xe	90 ppb

Table 2.1.: Composition of the atmosphere. Especially the mixing ratios of the short-lived gases contain large spatial and temporal variability, therefore, these species are not listed here. The values given here are taken from *IPCC* (2007), *Roedel and Wagner* (2011), *Platt and Stutz* (2008) and *Fontaine et al.* (2004).

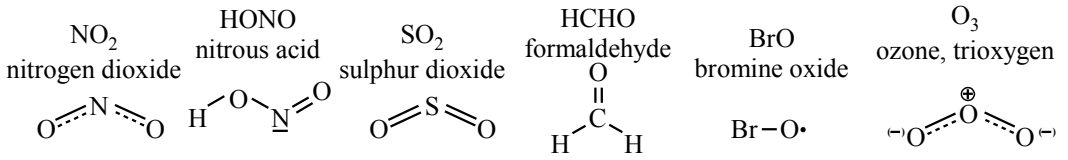

Figure 2.3.: Structural formulas of some gases mentioned in this chapter

It is believed that about four billion years ago, the atmosphere mainly consisted of carbon dioxide, nitrogen and water vapour. After the atmosphere cooled down, water condensed and CO_2 was washed out, predominantly being dissolved in the oceans, forming sedimentary carbonate rocks (*Seinfeld and Pandis*, 2006, p. 1). More and more, the nitrogen fraction grew. With the photosynthesis of plants, also the oxygen mixing ratio grew. Today, nitrogen and oxygen contribute to 99 % of the atmosphere (with respect to volume), another 0.9 % is contributed by Argon. Although the other gases in total contribute less than 0.1 % of the atmosphere, some of them play a key role in atmospheric chemistry and influence temperature due to the greenhouse effect, cf. Sect. 3.5.

Table 2.1 lists some of the most abundant trace gases with a rather uniform distribution in the atmosphere. Because the sources and sinks of nitrogen and oxygen are small compared to the atmospheric content, the mixing ratio of these gases is nearly constant within the homosphere (cf. 2.1.2). The same is true for the mixing ratio of those chemical widely inert gases, which have no strong sinks and sources.

A different behaviour is observed for water content (therefore not included in Table 2.1). Water exists in the atmosphere in all three phases (as water vapour, cloud droplets and ice particles) with strongly different amounts with respect to time and space – water vapour mixing ratios on the order of ppm until more than a percent can be found. Zonally averaged, the highest water content is found in the tropics around the equator (actually it is slightly shifted to the north due to the ITCZ, cf. Sect. 2.2), and the lowest in polar regions. Furthermore, the water content decreases with altitude because ascending air condenses due to the lower temperature in higher regions. The water content in the atmosphere and its spatial distribution has a major influence on the climate. It has a direct effect on the temperature due to the absorption and reflection of visible light (especially liquid and solid water particles in clouds) and the absorption of IR radiation (cf. Sect. 3.5). Furthermore it influences the circulation and energy transport due to the latent heat of moist air parcels, and the amount of precipitation affects the fertility of the landmasses. Therefore, the response of the hydrological budget to temperature changes and its feedback represents one of the largest uncertainties for predictions about climate change.

The currently most noted greenhouse gas carbon dioxide (CO_2) is in a rough approximation evenly distributed in the homosphere, but with a positive trend due to enhanced anthropogenic emission in the last decades (and centuries). This trend is overlaid by

an annual cycle. In spring and summer, plants act as a net sink of CO_2 due to their photosynthesis; in autumn and winter they act as a net source. Therefore, the seasonal cycle of the CO_2 content is shifted between the northern and the southern hemisphere by half a year. Because more land masses and thus more plants are in the northern hemisphere, this cycle is stronger in the northern hemisphere. Furthermore, some delay is observed in higher altitudes due to the transport time from the surface. Reactive gases with a short lifetime are mainly observed close to their source position (e.g. SO_2, Sect. 2.3.7) and some gases have a pronounced diurnal cycle due to photochemistry (e.g. NO_x, Sect. 2.3.2).

Aerosol

The air is an *aerosol*, a mixture of gaseous species, liquids and solid aerosol particles. Major sources of aerosol particles (the so-called *particulate matter*, PM) are the oceans (sea spray), plants (terpenes, pollen), soils (Saharan dust storms), volcanoes, biomass burning, stoves, traffic and industry. Accordingly, there is a large variety of the elemental composition (e.g. sulphuric compounds from volcanoes, mineral dust over the Sahara, organic compounds from biomass burning). The size of the particles (usually given in terms of a diameter d) ranges between a nanometer (nanoparticles) and around ten micrometers. Cloud and rain droplets, ice crystals, snow flakes and hailstones, which can reach diameters of several millimeters or even centimeters, are not counted among the aerosol particles. The particles are classified into a *fine mode* ($d < 1\mu$m) and a *coarse mode* ($d > 1\mu$m). With PM_1, $PM_{2.5}$ and PM_{10}, particles with a diameter below 1, 2.5 or 10 μm are subsumed. This categorisation is used for limitations of the particulate matter content in urban areas, because particles smaller than approximately 5 μm can reach the lower respiratory tract (*Taylor et al.*, 2002), which can lead to adverse health effects.

High PM concentrations are regularly found in urban and industrial areas, especially during inversions and low wind situations. The horizontal and vertical distribution of aerosol particles depends on their atmospheric residence time τ, which depends on the particle size. Small particles ($\lesssim$0.1 μm) grow by nucleation and coagulation typically during a few hours. For particles with a size of some hundred nanometer to some micrometer, washout is the dominant removal process from the atmosphere, therefore the lifetime of such aerosol particles typically ranges from days to weeks, depending on the meteorological conditions, cf. *Roedel* (2000, p. 409), *Jaenicke* (1978). With larger particles, sedimentation gets more important, therefore such heavy particles are mainly present in the lower troposphere not far from their sources (except for the case of strong convection or advection).

Aerosol particles have a direct effect on the radiation budget. They can absorb visible light (leading to a cooling effect) and thermal radiation (heating effect), and they scatter radiation (cf. Mie and Rayleigh scattering, Sect. 3.2). But they also have an indirect

climate effect, because they influence the occurrence, chemical composition and reflectivity of clouds and precipitation by acting as condensation nuclei for water droplets and ice crystals, e.g. *Cruz and Pandis* (1998), *Ramanathan et al.* (2001). Without such *cloud condensation nuclei* (CCN), high oversaturations (humidities above 100 %) would occur, bevor gaseous water condensates. Furthermore, aerosol particles are involved in a complex multiphase chemistry with atmospheric gases (e.g. *Ravishankara*, 1997).

2.3.2. Nitrogen Species, Nitrogen Oxides

Nitrogen Species are emitted into the atmosphere mainly in the form of three compounds, namely nitrous oxide (N_2O), nitric oxide (NO) and ammonia (NH_3) (*Roedel and Wagner*, 2011, p. 453). As they are involved in various reactions, further nitrogen species are formed, amongst them nitrogen dioxide (NO_2) and nitrous acid (HONO), two substances with absorption structures in the UV/VIS range and therefore detectable by the CARIBIC DOAS instrument, cf. Chap. 7. In *Glickman* (2000), *nitrogen oxides* are listed as "Family of compounds in which nitrogen is bound to oxygen" with nitrous oxide (N_2O) as the most abundant representative. However, in atmospheric chemistry, usually only NO and NO_2 are counted among the nitrogen oxides. 'NO_y' is used for *total reactive nitrogen* species, which are oxidized forms of nitrogen like NO, NO_2, HONO, HNO_3 and organic nitrates (*Glickman*, 2000). In *Ziereis et al.* (2000), the following definition of total reactive nitrogen can be found: "NO_y = NO + NO_2 + NO_3 + PAN + HNO_3 + HNO_2 + HNO_4 + $2N_2O_5$ + organic nitrates + aerosol nitrates"; *Seinfeld and Pandis* (2006, p. 37) states: "Reactive nitrogen, denoted NO_y, is defined as the sum of the two oxides of nitrogen (NO_x = NO + NO_2) and all compounds that are products of the atmospheric oxidation of NO_x."

Nitrous oxide (N_2O, also called *sweet air* or *laughing gas*) is emitted naturally from oceans and soil, mainly by bacterial processes (denitrification), and biomass burning. According to *IPCC* (2007, p. 3), "More than a third of all nitrous oxide emissions are anthropogenic and are primarily due to agriculture", and its "concentration increased from a pre-industrial value of about 270 ppb to 319 ppb in 2005". Because it is relatively unreactive, it has an atmospheric lifetime of roughly 110 years. N_2O has a global warming potential roughly 300 times that of CO_2 for a time horizon of 100 years (∼150 times for a horizon of 500 years). In the stratosphere, it is the dominant source of reactive nitrogen (*Platt and Stutz*, 2008, p. 16), cf. (2.50) p. 25.

The nitrogen oxides in a narrow sense are *nitric oxide* (NO, also *nitrogen oxide* or *nitrogen monoxide*) and *nitrogen dioxide* (NO_2, a toxic gas with a brown colour), subsumed as 'NO_x'. They are mainly produced at high temperatures like in combustion processes. Natural sources include biomass burning and soil emissions from microbial production. Apart from ground bases sources, lightning strikes during storms produce NO_x. Further but rather small contributions are given by the oxidation of ammonia (NH_3) and the decomposition of N_2O in the stratosphere, cf. *Lee et al.* (1997). To

a similar amount to natural sources, anthropogenic activities contribute to the NO_x production. Besides power stations and industrial facilities, the transport sector (automobiles, ships and aircrafts) plays an increasing role. Further contributions come from the warming of houses and burning wood (e.g. cooking stoves). A significant part of the biomass burning is caused by shifting cultivation for extending agricultural areas, also the artificial fertilisation influences the soil emission. The predominant process for the direct NO_x formation in combustion processes is the *extended Zeldovich mechanism* in which NO is formed from originally molecular nitrogen and oxygen and from the hydroxyl radical (OH), cf. *Miller and Bowman* (1989).

$$O + N_2 \longrightarrow NO + N \tag{2.11}$$

$$N + O_2 \longrightarrow NO + O \tag{2.12}$$

$$N + OH \longrightarrow NO + H \tag{2.13}$$

This process needs high temperatures ($T \gtrsim 2200\,K$) to break the bonds of the otherwise inert N_2. In exhaust gases, only a small fraction of NO_x consists of NO_2, but within several minutes, NO is oxidized to NO_2 in the presence of ozone.

$$NO + O_3 \longrightarrow NO_2 + O_2 \tag{2.14}$$

On the other hand, NO_2 can be photolysed back into NO and atomic oxygen, which than forms ozone together with molecular oxygen.

$$NO_2 \xrightarrow[\lambda \leq 420\,\mathrm{nm}]{h\nu} NO + O \tag{2.15}$$

$$O + O_2 + M \longrightarrow O_3 + M \tag{2.16}$$

For the dissociation of NO_2 the photon energy of $\approx$3 eV or more is necessary, which corresponds to $\lambda \leq 420\,\mathrm{nm}$. The reaction between O and O_2 needs a third partner M (catalyst) in order to fulfill the conservation of momentum and energy. The three reactions (2.14), (2.15) and (2.16) built a dynamical equilibrium, which is given by the *Leighton ratio* (*Leighton*, 1961).

$$L_{\mathrm{Leighton}} := \frac{[NO]}{[NO_2]} = \frac{J_{NO_2}}{k \cdot [O_3]} \tag{2.17}$$

Here, '[ ]' denotes the concentration of the respective substance and $J_{\mathrm{photo}}(NO_2)$ the photolysis frequency for (2.15). The reaction constant k_2 for (2.14) is given by $k_2 = 10^{-14}\mathrm{cm^3 s^{-1}}$ (*Atkinson et al.*, 2004). During daytime, L_{Leighton} is on the order of 0.1 to 1 (see also Sect. 7.5.8), meaning that NO_x mainly consists of NO_2 after the plume has reached some distance from the source.[8] During night time, virtually no NO is present in source remote regions.

[8] In case of a large NO point source, the conversion of NO to NO_2 can take several kilometers when ozone is limited (cf. *Walter*, 2008, p. 130).

The removal from NO_2 from the atmosphere occurs in form of several reactions, mainly ending in form of nitric acid (HNO_3), which again is removed by several processes like dry deposition and rainout (*Platt and Stutz*, 2008, p. 34). One of those processes is the direct conversion of NO_2 into HNO_3 in the presence of the hydroxyl radical (OH).

$$NO_2 + OH + M \longrightarrow HNO_3 + M \tag{2.18}$$

Sources of OH are nitrous acid (2.24) and especially ozone (indirectly), reacting with water (e.g. *Talukdar et al.*, 1998):

$$O_3 \xrightarrow[\lambda \leq 310\,\mathrm{nm}]{h\nu} O_2 + O(^1D) \tag{2.19}$$

$$O(^1D) + H_2O \longrightarrow 2\,OH \tag{2.20}$$

In both cases, (2.19) and (2.24), a photolytic dissociation occurs, therefore (2.18) takes only place during daytime. During night, however, NO_3 and N_2O_5 are produced as intermediate products, the latter one than reacts in a heterogeneous reaction with liquid water to HNO_3.

$$\begin{array}{rcl} NO_2 + O_3 & \longrightarrow & NO_3 + O_2 \\ NO_3 + NO_2 + M & \longrightarrow & N_2O_5 + M \\ N_2O_5 + H_2O & \xrightarrow{\text{het}} & 2\,HNO_3 \\ \hline \text{net:}\quad 2\,NO_2 + O_3 + H_2O & \longrightarrow & O_2 + 2\,HNO_3 \end{array} \tag{2.21}$$

Because the nitrate radical (NO_3) is rapidly photolysed during daytime, this process is only relevant during nighttime.

2.3.3. Nitrous Acid

Nitrous Acid (HONO) was first observed in the atmospheric by DOAS measurements (*Perner and Platt*, 1979; *Platt et al.*, 1980). It is found in the atmosphere with typical mixing ratios in the range of 0–15 ppb (cf. *Platt and Stutz* (2008, p. 46) and references therein). The major gas-phase reaction forming HONO is the reaction of NO with OH.

$$OH + NO + M \longrightarrow HONO + M \tag{2.22}$$

Furthermore, it is produced in heterogeneous reactions of NO_2 on surfaces (aerosol particles, ground), predominantly

$$2\,NO_2 + H_2O \longleftrightarrow HONO + HNO_3 \tag{2.23}$$

(e.g. *Sakamaki et al.*, 1983). Details about those mechanisms are yet unknown; especially for urban areas, soot aerosol particles and asphalt have been suggested as possible surface. In contrast, NO_2 reactions with secondary organic aerosols are not assumed to be important (*Bröske et al.*, 2003). Also in snow, formation of HONO takes place

(e.g. *Clemitshaw*, 2006). HONO is indirectly (via NO_x) and directly emitted by combustion processes, which plays a significant role in heavily polluted areas (*Stutz et al.*, 2002). HONO also was found in deep convective clouds due to lightning induced NO_x production, cf. *Dix et al.* (2009), *Heue et al.* (2013). However, the source strengths attributed to these mechanisms are not high enough to explain the measured HONO concentrations. Recent studies propose soil nitrite as a strong HONO source, based on biological nitrification and denitrification processes; thus, the release of HONO is assumed to increase with enhanced fertilizer use (*Su et al.*, 2011).

The major removal process for HONO is the photolysis with light with wavelengths between 300 nm and 405 nm, producing NO and OH radicals.

$$\mathrm{HONO} \xrightarrow[300\,\mathrm{nm} < \lambda < 420\,\mathrm{nm}]{\mathrm{h}\nu} \mathrm{NO} + \mathrm{OH} \tag{2.24}$$

In the early morning, the highest HONO mixing ratios occur. With sunset, more and more HONO is photolysed, leading to a morning peak in the HONO degradation. During this peak time, this process is the strongest contributor to OH production (measurements in Milan by *Alicke et al.* (2002)). Also in polar regions, the HONO photolysis can be the dominant OH source (*Li*, 1994). HONO is also degraded by OH, forming H_2O and NO_2 (*Platt and Stutz*, 2008, p. 47).

$$\mathrm{OH} + \mathrm{HONO} \longrightarrow \mathrm{H_2O} + \mathrm{NO_2} \tag{2.25}$$

A self-reaction of HONO, namely $\mathrm{HONO} + \mathrm{HONO} \longrightarrow \mathrm{NO_2} + \mathrm{NO} + \mathrm{H_2O}$ exists, but it is not relevant in the atmosphere, cf. *Kaiser and Wu* (1977), *Mebel et al.* (1998), *Stutz et al.* (2002). Furthermore, HONO is taken up by plants (*Schimang et al.*, 2006) and several heterogeneous reactions have been studied (e.g. *Clemitshaw*, 2006).

2.3.4. Formaldehyde

Formaldehyde (IUPAC name *methanal*, empiric formula HCHO or CH_2O) is the simplest species of the aldehydes (organic compounds containing a formyl group R−CHO). These again belong to the *volatile organic carbons* (VOCs), which are organic chemicals with a high vapor pressure under normal atmospheric temperatures, or whose boiling point is even below (as it is the case for formaldehyde with about -20 °C). In particular for *oxidized* VOCs like the aldehydes, also the acronym 'OVOC' is commonly used. HCHO is toxic, which can lead to adverse health effects inside buildings where it can off-gas e.g. from processed wood products like particle boards or be produced as by-product in indoor combustion (*Spengler and Sexton*, 1983). It is soluble in water, forming methanediol (formalin). Like other VOCs, HCHO contributes to the 'Los Angeles-type smog', e.g. *Hanst et al.* (1982) or *Calvert* (1976).

HCHO is the most abundant aldehyde in the atmosphere (*Peters et al.*, 2012). It is a product of the photochemical degradation of the rather evenly distributed methane

(CH_4) and other hydrocarbons, resulting in a background concentrations of about 0.2–1 ppbv in remote marine environments (*Weller et al.*, 2000). HCHO and other VOCs are emitted by fossil fuel consumption due to incomplete combustion and losses before the combustion (*Platt and Stutz*, 2008, p. 21; *Anderson et al.*, 1996); also the refining of oil and other industrial processes produce VOCs. Furthermore, HCHO is released from soils and emitted by plants and biomass burning (*Seco et al.*, 2007; *Kesselmeier*, 2001). As a major indirect source of HCHO, the photooxidation of methane is considered through several reactions pathways including CH_3, CH_3O_2, CH_3O and CH_3OOH as intermediate products; also the photooxidation of non-methane hydrocarbons (NMHCs) like ethane (C_2H_4), propene (C_3H_6) and isoprene (C_5H_4) yield HCHO, cf. *Weller et al.* (2000).

HCHO is degraded by photolysis with UV light, producing carbon monoxide or HCO and hydrogen radicals (*Weller et al.*, 2000).

$$HCHO \xrightarrow{h\nu} CO + H_2 \tag{2.26}$$

$$HCHO \xrightarrow{h\nu} HCO + H \tag{2.27}$$

It also influences the OH chemistry, here by the production of the HO_2 radical:

$$OH + HCHO \longrightarrow HCO + H_2O \tag{2.28}$$

$$CHO + O_2 \longrightarrow HO_2 + CO \tag{2.29}$$

According to *Arlander et al.* (1995), the degradation of HCHO is the major direct source for the global budgets of carbon monoxide (CO) and molecular hydrogen (H_2). HCHO is also removed by wet deposition, and it can be taken up by plants (*Seco et al.*, 2007). As consequence, it has an atmospheric lifetime of only a few hours, depending on the available light, OH and humidity. An average tropospheric lifetime of about 5 h is given by *Arlander et al.* (1995). Therefore, HCHO does not accumulate in the atmosphere on a larger spatial or temporal range, and enhanced HCHO values are found close to their sources like forests, biomass burnings, cities or ship routes (cf. *Marbach et al.*, 2009).

2.3.5. Bromine oxide

Because they only miss one electron with respect to nobel gas configuration, the halogens are highly chemical reactive, comprising the elements fluorine (F), chlorine (Cl), bromine (Br), iodine (I) and astatine (At). Chlorofluorocarbons (CFCs) are quite stable in the troposphere, however, they can be photolytical degraded by UV light in the stratosphere, leading to ozone depletion ('ozone hole', cf. Sect. 2.3.6). Astatine is radioactive with a lifetime of only several hours, thus, it is not relevant in atmospheric chemistry. Also chlorine, bromine and iodine are present in the atmosphere with only low concentrations, but they play a key role in the stratosphere and the polar boundary layer with respect to ozone depletion. Here, only a few reactions of bromine oxide (BrO)

are given, some of them also apply for ClO and IO; for details see various literature, e.g. *Wayne et al.* (1995) or *Simpson et al.* (2007).

BrO is formed in the lower atmosphere by the degradation of organic halogen compounds (e.g. CH_3Br, $CHBr_3$, CH_2Br_2) or by the oxidation of sea salt aerosol (*Platt and Hönninger*, 2003; *Wayne et al.*, 1995), which contains 55.7 % Cl, 0.19 % BrO and 0.2 ppm of I with respect to their mass (*Platt and Janssen*, 1995). Furthermore, BrO is formed within volcanic plumes, cf. *Bobrowski et al.* (2003): HBr emitted by the volcano is quickly converted to other substances (cf. *von Glasow* (2010) for details), amongst them molecular Br, which reacts with ozone (2.39). For typical tropospheric background ozone mixing ratios of ∼30 ppb, the time constant for this reaction is on the order of 1 s (*Bobrowski and Platt*, 2007; *Platt and Hönninger*, 2003), but within the volcanic plume, ozone is rapidly depleted. Depending on the amount of bromine and the mixing efficiency with the ambient air, this BrO formation needs on the order of an hour (than, the BrO accounts for roughly 15 % of the total gas phase bromine). This enrichment of BrO in the emerging plume can be observed by making simultaneous measurements of SO_2 in the plume. Regarding SO_2 as an 'inert reference tracer' (which is approximately true for short time periods of ∼1 h), the mixing ratio $[BrO]/[SO_2]$ correlates with the plume age (cf. *Bobrowski and Platt*, 2007).

BrO is dissolved by photolysis

$$BrO \xrightarrow{h\nu} Br + O \tag{2.30}$$

or by reaction with itself or other other halogen compounds:

$$BrO + XO \longrightarrow Br + X + O_2 \tag{2.31}$$

$$BrO + XO \longrightarrow BrX + O_2 \tag{2.32}$$

with X standing for Cl, Br or I. It can also react with HO_2 to form HOBr which is than photolysed to OH and Br.

$$BrO + HO_2 \longrightarrow HOBr + O_2 \tag{2.33}$$

$$HOBr \xrightarrow{h\nu} Br + OH \tag{2.34}$$

By this process (which also applies to Cl and I), HO_2 is converted to OH, thus influencing the atmospheric oxidation capacity (*Platt and Hönninger*, 2003). In volcanic plumes, sources for the needed HO_2 could be the oxidation of SO_2 or hydrogen (*Bobrowski and Platt*, 2007; *Gerlach*, 2004). Molecular Br can react according to (2.39) to again form BrO, or with formaldehyde, producing HBr (*Platt and Hönninger*, 2003).

$$Br + HCHO \longrightarrow HBr + CHO \tag{2.35}$$

Because HBr is water soluble, it can be removed from the atmosphere by deposition. Otherwise, HBr can be converted back to Br (and therefore to BrO, 'BrO recycling')

by reaction with OH

$$\mathrm{HBr + OH \longrightarrow Br + H_2O} \tag{2.36}$$

With a typical mixing ratio [HBr]/([BrO]+[Br]) between 10 and 20, HBr is the most abundant inorganic bromine species in the free troposphere (*Bobrowski and Platt*, 2007), acting as reservoir gas for Br; other reservoirs are $BrONO_2$ and HOBr.

The latter one, HOBr, is involved in heterogeneous reactions with surface Br^-, leading to the liberation of a Br_2 molecule, which can lead to the so-called *Bromine activation* or *Bromine explosion* (*Wennberg*, 1999; *Fan and Jacob*, 1992; *McConnell et al.*, 1992), which is summarized by the following reaction sequence (cf. *Simpson et al.*, 2007, p. 4381).

$$\mathrm{HOBr + (Br^-)_{surface} + H^+ \longrightarrow Br_2 + H_2O} \tag{2.37}$$

$$\mathrm{Br_2 \xrightarrow{h\nu} 2\,Br} \tag{2.38}$$

$$\mathrm{Br + O_3 \longrightarrow BrO + O_2} \tag{2.39}$$

$$\mathrm{BrO + HO_2 \longrightarrow HOBr + O_2} \tag{2.40}$$

$$\text{net: } \mathrm{H^+ + (Br^-)_{surface} + HO_2 + O_3 \xrightarrow{h\nu} Br + H_2O + 2\,O_2} \tag{2.41}$$

If Br_2 is photolysed in the presence of UV light, two Br radicals can form two BrO molecules by the reaction with ozone (2.39). After conversion of this two Br radicals to two HOBr molecules via (2.40), the next two Br^- ions can be released from the particle. As long as HOBr is the limiting factor of (2.37), this leads to an exponential growth in the production rate of reactive gas phase bromine (Br or BrO), therefore the term 'explosion'.

The main source for the bromine explosion is sea salt. In the Arctic troposphere, bromine can accumulate in the dark winter; than, in springtime, photolysis (2.38) initiates the reaction cycle of the bromine explosion. Such events can be observed by satellite measurements (*Wagner and Platt*, 1998; *Sihler et al.*, 2012; *Sihler*, 2012), also the CARIBIC DOAS system has observed them, cf.Sect. 7.3. Bromine explosions also take place in fresh volcanic plumes (e.g. *Bobrowski et al.*, 2007; *Heue et al.*, 2011).

While typically BrO mixing ratios of a few to several tens of ppt have been measured in the polar boundary layer (*Simpson et al.* (2007) and references therein), the average tropospheric mixing ratio is on the order of 1 ppt (*Platt et al.* (2004), *von Glasow et al.* (2004) and references therein). The highest average BrO concentrations occur in the lower stratosphere (∼15–22 km); the highest mixing ratios on the order of 10 ppt have been found at ∼25–30 km (*Pundt et al.*, 2002). In the stratosphere, BrO and other reactive halogen species are involved in the destruction of ozone, cf. (2.3.6).

2.3.6. Ozone

Ozone is a reactive trace gas which is produced in the stratosphere and in much lower concentrations in the troposphere. The total atmospheric column of ozone is on the

order of 300 Dobson Units (DU, $1\,\mathrm{DU} = 2.69 \cdot 10^{16}\,\mathrm{molec/cm^2}$), with strong seasonal variations predominantly in higher altitudes and polar regions, were over 450 DU are reached in late winter, cf. *Roedel and Wagner* (2011, p. 405) and references therein. On average, ∼90% of the total ozone column is located in the stratosphere (*Seinfeld and Pandis*, 2006, p. 53). The averaged tropospheric ozone mixing ratio is on the order of 30 ppb (cf. *Dütsch*, 1978; *Warneck and Williams*, 2012 p. 70), but strongly depends on temperature and the abundance of VOCs and nitrogen oxides. In the stratosphere, the mixing ratio increases with height until a maximum mixing ratio on the order of 10 ppm at ∼35 km altitude, above it decreases again (*Roedel and Wagner*, 2011, p. 404). In contrast to the mixing ratio, the ozone concentration peaks around 15–30 km (*Roedel and Wagner*, 2011, p. 17; *Dütsch*, 1978).

The ozone cross section contains two absorption bands in the UV range, namely the Hartley band (∼200–300 nm), and the Huggins band (∼310–380 nm, which is within the measurement range of the CARIBIC DOAS instrument), e.g. *Voigt et al.* (2001). This effect of shielding the earth's surface from UV light makes (stratospheric) ozone important for life on land, because UV light destroys biologic cells *Diffey* (1991). In the boundary layer, however, the toxic ozone has adverse effects for humans, animals and plants when present in high concentrations, which can occur in the presence of VOCs and NO_x. Furthermore, "Tropospheric ozone is (after CO_2 and CH_4) the third most important contributor to greenhouse radiative forcing" (*IPCC*, 2007, p. 547).

Stratospheric Ozone

The stratospheric ozone production is mainly based on the photolysis of oxygen. UV light with $\lambda < 240\,\mathrm{nm}$ can crack O_2 into two oxygen atoms in the ground state, which is typically indicated by the notation '$O(^3P)$'.

$$O_2 \xrightarrow[\lambda < 242\,\mathrm{nm}]{h\nu} O(^3P) + O(^3P) \tag{2.42}$$

These oxygen atoms can react with O_2 to form ozone.

$$O + O_2 + M \longrightarrow O_3 + M \tag{2.43}$$

On the other hand, ozone is decomposed by reactons with $O(^3P)$ or by photolysis (*Talukdar et al.*, 1998).

$$O(^3P) + O_3 \longrightarrow O_2 + O_2 \tag{2.44}$$

$$O_3 \xrightarrow{h\nu} O(^1D \text{ or } {}^3P) + O_2 \tag{2.45}$$

Furthermore, but with less probability, oxygen atoms can be removed from this cycle by

$$O(^3P) + O(^3P) + M \longrightarrow O_2 + M \tag{2.46}$$

These reactions belong to the so-called *Chapman cycle* (*Chapman*, 1930), which was devoloped in the 1920, predicting a steady state ozone mixing ratio. With this cycle,

the stratospheric ozone maximum can be explained (lack of UV radiation for (2.42) in the troposphere, lack of collision partner M in (2.43) in the upper stratosphere), but the mixing ratios predicted by the Chapman cycle were too high compared to measurements. Since the 1960s, new reactions leading to ozone production and ozone loss have been found, particularly catalytic cycles in the form of

$$\begin{aligned} O_3 + Z &\longrightarrow ZO + O_2 && (2.47)\\ ZO + O(^3P) &\longrightarrow Z + O_2 && (2.48)\\ \text{net:}\quad O(^3P) + O_3 &\xrightarrow{Z} O_2 + O_2 && (2.49) \end{aligned}$$

with Z being a substitute for the catalyst., i.e. Cl, Br, NO or OH (cf. *Platt and Stutz*, 2008, p. 67, 68). In the case of the NO_x cycle (cf. *Crutzen*, 1971), NO is converted to NO_2 (2.47) and back (2.48). The major precursor for stratospheric NO_x is N_2O (Sect. 2.3.2), which is transported to the stratosphere due to its long lifetime, where it reacts with atomic oxygen to NO:

$$N_2O + O(^1D) \longrightarrow 2\,NO \qquad (2.50)$$

A source for the excited oxygen atom represents (2.19) p. 19.

The so-called *ozone hole*, a strong decrease of the ozone column, which has been observed in the Antarctic spring since the late 1970s, is also based on the catalytic ozone destruction (2.47)–(2.49), in that case with Cl as catalyst, which had been released into the atmosphere in form of CFCs. While inactive during winter, chlorine is activated with the occurence of sunlight. In this context, heterogeneous reactions in Polar Stratospheric Clouds (PSCs) are needed, which are formed under temperatures below ∼190 K (e.g. *Voigt et al.* (2000) and references therein).

Tropospheric Ozone

Some fraction of the tropospheric ozone originates from the stratosphere ('stratosphere-troposphere exchange', STE), but the predominant fraction is produced in the troposphere itself (cf. *IPCC*, 2007, p. 547–549). The main reactions are (2.15) p. 18 and (2.16). The NO produced in (2.15) can be recycled (converted back to NO_2) according to (2.14), but in that case, the net ozone production of these three reactions is zero, and the equilibrium between NO and NO_2 is described by the Leighton ratio (2.17).

In order to obtain a net ozone production, the NO_x recycling of (2.14) has to be replaced by non ozone destructive reactions. This can be performed by hydrogen radicals (OH and HO_2, summarized as 'HO_x') or other peroxy radicals (RO_x) in a calatlyic cycle, e.g.

$$HO_2 + NO \longrightarrow NO_2 + OH \qquad (2.51)$$

$$OH + CO \longrightarrow CO_2 + H \qquad (2.52)$$

$$O_2 + H + M \longrightarrow HO_2 + M \qquad (2.53)$$

Hereby, NO is recycled back to NO_2 (without O_3 desctruction), while CO is converted to CO_2. Combining equations (2.15), (2.16), (2.51), (2.52) and (2.53) leads to a net ozone production:

$$\begin{aligned}
NO_2 &\xrightarrow[\lambda \leq 420\,\mathrm{nm}]{h\nu} NO + O \\
O + O_2 + M &\longrightarrow O_3 + M \\
HO_2 + NO &\longrightarrow NO_2 + OH \\
OH + CO &\longrightarrow CO_2 + H \\
O_2 + H + M &\longrightarrow HO_2 + M \\
\hline
\text{net:}\quad 2\,O_2 + CO &\longrightarrow CO_2 + O_3
\end{aligned} \tag{2.54}$$

cf. *Platt and Stutz* (2008, p. 24) for a schematic sketch summarizing these reactions. Similar or more complex reaction chains occur with hydrocarbons like methane and other VOCs instead of CO, or as precursor of CO (e.g. the CO production (2.26) by HCHO). In urban areas, both are available, NO_x as catalyst and VOCs as 'fuel', leading to high ozone concentrations (smog, cf. Sect. 2.3.4). Depending on their abundance, the terms 'VOC limited' or 'NO_x limited' are used. For the case of a VOC limited regime, an enhancement of NO_x can even lead to a reduction of the O_3 production, cf. *Sillman et al.* (1990).

Sinks of tropospheric ozone are chemical reactions and dry deposition: According to *Seinfeld and Pandis* (2006, p. 228), "Ozone loss occurs roughly as $O(^1D)$ + H_2O $\sim 40\%$; O_3 + HO_2 $\sim 40\%$; O_3 + OH $\sim 10\%$". Further information are given by *Roedel and Wagner* (2011, p. 422ff), *Seinfeld and Pandis* (2006, p. 227ff).

2.3.7. Sulphuric compounds

Sulphur is present in the atmosphere in the form of several substances in gaseous phase and as constituents of particles or dissolved in water droplets. The most important sulphur compounds are carbonyl sulphide (COS), dimethyl sulphide (DMS, CH_3SCH_3), hydrogen sulphide (H_2S) and sulphur dioxide (SO_2), furthermore dimethyl disulphide (DMDS, CH_3SSCH_3), carbon disulphide (CS_2), sulphuric acid (H_2SO_4) and methansulphonic acid (MSA, CH_3SO_3H). Natural sources of sulphur compounds are soils and the ocean, mainly emitting COS, H_2S and DMS, and volcanoes emitting SO_2 (*Platt and Stutz*, 2008, p. 19). The anthropogenic emissions predominantly consist of SO_2, see below. In a simplified summary of the sulphur cycle; atmospheric SO_2 is formed due to direct emission or from the precursors DMS, COS and H_2S, which are briefly introduced in the following paragraphs. Afterwards, SO_2 is directly removed by dry deposition or after conversion into other substances (SO_3, H_2SO_4, SO_4^{2-}); see Fig. 2.4 for an overview.

Carbonyl sulphide (abbreviated as 'COS' or 'OCS', the latter one following to the structural formula, cf. Fig. 2.3) is a result of biological processes, particularly in saline

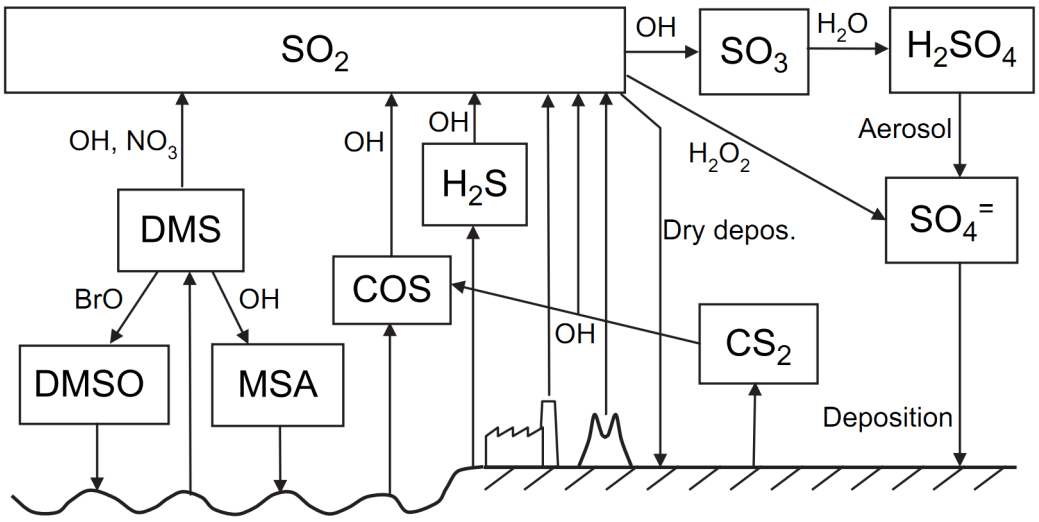

Figure 2.4.: Overview over the atmospheric sulphur cycle (From *Platt and Stutz*, 2008, p. 51)

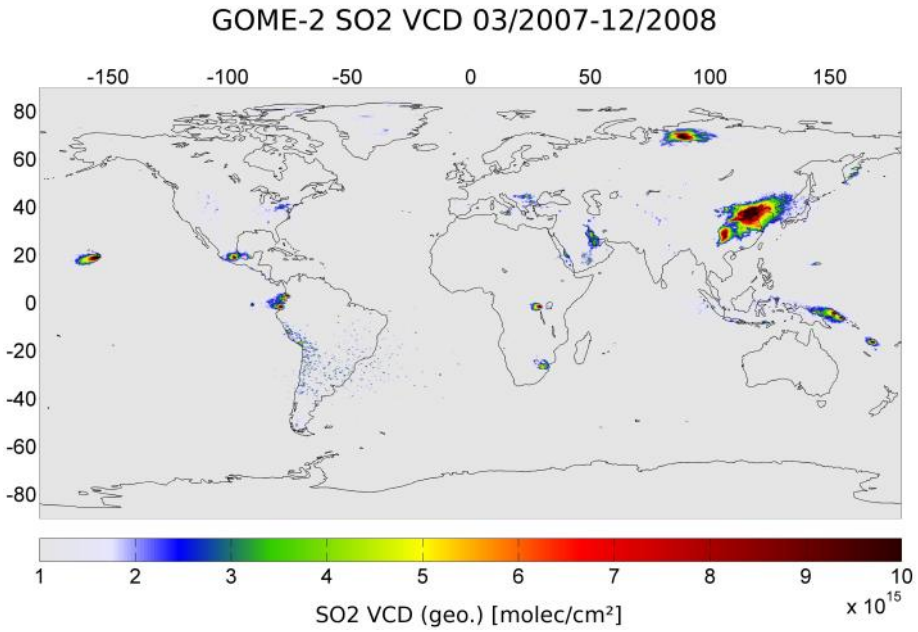

Figure 2.5.: GOME-2 SO_2 measurement (average over the time from March 2007 to December 2008) From C. Hörmann (Satellite Group of the Max Planck Institute for Chemistry).

ecosystems like oceans, salt marshes and estuaries (cf. *Brühl et al.*, 2012). COS is produced by photochemical reactions in sea water and precipitation, cf. *Andreae* (1990), *Mu et al.* (2004). Furthermore, it is produced by the oxidation of reduced sulphur gases, mainly DMS and CS_2 (*Brühl et al.*, 2012). Also wetlands anoxic soils, volcanoes and biomass burning and anthropogenic activities add to the COS production (*Watts*, 2000; *Crutzen*, 1976). Although the total source of COS is rather small compared to other sulphur compounds like SO_2 or DMS, on global average, it is the most abundant sulphur gas with a mean mixing ratio of ≈500 pptv (*Johnson et al.*, 1993). The reason for this high abundance is the long atmospheric lifetime of one to several years (a chemical lifetime of about 35 years and a total effective lifetime of more than two years are given by *Brühl et al.* (2012)). Because of that, COS is "the only sulphur compound which can enter the stratosphere (with the exception of SO_2 injections during violent volcanic eruptions)" (*Andreae*, 1990). Thus, COS plays a major role in the maintainance of the *Junge-layer*, which predominantly consists of sulphur and has been discovered by *Junge et al.* (1961): "[...] that a large, persistent aerosol layer exists in the stratosphere at an altitude of about 20 km." In the stratosphere, COS is converted by photodissociation and reaction with atomic oxygen to SO_2 (*Brühl et al.*, 2012). In the troposphere, COS can be taken up by plants (*Sandoval-Soto et al.*, 2005); furthermore, it is removed by reactions with OH.

Dimethyl Sulphide ('DMS', formula CH_3SCH_3) is formed of the precursor dimethylsulphonium propionate (DMSP), which is produced by marine algeae (*Andreae et al.*, 1985). DMS is also emitted by plants (*Lovelock et al.*, 1972; *Fall et al.*, 1988) and Arctic ice algae (pennate diatoms) (*Levasseur et al.*, 1994). Except during volcanic eruptions, DMS is the strongest natural source for atmospheric sulphur (*Platt and Stutz*, 2008, p. 53); a source estimate of 24.45 ± 5.30 Tg per year and an atmospheric lifetime of about one day is mentioned by *Watts* (2000). The degradation mechanisms are not yet completely understood, but the main atmospheric DMS sink is the reaction with OH during daytime, and the reaction with NO_3 during night time (*Barnes et al.*, 1994). Main resulting products are dimethyl sulphoxide (DMSO, formula $(CH_3)_2SO$), SO_2, sulphuric acid (H_2SO_4) and methane sulphonic acid (MSA, CH_3SO_3H). MSA and sulphuric acid have a low vapour pressure, so they quickly condense, forming small particles which can, under some conditions, act as cloud condensation nuclei (CCN). This has led to the *CLAW hypothesis*, named after their originators Charlson, Lovelock, Andreae and Warren, cf. *Charlson et al.* (1987), *Bates et al.* (1987). According to this controversial hypothesis, enhanced surface water temperatures lead to higher DMS production, thus more CCN and therefore more clouds which scatter back incoming solar radiation, leading to a cooling effect – a negative temperature feedback effect.

Hydrogen sulphide (H_2S) is mainly emitted from the oceans, by volcanoes, vegetation, wetlands, soils and biomass burning; also anthropogenic sources contribute to the H_2S budget, cf. *Brasseur* (1999, p. 196), *Watts* (2000). The reaction with OH is considered

to be the main sink of H_2O in the lower troposphere, with SO_2 as major product (*Watts*, 2000; *Cox and Sheppard*, 1980). The initial attack of OH occurs through the reaction

$$OH + H_2S \longrightarrow H_2O + HS \tag{2.55}$$

The detailed pathway of HS to form SO_2 is not clear yet; however, the reaction with ozone to SO as intermediate product seems to play a major role, cf. *Platt and Stutz* (2008, p. 52).

Sulphur dioxide (SO_2) is formed within the atmosphere by precursor species, mainly the aforementioned gases COS, H_2S and particularly DMS, but it is also emitted directly by natural and anthropogenic sources. The major natural source is represented by volcanoes and strongly varies in space and time. Volcanoes can emit SO_2 during quiet degassing, e.g. due to fumaroles (*Graf et al.*, 1997). During strong eruptions, the emission can be enhanced by orders of magnitude. Recent prominent eruptions took place in 2008 (Kasatochi) and 2010 (Eyjafjallajökull). The strongest eruption in the last decades was the one of Mt. Pinatubo in 1991 (e.g. *Guo et al.*, 2004). In that case, large amounts of SO_2 were directly injected into the stratosphere, dominating the stratospheric sulphate load for the subsequent 3–4 years (*Pyle et al.*, 1996). Apart from such events, anthropogenic emissions are the predominant atmospheric SO_2 sources. Main contribution come from power stations (∼50 %), manufacturing and construction industries (∼20 %), production of metals (∼10 %, cf. Sect. 7.5), residential sector, navigation and transportation (e.g. ships), cf. *EDGAR* (2011). Furthermore, SO_2 is emitted by biomass burning, cf. *Andreae and Merlet* (2001), *Wang et al.* (2002). The degradation of SO_2 takes places by dry deposition, in the liquid phase and through gas phase reactions. The dry deposition due to reactions with the ground accounts for 30–50 % of the removal of SO_2 (*Platt and Stutz*, 2008, p. 52). SO_2 has a high solubility in water (fog, clouds, rain droplets), therefore it is also removed by wet deposition. In the aquaeous solution, HSO_3^- and SO_3^{2-} ions are formed (details e.g. in *Brasseur* (1999), *Seinfeld and Pandis* (2006)). The most important gas phase mechanism is the oxidations initialized by OH, with SO_3 as intermediate product, investigated by *Stockwell and Calver* (1983).

$$\begin{aligned} OH + SO_2 + M &\longrightarrow HOSO_2 + M \\ HOSO_2 + O_2 &\longrightarrow HO_2 + SO_3 \\ SO_3 + H_2O &\longrightarrow H_2SO_4 \\ \hline \text{net:}\quad OH + SO_2 + O_2 + H_2O &\longrightarrow HO_2 + H_2SO_4 \end{aligned} \tag{2.56}$$

The production of sulphuric acid (H_2SO_4) is accompanied by the removal of an OH atom. However, the total HO_x is conserved in this reaction due to the production of HO_2. The lifetime τ of SO_2 is highly variable, as it depends on various parameters like temperature, solar radiative flux, precipitation, humidity, presence of clouds and wind (cf. *Stevenson et al.*, 2003). Also the vertical distribution of SO_2 (e.g. the altitude of a plume) plays a role (*Graf et al.*, 1997; *Khokhar*, 2006). Typically reported values for

τ are between 0.6 and 2.4 days for boundary layer anthropogenic emissions (*Khokhar et al.*, 2008; *Atkinson et al.*, 2007; *Brasseur*, 1999). Simulations for marine boundary layers yielded lifetimes of up to 10 days (*von Glasow et al.*, 2002).

As a consequence of the variable and rather short lifetime and the unequal source distributions, also the mixing ratio of SO_2 shows clear spatial differences, cf. (*Seinfeld and Pandis*, 2006, p. 33): "Mixing ratios of SO_2 in continental background air range from 20 ppt to over 1 ppb; in the unpolluted marine boundary layer levels range between 20 and 50 ppt. Urban SO_2 mixing ratios can attain values of several hundred parts per billion." A global view is shown in Fig. 2.5. While the hot spots over South America are mainly of volcanic origin, those over South Africa (e.g. *Walter*, 2008), Asia and Siberia (e.g. *Walter et al.*, 2012) are anthropogenic. As well as the variable lifetime, the contribution of different SO_2 sources to the global sulphur budget is also different, as summarized by *Chin and Jacob* (1996): "On a global scale, it is estimated that anthropogenic, biogenic, and volcanic emissions account for 70 %, 23 %, and 7 %, respectively, of the global sulphur source, but that they account for 37 %, 42 %, and 18 %, respectively, of the global column of atmospheric SO_4^{2-}."

Sulphur substances affect the environment in many aspects. In high concentrations, the toxic gas SO_2 and other sulphur compounds have adverse health effects for humans, animals and plants. Beside nitrogen, sulphur in the form of sulphuric acid is a main contributor to *acid rain*, i.e. acidic precipitation. Acid rain acidifies soils which may harm vegetation and can lead or contribute to forest decline, cf. *Sverdrup et al.* (1996). It also damages buildings and statues, especially limestone and marble, which contain large amounts of calcium carbonate (*Rapp*, 2009; *Cheng et al.*, 1987).

Sulphate aerosols influence climate directly and indirectly. They reflect sunlight into space which has a cooling effect on the climate. Of particular importance is stratospheric sulphur due to its longer residence time. After the eruption of Mt. Pinatubo, a cooling of the global surface temperature was observed (*Hansen et al.*, 1992; *Crutzen*, 2006). Besides this direct radiation effect, sulphate aerosols indirectly influences climate, as sulphur particles can act as CCN, cf. p. 17. Due to the cooling effect on climate, some ideas of a sulphur based climate engineering have been increasingly discussed in the last decade, e.g. *Crutzen* (2006), *Kuebbeler et al.* (2012).

Since the 19th century, anthropogenic emissions of SO_2 grew from estimated $\sim$1 Mt/year in 1850 to $\approx$70 Mt/year in 1980; since than, a decline has been observed due to changes in fossil fuel use and processes for reducing SO_2 emissions (*Lefohn et al.*, 1999; *Smith et al.*, 2004).

3. Radiative Transfer

After an overview over several quantities to describe the amount of light, this chapter deals with scattering, absorption and emission processes of light occurring in the atmosphere. They are summarized by the Radiative Transfer equation; from that equation the Lambert-Beer's law is derived, which will be used as basic equation for the DOAS approach (cf. Chap. 4). This chapter summarizes common knowledge, more details can be found in various literature, e.g. *Roedel and Wagner* (2011), *Platt and Stutz* (2008), *Demtröder* (2004).

3.1. Common Quantities

There are several quantities used for quantifying radiation, depending on the specific context. Figure 3.1 contains an overview over some of the most common basic quantities (left side) and their SI units (right side) used in radiometry.

The *radiance* I_{rad} specifies the radiation power per area and solid angle, so it describes, how many photons moving in direction (θ, ϕ) cross an infinitesimal area $\mathrm{d}A$, whose normal $\vec{A}$ also points in (θ, ϕ) direction. Therefore, I_{rad} is a function of position and direction.

The *irradiance* I_{irr}, also called *radiant flux density*, is the result of the integration of

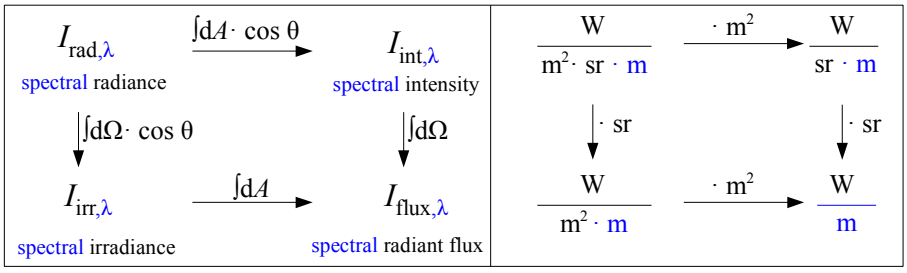

Figure 3.1.: Overview of quantities (left) and their coherent SI units (right) for describing electromagnetic radiation. Here, the *spectral* quantities with respect to the wavelength λ are given; for the integrated quantities ($\bar{I}_{\mathrm{rad}}$, $\bar{I}_{\mathrm{int}}$, $\bar{I}_{\mathrm{irr}}$, $\bar{I}_{\mathrm{flux}}$), the blue 'm' ('per wavelength interval') has to be removed in the units. (Adapted from *Walter*, 2008)

the radiance I_{rad} over a full hemisphere.

$$\begin{aligned} I_{\text{irr}} &= \int_{\text{hemisphere}} I_{\text{rad}} \cdot \cos\theta \cdot \mathrm{d}\Omega \\ &= \int_0^{2\cdot\pi} \int_0^{\pi/2} I_{\text{rad}} \cdot \cos\theta \cdot \sin\theta \cdot \mathrm{d}\theta \cdot \mathrm{d}\phi \end{aligned} \tag{3.1}$$

It is used to describe the emitted or impinging radiation power per area of a surface (cf. solar constant, Sect. 3.5). θ and ϕ are the polar angle and azimuth angle of a spherical coordinate system, in which the surface normal represents the z-axis. In the case of a so-called *Lambertian emitter*, the radiance I_{rad} of the emitted light is *isotropic*, which means, that it is independent of the direction (θ, ϕ) – 'the object has the same brightness, independent from the direction someone looks at'. In that case, (3.1) can be simplified to

$$I_{\text{irr}} = \pi \cdot I_{\text{rad}} \tag{3.2}$$

Integrating the radiance over an area instead of a hemisphere leads to the *radiant intensity* I_{int}, a quantity that can be used to describe the directional characteristic of a torch, for example.

$$I_{\text{int}} = \int_A I_{\text{rad}} \cdot \cos\theta \cdot \mathrm{d}A \tag{3.3}$$

Integrating the radiance over both, area and direction, leads to the *radiant flux* I_{flux}, also called *radiant power*, as it describes the amount of radiative energy per time, emitted by a surface, e.g. a lamp.

$$I_{\text{flux}} = \int_{\text{hemisphere}} \int_A I_{\text{rad}} \cdot \cos\theta \cdot \mathrm{d}A \cdot \mathrm{d}\Omega \tag{3.4}$$

Conversely, starting with the radiant flux as basic quantity, the irradiance, intensity and radiance can be regarded as the quotient of I_{flux} and A or Ω:

$$I_{\text{irr}} = \frac{\mathrm{d}I_{\text{flux}}}{\mathrm{d}A}, \quad I_{\text{int}} = \frac{\mathrm{d}I_{\text{flux}}}{\mathrm{d}\Omega}, \quad I_{\text{rad}} = \frac{\mathrm{d}I_{\text{flux}}}{\mathrm{d}\Omega \cdot \mathrm{d}A \cdot \cos\theta} \tag{3.5}$$

To be more precise, it has to be distinguished between *spectral* and *integrated* quantities. While the spectral radiant flux $I_{\text{flux},\lambda}$ (also called *specific* radiant flux) denotes the power emitted at a given wavelength λ per infinitesimal wavelength range $\mathrm{d}\lambda$, the integrated radiant flux $\bar{I}_{\text{flux}}$ describes the radiant power of the whole wavelength spectrum or a certain wavelength interval.[1]

$$\bar{I}_{\text{flux}} = \int_0^{\infty} I_{\text{flux},\lambda} \cdot \mathrm{d}\lambda \quad \text{or} \quad I_{\text{flux},\lambda} = \frac{\mathrm{d}\bar{I}_{\text{flux}}}{\mathrm{d}\lambda} \tag{3.6}$$

The coherent SI unit of the integrated flux $\bar{I}_{\text{flux}}$ is 1 W. For the spectral flux $I_{\text{flux},\lambda}$, it is 1 W/m, however, for light in the visible range, 1 W/nm is typically used. Sometimes, the

[1] In radiometry, with 'radiant flux', usually the integrated version is meant. However, for spectroscopic approaches like DOAS, the spectral information is essential, therefore here the spectral version is meant. The same applies for radiance, irradiance and intensity.

spectral flux is not given with respect to the wavelength λ but in a analogous way with respect to the frequency ν of the photons, thus having the unit 1 W/Hz. Analogously to (3.6), it is

$$\bar{I}_{\text{flux}} = \int_0^\infty I_{\text{flux},\nu} \cdot \mathrm{d}\nu \quad \text{or} \quad I_{\text{flux},\nu} = \frac{\mathrm{d}\bar{I}_{\text{flux}}}{\mathrm{d}\nu} \tag{3.7}$$

The same distinction between the integrated and the spectral quantity applies to the radiance, the irradiance and the intensity. The abovementioned equations (3.1) to (3.5) apply for all three cases, $\bar{I}$, I_λ and I_ν.[2]

Further Quantities, differing terms

The terms and especially the symbols for radiometric and optical quantities differ in literature. The symbols recommended by the International Commission on Illumination (cf. *Sliney*, 2007) for the integrated quantities are: L for the radiance, I for the intensity, E for the irradiance and Φ or P for the flux. The adding of subscript e (for 'energetic', e.g. L_e) is recommended to avoid the confusion with the corresponding photometric quantities or photon quantities (see below). The spectral quantities are indicated by adding subscript λ, e.g. $L_{\mathrm{e},\lambda}$. Other symbols found for the (integrated) radiance, intensity, irradiance and flux are I, F, B and Φ (e.g. *Platt and Stutz*, 2008) and further more.

The term *intensity* is not always used in a strict way as integrated radiance over an area or flux in a specific angle according to (3.3) and (3.5). Sometimes, it is used instead of *radiance* or in a more general sense to describe the strength of radiation. Also in this thesis, *intensity* I will sometimes be used in such a general sense, and it will be used as spectral quantity.

The aforementioned terms belong to the *radiometry*, which describes electromagnetic radiation with respect to the power or energy. In contrary, *Photon quantities* are based on photon numbers or photon densities; for example the photon irradiance is specified in *photons* per square meter and second. A conversion between the spectral photon irradiance and the spectral radiant irradiance is possible with the help of the energy-wavelength-relation ($E = h \cdot c/\lambda$ in vacuum), but for the integrated quantities, this is not possible without knowing the spectral distribution.

There are further quantities oriented on actinic effects (i.e. photochemical effects) in biological entities like plants (photosynthesis) or animals (skin cancer from UV light, vision of the eyes). One of them is the *luminous intensity*, one of the seven SI base quantities, with unit *candela*, abbreviated as 'cd'. For a monochromatic light source with a frequency of $540 \cdot 10^{12}$ hertz, a luminous intensity of 1 cd corresponds to an integrated radiant intensity of $\frac{1}{683}$ W/sr, per definition of the candela (cf. so-called *SI brochure*, *BIPM* (2006)). For other light sources, the relationship between the 'purely

[2] Depending on the context, the annexes 'rad', 'irr', 'int', 'flux', 'λ', 'ν' and '$^-$' will be omitted in the following, when the distinction is not important.

physical' radiometric quantity and the 'biological' photometric quantity depends on several factors like the human eye, however, standard functions are used for conversions (cf. 'V-function', 'luminous efficacy', e.g. in *Zwinkels et al.* (2010)).

3.2. Scattering, Absorption and Emission

For a photon transmitting a parcel of medium (here the air), the following cases can occur (cf. Fig. 3.2a).

- The photon transmits the parcel without any reaction and therefore without a change of its energy or direction.
- The photon is scattered elastically, thus its direction is changed, but not the energy (Rayleigh scattering, Mie scattering).
- The photon is scattered inelastically, called *Raman scattering*, resulting in a change of both, its direction and energy.
- The photon is absorbed.

If a photon is absorbed, its energy is transferred to the medium. This leads to a heating of the medium unless the energy can be released by heat transfer, convection or thermal

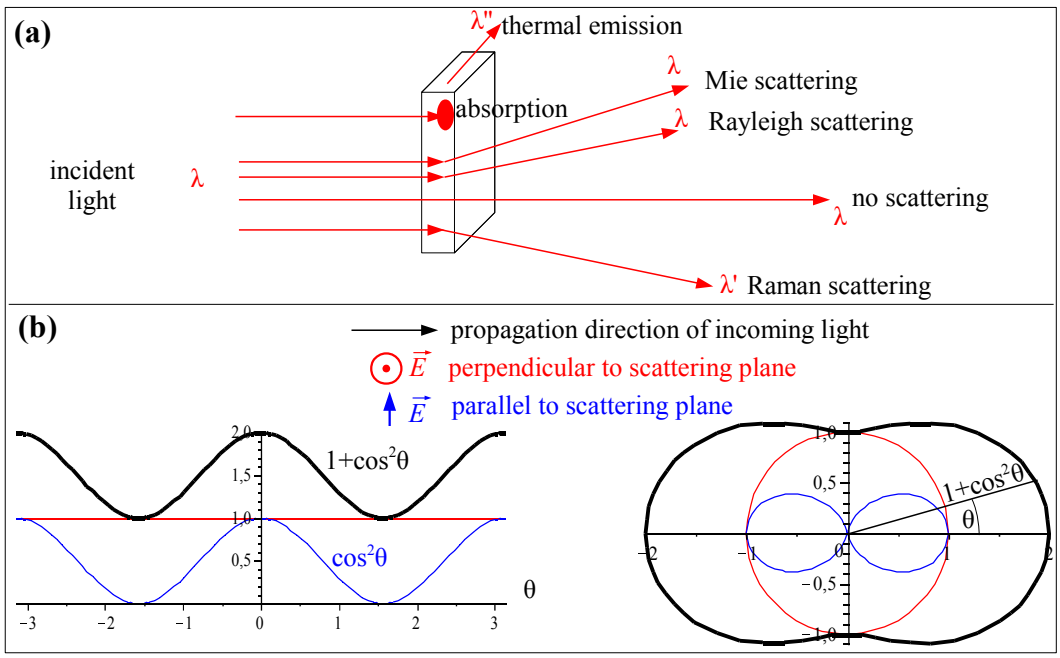

Figure 3.2.: (**a**) Physical processes which can occur, when light transmits a medium (**b**) phase diagram of Rayleigh scattering in a plane perpendicular to $\vec{E}$ (red line) and perpendicular to $\vec{B}$ (blue line), depicted vs scattering angle θ in Cartesian coordinates (left) and in a polar diagram (right). The scatter plane shall be in the picture plane in both cases. The thick black line applies for unpolarized incoming light. (Adapted from *Walter*, 2008)

emission. Elastic scattering processes are usually divided into *Rayleigh scattering* for the scattering on molecules and very small aerosol particles and the *Mie scattering* on larger particles. However, these terms do not describe physically fundamental different phenomena, but they are different approaches to describe scattering approximatively in a classical way.

3.2.1. Rayleigh Scattering

Rayleigh scattering[3] denotes the elastic scattering of light on particles which are small compared to the wavelength of the light. For visible light (∼400–800 nm), these are air molecules and small aerosol particles. In the classical view of light as a propagating electromagnetic wave with an electrical field vector $\vec{E}$ (and a magnetic field $\vec{B}$ perpendicular to the propagating direction and to $\vec{E}$), the scattering molecule can be interpreted as a *Hertzian dipole* which can be excited by the light. Such a dipole emits light of the same frequency – the scattered photons in a particle view. Experiments have shown that the cross section[4] of a molecule with respect to Rayleigh scattering, σ_{Rayleigh} strongly depends on the wavelength λ of the light. In a good approximation, σ_{Rayleigh} is proportional to λ^{-4}. That means that the cross section for blue light ($\lambda = 400\,\text{nm}$) is $2^4 = 16$ times higher than that one for red light ($\lambda = 800\,\text{nm}$).

This can be observed in the colours of the sky. During daytime, sky appears in blue, because much more blue photons are scattered than photons of higher wavelength. On the contrary, during sunrise or sunset, the sun has an orange or even reddish appearance, because most green and blue photons are scattered during the 'long journey through the atmosphere'.

The λ^{-4} relation can be explained in the aforementioned dipole picture (see *Roedel* (2000, p. 31ff) for details): The electrical field induced by the dipole is proportional to the second temporal derivative of the dipole field $p = p_0 \cdot \mathrm{e}^{\mathrm{i}\cdot\omega\cdot t}$ and therefore to ω^2, with the angular frequency $\omega = 2 \cdot \pi \cdot \mathrm{c}/\lambda$. Furthermore, the power emitted by a dipole is proportional to the square of the electric field, and therefore proportional to ω^4 or λ^{-4}. The cross section is also dependent on the number density of the air (and therefore height dependent). However, a rough estimation of the Rayleigh cross section allows the following equation, which can be found together with more precise formula in *Platt and Stutz* (2008, p. 93).

$$\sigma_{\text{Rayleigh}}(\lambda) \approx 4.4 \cdot 10^{-16}\,\text{cm}^2 \cdot \text{nm}^4 \cdot \lambda^{-4} = 4.4 \cdot 10^{-56}\,\text{m}^6 \cdot \lambda^{-4} \tag{3.8}$$

As mentioned in various literature (e.g. *Demtröder*, 2004, p. 338), Rayleigh scattering causes a partial polarisation of the light, which also can be explained in the dipole

[3] Named after J. W. Strutt, 3rd Baron Rayleigh, an English physicist (1842–1919).

[4] The cross section of a molecule with respect to a scattering or absorption process is a measure for the scattering probability. The cross section might be interpreted as the cross-sectional target area of the molecule, which a photon must hit in order to be scattered. Accordingly, the cross section has the units of an area, namely m^2 or cm^2. However, this purely geometric picture is not correct.

model. The charge carrier of the dipole oscillate parallel to the electrical field vector $\vec{E}$. The intensity of such a dipole in a plane orthogonal to $\vec{E}$ is independent of the scattering angle $\theta_{\perp E}$, cf. red line in Fig. 3.2b. But in the plane orthogonal to $\vec{B}$ (i.e. the plane spanned by $\vec{E}$ and vector of to the lights initial propagating direction), the intensity is proportional to $\cos^2(\theta_{\perp B})$, cf. blue line. This means that no light is scattered in direction $\theta_{\perp B}$, which is parallel to $\vec{E}$. For initially unpolarized light, the result is a superposition of both cases, so the scattered intensity is approximatively proportional to $1 + \cos^2(\theta)$, cf. thick black line.[5]

3.2.2. Aerosol Scattering

The aforementioned model for Rayleigh scattering is only valid for particles much smaller than the wavelength of the light. This is not the case for water droplets in fog or clouds and aerosol particles (except very small ones). A theoretical approach for such larger particles, the *Mie solution* (also called *Lorenz-Mie solution* or *Lorenz-Mie-Debye solution*), was introduced by the German physicist *Mie* (1908), originally focusing on metal solutions. Therefore the term *Mie scattering* is often used for elastic aerosol scattering. While Rayleigh scattering is mainly caused by single gas molecules, many molecules in a particle contribute to Mie scattering according to Maxwell's equations.

The scattering cross section does not only depend on the size of the particle but also on its shape, therefore precise formula are not available. Often, approximations in the form of λ^{-n} are given with a 'suitable' fractional n. Compared to Rayleigh scattering, this wavelength dependency is rather moderate – typically, n is between 1 and 1.5 (but also numbers smaller than 1 or larger than 3 can be more appropriate depending on the given aerosol). Along general lines, n decreases with increasing particle sizes, therefore large aerosol particle (with diameter much larger than the wavelength) scatter nearly 'wavelength independent'. This can be observed in clouds, whose water droplets have a typical size on the order of the wavelength of visible light. Therefore, Mie scattering takes places. Due to the low wavelength dependency, photons of different colours are scattered with a similar probability, so the clouds are observed to be white or gray (unless they are illuminated by 'coloured' light, e.g. during sunset).

The dependence of the scatter angle, however, is larger for Mie scattering than for Rayleigh scattering, with a pronounciation to the forward direction – especially for large particle, most photons are scattered by only a few degree, cf. *Roedel and Wagner* (2011, p. 28). Several algorithms have been established for the calculation of the scattering phase function, also parametrisations for approximating the scattering of the aerosol particles present in the atmosphere are available, e.g. the Henyey-Greenstein parametrisation (*Henyey and Greenstein*, 1941).

[5] Here, θ denotes the scattering angle in an arbitrary plane containing the lights initial propagating direction.

3.2.3. Raman Scattering

In contrast to the aforementioned scattering processes, Raman scattering (named after C.V. Raman, cf. *Raman* (1928)) is *inelastic*, which means, that the wavelength of the light is changed during that process. This process can be explained by a combination of an absorption of a photon by a molecule and a subsequent reemission of a photon. If the energy level of the molecule after this absorption and reemission process is higher than before, the Raman scattered photon has a lower energy and therefore a larger wavelength than the initial one. In the emission spectrum, such lines are called *Stokes lines*. Contrary, already excited molecules can change to a lower state than before, leading to photons of higher energy and lower wavelength, known as *anti-Stokes lines* in the spectrum, however, this effect is much weaker.

The cross section for Raman scattering, σ_{Raman}, approximatively shows a λ^4 wavelength dependency – similar to Rayleigh scattering. Although the Raman scattered light intensity is much lower than those of Rayleigh or Aerosol scattering, Raman scattering has to be considered in the DOAS evaluation, cf. Sect. 4.2.7.

3.2.4. Absorption and Emission

According to quantum mechanics, isolated atoms have discrete energy levels. These energy levels are eigenvalues of the Hamilton operator H in the Schrödinger equation $\mathrm{i} \cdot \hbar \cdot \frac{\partial \Psi}{\partial t} = H\Psi$ with imarinary unit i and reduced Planck constant $\hbar$. For an eigenvalue E, the wave function Ψ only changes by multiplying with a complex scalar number, which still belongs to the same physical state. Therefore, an isolated atom in such an *eigenstate*, also called *stationary state*, does not change its state, it is stable. Isolated atoms have several eigenstates with a discrete spectrum of eigenvalues. Because those eigenvalues correspond to the classical quantity *energy*, they are called *energy levels*.

When a photon is absorbed by an atom, the photon's energy $E = \mathrm{h} \cdot \nu$ is transferred to the atom by exciting the atom into an eigenstate with a higher energy level. Therefore a photon is only absorbed, if its energy is (nearly, see 'broadening' below) equal to the difference between the current eigenstate of the atom and a higher one. Typically the eigenstates are labeled with so-called *quantum numbers* n, l, m_l, s, m_s. In first approximation, the energy level is given by the first one, n, called *principle quantum number*. The energy difference $E_{n+1} - E_n$ between state n and $n+1$ is on the order of 1 eV, which is on the order of the energy of visible light. The other quantum numbers correspond to the angular momentum, magnetic angular momentum and spin of the atom, leading to small corrections in the energy level, cf. *fine structure* and *hyperfine structure* in various literature about quantum mechanics and atomic physics. As a consequence, the absorption spectrum of a substance of independent atoms (noble gases are a good approximation for such a substance) contains many almost discrete lines.

If an atom would be strictly isolated from external influences and be hit by a photon

of the exact energy to be in an excited energy eigenstate, it should remain in that state forever. In reality, excited states are typically very sensitive to minimal disturbances, so they only have a short lifetime, before the excited atom 'falls back' into the lower energy level by emitting a photon. A proper explanation is given by the quantum field theory, keywords 'spontaneous decay', 'vacuum fluctuations'. Analogous to an acoustic wave (tone) of finite length, an atom in such an excited state with a limited lifetime does not have an exact energy level. Instead, an energy distribution is given with a finite with, called *natural line with.*[6] This effect can be found in both, the absorption spectrum and the emission spectrum. The relative linewidth $\frac{\Delta\nu}{\nu}$ is on the order of 10^{-8}.

However, the natural broadening is usually dominated by two effects called *Doppler broadening* and *Power broadening.* Doppler broadening is a consequence of the motion of the atoms, leading to a Doppler shift. For atoms moving against the light, the photons have a shorter wavelength (thus a higher energy, blue-shift), while for atoms moving in light direction, the light is red-shifted. This effect increases with the speed of the atoms and therefore with temperature. Power broadening arises from the interaction of the atoms with each other – as mentioned before, excited states are usually very sensitive to disturbances. The higher the pressure (and therefore the number density) in a gas, the higher the frequency of such interactions and therefore the lower the lifetime of an excited state. For atmospheric conditions, power broadening causes a relative linewidth $\frac{\Delta\nu}{\nu}$ on the order of $5 \cdot 10^{-6}$.

Also molecules have energy levels. Due to their more complex structure and the interaction between their atoms, there are much more of them. Besides the aforementioned inner atomic levels, a substructure due to different vibrational and rotational levels occur.[7] Typically, the distance between adjacenting vibration niveaus is on the order of 0.1 eV (infrared); for rotational niveaus, the energies are even lower by one or two orders of magnitude. Besides the correct energy amount, there are further restrictions for possible transitions between states. Therefore some transitions are not possible or very improbable, so atoms or molecules can stay in stable or semi stable states with energy lever higher than the ground state (e.g. *Demtröder*, 2000, p. 208).

If the energy distances between adjacent levels are lower than the linewidth, the spectral lines overlap. Such *bands* of overlapping lines are typical for many atmospheric gases. In liquid and solid bodies, the interactions are so strong, that no single absorption or emission lines can be discerned any more. The energy of the incoming light is spread over many atoms as thermal energy. As an extreme and ideal case, a Planckian radiator absorbs and emits light of every wavelength, cf. following section.

[6] The shorter the lifetime is, the broader is the linewidth. This phenomenon is known as *energy-time-uncertainty*, in narrow analogy to Heisenberg's uncertainty principle.

[7] In a semiclassical view, the atoms swing against each other and the molecule rotates, but again, only certain energies are 'allowed'.

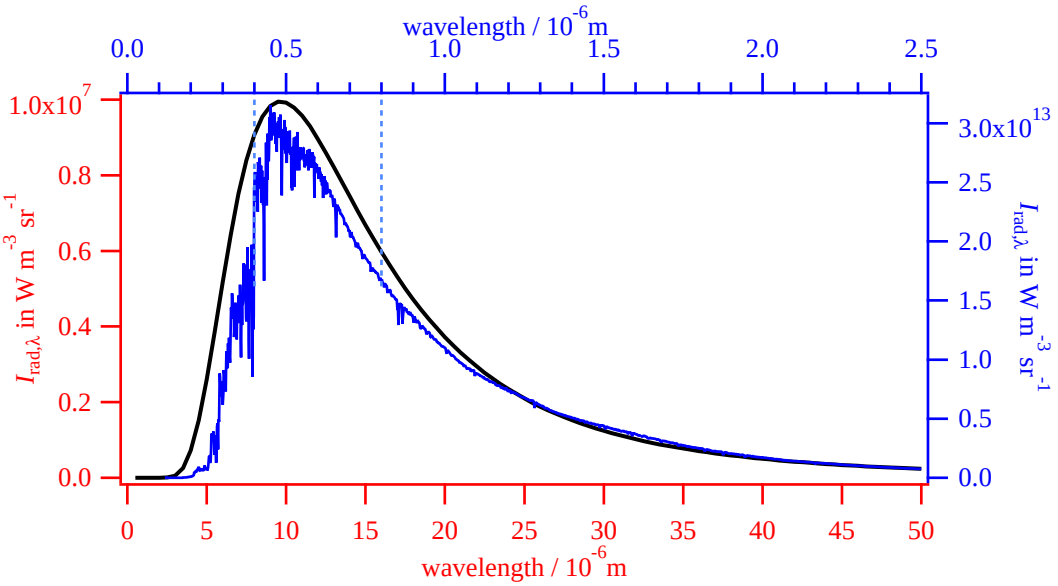

Figure 3.3.: Planck's law for a black body (black line). The left and the lower axes apply for a black body of 300 K, which is slightly above the average earth's surface temperature. The right and the top axes apply for a black body of 6 000 K, cf. sun's surface temperature. The blue line (belonging to top and right axes) shows the solar spectrum as observed outside the earth's atmosphere according to ASTM Standard (*ASTM*, 2000). The dashed vertical lines indicate the visible range of humans.

3.3. Thermal Emission

Light impinging on matter, e.g. a solid body, is absorbed with a certain probability (otherwise it could transmit the body or it could be scattered or reflected). This probability, the *absorptivity*, ranges from 0 to 1 with 1 meaning that all light is absorbed. It is dependent on the structure of the body; in case of non transparent bodies, the kind of surface is essential. Furthermore, the absorptivity α_λ (also *coefficient of absorption*, *spectral absorption coefficient*) is wavelength dependent; in general, also the angle of impact and the polarisation are relevant. A special case is the *black body*, a body absorbing the light completely for all wavelengths, polarisation and angles of impact, thus $\alpha_\lambda = 1$. Such a black body is an ideal case, but it can be realized in good approximation by a matt, rough and porous surface, e.g. a soot coated body. Especially a small hole in an empty (soot coated) box 'looks very black'.

When light is absorbed by matter, the energy of the photon is transferred to the material. Especially in the case of solids, this energy is distributed between surrounding atoms in terms of thermal energy, leading to a temperature enhancement of the body. On the other hand, photons are emitted by the body, decreasing temperature again. In a thermal equilibrium, the absorbed and emitted energy are equal. The thermal emission of a black body is described by *Planck's law*, which can be found in several forms, typically as spectral energy density distribution in a cavity or in form of the emission

of a black surface. The following equation describes the latter one – the radiation of a black surface due to thermal emission for a infinitesimal wavelength range $\mathrm{d}\lambda$.

$$I_{\mathrm{rad},\lambda}(T) \cdot \mathrm{d}\lambda = \frac{2 \cdot \mathrm{h} \cdot \mathrm{c}^2}{\lambda^5} \cdot \frac{\mathrm{d}\lambda}{\exp\left(\frac{\mathrm{h}\cdot\mathrm{c}}{\lambda \cdot \mathrm{k_B} \cdot T}\right) - 1} \tag{3.9}$$

T is the thermodynamic temperature, c the light speed, $\mathrm{k_B} \approx 1.38 \cdot 10^{-23}\,\mathrm{J/K}$ the Boltzmann constant, $\mathrm{h} \approx 6.62607 \cdot 10^{-34}\,\mathrm{J \cdot s}$ the Planck constant and $I_{\mathrm{rad},\lambda}$ the spectral radiance as introduced in (3.6). This law is depicted in Fig. 3.3 for a black body (black curve) with a temperature of 300 K (red axes) and for a black body with 6 000 K (also black curve, but blue axes), which roughly corresponds to the mean surface temperature of the earth (≈288 K) and the sun (∼5 700 K).

From (3.9), it follows that the maximum $\lambda_{\max}(T)$ of $I_{\mathrm{rad},\lambda}$ shows a $1/T$ dependency:

$$\lambda_{\max}(T) \approx \frac{2.8978 \cdot 10^{-3}\ \cdot \mathrm{m} \cdot \mathrm{K}}{T} \tag{3.10}$$

This shift of the maximum with increasing temperature is known as *Wien's displacement law*. It can be observed when heating an iron plate. For 300 K, the maximum of $I_{\mathrm{rad},\lambda}$ is around 10 μm – in the visible range almost no photons are emitted. For 1000 K, $\lambda_{\max}$ is about 2.9 μm, still not in the visible range (∼ 400–800 nm), but the radiation at 800 nm is already strong enough to be seen by human eye. Thus, the iron plate appears red ('red heat'). For higher temperature, also the emission of photons with shorter wavelength gains importance, leading to 'white heat'.

As the black body is a Lambertian emitter (Sect. 3.1), the emission is isotropic, so (3.2) applies for the irradiance of a black body. For real bodies, (3.9) has to be modified by inserting a factor ϵ_λ, called *spectral emission coefficient* or *emissivity*. It ranges from 0 to 1, like the spectral absorption α_λ. Therefore, the black body radiation constitutes the upper radiation limit for a given temperature. According to *Kirchhoff's law*, the spectral emission and the spectral absorption are equal for all wavelengths: $\alpha_\lambda = \epsilon_\lambda$. Kirchhoff's law does not only apply on solid bodies but also on liquids and gases. It is a consequence of the second law of thermodynamics.

The integrated irradiance $\bar{I}_{\mathrm{irr}}$ (i.e. the integral of $I_{\mathrm{rad},\lambda}$ over a hemisphere and over λ, cf. (3.6)) describes the power emitted per surface area of a body. For a black body, it is given by the *Stefan-Boltzmann law*.

$$\bar{I}_{\mathrm{irrad}} = \sigma_{\mathrm{SB}} \cdot T^4 \quad \text{with} \quad \sigma_{\mathrm{SB}} = \frac{2 \cdot \pi^5}{15} \cdot \frac{\mathrm{k_B^4}}{\mathrm{h^3} \cdot \mathrm{c^2}} \approx 5.670 \cdot 10^{-8}\ \frac{\mathrm{W}}{\mathrm{m^2} \cdot \mathrm{K^4}} \tag{3.11}$$

σ_{SB} is the *Stefan-Boltzmann constant*, also *Stefan's constant*. Due the 4th order dependency, a doubling of the temperature of a body causes a 16 times higher emission power. Like Planck's law, also the Stefan-Boltzmann law has to be modified for a non black body by inserting a correction factor ϵ with $0 < \epsilon < 1$. In general, ϵ is dependent on temperature T, therefore the proportionality $\bar{I}_{\mathrm{irrad}} \propto T^4$ is not strict any more; however, for many bodies, it is still a good approximation.

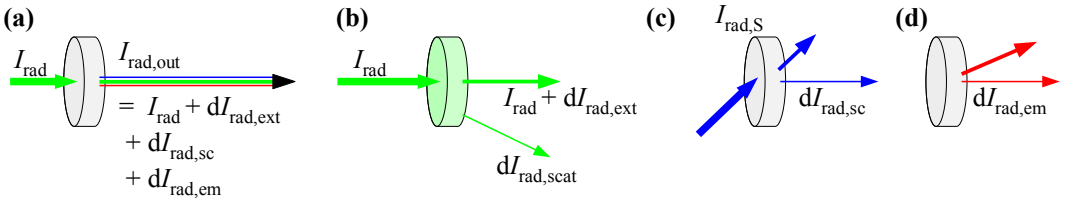

Figure 3.4.: Change of the initial radiance I_{rad} when traversing an air volume element of length $\mathrm{d}l$. (**a**) $I_{\mathrm{rad,out}}$ consists of three parts, namely $I_{\mathrm{rad,in}} + \mathrm{d}I_{\mathrm{rad,ext}}$, $\mathrm{d}I_{\mathrm{rad,sc}}$ and $\mathrm{d}I_{\mathrm{rad,em}}$. (**b**) The radiance is attenuated due to scattering and absorption, therefore $\mathrm{d}I_{\mathrm{rad,ext}}$ is negative. (**c**) Some light is scattered from other directions into the direction of interest. (**d**) The parcel emits radiation. (Adapted from *Walter*, 2008)

3.4. Radiative Transfer Equation, Lambert-Beer's Law

Radiative Transfer Equation

The *Radiative Transfer Equation* (RTE) describes the change of the radiation I_{rad} of light when traveling through a parcel of air (or some other mixture of gases).

$$\frac{\mathrm{d}I_{\mathrm{rad}}}{\mathrm{d}l} = \frac{\mathrm{d}I_{\mathrm{rad,ext}}}{\mathrm{d}l} + \frac{\mathrm{d}I_{\mathrm{rad,sc}}}{\mathrm{d}l} + \frac{\mathrm{d}I_{\mathrm{rad,em}}}{\mathrm{d}l} \tag{3.12}$$

The change $\mathrm{d}I_{\mathrm{rad}}$ per path length $\mathrm{d}l$ consists of three parts. The radiation is attenuated due to absorption and scattering *into* another direction (extinction, first summand), but on the other hand, it is increased due to scattering *from* other direction (second summand) and due to thermal emission of the air parcel (third summand), see also Fig. 3.4. These three summands are:

First summand: Extinction The radiance is attenuated due to absorption by gas molecules and aerosol particles.

$$\frac{\mathrm{d}I_{\mathrm{rad,abs}}}{\mathrm{d}l} = -K_{\mathrm{abs}} \cdot I_{\mathrm{rad}} \quad \text{with} \quad K_{\mathrm{abs}} = \sum_k c_k \cdot \sigma_{\mathrm{abs},k} \tag{3.13}$$

As a basic assumption, the absorption coefficient K_{abs} is proportional to the concentration c_k of a species № k and its spectral absorption cross section $\sigma_{\mathrm{abs},k}$. The cross sections strongly depend on the wavelength (cf. Sect. 3.2), but there is also a dependency on temperature and pressure. Furthermore, I_{rad} (which describes the radiance in a specific direction of interest) is reduced due scattering of photons into other directions. Analogously to the absorption, this effect can be described by the scattering coefficient K_{scat}, thus $\frac{\mathrm{d}I_{\mathrm{rad,scat}}}{\mathrm{d}l} = -K_{\mathrm{scat}} \cdot I_{\mathrm{rad}}$. Both effects (absorption and scattering into another direction) are summarized as *extinction*, with an extinction coefficient $K_{\mathrm{ext}} = K_{\mathrm{abs}} + K_{\mathrm{scat}}$. Therefore, the first summand of (3.12) is negative, given by

$$\frac{\mathrm{d}I_{\mathrm{rad,ext}}}{\mathrm{d}l} = \frac{\mathrm{d}I_{\mathrm{rad,abs}}}{\mathrm{d}l} + \frac{\mathrm{d}I_{\mathrm{rad,scat}}}{\mathrm{d}l} = (-K_{\mathrm{abs}} - K_{\mathrm{abs}}) \cdot I_{\mathrm{rad}} = -K_{\mathrm{ext}} \cdot I_{\mathrm{rad}} \tag{3.14}$$

Second summand: Scattering in Light coming from another direction can be scattered into the direction of I_{rad}, leading to an increase of I_{rad}. To quantify this

amount, the radiations $I_{\mathrm{rad},S}(\theta,\phi)$ have to be known for all directions, which are given here by the polar angle θ and the azimuth angle ϕ (with $\theta = 0$ for the direction of I_{rad}). Furthermore, the direction dependency of the scattering cross section is need, which is described by a distribution function $S(\theta,\phi)$. Integrating over all angles leads to

$$\frac{\mathrm{d}I_{\mathrm{rad,sc}}}{\mathrm{d}l} = K_{\mathrm{scat}} \cdot \int_0^{\pi} \int^{2\cdot\pi} I_{\mathrm{rad,S}} \cdot \frac{S(\theta,\phi)}{4\cdot\pi} \cdot \mathrm{d}\phi \cdot \sin\theta \cdot \mathrm{d}\theta \tag{3.15}$$

with

$$S(\theta,\phi) = 4\cdot\pi \cdot \frac{1}{\sigma_{\mathrm{streu}}} \cdot \frac{\mathrm{d}\sigma_{\mathrm{streu}}}{\mathrm{d}\Omega} \tag{3.16}$$

For isotropic scattering, $S(\theta,\phi)$ would be 1 for all angles, but this is not the case for Rayleigh and Mie scattering, cf. Sect. 3.2.

Third summand: Thermal Emission Like any body, the parcel emits thermal radiation, also in the direction of I_{rad}. The amount is given by Planck's law, see (3.9).

$$\frac{\mathrm{d}I_{\mathrm{rad,em}}}{\mathrm{d}l} = K_{\mathrm{abs}} \cdot \frac{2\cdot \mathrm{h}\cdot \mathrm{c}^2}{\lambda^5} \cdot \frac{1}{\exp\left(\frac{\mathrm{h}\cdot\mathrm{c}}{\lambda\cdot \mathrm{k_B}\cdot T}\right) - 1} \tag{3.17}$$

Because a gas is not a black body, the emission coefficient has to be added, which is equal to the absorption coefficient $K_{\mathrm{abs},\lambda}$ (Kirchhoff's law). In contrast to the other two summands, the thermal emission does not explicitly depend on the incoming radiation, but indirectly, because the temperature increasing with increasing irradiation due to the absorption.

Combination. Finally, inserting (3.14), (3.15) and (3.17) in (3.12) leads to

$$\begin{aligned}
\frac{\mathrm{d}I_{\mathrm{rad}}}{\mathrm{d}l} &= \frac{\mathrm{d}I_{\mathrm{rad,ext}}}{\mathrm{d}l} + \frac{\mathrm{d}I_{\mathrm{rad,sc}}}{\mathrm{d}l} + \frac{\mathrm{d}I_{\mathrm{rad,em}}}{\mathrm{d}l} \\
&= -K_{\mathrm{ext}} \cdot I_{\mathrm{rad}} \\
&+ K_{\mathrm{scat}} \cdot \int_0^{\pi} \int^{2\cdot\pi} I_{\mathrm{rad,S}} \cdot \frac{S(\theta,\phi)}{4\cdot\pi} \cdot \mathrm{d}\phi \cdot \sin\theta \cdot \mathrm{d}\theta \\
&+ K_{\mathrm{abs}} \cdot \frac{2\cdot \mathrm{h}\cdot \mathrm{c}^2}{\lambda^5} \cdot \frac{1}{\exp\left(\frac{\mathrm{h}\cdot\mathrm{c}}{\lambda\cdot \mathrm{k_B}\cdot T}\right) - 1}
\end{aligned} \tag{3.18}$$

It should be remembered, that this is a 'spectral' equation, as I_{rad}, K_{ext}, K_{scat}, K_{abs} and S are dependent of the wavelength λ. The Raman scattering is not completely accounted for. The attenuating effect of Raman scattering of light into another direction can be expressed by the first summand. But in order to incorporate the Scattering of photons with $\lambda' \neq \lambda$ from other directions into the direction of I_{rad}, an integration over λ' would have to be added in the second summand.

For the case of the DOAS instruments onboard CARIBIC, sunlight is measured indirectly (cf. Fig. 6.1b p. 88), after it has been reflected on the earth's surface or scattered within the atmosphere according to the second summand of (3.18). The attenuation due to extinction (first summand) is the basis of absorption spectroscopy like DOAS, cf. following subsection on 'Lambert Beer's Law'. Thermal emission by the surface or molecules in the atmophere is not relevant for DOAS applications (see below), but it is important for the atmospheric radiative budget, cf. Sect. 3.5.

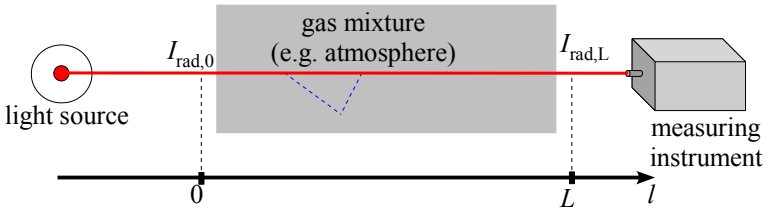

Figure 3.5.: A narrow light beam of a light source traverses a gas mixture, e.g. the atmosphere. $I_{rad,0}$ and $I_{rad,L}$ are the radiances for $l = 0$ and $l = L$ (before and after traversing the gas). (Adapted from *Walter*, 2008)

Lambert Beer's Law

Lambert Beer's Law can be interpreted as a restriction of the RTE to the first summand (cf. (3.18), describing the attenuation of the radiance. A typical case, where the other two terms of the RTE can be neglected, is a narrow light beam as sketched in Fig. 3.5. If there is only the depicted light source, there are no photons coming from outside which could be scattered into the beam. One can argue that it is possible that a photon is first scattered out of the beam, then scattered again towards the beam and then (just when crossing the beam) scattered again into the beam's direction (blue dashed line in Fig. 3.5), but this is a very improbable case, as long as the light beam is narrow enough.

Also the third summand of the RTE, namely the thermal emission can be neglected for visible light and a gas temperature, that can be found in the atmosphere. For example, a gas with temperature $T = 300\,\mathrm{K}$ emits predominantly around $10\,\mu\mathrm{m}$ (cf. Wien's displacement law, (3.10)). If the emission coefficient is roughly independent from the wavelength, then the radiance emitted in the visible range ($\lambda \sim 500\,\mathrm{nm}$) is $\sim 10^{-35}$ times lower than for $10\,\mu\mathrm{m}$, so virtually no visible light is emitted by a body of 300 K.

Thus, (3.18) can be reduced to the attenuation term, namely

$$\frac{\mathrm{d}I_{\mathrm{rad}}}{\mathrm{d}l} = -K_{\mathrm{ext}} \cdot I_{\mathrm{rad}} \quad \text{with} \quad K_{\mathrm{ext}} = \sum_k \sigma_k \cdot c_k \tag{3.19}$$

As mentioned above, σ_k and c_k denote the cross section and number concentration of species № k, which are gases and aerosol particles. Here, absorption and scattering are combined, i.e.

$$\sigma_k = \sigma_{\mathrm{abs},k} + \sigma_{\mathrm{Rayleigh},k} + \sigma_{\mathrm{Mie},k} + \sigma_{\mathrm{Raman},k} \tag{3.20}$$

After a distance L, the initial radiance $I_{\mathrm{rad},0}$ is attenuated to $I_{\mathrm{rad},L}$ (cf. Fig. 3.5); the integration of (3.19) yields

$$I_{\mathrm{rad},L} = I_{\mathrm{rad},0} \cdot \exp\Big(-\sum_k \int_0^L \sigma_k \cdot c_k(l) \cdot \mathrm{d}l\Big) \tag{3.21}$$

This equation is known as *Lambert-Beer's law* or *Bouguer-Lambert law*, after the physicists Pierre Bouguer, Johann H. Lambert and August Beer (*Platt and Stutz*, 2008,

p. 137). It has to be considered, that in general, σ_k is implicitly dependent on the position l, if temperature T or pressure p are not constant along l.

3.5. Radiation Budget of the Atmosphere

The solar constant describes the power from solar radiation reaching the earth's top of the atmosphere (TOA). It is 1368 W for an area of $1\,\mathrm{m}^2$ perpendicular to the sun. Due to the yearly cycle of the distance between sun and earth and due to changes in the sun activity, this value varies with time. For the averaged insolation is has to be considered, that the solar radiation hits the earth's atmosphere at an area of $\pi \cdot R^2_{\mathrm{earth}}$, whereas the surface of the earth is $4 \times \pi \cdot R^2_{\mathrm{earth}}$ (neglecting the dimensions of the atmosphere and the fact, that the earth is not a perfect sphere). Therefore, only 1/4, namely 342 $\mathrm{W/m}^2$ reach the TOA on average.

Figure 3.6 gives an overview of the annual global mean energy budget as summarized by *Kiehl and Trenberth* (1997). The values are given in $\mathrm{W/m}^2$, thus having the dimension of an spectrally integrated irradiance $\bar{I}_{\mathrm{irr}}$ (cf. Sect. 3.1), i.e. the flux downwards or upwards per area. The aformentioned solar radiation of 342 $\mathrm{W/m}^2$ (here set to 100 %) reaching the TOA mainly consists of visible light (maximum of $I_{\mathrm{irr},\lambda}$ the green wavelength range), near IR and near UV. A part of it (168 $\mathrm{W/m}^2$ or 49 %) directly reaches the ground, while the other part is reflected scattered or absorbed by clouds, aersol particles or air molecules. Especially most of the UV light is absorbed by the ozone layer.

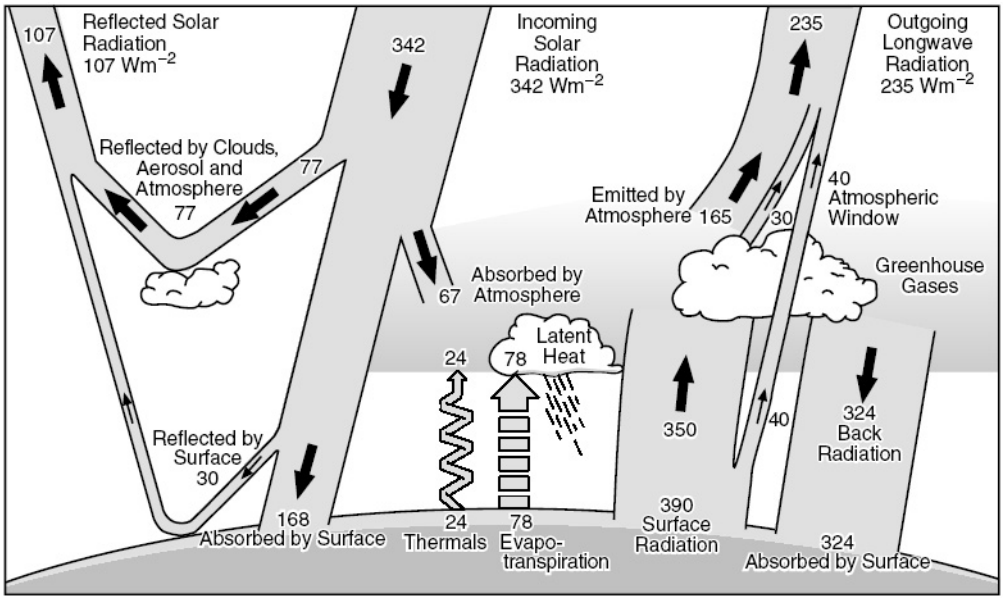

Figure 3.6.: Radiative budget of the atmosphere. Predominantly shortwave solar radiation (visible light, UV, near IR) is shown on the left part; the longwave (thermal IR, $\sim 10\,\mu\mathrm{m}$) radiation is depicted on the right part. (From *Kiehl and Trenberth*, 1997)

The light reaching the ground is absorbed or reflected. The *surface albedo* (i.e. the ratio between the reflected and the impinging light) can be up to about 90 % for the case of fresh snow (cf. *Kleipool et al.* (2008)) but also 20 % or less for the case of dark porous material, wet sand or surfaces covered by pants (forests), cf. *Ångström* (1925). The albedo of water is dependent on the impinging angle. On global average, $30\,\mathrm{W/m^2}$ of the $168\,\mathrm{W/m^2}$ are reflected. The absorbed light heats the surface which re-emits radiations, but, according to Planck's law, with a maximum in the infrared range around $10\,\mu\mathrm{m}$. With 350 $\mathrm{W/m^2}$, this *long wave radiation* contains more power than the solar insolation, but only $40\,\mathrm{W/m^2}$ directly leave the atmosphere 'through the atmospheric window'. The larger fraction is absorbed or scattered in the atmosphere. $324\,\mathrm{W/m^2}$ of infrared radiation emitted in the atmosphere reach the surface. This effect is known as *greenhouse effect*, predominantly caused by water vapour, CO_2 and further *greenhouse gases* like methane, nitrous oxide and ozone. Besides radiation, also convection contributes to the vertical energy transport in terms of thermal energy ($24\,\mathrm{W/m^2}$) and latent heat ($78\,\mathrm{W/m^2}$). The radiation leaving the atmosphere consists of reflected solar radiation ($107\,\mathrm{W/m^2}$), emission by the atmosphere ($195\,\mathrm{W/m^2}$) and direct infrared emission from the ground ($40\,\mathrm{W/m^2}$). In total, this should be the same amount as the incoming radiation ($342\,\mathrm{W/m^2}$).

If the outgoing radiation was slightly smaller, the earth would heat up. Actually this has been observed in the last century, and model predictions for the year 2100 show an ongoing global warming. The main reason is the increase of greenhouse gases in the atmosphere, leading to a higher back radiation, which is compensated by a higher thermal emission of the surface and the lower troposphere, cf. Stefan-Boltzmann law (3.11).

4. Differential Optical Absorption Spectroscopy

A large variety of measurement techniques have been established for measuring atmospheric gases. Depending on the species of interest, different requirements are important. For long-lived gases like O_2 or CO_2, a high precision is needed to observe the small changes with respect to the ambient concentrations. For trace gases, a low detection limit is essential to detect them at all. A measurement technique should be specific in order to be able to discern between different substances.

Since the discovery of the Fraunhofer lines in the solar spectrum by William Wollaston and Joseph Fraunhofer and the connection to absorption lines of gases, found by Gustav Kirchhoff and Robert Bunsen in the 19th century, spectroscopy has become widely used. One famous application is the monitoring of the atmospheric ozone column, initially by an 'ozone spectrophotometer' (*Dobson*, 1968), leading to the 'Dobson unit' (DU) for column densities; i.e. $1\,\mathrm{DU} = 2.69 \cdot 10^{16}\,\mathrm{molec/cm^2}$.

With the emergence of computers, it became applicable to analyse high resolved spectra: In 1978, formaldehyde, ozone and NO_2 were measured simultaneously by *Differential Optical Absorption Spectroscopy* (DOAS), cf. *Platt et al.* (1979). Also with DOAS, nitrous acid (HONO) was found to be present in the atmosphere in 1979 (*Perner and Platt*, 1979; *Platt et al.*, 1980).

Due to the long light path, low detection limits are possible for DOAS applications. The analysis of high resolved spectra makes DOAS specific to certain gases due to their unique absorption features. In most cases, DOAS is used as a remote sensing technique, thus interactions of the measuring setup with the probed gases (e.g. wall effects) are excluded.

This chapter starts with the introduction of the DOAS principle. Afterwards the differences between direct light and scattered light measurements are dealt with. The impacts of using a real instrument instead of an ideal spectrograph are addressed in Sect. 4.3. Afterwards, a brief overview over DOAS applications is given.

In combination with wind data, the columns densities retrieved by the DOAS approach can be used to calculate trace gas fluxes. The theoretical background for such calculations is given in Sect. 4.5, which will be used to estimate the SO_2 source strength of Norilsk and the NO_2 source strength of Paris, cf. Chap. 7.

4.1. DOAS Principle

Figure 3.5 shows as sketch for a typical DOAS setup, consisting of a light source, the gas mixture (which shall be analyzed) and the measuring instrument. The light source might be the sun (sun occultation measurements) the moon or a lamp (cf. 'long path DOAS', Sect. 4.4). The gas mixture can be the ambient atmospheric air or a sample in a cuvette in a laboratory setup. The measuring instrument usually contains a grating spectrometer, thus analysing the spectral composition of the light. For describing the attenuation of the light beam, Lambert-Beer's law is used as introduced in (3.21) p. 43. The instrument is not sensitive to only one specific direction, instead it measures the incoming radiation of small but finite solid angle, the *field of view*. Furthermore, the instrument has a finite area, therefore the distinction between the terms 'radiance', 'irradiance', 'intensity' and 'flux' is not helpful here. Thus, in the following, *intensity* is used in a more general sense – more or less synonym to the term *spectrum* –, and Lambert Beer's law (3.21) is written as

$$I(\lambda) = I_0(\lambda) \cdot \exp\Big(\underbrace{-\sum_k \int_0^L \sigma_k(\lambda, T, p) \cdot c_k(l) \cdot \mathrm{d}l}_{=:\tau(\lambda)}\Big) = \mathrm{e}^{-\tau(\lambda)} \tag{4.1}$$

I is the the intensity reaching the measuring instrument, here written as a function of the wavelength λ; I_0 is the intensity of the light before it is transmitted through the air. Again, σ_k and c_k denote the cross section (for absorption and scattering) and number concentration of species № k, which are gases or aerosol particles. It is assumed that the prerequisites for the applicability of Lambert-Beer's law are fulfilled (cf. Sect. 3.4), meaning that virtually no light is scattered into the beam from another light source or by multiple scattering. Therefore, the light beam shall be narrow, and the instrument's field of view shall be small.[1]

The negative exponent of (4.1), τ, is called *optical density* (also *optical depth*, *optical thickness* or *absorbance*, cf. *Nic et al.* (2012)).

$$\tau(\lambda) = -\ln \frac{I(\lambda)}{I_0(\lambda)} = \ln \frac{I_0(\lambda)}{I(\lambda)} \overset{(4.1)}{=} \sum_k \int_0^L \sigma_k(\lambda, T, p) \cdot c_k(l) \cdot \mathrm{d}l \tag{4.2}$$

A further important quantity (actually the result of a DOAS retrieval) is the *slant column density* (SCD), S_i, defined as the integrated number concentration along the light path.

$$S_k := \int_0^L c_k(l) \cdot \mathrm{d}l \tag{4.3}$$

The SCD describes, how many molecules of species № k there are in the light beam, divided by the cross-sectional area of the light beam. It's unit is $1/\mathrm{m}^2$ or, more common, $1/\mathrm{cm}^2$, often written as 'molec/cm^2'. If, for example, a light beam with a radius of

[1] Otherwise, the *Ring effect* might not be negligible, cf. Sect. 4.2.7.

$1\,\mathrm{cm}^2$ traverses a cuvette of 1 m length, which contains 10^{20} molecules per cm^3, then $S_i = 10^{20}\,\mathrm{cm}^{-3} \cdot 100\,\mathrm{cm} = 10^{22}\,\mathrm{cm}^{-2}$, meaning that 10^{22} molecules are in the light beam. Furthermore, S_i/L is the average concentration of the gas (arithmetic mean). When the cross sections are constant along the light path, they can be factored out of the integral, thus (4.1) and (4.2) can be written with the help of S_k as

$$I(\lambda) = I_0(\lambda) \cdot \exp\Big(-\sum_k \sigma_k(\lambda, T, p) \cdot S_k\Big) \tag{4.4}$$

$$\tau(\lambda) = \ln \frac{I_0(\lambda)}{I(\lambda)} = \sum_k \sigma_k(\lambda, T, p) \cdot S_k \tag{4.5}$$

This is valid, if temperature T and pressure p are constant along the light path or if the dependence of σ_k with respect to T and p is small enough.

In practice, it is not possible to account for the scattering and absorption processes of all the air constituents. Especially aerosol particles are difficult to deal with, because each particle has its individual shape, thus having its individual cross section. Fortunately, the cross sections of Rayleigh and Mie scattering show very broad spectral characteristics, also the absorption cross sections of aerosol particles, whereas the absorption and Raman cross sections of several trace gases contain distinctive narrowband structures (cf. Sect. 3.2). The basic idea of DOAS is to use this fact by separating the cross section σ_k of a species or process into a narrowband part σ'_k and a broadband part σ''_k.

$$\sigma_k = \sigma'_k + \sigma''_k \tag{4.6}$$

With this separation, (4.1) can be written as

$$I(\lambda) = I_0(\lambda) \cdot \exp\Big(-\underbrace{\sum_k \int_0^L \sigma'_k(\lambda, T, p) \cdot c_k(l) \cdot \mathrm{d}l}_{=:\tau'(\lambda)} - \underbrace{\sum_k \int_0^L \sigma''_k(\lambda, T, p) \cdot c_k(l) \cdot \mathrm{d}l}_{=:\tau''(\lambda)}\Big) \tag{4.7}$$

Here, also the optical density τ was separated into a narrowband τ' and a broadband part τ'' with $\tau = \tau' + \tau''$. As only the absorption and Raman scattering of the gases contribute to the narrowband τ', it is sufficient to summarize over the gaseous species (let K be the number of gases with narrowband absorption lines in the investigated wavelength range, which shall be counted with index k), cf. (4.7):

$$\tau'(\lambda) = \sum_{k=1}^{K} \int_0^L \sigma'_k(\lambda, T, p) \cdot c_k(l) \cdot \mathrm{d}l \overset{(4.3)}{=} \sum_{k=1}^{K} \sigma'_k(\lambda, T, p) \cdot S_k \tag{4.8}$$

As mentioned above, the second equality sign presumes the cross sections σ'_k to be constant along the light path. Because the broadband shape of the optical density is a result of too many factors to be calculated in the practice of atmospheric measurements, τ'' is approximated by a polynomial

$$\tau''_{\mathrm{approx}}(\lambda) = \sum_{q=0}^{q_\mathrm{o}} p_q \cdot \lambda^q \tag{4.9}$$

with q_o as polynomial order and coefficients p_q. Combining (4.8) and (4.9) yields

$$\underbrace{\ln \frac{I_0(\lambda)}{I(\lambda)}}_{=\tau(\lambda)} \simeq \underbrace{\sum_{k=1}^{K} \sigma'_k(\lambda, T, p) \cdot S_k + \sum_{q=0}^{q_\mathrm{o}} p_q \cdot \lambda^q}_{=\tau_\mathrm{approx}(\lambda)} \tag{4.10}$$

This equation contains K sought-after quantities, namely the SCDs S_k. The intensity I is measured by the instrument, and I_0 shall also be known (cf. Sect. 4.2). The cross sections of σ_k of the considered gases are taken from from literature (cf. Sect. 6.7.3), the narrowband part σ'_k is gained by a highpass filter, which can be done by subtracting the broadband part σ''_k from σ_k, whereat σ''_k is typically a polynomial fit to σ_k. Besides the SCDs, the $q_\mathrm{o}+1$ coefficients p_q of the polynomial are unknown. In total, the equation contains $K+q_\mathrm{o}+1$ unknown variables. On the other hand, it has to fit for any wavelength, so theoretically, (4.9) describes not only one equation but a system of infinitely many equations. In reality, the measuring instrument provides a limited number (2048 for CARIBIC DOAS) of wavelength bins (called channels), of which only a part is used (typically ∼200–500 channels). However, there are still much more available equations than unknown variables – the system of equations is over-determined. Because normally there is no solution for which τ_approx approximates the measured τ exactly, a 'best approximation' has to be found. Therefore, it is necessary to define a measure for the quality of the fit.

The *least square fitting technique* is a method which measures the 'difference' χ^2 between the measured values or a function of them (here the optical density τ) and a model function (here τ_approx).

$$\chi^2 = \sum_{n=1}^{N} \left(\frac{\tau(\lambda_n) - \tau_\mathrm{approx}(\lambda_1, \ldots, \lambda_N, a_0, a_1, \ldots)}{\epsilon(n)} \right)^2 \tag{4.11}$$

Here, the independent parameters λ_n are wavelengths (or more precisely wavelength bins, in the case of CARIBIC DOAS with a range of ≈1/15 nm), and the parameters a_0,a_1,..., which have to be adapted, are the unknown variables $S_1, \ldots, S_K, p_0, \ldots, p_{q_\mathrm{o}}$. The measuring values can be weighted with $1/\epsilon(n)$, usually the statistical error of $\tau(\lambda_n)$ is taken. If all $\epsilon(n)$ are equal, χ^2/ϵ^2 is the square of the standard deviation of $\tau - \tau_\mathrm{approx}$. In that case, ϵ is often omitted, the fit is then called 'unweighted least squares fit'.

Inserting (4.10) into (4.11) yields

$$\chi^2 = \frac{1}{\epsilon} \cdot \sum_{n=1}^{N} \Big(\ln \frac{I_0(\lambda_n)}{I(\lambda_n)} - \sum_{k=1}^{K} \sigma'_k(\lambda_n, T, p) \cdot S_k - \sum_{q=0}^{q_\mathrm{o}} p_q \cdot \lambda_n^q \Big)^2 \tag{4.12}$$

The aim of the least square fitting technique is to find the appropriate values for $S_1, \ldots, S_K, p_0, \ldots, p_{q_\mathrm{o}}$ to minimize χ^2. Because (4.12) is linear with respect to these values, there is always a unique solution available. However, in practice, non-linear effects like a wavelength shift occur (cf. Sect. 4.3.4). For details about several fitting routines used for DOAS see *Platt and Stutz* (2008, Chap. 8).

The *residuum* spectrum τ_{res} contains informaion about the quality of the result.

$$\begin{aligned}\tau_{\text{res}}(n) &:= \tau(\lambda_n) - \tau_{\text{approx}}(\lambda_1, \dots, \lambda_N, a_0, a_1, \dots) \\ &= \ln \frac{I_0(\lambda_n)}{I(\lambda_n)} - \sum_{k=1}^{K} \sigma'_k(\lambda_n, T, p) \cdot S_k - \sum_{q=0}^{q_o} p_q \cdot \lambda_n^q \end{aligned} \tag{4.13}$$

In ideal case, the residuum only consists of statistical noise, caused by photon noise, cf. Sect. 6.4.2. Furthermore, a polynomial of order q_o only approximates the broad band structure. Thus, the residuum spectrum should show only minor broadband structures and therefore and average close to zero. However, in practice, there are further contributions which contribute to a higher residuum, cf. Sect. 4.3.5.

An often used indicator for the quality of the fit is the 'Root Mean Square' (RMS), given by

$$R_{\text{RMS}} = \frac{\sqrt{\chi^2}}{N} \tag{4.14}$$

with N being the number of channels within the analysed wavelength range.

4.2. Direct and Scattering Measurements

In contrast to the setup assumed in the previous section, the CARIBIC DOAS system receives no direct sunlight, but light reflected at the ground or scattered within the atmosphere. To account for such *scattered light measurements*, two commonly used quantities – namely the vertical column density and the air mass factor – are introduced, first for the case of direct light measurements, afterwards for scattered light measurements. The concrete geometry for CARIBIC is described in Sect. 6.1.

4.2.1. Direct Light Measurements, AMF, VCD

Direct light measurements use a setup like in Sect. 4.1, where the measuring instrument is aligned towards the light source (e.g. the sun or the moon). Scattered light is assumed to be negligible. In Fig. 4.1, three such cases are depicted, The *elevation angle* α of the instrument is given by $\alpha = 90° - \theta$ with solar zenith angle θ.

In the easiest case (a), the concentration c_k of gas № k shall be constant within a layer of thickness H. After (4.3), the SCD calculates to $S_k = c_k \cdot L = c_k \cdot H \cdot \frac{1}{\cos\theta}$, so it depends on the solar zenith angle (SZA) and thus on the light path, but a quantity independent of the light path is desired. Therefore, the *vertical column density* (VCD) is defined as the concentration integrated along the vertical axis (i.e. the height z):

$$V_k := \int_0^{Z_{\text{TOA}}} c_{\text{v},k}(z) \cdot \mathrm{d}z \tag{4.15}$$

The subscript 'TOA' at the upper bound of the integral stands for *top of the atmosphere* (cf. p. 5). The subscript'v' (for 'vertical') shall indicate that $c_{\text{v},k}$ is treated as a function

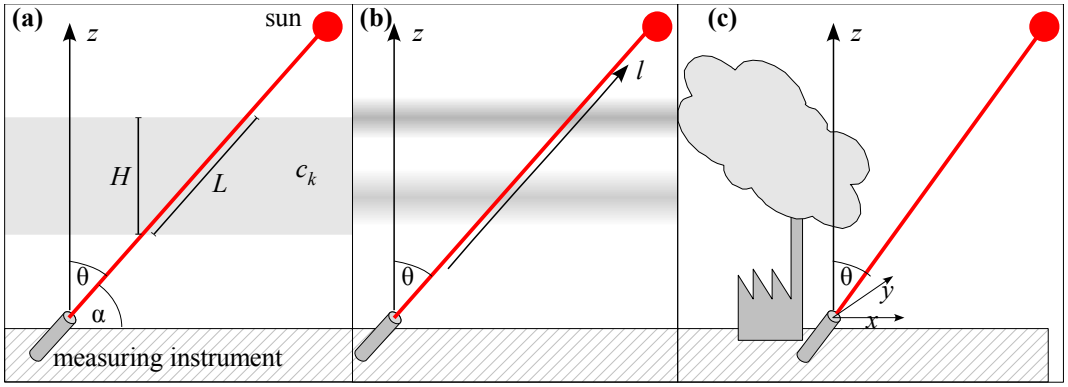

Figure 4.1.: Direct light measurements. (**a**) The concentration c_k is constant within the layer of thickness H. (**b**) The concentration is horizontally constant, i.e. it can be written as function of the height z. (**c**) The concentration varies vertically and horizontally. (Adapted from *Walter*, 2008)

of the height z, not of the position l along the slant light path (however, in case (a), $c_{\mathrm{v},k}(z)$ is constant within the layer, namely c_k). Analogously to the SCD, the VCD is the number of molecules per surface area in a vertical column from ground to TOA. Sometimes, not the *total* VCD (the column from 0 to TOA) is desired but only a partial VCD, e.g. the tropospheric or stratospheric VCD. In that case, the limits of integration have to be adopted.

The conversion factor between the SCD (which is the result of the DOAS analysis) and the VCD is called *air mass factor* (AMF), defined as

$$A_k := \frac{S_k}{V_k} \tag{4.16}$$

For the special case of a vertical light path (if the sun is in zenith, i.e. $\theta = 0°$), SCD and VCD are equal, thus $A_k = 1$, otherwise

$$A_k = \frac{1}{\cos\theta} \tag{4.17}$$

Here, the curvature of the earth is not considered, but, it is a good approximation for $\theta \lesssim 75°$. The corresponding AMF for the CARIBIC instrument will be given in Sect. 6.7.5 p. 123.

More realistic is case (b), where the concentration is considered to be horizontally constant, but varying vertically. Therefore, the concentration can be written as a function $c_{\mathrm{v},k}(z)$ of height z, or as a function $c_{\mathrm{s},k}(z)$ of the position l within the slant light path. Between the SCD and the VCD, the following relation is given (considering $\mathrm{d}z/\mathrm{d}l = \cos\theta$).

$$S_k \overset{(4.3)}{=} \int_0^{L_{\mathrm{TOA}}} c_{\mathrm{s},k}(l) \cdot \mathrm{d}l = \int_0^{Z_{\mathrm{TOA}}} c_{\mathrm{v},k}(z) \cdot \frac{\mathrm{d}z}{\cos\theta} \overset{(4.15)}{=} V_k \cdot \frac{1}{\cos\theta} \tag{4.18}$$

It shows, that also in this case, (4.17) applies. In contrast to that, a spatial limited plume is shown in case (c). While the slant light path misses the plume, the VCD

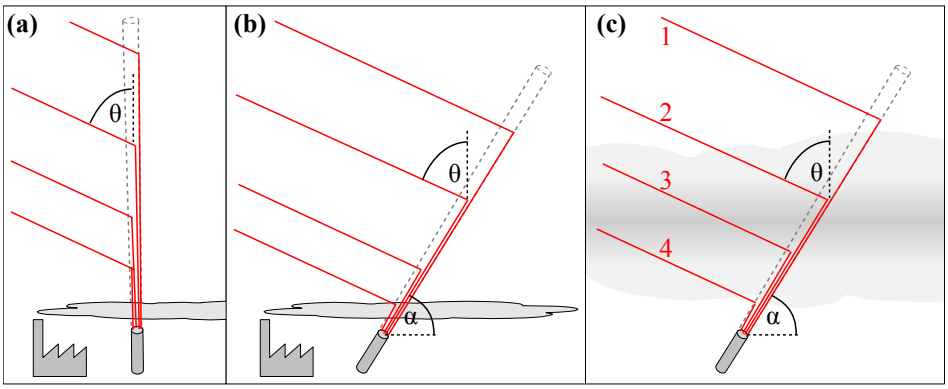

Figure 4.2.: Scattered light measurements. (**a**) The instrument is aligned in zenith direction, the gas to be measured shall be within a thin layer directly above the instrument. (**b**) The elevation angle is smaller than 90°, otherwise like (a). (**c**) The gas to be measured is dispersed within a thick layer. (Adapted from *Walter*, 2008)

above the the instrument is not zero. Therefore, the concept of the AMF does not fit to such a case.

4.2.2. Scattered Light Measurements

In contrast to the previous section, the instrument is not directed to the sun anymore, thus it only receives scattered light. Again, three cases (see Fig. 4.2) shall demonstrate the meaning of the SCD and the AMF, and the gas of interest shall only be present within the layer depicted in gray.

In case (a), the gas of interest is assumed to be inside a thin layer not far above the instrument, therefore the amount of light being scattered within that layer shall be negligible. Instead, all the received light shall be scattered above the layer in different altitudes. For the measured SCD, the scattering height is not relevant (as long as it is above the layer); furthermore, the SCD is (in ideal case) independent from the SZA θ. The SCD is equal to the VCD (i.e. $S_k = V_k$, thus $A_k = 1$), because the instrument is directed into zenith direction (elevation angle $\alpha = 90°$). Case (b) is like (a), except that the instrument is not directed into the zenith any more, thus the SCD is bigger than the VCD – according to (4.17), it is $A_k = S_k/V_k = 1/\sin\alpha$.

But the situation changes in case (c), where the layer is higher above or its thickness is not negligible any more. Per definition, the VCD V_k is still independent from the light path and the SZA, but not so the SCD (and therefore the AMF). For the four light paths in Fig. 4.2c, the SCDs are different. Light traveling along path № 1 is scattered above the layer, therefore the SZA θ is not relevant for this path. But for the other paths, the length within the layer and therefore the SCD increases with a larger SZA. On the other hand, for № 4, the elevation α of the instrument is not relevant because the scattering takes place below the layer.

The different paths would yield different SCDs, but the instrument only measures

one spectrum I, thus only one result S_k per species is retrieved by the DOAS algorithm, cf. (4.10) or (4.8):

$$\tau'(\lambda) = \sum_{k=1}^{K} \sigma'_k \cdot S_{\mathrm{ACD},k} \tag{4.19}$$

The subscript 'ACD' for *apparent column density* (*Platt and Stutz*, 2008, p. 253, 338) shall indicate that $S_{\mathrm{ACD},k}$ is not a 'real slant column density in the historical sense' as concentration integrated along *the* light path, cf. (4.3). However, $S_{\mathrm{ACD},k}$ can be interpreted as an average of the SCDs of the possible light paths, weighted by the probability of those paths – see Sect. 4.2.5 for a brief discussion of the validity of this interpretation.[2]

The probability for a certain light path is connected with the scattering cross sections of the air molecules and aeorsol particles, which are dependent of the scattering angle and the wavelength. Therefore, the apparent column density shows a dependency of the chosen wavelength range for the DOAS fit.

Summarized, the SCD is not only a result of the concentration profile c_k of the species № k, but it also depends on the elevation angle α, the SZA θ, the spatial distribution of the scattering and absorbing species and the chosen wavelength range. This shows, that here, a solely geometric approach like (4.17) is not valid any more. Instead, radiation transport calculations or simulations are necessary, see following section.

4.2.3. Radiative Transfer Models

The aim of a radiative transfer model (RTM) in regard to the conversion of SCDs to VCDs is to calculate the probability distribution of the possible light paths, which photons contributing to the measurements might have taken. For the case of only single scattering and a horizontally homogeneous atmosphere as depicted in Fig. 4.2c, a Radiative Transfer model could calculate such probabilities for a certain number of scattering heights. However, in reality, a photon can be scattered several times before reaching (or missing) the detector. Especially when furthermore considering three-dimensional features like aerosol layers with a limited horizontal scale, it becomes difficult to find an appropriate gridded search space for modeling all relevant light paths.

Instead, approaches based on Monte Carlo simulations are often used by RTMs, like in the case of the model used in this work, namely the *Monte Carlo Atmospheric Radiative Transfer Inversion Model* 'McArtim' (*Deutschmann*, 2009). In this model, photons are emitted by the instrument (inverse light paths) into a random direction within the field of view of the instrument. After some distance, the photon can be scattered. This distance between measurement instrument and the first scattering event is an output of a random algorithm, which factors in the probability distribution, calculated based

[2] Commonly, the term 'slant column density' and especially the acronym 'SCD' is used for both, the 'historical SCD' and the apparent column density, which is also done within this thesis.

on the assumed profile of scattering species (gas molecules, aerosol particles). Also the direction of the photon after the scattering effect is a random value considering dependency of the scattering cross section on the scattering angle. This random process is repeated until it reaches the top of the atmosphere (and therefore the sun) or until it is aborted (in case the probability for that process falls below a certain threshold). This simulation is performed for a large number of photons in order to obtain statistical information about the probabilities of the possible light paths.

Detailed information about RTMs, particularly about McArtim and its precursor TRACY-II, are given by *Deutschmann* (2009) and *Deutschmann et al.* (2011).

4.2.4. Box Air Mass Factors

In Sect. 4.2.1, (4.16), the AMF was introduced as conversion factor between the VCD and the SCD. For the case of scattered light measurements, the SCD S is an *apparent column density*, cf. Sect. 4.2.2. If the atmosphere is assumed to be horizontally homogeneous in the vicinity of the DOAS instrument, the concept of *Box Air Mass Factors* (Box-AMFs) is useful to describe the sensitivity of the measurement setup (for a given geometry, viewing direction and SZA) to the measured trace gas at different altitudes (cf. *Platt and Stutz*, 2008, p. 369). Therefore, the atmosphere is vertically divided into layers (or 'boxes'), numbered by the index j) of height h_j. The concentration c_j of the trace gas of interest is assumed to be constant within a layer, so the VCD of the gas within layer № j is given by $V_j = h_j \cdot c_j$. The Box-AMF A_j describes the sensitivity of the SCD towards layer № j, so $A_j \cdot V_j$ is the contribution of that layer to the retrieved SCD S, which calculates to

$$S = \sum_j S_j = \sum_j A_j \cdot V_j = \sum_j A_j \cdot h_j \cdot c_j \tag{4.20}$$

Using (4.16), the total AMF A can be written as

$$A = \frac{S}{V} = \frac{\sum_j A_j \cdot h_j \cdot c_j}{\sum_j h_j \cdot c_j} \tag{4.21}$$

As mentioned in Sect. 4.2.2 for the SCD, also the Box-AMF depend on the elevation angle α, the SZA θ, the spatial distribution of the scattering and absorbing species and the chosen wavelength range. As long as the trace gas of interest has a low optical density (which means that its presence has a negligible effect on the probability distribution of the light paths), the Box-AMF B_j are independent of the concentration profile. In contrast to that, at least the *shape* of the profile (the 'relative profile', cf. Sect. 4.5.2) has to be known (or assumed) in order to calculate the total AMF A and therefore to convert the SCD into a VCD.

4.2.5. Apparent Column Density, Light Path Integrals

In Sect. 4.2.2, it was stated that the apparent column density $S_{\mathrm{ACD},k}$ could be interpreted as an average of the SCDs of the possible light paths, weighted by the probability of those paths, i.e.

$$S_{\mathrm{ACD},k} \approx S_{\mathrm{average},k} \tag{4.22}$$

with

$$S_{\mathrm{average},k} = \frac{\int S_{\mathrm{p},k}(\Gamma) \cdot I_{\mathrm{p}}(\Gamma) \cdot \mathrm{d}\Gamma}{\int I_{\mathrm{p}}(\Gamma) \cdot \mathrm{d}\Gamma} \tag{4.23}$$

Here, $S_{\mathrm{p},k}(\Gamma)$ is the SCD of species № k for a specific light path (Γ) according to the 'historic sense' (4.3), $I_{\mathrm{p}}(\Gamma)$ the 'intensity' or probability of that lightpath.

Actually, (4.22) is only an approximation, which shall be shown in the following equations for the simplified case of only one absorber (therefore the index k will be omitted), in which case (4.19) can be written as $S_{\mathrm{ACD}} = \tau'/\sigma'$; cf. *Platt and Stutz* (2008, p. 351ff) for details.

When assuming the cross section σ of the trace gas to be constant and neglecting the difference between $\frac{\tau}{\sigma}$ and its differential analogue $\frac{\tau'}{\sigma'}$, S_{ACD} is connected to S_{average} by the following transformation:

$$\begin{aligned}
S_{\mathrm{ACD}} &= \frac{\tau}{\sigma} \overset{(4.2)}{=} \frac{1}{\sigma} \cdot \ln \frac{I_0}{I} \overset{(*)}{=} \frac{1}{\sigma} \cdot \ln \frac{\int I_{\mathrm{p},0}(\Gamma) \cdot \mathrm{d}\Gamma}{\int I_{\mathrm{p}}(\Gamma) \cdot \mathrm{d}\Gamma} \\
&\overset{(4.4)}{=} \frac{1}{\sigma} \cdot \ln \frac{\int I_{\mathrm{p},0}(\Gamma) \cdot \mathrm{d}\Gamma}{\int I_{\mathrm{p},0}(\Gamma) \cdot \exp(-\sigma \cdot S_{\mathrm{p}}(\Gamma)) \cdot \mathrm{d}\Gamma} \\
&\overset{(4.25)}{\approx} \frac{1}{\sigma} \cdot \ln \frac{\int I_{\mathrm{p},0}(\Gamma) \cdot \mathrm{d}\Gamma}{\left(\int I_{\mathrm{p},0}(\Gamma) \cdot \mathrm{d}\Gamma\right) \cdot \exp(-\sigma \cdot S_{\mathrm{average}})} = S_{\mathrm{average}}
\end{aligned} \tag{4.24}$$

In step $(*)$, the measured signals I_0 and I were replaced by the integral over all light paths Γ contributing to I_0 and I. If the SCDs $S_{\mathrm{p}}(\Gamma)$ were the same for each light path, $S_{\mathrm{p}}(\Gamma)$ could be taken out of the integral, thus $S_{\mathrm{ACD}} = S_{\mathrm{average}}$ would be fulfilled. This is also largely the case for a rather narrow light beam with 'only a few' dominating paths. Otherwise, the following approximation is applicable for the denominator of (4.24) as long as the optical density is small compared to 1.

$$\begin{aligned}
\int I_{\mathrm{p},0}(\Gamma) \cdot \exp(-\sigma \cdot S_{\mathrm{p}}(\Gamma)) \cdot \mathrm{d}\Gamma &\overset{(4.26)}{\approx} \int I_{\mathrm{p},0}(\Gamma) \cdot (1 - \sigma \cdot S_{\mathrm{p}}(\Gamma)) \cdot \mathrm{d}\Gamma \\
&= \int I_{\mathrm{p},0}(\Gamma) \cdot \mathrm{d}\Gamma - \sigma \cdot \int I_{\mathrm{p},0}(\Gamma) \cdot S_{\mathrm{p}}(\Gamma) \cdot \mathrm{d}\Gamma \\
&= \int I_{\mathrm{p},0}(\Gamma) \cdot \mathrm{d}\Gamma - \sigma \cdot S_{\mathrm{average}} \cdot \int I_{\mathrm{p},0}(\Gamma) \cdot \mathrm{d}\Gamma \\
&= \left(\int I_{\mathrm{p},0}(\Gamma) \cdot \mathrm{d}\Gamma\right) \cdot (1 - \sigma \cdot S_{\mathrm{average}}) \\
&\overset{(4.26)}{\approx} \left(\int I_{\mathrm{p},0}(\Gamma) \cdot \mathrm{d}\Gamma\right) \cdot \exp(-\sigma \cdot S_{\mathrm{average}})
\end{aligned} \tag{4.25}$$

Here, the first order of the Taylor series of the exponential function was used:

$$\mathrm{e}^x \approx 1 + x \quad \text{for} \quad |x| \ll 1 \tag{4.26}$$

For absorbers with high column densities and strong absorption lines, the error resulting from the high optical densities gets significant and (4.22) is not valid any more. In such cases, the DOAS retrieval and RTM calculations for determining the AMF cannot be done separately any more, cf. *Richter* (1997). For the case of the CARIBIC DOAS observations, the optical density of the measured trace gases is low enough to justify the abovementioned approximations and thus the abovementioned interpretation of the measured SCD.

4.2.6. Fraunhofer Reference Spectrum

Up to now, I_0 was assumed to be the known spectrum of the light source before traversing the atmosphere (cf. (4.1) and Fig. 3.5). However, for the case of ground-based or airborne measurements using sunlight, I_0 cannot be directly measured. Theoretically, a solar spectrum taken by a satellite could be used. Alternatively, a ground spectrum taken from an elevated altitude could be taken (in the DOAS community commonly called *Kurucz spectrum*, cf. *Kurucz et al.* (1984)), however, such a spectrum is already influenced by the atmosphere. But on the strength of past experience, both kinds of solar spectra have not shown to be suitable for I_0. The main reason is, that each instrument only can measure with a finite spectral resolution and a limited accuracy, therefore it would be necessary to convert the solar spectrum measured by a satellite into a spectrum, which the measurement instrument would have obtained. With the help of the *instrument function* (cf. Sect. 4.3.1 and Sect. 6.3.2), an approximation would be possible, but not with sufficient accuracy.

Therefore, as a substitute for I_0, one of the spectra recorded by the measuring instrument is taken (here referred to as I_{FRS} for *Fraunhofer reference spectrum*, FRS). Thus, in (4.10), the parameters have to be fitted to approx $\ln \frac{I_{\mathrm{FRS}}}{I}$ instead of $\ln \frac{I_0}{I}$

$$\ln \frac{I_{\mathrm{FRS}}(\lambda)}{I(\lambda)} = \tau_\Delta(\lambda) \approx \tau_{\Delta,\mathrm{approx}}(\lambda) = \sum_{k=1}^{K} \sigma'_k(\lambda, T, p) \cdot S_{\Delta,k} + \sum_{q=0}^{q_\mathrm{o}} p_{\Delta,q} \cdot \lambda^q \tag{4.27}$$

Like in (4.10), the parameters $S_{\Delta,k}$ are the results of the DOAS fit. To answer the question about the physical meaning of $S_{\Delta,k}$, the left side of (4.27), namely $\tau_\Delta(\lambda)$ can be (merely mathematically) transformed by inserting the unknown spectrum I_0:

$$\ln \frac{I_{\mathrm{FRS}}(\lambda)}{I(\lambda)} = \ln\Big(\frac{I_0(\lambda)}{I(\lambda)} \cdot \frac{I_{\mathrm{FRS}}(\lambda)}{I_0(\lambda)}\Big) = \ln \frac{I_0(\lambda)}{I(\lambda)} - \ln \frac{I_0(\lambda)}{I_{\mathrm{FRS}}(\lambda)} \tag{4.28}$$

According to (4.5), this further leads to

$$\ln \frac{I_{\mathrm{FRS}}(\lambda)}{I(\lambda)} = \tau(\lambda) - \tau_{\mathrm{FRS}}(\lambda) = \sum_{k=1}^{K} \Big(\sigma_k(\lambda, T, p) \cdot (S_k - S_{\mathrm{FRS},k})\Big) \tag{4.29}$$

This shows, that the retrieved quantities $S_{\Delta,k}$ are the approximations for $S_k - S_{\mathrm{FRS},k}$, i.e. the difference between the SCD S_k of the current spectrum I and the SCD $S_{\mathrm{FRS},k}$

of the FRS I_{FRS}.

$$S_{\Delta,k} \simeq S_k - S_{\mathrm{FRS},k} \tag{4.30}$$

$S_{\Delta,k}$ is called *differential slant column density* ('dSCD'). Usually, a spectrum containing a low SCD is taken as FRS, otherwise a negative dSCD $S_{\Delta,k}$ occurs, if $S_k < S_{\mathrm{FRS},k}$. For ground-based measurements of a gas without a diurnal cycle, it is possible to get rid of S_k with the help of a so-called *Langley-Plot*, cf. *Platt and Stutz* (2008, p. 344). For the case of airborne observations, a spectrum over a remote region is taken as FRS which contains a low SCD of pollutant gases (e.g. NO_2).

To simplify matters, in the following, the term 'differential' and the subscript '$_\Delta$' will be omitted and the FRS will be denoted as I_0.

4.2.7. Ring Effect

In 1961, Grainger and Ring recorded moonlight spectra and compared them with spectra from scattered sunlight. Thereby they observed that the Fraunhofer lines in the scattered solar spectrum were not as deep as those from moonlight. The same effect – which is called *Ring effect* – can be observed when performing zenith measurements over a day. With increasing solar zenith angle, the Fraunhofer lines are increasingly 'filled up'. The reason for this 'extra light reaching us from the sky' (*Grainger and Ring*, 1962) was unclear for some years; there were speculations about a daylight airglow, caused by aerosol fluorescence. However, studies in the last decades strengthened the confidence, that rotational Raman scattering is the main causer of the Ring effect, cf. (*Bussemer*, 1993; *Fish and Jones*, 1995). As mentioned in Sect. 3.2.3, the wavelength of a photon changes due to Raman scattering. Because the intensity $I(\lambda_{\mathrm{FRL}})$ of a Fraunhofer line is lower than the intensity $I(\lambda_{\mathrm{noFRL}})$ of an ambient wavelength λ_{noFRL}, more photons are available for the change from λ_{noFRL} to λ_{FRL} than otherwise. In consequence, the spectrum is smoothed, i.e. the Fraunhofer lines are filled up – just as observed by Grainger and Ring.

Lambert Beer's Law (4.1), does not account for this effect. For the case of direct light measurements like in Sect. 4.2.1, the effect is negligible, if the field of view of the instrument is small enough, because than, the number of photons being scattered into the beam is very low compared to the number of photons coming directly from the source. For the case of scattered light measurements, however, all the light has been scattered. Although the fraction of Raman scattered photons in the measured spectrum is only on the order of a percent, the effect can not be neglected in the DOAS analysis, because the optical density of weak absorbers that shall be measured is much smaller.

A commonly used method to account for the Ring effect is to include a *Ring spectrum* in the DOAS fit like the cross section of an absorber. To see how a such a Ring spectrum shall look like and why this approach is feasible, the measured spectrum I is interpreted as a sum of the light scattered by Raman scattering, I_{Raman}, and I_{elastic}, the elastic

scattered light (Rayleigh and Mie scattering). Then, the logarithm of I can be written as

$$\begin{aligned} \ln(I) &= \ln(I_{\text{elastic}} + I_{\text{Raman}}) \\ &= \ln(I_{\text{elastic}} \cdot (1 + \frac{I_{\text{Raman}}}{I_{\text{elastic}}})) \\ &= \ln(I_{\text{elastic}}) + \ln(1 + \frac{I_{\text{Raman}}}{I_{\text{elastic}}}) \\ &\approx \ln(I_{\text{elastic}}) + \frac{I_{\text{Raman}}}{I_{\text{elastic}}} \end{aligned} \tag{4.31}$$

In the last step, the logarithm was approximated by its Taylor expansion (only until the linear term), namely

$$\ln(1 + x) \approx x \quad \text{for} \quad |x| \ll 1 \tag{4.32}$$

This approximation is justifiable, because $I_{\text{Raman}} \ll I_{\text{elastic}}$. By defining I_{Ring} as

$$I_{\text{Ring}} := \frac{I_{\text{Raman}}}{I_{\text{elastic}}} \tag{4.33}$$

the elastic part of the scattering, I_{elastic}, which is the one described by Lambert Beer's law, is given by

$$\ln(I_{\text{elastic}}) \approx \ln(I) - I_{\text{Ring}} \tag{4.34}$$

Inserting I_{elastic} instead of I in (4.10) results in

$$\tau(\lambda) = \ln \frac{I_0(\lambda)}{I(\lambda)} = \sum_{K=1}^{K} \sigma'_K(\lambda, T, p) \cdot S_K + \sum_{q=0}^{q_o} p_q \cdot \lambda^q - p_{\text{Ring}} \cdot I_{\text{Ring}} \tag{4.35}$$

Here, a fit coefficient p_{Ring} was added, because the total size of I_{Ring} is not known.

A Ring spectrum I_{Ring} can be obtained experimentally or by calculation. The experimental approach uses the different behaviour of elastic and inelastic scattering with respect to polarisation – Raman scattered light is significantly less polarized than Rayleigh scattered light (cf. *Solomon et al.*, 1987). However, this approach has some disadvantages. The elastic scattered light results not only from Rayleigh scattering, but also from Mie scattering, thus the experimental separation between elastic and inelastic scattering is imperfect. Furthermore, different light paths contain different amounts of the sought-after trace gases, which distorts the result, cf. (*Wagner*, 1999, p. 50). Besides that, the instrument would have to be sensitive towards polarisation, which would make the setup more complicated and therefor more error-prone.

More common today is to calculate a Ring spectrum based on the known rotation energy levels of the main components of air, namely nitrogen and oxygen. For this calculation, high resolved solar spectrum can be used or a spectrum taken by the measurement instrument (typically the FRS). The latter one has the advantage, that the convolution of the high resolved spectrum is not necessary, thus avoiding errors due to an imperfect known instrument function (cf. Sect. 6.3.2).

The second approach was also taken here for the evaluation of the CARIBIC data, using the DOASIS program (cf. *Kraus*, 2006) for calculating I_{Ring}. Further information about Ring spectra including a more sophisticated approach based on Monte Carlo radiative transfer models are given by *Wagner et al.* (2009).

4.3. Considerations Concerning a Real Instrument

A real instrument will not provide the precise spectrum of the impinging light. Instead, the light is dispersed in a spectrograph with a limited resolution, then detected by a finite number of pixels. The real signal is furthermore superimposed by straylight, dark current and offset. This section deals with the theoretical part of these aspects, and in principle how to take care about them in the analysis. The practical aspects concerning the CARIBIC instrument are given in Chap. 6.

4.3.1. Wavelength-Channel-Mapping, Convolution and Discretisation

As depicted in Fig. 4.3a for an ideal spectrograph, light with spectrum I enters the spectrograph. Like in a prism, the light is dispersed into its spectral colors before it reaches the detector. Therefore, $I(\lambda)$ is mapped to $I^*(\Lambda)$, where I^* is a function of the position Λ at the detector surface – with the mapping function Γ_{S} between the wavelength λ and the corresponding position Λ:

$$\Lambda = \Gamma_{\mathrm{S}}(\lambda) \quad \text{or} \quad \lambda = \Gamma_{\mathrm{S}}^{-1}(\Lambda) \tag{4.36}$$

The light impinging on the surface of the detector is converted into a digital signal $I^{\times}(n)$, a function of the channel number: $n \in \{1, \ldots, N\}$. For the case of CARIBIC, it is $N = 2048$ – the detector has 2048 channels. With Γ_{S} as mapping function between Λ and n, the combined function Γ_{DS} or its reverse function $\Gamma_{\mathrm{DS}}^{-1}$ is called *dispersion function* or *wavelength calibration*.

$$n = \Gamma_{\mathrm{D}}(\Lambda) = \Gamma_{\mathrm{D}}(\Gamma_{\mathrm{S}}(\lambda)) =: \Gamma_{\mathrm{DS}}(\lambda) \tag{4.37}$$

$$I^{\times}(n) \mathrel{\widehat{=}} I^*(\Lambda) \mathrel{\widehat{=}} I(\lambda) \tag{4.38}$$

Actually, Γ_{D} and Γ_{DS} are not injective, because they project real-valued quantities Λ or λ to discrete numbers; therefore Γ_{D}^{-1} and $\Gamma_{\mathrm{DS}}^{-1}$ do not exist in a strict sense. However, pragmatically, $\lambda = \Gamma_{\mathrm{DS}}^{-1}(n)$ could be defined to be the middle of the wavelength for which $\Gamma_{\mathrm{DS}}(\lambda) = n$ applies. Besides the finite number of channels, also the 'intensity' $I^{\times}(n)$ of pixel n is a discrete number. For a 16 bit analog-digital-converter, this is an integer in the range from 0 to $2^{16} - 1 = 65535$. For a concrete wavelength calibration see Sect. 6.3.3.

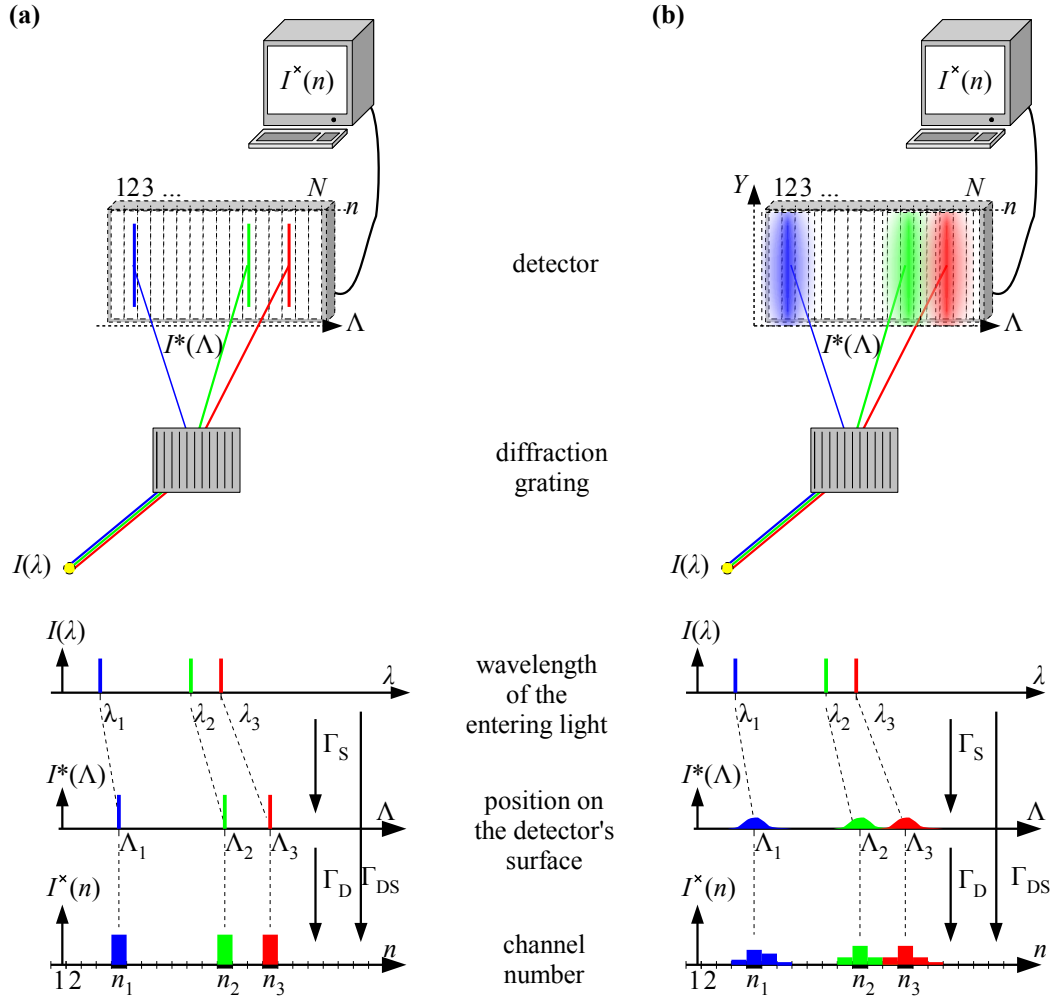

Figure 4.3.: Sketch of the steps from the real spectrum I to the digitally stored spectrum $I^{\times}$. First, the light is dispersed before reaching the detector at position Λ. (a) shows the case for an ideal spectrograph, (b) for a real one, where a convolution due to the limited resolution takes place. The spectrograph specific function Γ_S maps wavelength λ to the position Λ; the detector specific function Γ_D maps the position Λ to pixel number n. (Adapted from *Walter*, 2008)

Convolution

In an ideal spectrograph, monochromatic would reach the detector at a sharp position $\Lambda = \Gamma_S(\lambda)$, so I^* would be a delta distribution. In a real spectrograph, however, I^* is an approximately Gaussian shaped function with a finite with, cf. Fig. 4.3b. If I^* was known for monochromatic light of each wavelength λ, the I^* could be calculated for any other spectrum I by

$$I^* = \boldsymbol{H}_S\, I \quad \text{or} \quad I^*(\Lambda) = (\boldsymbol{H}_S\, I)(\Lambda) \tag{4.39}$$

with a spectrograph specific operator $\boldsymbol{H}_S$. To be precise, it has to be mentioned that also the direction of the incoming light within the field of view is relevant, but as long

as the incoming radiance does not strongly differ within the field of view, this fact can be neglected. Then, the operator $\boldsymbol{H}_\mathrm{S}$ can be replaced by a function $\tilde{H}_\mathrm{S}$ of the incoming wavelength λ' and the position Λ at the detector, and (4.39) can be written as

$$I^*(\Lambda) = \int I(\lambda') \cdot \tilde{H}_\mathrm{S}(\Lambda, \lambda') \cdot \mathrm{d}\lambda' = \int I(\lambda') \cdot \tilde{H}_\mathrm{S}(\Gamma_\mathrm{S}(\lambda), \lambda') \cdot \mathrm{d}\lambda' \tag{4.40}$$

If $\tilde{H}_\mathrm{S}(\Gamma_\mathrm{S}(\lambda), \lambda')$ is only dependent on the difference between the wavelength λ' of the entering light and λ (which here is the 'wavelength' corresponding to position Λ according to $\lambda = \Gamma_\mathrm{S}^{-1}(\Lambda)$), than $\tilde{H}_\mathrm{S}$ can be replaced by a function H_S with $H_\mathrm{S}(\lambda - \lambda') = \tilde{H}_\mathrm{S}(\Gamma_\mathrm{S}(\lambda), \lambda')$. In that case, (4.40) describes a convolution:

$$I^*(\Lambda) = I^*(\Gamma_\mathrm{S}(\lambda)) = \int I(\lambda') \cdot H_\mathrm{S}(\lambda - \lambda') \cdot \mathrm{d}\lambda' =: (I * H_\mathrm{S})(\lambda) \tag{4.41}$$

In practice, the convolution function H_S is determined by taking a spectrum (or many spectra to reduce noise) of a spectral lamp (e.g. a mercury gas lamp), using an isolated spectral line. This spectral line should be within or close to the wavelength range used for the DOAS analysis, because the convolution approach is a good approximation for $\tilde{H}_\mathrm{S}$ only for a limited area of the detector's surface – 'H_S is slightly Λ dependent'.

Discretisation

The discretisation of the spectrum I^* into the digital signal $I^\times$ according to

$$I^\times = \boldsymbol{H}_\mathrm{D}\, I^* = \boldsymbol{H}_\mathrm{D}\, \boldsymbol{H}_\mathrm{S}\, I \quad \text{or} \quad I^\times(n) = (\boldsymbol{H}_\mathrm{D}\, I^*)(n) = (\boldsymbol{H}_\mathrm{D}\, \boldsymbol{H}_\mathrm{S}\, I)(n) \tag{4.42}$$

with a detector specific operator $\boldsymbol{H}_\mathrm{D}$, which incorporates the quantum efficiency of the detector and the characteristics of the analog-digital-converter. The operator $\boldsymbol{H}_\mathrm{D}$ can be replaced by H_D, a function solely dependent on the channel number n, and $I^\times$ can be written as

$$I^\times(n) = H_\mathrm{D}(n) \cdot \int_{\Lambda_\bullet(n)}^{\Lambda^\bullet(n)} I^*(\Lambda) \cdot \mathrm{d}\Lambda \tag{4.43}$$

with $\Lambda_\bullet(n)$ as lower and $\Lambda^\bullet(n)$ as upper edge of channel n.

However, from (4.42) to (4.43), some assumptions and approximations were made. The integration of light impinging on the detector has to be performed in both directions, along the Λ and along the Y axis (cf. Fig. 4.3; here, $I^*(\Lambda)$ is interpreted to be already integrated along Y). With this integration along Λ and Y, a possible imhomogenity of the pixel is neglected.[3] Also the detector's sensitivity with respect to the impinging angle is not accounted for, but as most light should come from a rather narrow spherical angle (for a specific pixel), this dependency should be unproblematic. The quantum efficiency of a pixel significantly depends on the wavelength of the photons (cf. Fig. 6.18 p. 110), which is also not explicitly considered in (4.43). However, due

[3] The pixels of most CCD detector chips area arranged in a two-dimensional matrix, thus one channel is a result of vertical of several pixels. This applies also for the CARIBIC DOAS instrument.

to the dispersion in the spectrograph, each pixel should only receive light of a narrow wavelength range (less than ∼1 nm), in which the quantum efficiency can be regarded to be constant and therefore included in the prefactor $H_{\mathrm{D}}(n)$. Equation (4.43) states $I^{\times}$ to be proportional to I^{*}. Already the discretisation by the analog-digital-converter to a 16 bit number shows, that this can not be exactly true. Also an offset and dark current signal contribute (see below). Besides that, the linearity of the detector is a good approximation for a certain intensity range. With higher intensities, the digital signal increases slower until it reaches saturation. An assessment of the importance of the linearity is given in *Platt and Stutz* (2008, p. 227).

Furthermore, $I^{\times}$ contains additional contributions which have to be added to (4.43), which only includes the 'real' part of the digital signal.

$$\begin{aligned} I^{\times}(n) &= I^{\times[\mathrm{real}]}(n) + I^{\times[\mathrm{s}]}(n) + I^{\times[\mathrm{o}]}(n) + I^{\times[\mathrm{d}]}(n) \\ &= H_{\mathrm{D}}(n) \cdot \int_{\Lambda_{\bullet}(n)}^{\Lambda^{\bullet}(n)} I^{*}(\Lambda) \cdot \mathrm{d}\Lambda + I^{\times[\mathrm{s}]}(n) + I^{\times[\mathrm{o}]}(n) + I^{\times[\mathrm{d}]}(n) \end{aligned} \tag{4.44}$$

The *straylight* $I^{*[\mathrm{s}]}$ and thus the signal $I^{\times[\mathrm{s}]}$ is caused by undesired lightpaths inside the spectrograph, cf. Sect. 4.3.3 and Sect. 6.3.4. An offset signal $I^{\times[\mathrm{o}]}$ is caused by the analog-digital-converter to avoid negative numbers; furthermore, a temperature dependent dark current signal $I^{\times[\mathrm{d}]}$ occurs, cf. Sect. 6.4.2. Both can be measured in the absence of light and therefore subtracted from $I^{\times}$, cf. Sect. 6.7.2.

The abovementioned measurement of a mercury lamp does actually not yield I^{*} but $I^{\times}$, thus the convolution function H_{S} and the detector function H_{D} are not measured independently. Instead, a combination H_{DS} of both is measured. Because the total intensity is not important for the DOAS approach, H_{DS} can be scaled by an arbitrary factor, usually it is normalized to 1 with respect to its maximum or integral. As it describes the instrument's behaviour, it is called *instrument function*, also named *slit function*, because it depends on the width of the spectrograph's entrance slit. The instrument function for CARIBIC DOAS is given in Sect. 6.3.2. For DOAS applications, the width of H_{DS} is typically on the order of 5 channels as a compromise between a high spectral resolution and avoiding aliasing effects: The shape of a narrow slit function with a width of only one or two channels would significantly change with a small wavelength shift, cf. illustration in *Frieß* (2001, p. 79).

4.3.2. Convoluted Cross Sections, I_0 Effect

Equation (4.5) gives the relation between the optical depth (as logarithm of the quotient of I_0 and I) and the cross sections of the absorbing species. But in reality, instead of the precise (high resolution) spectrum I, the convoluted and discretised spectrum $I^{\times}$ is measured, likewise $I_0^{\times}$ instead of I_0. To account for that, the high resolution cross sections σ_k on right sight of the equation is replaced by $\sigma_k^{\times} = H_{\mathrm{DS}}\,\sigma_k$, which is σ_k after the convolution and discretisation with the instrument function H_{DS}. Thus, (4.5)

becomes

$$\ln \frac{I_0^{\times}(n)}{I^{\times}(n)} \approx \sum_k \sigma_k^{\times}(n) \cdot S_k \tag{4.45}$$

However, this is not precise, because there are several approximations necessary to come from the left to the right side of this equation.

$$\begin{aligned} \ln \frac{I_0^{\times}}{I^{\times}} \quad &= \quad \ln \frac{[[I_0]^*]^{\times}}{[[I]^*]^{\times}} = \ln \frac{[[I_0]^*]^{\times}}{[[(I_0 \cdot \exp(-\sum_k \sigma_k \cdot S_k))]^*]^{\times}} \\ &\overset{(4.47)}{\approx} \quad \ln \frac{[[I_0]^*]^{\times}}{[[I_0]^*]^{\times} \cdot [[\exp(-\sum_k \sigma_k \cdot S_k)]^*]^{\times}} = -\ln([[\exp(-\sum_k \sigma_k \cdot S_k)]^*]^{\times}) \\ &\overset{(4.48)}{\approx} \quad -[[-\sum_k \sigma_k \cdot S_k]^*]^{\times} \overset{(4.49)}{=} \sum_k [[\sigma_k]^*]^{\times} \cdot S_k = \sum_k \sigma_k^{\times} \cdot S_k \end{aligned} \tag{4.46}$$

Here, the convolution and the discretisation were indicated by '$[]^*$' and '$[]^{\times}$'. In the first approximation, the multiplication was commutated with the convolution and the discretisation according to

$$[A \cdot B]^* \approx [A]^* \cdot [B]^* \quad \text{and} \quad [A \cdot B]^{\times} \approx [A]^{\times} \cdot [B]^{\times} \tag{4.47}$$

for two function A and B. In the second approximation, the logarithm was commuted with the discretisation and the convolution according to

$$\ln([A]^{\times}) \approx [\ln A]^{\times} \quad \text{and} \quad \ln([A]^*) \approx [\ln A]^* \tag{4.48}$$

Furthermore, the convolution and the discretisation are considered to be linear in the sense of

$$[\alpha \cdot A + \beta \cdot B]^* = \alpha \cdot [A]^* + \beta \cdot [B]^* \quad \text{and} \quad [\alpha \cdot A + \beta \cdot B]^{\times} = \alpha \cdot [A]^{\times} + \beta \cdot [B]^{\times} \tag{4.49}$$

with coefficients α and β. For the convolution, this is the case; for the discretisation, it is the case for the calculation of $\sigma_i^{\times}$, because the instrument function H_{DS} is assumed to be linear. However, whether the same applies to the left side (the measured spectra $I^{\times}$ and $I_0^{\times}$), depends on the linearity of the detector.

I_0 Effect

The abovementioned approximations are feasible for absorbers with small optical densities. For very strong absorbers, they lead to a not negligible error. This is called I_0 *effect*, because it is a consequence of the highly structured solar spectrum. Instead of a 'standard' cross section $\sigma_k^{\times}$, an I_0 corrected version $\sigma_{\mathrm{corr},k}^{\times}$ can be used to minimise or correct the error:

$$\sigma_{\mathrm{korr},k}^{\times}(n) = -\frac{1}{S_k} \cdot \ln \frac{[[I_0 \cdot \mathrm{e}^{-\sigma \cdot S_k}]^*]^{\times}(n)}{[[I_0]^*]^{\times}(n)} \tag{4.50}$$

For the case of only one species, inserting $\sigma_{\mathrm{korr},k}^{\times}$ into (4.49) directly shows the correctness of that approach; more details are given in *Frieß* (2001, p. 81ff) and *Johnston*

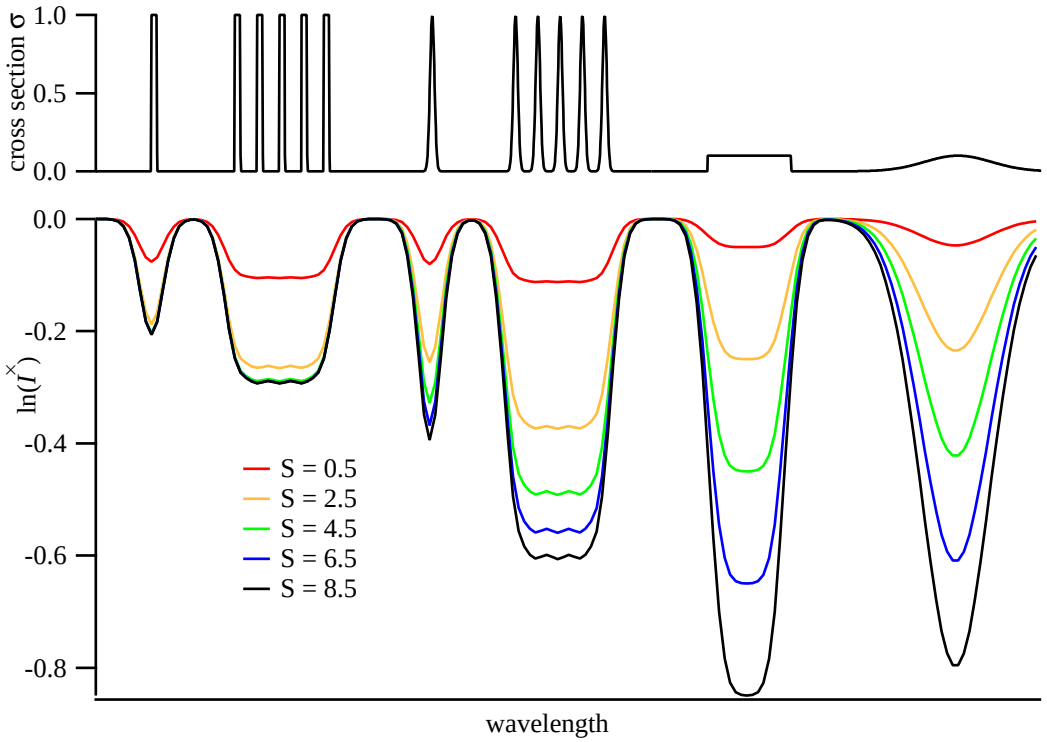

Figure 4.4.: Demonstration of the Saturation effect for only one absorber and a completely 'flat' light source $I_0(\lambda) = 1 = \text{const}$. Upper part: Cross section σ of the absorber (left: rectangular shapes with a with corresponding to 1 pixel, middle: Gaussian shaped lines, right: broad rectangular and Gaussian line). Lower part: $\ln(I^\times)$ for different SCDs S

(1996). However, to calculate $\sigma^\times_{\text{korr},k}$, the spectra I_0 and the SCD S_k have to be known, which is not the case. Instead of the measured FRS I_0, a high resolved solar spectrum is taken, e.g. *Kurucz et al.* (1984). For S_k, an initial guess already leads to feasible results, which can be improved by an iterative approach. Several tests with CARIBIC data showed only small differences when using a I_0 corrected or standard convoluted cross sections.

Saturation

Not only the structure of I_0 causes problems; also cross section with a strong and narrow structure and a high optical density lead to errors. Especially the commutation between the logarithm and the convolution and discretisation (4.48) in (4.46) is not feasible any more. While $\ln(I_0/I)$ still is proportional to the sum of the real SCDs S_k, the convoluted quantitiy $\ln(I_0^\times/I^\times)$ and therefore the SCDs retrieved from the DOAS fit increase more and more slowly. This effect also occurs for a smooth (or even wavelength independent) spectrum I_0 (in that case it is practically $I_0 = I_0^\times$).

Figure 4.4 illustrates this effect for an artificial and exaggerated case, assuming $I_0(\lambda) = 1 = \text{const}$ and only one absorber. The cross section σ and thus the optical

density $\tau = S \cdot \sigma$ of that absorber is depicted in the upper part of the figure; it shall contain (from left to right) several rectangle shaped and Gaussian shaped lines, with a width corresponding to one pixel, and two rather broad lines. The instrument function is assumed to be Gaussian with a FWHM (full width half maximum) of 5 pixels. In the lower part, the logarithm of the measured spectrum $I^{\times}$ is shown for five different SCDs. The precise $\ln(I)$ would be proportional to the SCD, which is also approximatively the case for the broad shapes on the right side or for small SCD (and thus small optical densities). But for the case of the rectangle shaped structures on the left, $\ln(I)$ does hardly change any more for $S \gtrsim 5$, 'saturation' is reached. For the case of Gaussian shaped lines (middle part), $I^{\times}$ still changes (but not proportional to the SCD any more), because the rims of the lines increasingly contribute to the absorption with increasing SCD.

4.3.3. Correction for Straylight

According to the wavelength-pixel-mapping (Sect. 4.3.1), each pixel should only receive light of a narrow wavelength range. In a real spectrograph, so-called *straylight* occurs, meaning that light of undesired wavelengths (mainly light in the visible range and infrared) reaches the detector, leading to an additional signal $I^{\times[\mathrm{s}]}(n)$, cf. (4.44) p. 62. As long as the straylight $I^{\times[\mathrm{s}]}$ is a rather smooth function with respect to n, it can be approximated by a polynomial. In principle, this leads to an additional non-linear term in the DOAS fit routine, but if $I^{\times[\mathrm{s}]}$ is small compared to the measured signal $I^{\times}$, straylight can be accounted for also in the linear fit.

In order to adumbrate this, (4.10) p. 49 is written in the simplified form

$$\ln I^{\times[\mathrm{real}]} = \ln I_0^{\times[\mathrm{real}]} + P \tag{4.51}$$

with P as abbreviation for the term $\sum_{k=1}^{K} \sigma'_k(\lambda, T, p) \cdot S_k + \sum_{q=0}^{q_\mathrm{o}} p_q \cdot \lambda^q$.
Using the approximation

$$\ln(y+x) = \ln(y) + \ln(1+\frac{x}{y}) \overset{(4.32)}{\approx} \ln(y) + \frac{x}{y} \quad \text{for} \quad |x| \ll |y| \tag{4.52}$$

and writing $I^{\times[\mathrm{real}]}$ and $I_0^{\times[\mathrm{real}]}$ as $I^{\times[\mathrm{real}]} = I^{\times} - I^{\times[\mathrm{s}]}$ and $I_0^{\times[\mathrm{real}]} = I_0^{\times} - I_0^{\times[\mathrm{s}]}$, (4.51) can be transformed to

$$\begin{aligned}
\ln(I^{\times} - I^{\times[\mathrm{s}]}) &= \ln(I_0^{\times} - I_0^{\times[\mathrm{s}]}) + P \\
\overset{(4.52)}{\rightsquigarrow} \ln(I^{\times}) - \frac{I^{\times[\mathrm{s}]}}{I^{\times}} &\approx \ln(I_0^{\times}) - \frac{I_0^{\times[\mathrm{s}]}}{I_0^{\times}} + P \\
\rightsquigarrow \ln(I^{\times}) &\approx \ln(I_0^{\times}) + \frac{1}{I^{\times}} \cdot I^{\times[\mathrm{s}]} - \frac{1}{I_0^{\times}} \cdot I_0^{\times[\mathrm{s}]} + P
\end{aligned} \tag{4.53}$$

For the case that the straylight signals $I^{\times[\mathrm{s}]}$ and $I_0^{\times[\mathrm{s}]}$ were constant with respect to channel n, the measured terms $\frac{1}{I^{\times}}$ and $\frac{1}{I_0^{\times}}$ can be fitted analogously to cross sections, with fit parameters $I^{\times[\mathrm{s}]}$ and $I_0^{\times[\mathrm{s}]}$.

This method can also be applied for $I^{\times[s]}$ (and analogously $I_0^{\times[s]}$) being a polynomial $I^{\times[s]} = \sum_{q=0}^{q_o} s_q \cdot n^q$, because than, the term $\frac{1}{I^\times} \cdot I^{\times[s]}$ can be written as

$$\frac{1}{I^\times} \cdot I^{\times[s]} = \frac{1}{I^\times} \cdot s_0 + \frac{n}{I^\times} \cdot s_1 + \cdots + \frac{n^{q_o}}{I^\times} \cdot s_{q_o} \tag{4.54}$$

with fit coefficients s_q. Further information about the dealing with straylight is given in *Platt and Stutz* (2008, p. 326ff), *Kraus* (2006, p. 92ff).

4.3.4. Shift and Squeeze

Because the spectrographs are not air tight, the pressure inside the spectrograph changes with some delay according to the ambient pressure in the aircraft's cargo room. With changing pressure, the light speed and the refractive index of the air slightly changes, which causes a shift in the wavelength of the photons. Because of that, a mismatch of the spectral position of Fraunhofer lines of the reference spectrum and the current measurement spectrum occurs, the same is true for the absorption structures of the gases included in the DOAS fit.

This leads to residual structures in the DOAS fit. In principle, a new wavelength calibration could be performed for each spectrum, cf. Sect. 6.3.3, but this would cause a large computational effort. Instead, a adaptable shift of the wavelengths is included in the fit routine, based on minimizing the residual structure. Beside a shift of the wavelengths, also a small stretch is allowed, in principle also corrections of higher order are possible. However, this kind of fit is not linear any more and therefore needs enhanced computational effort. Typically, the iterative fitting algorithm contains a sequence of linear and non-linear fitting steps. The WinDOAS (*Fayt and van Roozendael*, 2001) program used in this work for the analysis uses the *Levenberg-Marquard method*, cf. *Marquardt* (1963), *Platt and Stutz* (2008, p. 291ff).

4.3.5. Error Considerations

Because electromagnetic radiation is quantised in kind of photons, which are emitted in a stochastic process by a thermal radiator (here the sun), the real spectrum I and therefore also the stored spectrum $I^\times$ contain photon noise, which can be described by a Poisson static. In the Gaussian approximation, this noise σ_{ph} is given by $\sigma_{\mathrm{ph}} = \sqrt{n_{\mathrm{ph}}}$ with n_{ph} being the number of impinging photons (e.g. on a certain pixel), cf. Sect. 6.4.2. Essential for the fit quality is the signal-to-noise ratio, namely

$$n_{\mathrm{ph}}/\sigma_{\mathrm{ph}} = n_{\mathrm{ph}}/\sqrt{n_{\mathrm{ph}}} = \sqrt{n_{\mathrm{ph}}} \tag{4.55}$$

This means that the signal-to-noise ratio is proportional to the square of the number of photons and thus to the square of the exposure time. The exposure time is limited by the capacity of the detector (Sect. 6.4.1), but several scans can be added for one spectrum, furthermore several spectra can be coadded for the analysis. However, in practise, the

feasible time span is still limited because of temporal changes of the instrument, the light source or other circumstances like the desired temporal resolution of the measurements. The latter one is the most limiting factor for airborne measurements due to the fast forward movement of the aircraft.

During the acquisition and readout process further statistical noise σ_{inst} is added by the instrument. Apart from the detector's quality and temperature, this kind of noise predominantly depends on the number of scans, cf. Sect. 6.4.2.

This noise leads to a non zero χ^2 and a residual structure τ_{res} in the DOAS fit, cf. (4.12) and (4.13). Based on the residuum, the statistical error of the retrieved SCDs can be estimated, as described in *Stutz and Platt* (1996). Such statistical SCD errors given in this thesis were calculated together with the SCDs by the analysis program WinDOAS *Fayt and van Roozendael* (2001). As reported in *Heue* (2005, p. 17), a comparison between the the WinDOAS error retrieval and the approach suggested in *Stutz and Platt* (1996) had shown good agreement.

However, several additional error sources for the SCD retrieval occur with predominantly systematic character, which are not accounted for in the statistical error retrieval:

- The broadband shape of the scattering is only approximated by the DOAS polynomial. If the chosen order of the polynomial is too low, the residual structure is high. On the other hand, a polynomial of high order could imitate the shape of cross sections containing rather broadband features, e.g. O_4, which would lead to a distortion of the retrieved SCD. For the CARIBIC data, usually a polynomial of 4th order was taken.

- Because scattering shows a broadband wavelength dependency, also the light path and therefore the SCD changes with the wavelength, cf. Sect. 4.2.5. The wider the fitting window is, the larger the error caused by this effect.

- Straylight in the detector causes an additional signal, cf. Sect. 4.3.3.

- The convolution of the high resolved literature spectra is not perfect, because instead of the spectrograph function H_S only the instrument function H_{DS} is known, which contains only a limited number of discrete points. This leads to aliasing effects, cf. Sect. 4.3.1. Furthermore, the spectrograph function is not the same for all wavelengths, which is assumed when performing a convolution (Sect. 4.3.1). Moreover, the spectrograph function can slightly change with time in a non stable instrument.

- Especially for optical thick absorbers with narrowband structures, the I_0 effect and the saturation effect can get relevant, cf. Sect. 4.3.2.

- Cross-sensitivities between the species can occur, which means that the occurance of one gas distorts the retrieved SCD of another gas. Typically, these cross-

sensitivities are large if two or more gases show similar absorption structures after their convolution, and if the residual structure of the DOAS fit is high.

- Imprecise wavelength calibrations (cf. Sect. 4.3.1) lead to structures in the residuum, which can cause cross-sensitivity to other gases. Drifts of the wavelength calibrations occur due to instabilities of the instrument, caused by temperature and pressure changes.

- The cross section of the gases can contain errors themselves (with respect to intensity and wavelength calibration), or they may apply for other temperatures than the temperature of the measured gas. If a gas is distributed over a large vertical range and therfore over a large temperature range, it can help to fit two cross sections of the same species but for different temperatures. Here, this was done for ozone. To reduce the problem of cross sensitivity between the two cross sections, one of them was orthogonalized to the other.

- Systematic structures in the residuum can also be an indication for the occurrance of an absorber that was not included in the fit routine. On the other hand, the number of included cross sections should be restricted to avoid the aforementioned cross-sensitivities.

- The detector is not perfectly linear, i.e. the number of counts is not strictly proportional to the number of photons. This is particularly the case for overexposed spectra.

- Errors in the dark current and offset correction occur, if the those signals change with time due to changes in the temperature (Sect. 6.4.2). Also electromagnetic interfering between adjacent electronic parts of the instrument can disturb the measurement.

Further errors occur when the SCDs shall be converted to VCDs (cf. Sect. 4.2) mainly due to uncertainties concerning the surface albedo and the aerosol and trace gas profile, especially clouds are challenging. The same applies for the conversion into concentrations, cf. Sect. 4.5.1. Additional uncertainties arise in applications like flux calculations (Sect. 4.5.1), which will be discussed for the concrete cases in Chap. 7, especially in Sect. 7.5.4.

4.4. Applications

DOAS measurements can be classified in active and passive setups. Active DOAS measurements use an artificial light source (e.g. xenon lamp, halogen lamp or LED), while passive setups use the light from the sun or other stars.

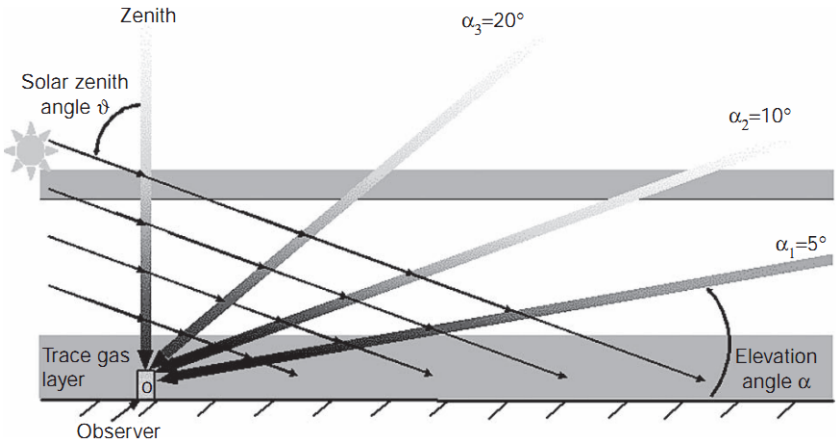

Figure 4.5.: Geometry of MAX-DOAS measurements. For a small elevation angle α, the light path in lower altitudes is higher compared to large elevation angles. In contrast to that, the stratospheric light path is hardly effected by a change in α. (From *Platt and Stutz*, 2008, p. 342)

Long path instruments (LP-DOAS) constitute the oldest category of active DOAS instruments. For the setup used by *Platt et al.* (1979), a xenon high pressure lamp was used as light source, placed in a distance of about 5–10 km from the measuring instrument, which contained a concave mirror to focus the light beam of the xenon lamp onto the entrance slit of the spectrometer. Instead of putting the light source far away from the instrument, a reflector (typically a retroreflector array) can be used. Because the light path is well-known, the concentration (average along the light path) of the measured gas can be easily calculated by dividing the SCD through the length of the light path. In recent developments, LEDs have been tested as light source, and the use of optical fibres was studied (e.g. *Merten*, 2008; *Chan et al.*, 2012). In a setup of several light paths over a city, LP-DOAS can be used for retrieving spatial distributions using tomographic calculations, cf. *Pöhler* (2010), *Mettendorf* (2005).

DOAS can also be applied in a combination of *Cavity Enhanced Absorption Spectroscopy* (CEAS, also known as CRDS for 'Cavity Ring-Down Spectroscopy') with broadband light sources, termed as *Broadband Cavity Enhanced Differential Optical Absorption Spectroscopy* (CE-DOAS). In a resonator (typical length 1–2 m) containing two highly reflective mirrors, light is reflected many times before it finally reaches the detector (one of the mirrors has a small transmissivity). With such a setup, light paths of more than a kilometre can be achieved; cf. *Platt et al.* (2009) and references therein. Due to small size and weight compared to other active DOAS systems like LP-DOAS, the application on unmanned aerial systems is currently tested (*Horbanski et al.*, 2012). Another system for achieving an enhanced light path is a White cell (*White*, 1942). DOAS measurements using a White system in a smog chamber for measuring BrO, ClO and OClO were performed by *Buxmann* (2012).

Multi AXes DOAS (MAX-DOAS) allows to discern between stratospheric and tropo-

spheric trace gas columns (*Hönninger et al.*, 2004). MAX-DOAS observations consist of several measurements under different elevation angles. For a low elevation angle α, the light path in the lower atmosphere is longer than for the case of high elevation angles (cf. Fig. 4.5). In contrast to that, the length of the stratospheric part does hardly change with α. If, for example, the retrieved SCD was the same for low and high elevation angles, the measured gas had to be present in higher altitudes. By measuring under several elevation angles, vertical concentration profiles can be obtained based on priori assumptions, cf. *Yilmaz* (2012). Technically, MAX-DOAS instruments are equipped with stepper motors. Therefore such instruments can be also be used to scan through plumes of volcanoes to monitor their emission of SO_2 and BrO (e.g. *Bobrowski et al.*, 2003; *Galle et al.*, 2010). In such field measurements, their mobility due to a rather small size and a low energy consumption is of advantage.

DOAS has been installed on various platforms like ships (e.g. *Leser et al.*, 2003), cars (e.g. *Shaiganfar*, 2012) or balloons (e.g. *Fitzenberger et al.*, 2000). Because satellite provide a global view, spectrographs with various wavelength ranges and spectral and spatial resolution were/are installed on research satellites, some of them are used for DOAS retrievals, e.g. GOME, GOME-2, SCIAMACHY, OMI (*Burrows et al.*, 2011).

Various implementations have been realized onboard research aircraft, amongst them MAX-DOAS instruments for retrieving vertical profiles, cf. *Heue* (2005), *Heue et al.* (2005). A sophisticated instrument including mechanism for compensation changes in the aircraft's attitude is described in *Baidar et al.* (2013). Onboard the German research aircraft 'Falcon', an instrument for limb measurements has been operated *Prados-Roman et al.* (2011). Also in the new research aircraft *HALO* ('High Altitude and LOng range reseach aircraft', "www.halo.dlr.de"), a mini-DOAS system is installed with spectrographs in the UV, visible and IR range. This instrument also performs limb measurements for the retrieval of vertical profiles (T. Hüneke, pers. comm., May 2013).

Also Imaging DOAS, which had been already used before in satellite instruments and in ground-based applications (*Lohberger et al.*, 2004) are suitable in aircraft for retrieving twodimensional trace gas maps (*Heue et al.*, 2008). An Imaging-MAX-DOAS instrument containing three scanning devices for obtaining two-dimensional maps and vertical profiles has recently been built for airborne measurement campaigns including flights onboard HALO (S. General, pers. comm., May 2013, publ. in prep.).

Within CARIBIC (Chap. 5), the first DOAS instrument was operating onboard passenger aircraft on a regular basis from 2005 to 2009 (*Dix*, 2007), before it was replaced by the instrument described in Chap. 6.

4.5. Emission Estimation Based on a Flux Calculation

In order to understand the atmospheric cycles of gases, the knowledge of their sources and their strength are needed. Some of them, e.g. SO_2 and NO_2, are produced to a

large extend by large industrial plants or cities. These emissions can be estimated by flux measurements in the vicinities of the sources. As described in Sect. 4.1, a DOAS instrument does not measure a concentration at a given point, but the SCD, which can be converted into the VCD, which is the concentration integrated along the height (Sect. 4.2). In combination with the fast forward movement of the aircraft, DOAS measurements allow the measurement of trace gases over an extended area. In combination with wind data, this makes DOAS an applicable measurement technique for the calculation of trace gas fluxes and therefore for the estimation of source strengths of individual sources. Such remote sensing based flux retrievals have been done by *Melamed et al.* (2003), *Wang et al.* (2006) and *Heue et al.* (2008) using research aircraft.

Also ground-based flux calculations are possible. In that case, the integration over the second dimension (which is automatically performed by the forward movement for the case of an aircraft) is achieved by scanning along a certain range of viewing directions. A typical application is the scanning of volcanic plumes by ground-based DOAS instruments, cf. *Galle et al.* (2010). In principle, flux measurements are also possible by making a large number of in-situ measurements as done by *White et al.* (1976), using an aircraft to measure air pollutants in the downdraught of the city of St. Louis, or by *Trainer et al.* (1995) for the investigation of the plume downwind of Birmingham, Alabama. However, such a set of in-situ measurements is elaborate and time consuming, and the the rather low number of point measurements cause uncertainties in the flux calculation.

In this section, the theoretical background for this approach is given and the assumptions to be made are pointed out. This approach was applied for two CARIBIC flights to estimate the SO_2 source strength of a nickel smelter in Norilsk (Sect. 7.5) and the NO_2 emission of the city of Paris (Sect. 7.6). The applicability for further flights and other passenger aircraft is discussed in Chap. 8. In order to be more concrete, the following considerations contain hints to the Norilsk flight (Sect. 7.5).

4.5.1. Flux Theory and Assumptions

The idea behind this approach is to retrieve the source strength Q by measuring the flux through a surface (or the relevant part of it). The aim of this section is to derive (4.59) from the fundamental continuity equation, using assumptions whose validity will be discussed in Sect. 7.5.4 for the case of Norilsk.

According to the continuity equation

$$Q_{\mathrm{net}} = \oint_{\mathrm{surface}} \vec{J} \cdot \mathrm{d}\vec{A}_{\mathrm{area}} + \int_{\mathrm{volume}} \frac{\partial c}{\partial t} \cdot \mathrm{d}V_{\mathrm{vol}} \tag{4.56}$$

the net source strength Q_{net} inside a closed volume V_{vol} is the sum of the flux J through the surface A_{area} of the volume, plus the temporal change of the number concentration c inside the volume V_{vol}. In the case of a certain chemical species, this means, that the

amount of molecules inside the fixed volume can only change due to transport (flux through the surface) or due to production (sources) or destruction (sinks) inside the volume in form of chemical reactions (nuclear reactions can be neglected) – Q_{net} is the difference between the sources and the sinks.

To determine the source of strength Q (the emission rate of SO_2 for the case of Norilsk), the following assumptions are made:

1. $Q_{\mathrm{net}} = Q$,
   i.e. the Nickel Mine is the only source of the detected SO_2 and there are no sinks.

2. The amount of SO_2 inside the volume is constant in time,
   i.e. we assume steady state conditions. This simplifies (4.56) to
   $$Q_{\mathrm{net}} = \oint_{\mathrm{surface}} \vec{J} \cdot \mathrm{d}\vec{A}_{\mathrm{area}} \tag{4.57}$$

3. The flight route crosses over the complete plume.
   In that case, it is not necessary to integrate over a complete closed surface, but it is sufficient to integrate over the area below the flight route (cf. Fig. 4.6).

The flux $\vec{J}$ is the product of the concentration c and the drift velocity $\vec{v}$ of the molecules, which is the same as the wind velocity. Therefore, (4.57) can be written as

$$Q = \int \vec{J} \cdot \mathrm{d}\vec{A}_{\mathrm{area}} = \int c \cdot \vec{v} \cdot \mathrm{d}\vec{A}_{\mathrm{area}} \tag{4.58}$$

or in a discrete form with $\mathrm{d}\vec{A}_{\mathrm{area}} = \vec{A}_{\mathrm{area}\,i,j} = h_j \cdot s_i$ as

$$Q = \sum_i \Big(s_i \cdot \sum_j h_j \cdot c_{i,j} \cdot v_{i,j} \cdot \sin \beta_{i,j} \Big) \tag{4.59}$$

Here, s_i is the width and h_j is the height of a cell of the chosen grid box (hatched rectangle in Fig. 4.6). $\beta_{i,j}$ is the angle between the flight route and the wind direction in grid cell i, j.

The retrieval of the concentration based on the SCD is described below. For the wind speed $v_{i,j}$, ECMWF data are used in the case of Norilsk (Sect. 7.5.3); for the Paris flight, also data from a sounding station were available (Sect. 7.6).

4.5.2. Radiative Transfer, Relative Concentration Profile

To convert the retrieved SCD into concentrations, a relative vertical concentration profile $c_{\mathrm{R}}(h)$ (or $c_{\mathrm{R}j}$ for the discrete case of layers numbered by the index j) has to be assumed, for example a box profile as shown in Fig. 7.25b p. 155. The units for such a relative concentration profile are arbitrary.

As introduced in Sect. 4.2.4, the SCD S_i at a certain measurement interval i can be written with the help of Box-AMFs as

$$S_i = \sum_j S_{i,j} = \sum_j A_j \cdot h_j \cdot c_{i,j} \tag{4.60}$$

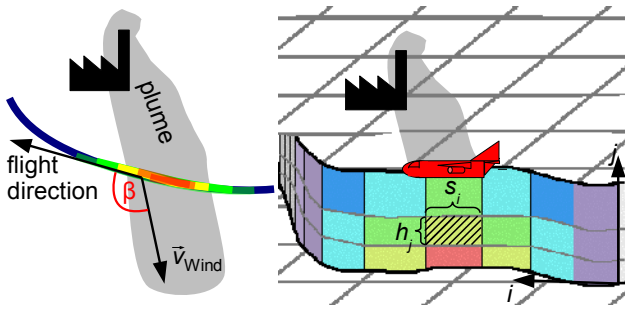

Figure 4.6.: Flux calculation. The left part shows the angle β between the flight direction and the wind direction. In the right part the discretisation of the area under the flight route is depicted, showing a box of height h_j and length s_i as used in (4.59). (Adapted from *Walter*, 2008)

Inserting $c_{\mathrm{R}j}/c_{\mathrm{R}j}$ into (4.60) leads to

$$S_i = \sum_j A_j \cdot h_j \cdot c_{\mathrm{R}j} \cdot (\frac{c_{i,j}}{c_{\mathrm{R}j}}) \tag{4.61}$$

The assumption of a relative concentration profile means that the ratio $(c_{i,j}/c_{\mathrm{R}j})$ between the real concentration $c_{i,j}$ and the relative concentration $c_{\mathrm{R}j}$ shall be the same for each height h_j. Then this ratio can be factored out from the sum:

$$S = (\frac{c_{i,j}}{c_{\mathrm{R}j}}) \cdot \sum_j A_j \cdot h_j \cdot c_{\mathrm{R}j} \tag{4.62}$$

and the equation can be resolved for the desired concentration:

$$c_{i,j} = \frac{c_{\mathrm{R}j}}{\sum_j A_j \cdot h_j \cdot c_{\mathrm{R}j}} \cdot S_i \tag{4.63}$$

As indicated by the index i, the SCDs S_i and therefore also the concentrations $c_{i,j}$ horizontally change along the flight route, whereas the relative profile, $c_{\mathrm{R}j}$, was assumed to be constant in the relevant part[4].

Although not explicitly needed for the flux calculation according to (4.59) and (4.63), the total AMF, $A = S/V$, can be calculated for a given (relative) concentration profile according to (4.21):

$$A = \frac{S_i}{V_i} = \frac{\sum_j A_j \cdot h_j \cdot c_{i,j}}{\sum_j h_j \cdot c_{i,j}} = \frac{\sum_j A_j \cdot h_j \cdot c_{\mathrm{R}j}}{\sum_j h_j \cdot c_{\mathrm{R}j}} \tag{4.64}$$

For the retrieval of the Box-AMF A_j, the radiative transfer model 'McArtim' (*Deutschmann*, 2009) was used, which simulates photon pathways based on a Monte Carlo method, cf. Sect. 4.2.3. For the SZA, 81.5 ° was taken for the case of Norilsk. In the Norilsk standard scenario (cf. Sect. 7.5.4 for further scenarios), a ground height of

[4] In general, also the relative concentration profile and the Box-AMFs can change, for example in case of a changing surface height

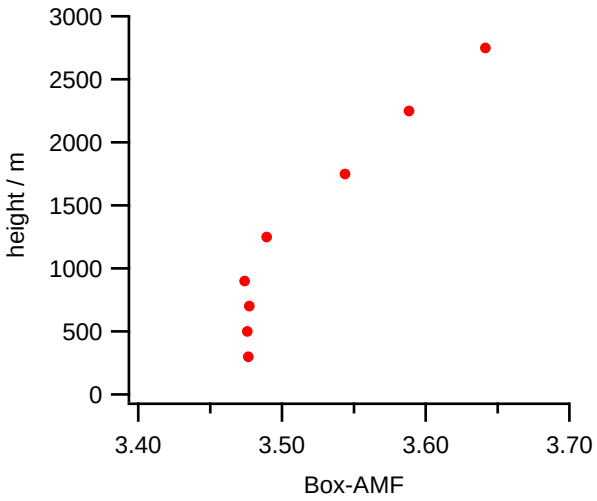

Figure 4.7.: Vertical profile of the Box-AMF. Retrieved by the Monte-Carlo based Radiative Transfer Model 'McArtim' for scenario 1, cf. Table 7.1 (From *Walter et al.*, 2012)

0.2 km above sea level and an upper plume height of 1.5 km (cf. Sect. 7.5.3) was taken. A standard profile for ozone and air pressure was included. A crucial value is the surface albedo. For Norilsk, 90 % was used (assuming a snow-covered surface). The resulting Box-AMF are shown in Fig. 4.7.

5. CARIBIC

In this chapter, the CARIBIC system is described, beginning with the introduction of the project, the installation in the aircraft and the inlet system. Afterwards, an overview over the instruments in the measurement container and the CARIBIC dataset is given.

5.1. The CARIBIC project

'Civil Aircraft for the Regular Investigation of the atmosphere Based on an Instrument Container' is a long-term project for investigating the atmosphere during regular passenger flights. The aim of CARIBIC is to provide detailed measurement data of gases, aerosol and water in the UTLS. These data shall help to develop a better understanding of atmospheric processes like long range transport of pollution or stratosphere-troposphere exchange. CARIBIC observations have been performed on a monthly basis from 1997 to 2002 (phase 1) and from December 2004 onwards (phase 2), with some gaps in observation due to improvements and maintainance of the instruments or the aeroplane.

In phase 1, a smaller measurement container was operated onboard a Boeing 767-300 ER of LTU International Airways. It was installed in the forward cargo bay and connected to an inlet pylon permanently mounted directly underneath the container outside the fuselage, cf. *Brenninkmeijer et al.* (1999). The observations started in 1997 and had to be stopped after April 2002 when LTU stopped its support for the project.

In phase 2, the 'Leverkusen', an Airbus A340-600 of Lufthansa German Airlines, is used. Because of its range of 14 000 km, it is predominantly used for long distance flights. For this aircraft, a new, extended container and a new inlet system were designed. Like in phase 1, the inlet pylon is permanently mounted under the aircraft's belly, whereas the container stays in the cargo compartment for four consecutive flights. The first successful measurement flight took place in December 2004, regular flights have been performed since May 2005. A longer break was in winter 2009/2010, when the container was updated with new instruments. Phase 2 with the currently installed instruments is planned to continue at least until 2014, after which the next major revision shall take place.

CARIBIC is the result of a collaboration of several European research institutes, supported by Deutsche Lufthansa AG and Lufthansa Technik and funded by the German Ministry of Education and Science (AFO 2000), the European Commission's DGXII

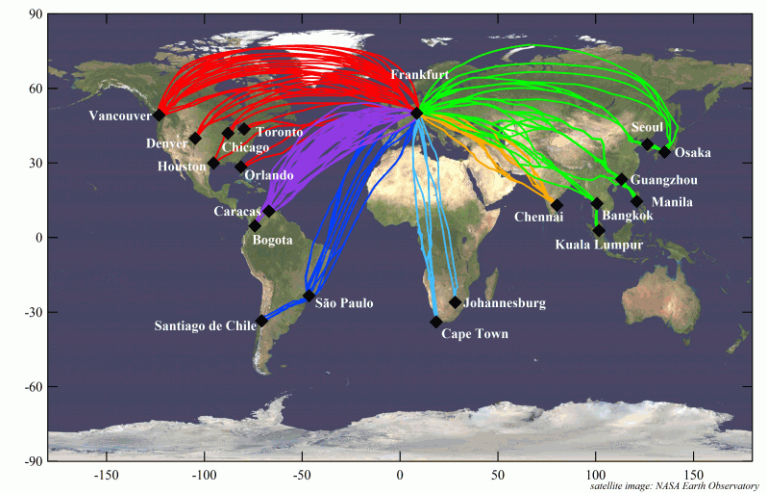

Figure 5.1.: Flight routes of CARIBIC from May 2005 until March 2013 (flights 110–420). (Created by A. Rauthe-Schöch)

Environment RTD 4th, 5th and 6th Framework programs and the Max Planck Society. It is integrated in IAGOS ('In-service Aircraft for a Global Observing System', "www.iagos.org"), The CARIBIC project is coordinated by the Max Planck Institute for Chemistry (MPIC), where the container is maintained between the measurement flights.

An overview of the CARIBIC phase 2 flights is given in Fig. 5.1 and in the table on p. 206ff, ongoing information about CARIBIC is offered by the project website "http://www.caribic-atmospheric.com/".

5.2. CARIBIC instruments, measured species

5.2.1. Installation in aircraft and inlet system

Figure 5.2 shows the position of the measurement container and the inlet pylon. Because the container stays during four consecutive flights, it has to be put at the end of the

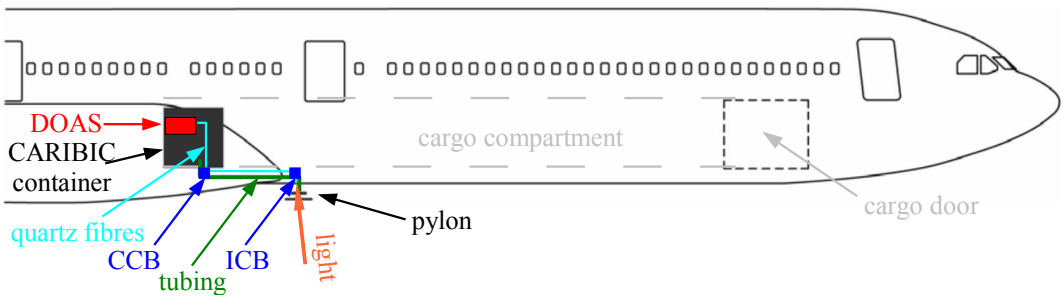

Figure 5.2.: Position of the container and the pylon inside the modified Lufthansa Airbus A340-600 (Adapted from *Brenninkmeijer et al.*, 2007)

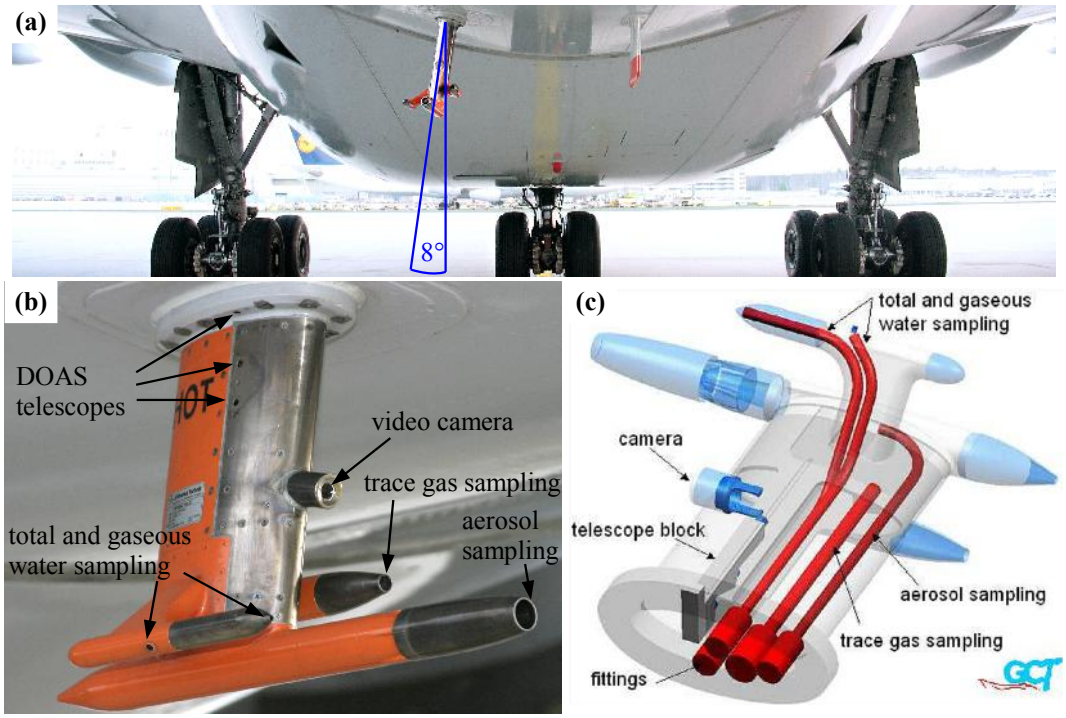

Figure 5.3.: (**a**) The pylon is fixed permanently under the aircraft's belly, under an angle of 8°. (**b**) inlets, telescope apertures and window for video camera (**c**) schematic sketch of the pylon, adapted from Garner CAD Technik

cargo compartment in order to allow the loading of other airfreight without removing the container each time. The container is connected to an inlet system (also denoted as 'CARIBIC pylon'), which is installed permanently under the aircraft's belly. The inlet pylon is mounted further to the front, because just below the container, the 'belly fairing' excludes the mount of an inlet system. Due to technical reasons, the complete pylon is tilted 8° clockwise when looking against flight direction (Fig. 5.3a). The size of the pylon is a result of several factors. It must not affect the aerodynamics of the aircraft and the stability of the aircraft's hull has to be assured. On the other hand, the inlet nozzles shall be not too close to the belly in order to avoid aerodynamic influences of the aircraft's belly. Thus, the pylon is about 35 cm tall and 55 cm long. It houses three inlet tubes for gases, aerosols and water (Fig. 5.3b,c). Also three tiny telescopes for the DOAS system are included (Sect. 6.1) and a video camera for observing clouds and other events (e.g. passing aircrafts). To connect the container with the pylon (distance ~2.4 m long), tubes are integrated under the floor of the cargo compartment. An 'Inlet Connector Bracket' (ICB) serves as an airtight connection between the pylon and the tubes inside the aircraft. These permanently installed components are connected with the container at the 'Container Connector Bracket' (CCB). These modification of the aircraft took place in November 2004 during a grounding period of the aircraft used for retrofitting it with a broadband internet system (*Brenninkmeijer et al.*, 2007).

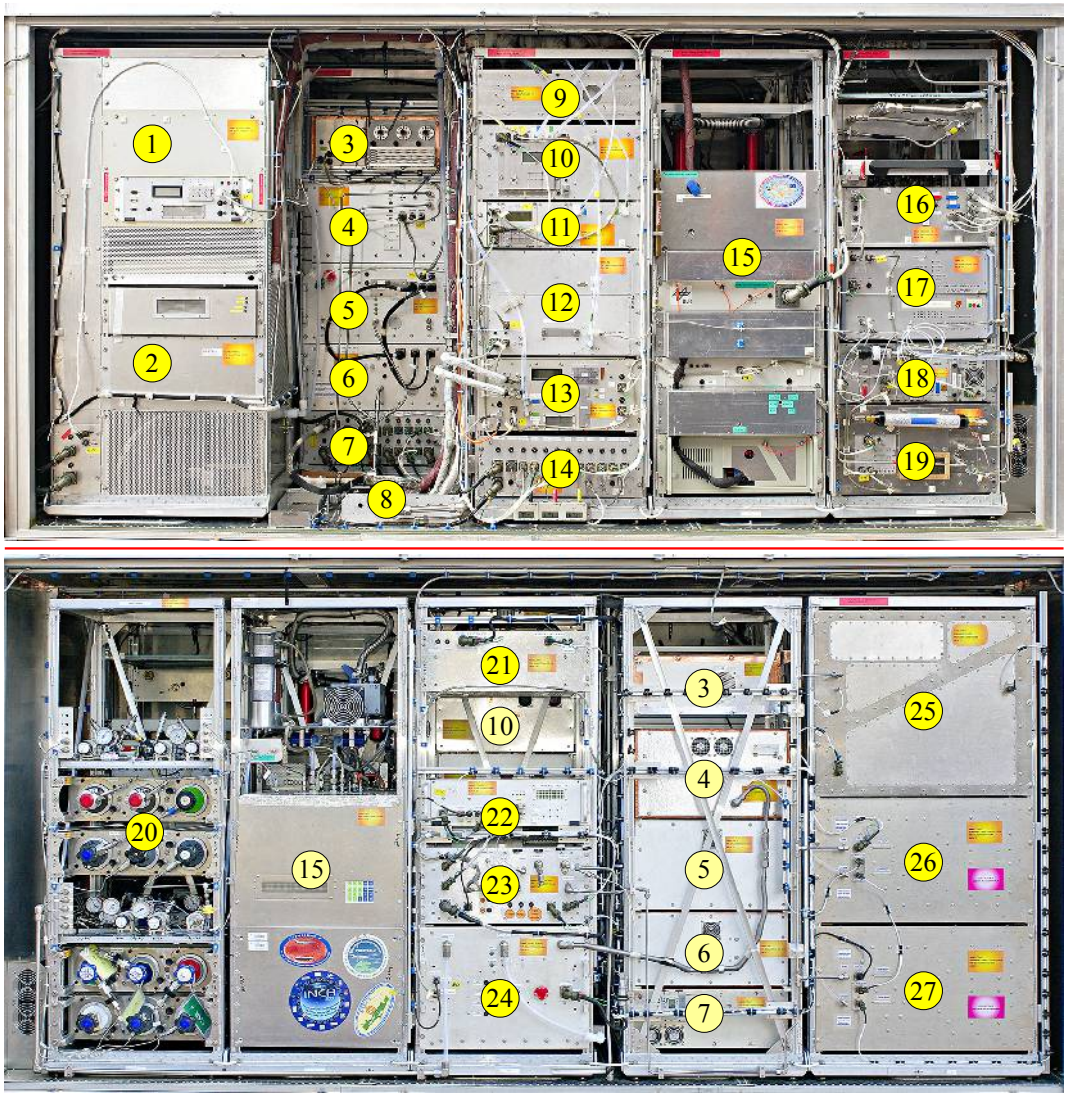

Figure 5.4.: CARIBIC container. **Top**: front side. **Bottom**: back side. See Table 5.1 for the numbered instruments.

5.2.2. Instruments in the measurement container

Figure 5.4 shows both sides of the measurement container after its extension in 2010. An overview over the instruments is given in Table 5.1. The container is 3.1 m wide, 1.6 m height and 1.5 m deep and has a mass of 1.6 tons. During flight, it is closed by aluminum doors. Apart from mechanical protection, these doors prevent electromagnetic radiation leaving the container (Faraday cage). In the aircraft, the back side is put at the end of the cargo compartment, whereas the front doors can be opened during the installation. The cables and tubing installed in the cargo floor are connected to the aircraft-container interface (№ 8).

The container receives power from the aircraft's generators (115 V, 400 Hz). The conversion to continuous current (DC) is performed by the Basic Power Supply (BPS,

24 V, № 14) and the Transformer Rectifier Unit (TRU, 28 V, № 7). During and shortly after take-off, the aircraft needs more power, so the container is not allowed to consume full power in that period. Therefore, the TRU is switched on later while the BPS is always activated when the container gets power. At take-off and landing itself, the power supply for the container is completely switched off.

In the following, a brief description of the installed instruments is given (mainly based

№	Instrument	Inst.	Name Tag	Time resolution / s
1	ISOWAT (Water isotopes)	KIT	WI	1 s
2	PTRMS	KIT	AC, AN, ME	∼30 s
3	DOAS (MAX-DOAS system)	IUP, MPIC	DU, DD, DN	8 s
4	OPC (Optical Particle Counter)	IFT	SD	300 s or 30 s
5	CPC1 (2 Condens. Particle C.)	IFT	CN	2 s
6	CPC2 (CPC, particle sampler)	IFT	CN, AE	2 s
7	TRU (Transformer Rectifier Unit)	MPIC		
8	aircraft-container interface	MPIC		
9	WASP (WAter Sampling Pump)	MPIC		
10	CH_4/CO_2 (Los Gatos)	KIT	CM	1 s
11	Ozone (OMCAL, OSCAR)	KIT	OM	UV: 4 s, CLD: 0.1 s
12	HG (Mercury)	HZG	HG	300 s or 600 s
13	Water	KIT	WA, WB	PA: 3 s; CR2: ∼5–180 s
14	BPS (Basic Power Supply)	MPIC		
15	NO_y (NO, NO_2, NO_y)	DLR	NO	1 s
16	MA (Master computer)	MPIC	MA	
17	O_2	Uni Bern	O2	
18	CO	MPIC	CO	1 s
19	CO2	CNRS	C2	1 s
20	gas bottles	MPIC		
21	DDB (Data Distribution Box)	MPIC		
22	TRAC computer	MPIC		
23	pumping unit	MPIC		
24	pumping unit	MPIC		
25	HIRES	MPIC	GHG, WAS	
26	TRAC	MPIC, UEA	GHG, WAS	
27	TRAC	MPIC, UEA	GHG, WAS	

Table 5.1.: Overview over the instruments in the CARIBIC container. The first column refers to the numbers in Fig. 5.4. Column 'Inst.' contains the responding institute (CNRS: Centre National de la Recherche Scientifique, Paris; DLR: Deutsche Zentrum für Luft- und Raumfahrt, Oberpfaffenhofen; HZG: Helmholtz-Zentrum Geesthacht. IFT: Leibniz-Institut für Troposphärenforschung, Leipzig; IUP: Institut für Umweltphysik, Uni Heidelberg; KIT: Karlsruhe Institute of Technology; MPIC: Max-Planck-Institut für Chemie, Mainz; UEA: University of East Anglia, Norwich). In 'Name Tag', the abbreviations of the instrument or the data products are given, which is used in the CARIBIC dataset, cf. Sect. 5.3.

on information given in the Wiki pages of the CARIBIC project, "http://wiki.caribic-atmospheric.com/"), together with references for further reading.

Master computer (№ 16) The Master computer is the central controller unit of the container. It is connected with the Basic Power Supply (BPS) in order to be among the first instruments to boot up after take-off and the last ones to been switched off. The Master computer receives and stores ARINC data (cf. Sect. 5.3). It also is in contact with all other instruments via Ethernet connections. The Master sends its 'permission' for starting measurement mode to the instruments by communicating the current flight phase. The Master also exchanges its timestamp with other instruments. If an instrument has an incorrect time, the communication protocol can be used for time correction. In fact, for the DOAS instrument, this feature has been proved to be very useful, cf. Sect. 6.5.2.

ISOWAT (№ 1) The 'Water isotope analyser ISOWAT' measures the isotope ratios $^{18}O/^{16}O$ and D/H (deuterium) in water, using Diode Laser Absorption Spectroscopy. The instrument in onboard CARIBIC since the last renovation in 2010. See *Dyroff et al.* (2010) for further details.

PTRMS (№ 2) The 'Proton-Transfer-Reaction Mass Spectrometer' measures acetone, acetonitrile and methanol by the protonation of VOCs using H_3O^+, cf. *Sprung and Zahn* (2010).

DOAS (№ 3) The 'Differential Optical Absorption Spectroscopy' instrument is described in detail in Chap. 6.

OPC (№ 4) The Optical Particle Counter detects particles and measures their size based on scattered laser light. The OPC is set up for particle size distributions in the range between 0.125 μm and 1.3 μm diameter. Its first mission was the probing of the plume of the Eyjafjallajökull volcano in 2010, cf. Sect. 7.2 and *Rauthe-Schöch et al.* (2012).

CPC (№ 5,6) Three Condensation Particle Counters have already been installed in the former container of CARIBIC phase 1 for measuring particles with a diameter larger than 4 nm, 12 nm or 18 nm, respectively. The upper limit is around 2 μm. By subtracting the results between the 4 nm and the 12 nm channel, particle concentrations for 4–12 nm are obtained. The particles are detected by a laser diode after they have grown inside the CPC due to condensation of butanol vapor. Further information is given by *Hermann and Wiedensohler* (2001).

CH_4/CO_2 (№ 10) The carbon dioxide and methane analyser, a modified 'Los Gatos' instrument was installed in 2010. It is based on ICOS ('Integrated Cavity Output Spectroscopy', cf. *O'Keefe et al.* (1999)), measuring the absorption of laser radiation.

Ozone (№ 11) The ozone analyser consists of two parts: A UV photometer measures the absorption of UV light from a LED (∼255 nm). A photomultiplier detects light which is emitted by the chemiluminescence reaction of ozone with a dye adsorbed on a sensor disc (CLD). While the UV photometer has a high accuracy, the CLD is very fast (0.1 s time resolution), cf. *Zahn et al.* (2012).

Mercury (№ 12) The mercury analyser is a modified 'Tekran 2537A' analysator. Gaseous mercury is sampled on a gold trap by amalgamation. Afterwards the trap is heated and the Hg enriches the flushing gas Argon. The Hg is detected by 'cold vapor atomic fluorescence spectroscopy' (CVAFS). See *Slemr et al.* (2009) or *Brenninkmeijer et al.* (2007) for further information.

Water (№ 13) The total and gaseous water analyser consists of two instruments, CR2 and PA. The *CR2* instrument ('chilled mirror frost point') is based on the dew-point and the frost point determination using a mirror whose temperature is controlled to be in equilibrium with the humidity of the air. The *PA* ('photoacoustic laster spectrometer') excites water molecules at a wavelength around 1.4 mm. A microphone senses the sound (pressure wave) generated due to the thermal relaxation of the water molecules, cf. *Bozóki et al.* (2003).

NOy (№ 15) The nitrogen oxides analyser uses two 'Ecophysics CLD-790 SR' based on chemiluminescence for measuring NO, NO_2 and NO_y. A photomultiplier detects light emissions from the reaction of NO with O_3. NO_y species are reduced with hydrogen to NO in a heated gold tube. For the NO_2 measurement, NO_2 is converted to NO by a blue LED light. Because NO disappears after sunset, the NO channel is not active during night. Cf. *Ziereis et al.* (2000).

Oxygen (№ 17) The O_2 analyser contains electrochemical cells giving a voltage proportional to the partial pressure of O_2 (20 mV / 20 % O_2). An additional CO_2 instrument should help to detect fractionation effects and allow a correction, cf. *Brenninkmeijer et al.* (2007).

CO (№ 18) Carbon monoxide is measured by a modified 'AL 5002 Aero-Laser' based on 'vacuum ultraviolet resonance fluorescence' (VUVRF). CO is excited by the light of a discharge resonance lamp. The fluorescence light (wavelength range ∼200–300 nm) is detected by a photomultiplier. See *Scharffe et al.* (2012) for details.

CO_2 (№ 19) The modified 'Licor Li-6262' instrument is a 'differential, non-dispersive infrared' (NDIR) analyser, cf. *LI-COR* (1996).

Air sampler system TRAC and HIRES (№ 26,27,25) Three air sampling units are installed in the CARIBIC container. Both *TRAC* units ('triggered retrospective air

collector') include 14 glass canisters each. The volume of one canister is 2.5 litre. In 2010, a third air sampler was added: *HIRES* ('high resolution air sampler') includes 88 stainless steel flask (one liter each). Altogether, 116 samples can be taken during a set of flight. This allows a detailed after-flight lab analysis of greenhouse gases (*Schuck et al.*, 2009), non-methane hydrocarbons, halocarbons and isotopes of molecular hydrogen (*Baker et al.*, 2010; *Batenburg et al.*, 2012).

5.3. CARIBIC data and related datasets

During flight, the raw data and log files are stored on memory cards within the respective instruments. After flight, the memory cards are read out, and the data are transferred to the CARIBIC data server[1]. The analysis of the data is with the respective instrument owners (they return the calibrated data to the data server).

For sharing the evaluated data with other CARIBIC partners and for providing the dataset to external users, a uniform data format is needed. The ARC[2] had developed file conventions for datasets, mainly of atmospheric measurements. For CARIBIC, version 1 of the 'ASCII File Format Specification for Data Exchange'[3] was taken as guideline, with several adaptations and specifications. In the following, this data format (including the CARIBIC specification) is referred to as *NASA Ames* format. A NASA Ames file is an ASCII file, consisting of header lines followed by the data lines. The header contains a variable amount lines including basic information about the flight (number, destinations, start date), some settings of the instrument or the analysis, special comments and information about the content of the data columns. The data below the header are arranged as tab-separated values with the CARIBIC time as independent variable in the first column. Therefore, NASA Ames files can easily imported by virtually any common analysis software. For the case of the DOAS instrument, three files are created with name tags 'DU', 'DD' and 'DN' (cf. Table 5.1) for the three viewing directions $+10°$ ('upwards'), $-10°$ ('downwards') and $-82°$ ('nadir'). The different instruments inside the container have different temporal resolution. To facilitate comparisons, files on a common time grid (one time step every 10 seconds) are provided additionally.

The NASA Ames files of the Master computer ('MA') contain the time (see also Sect. 6.7.1) and the navigation parameters which are measured by the aircraft, like the position as longitude and latitude (based on a gyroscope, see also Sect. 5.4). Further contained information are the pressure based altitude, the flight phase, true heading,

[1] Currently, the data are stored in "\\fs.mpic.de\groups\CARIBIC\intern". External users can access a copy of the data via "ftp://ftp.mpic.de/CARIBIC/"

[2] The 'Ames Research Center' (ARC, web: "http://www.nasa.gov/") is a research center of the 'National Aeronautics and Space Administration' (NASA), situated in California, USA

[3] An overview about these conventions is given by *Gaines and Hipskind* (2001), further information can be found on the websites "http://cloud1.arc.nasa.gov/solve/archiv/archive.tutorial.html" and "http://badc.nerc.ac.uk/help/formats/NASA-Ames/".

pitch and roll angle, wind speed and direction, pressure and ground speed. These so-called 'ARINC'[4] data are provided by the data bus system of the aircraft. The raw ARINC data stream is filtered by the Data Distribution Box (DDB, № 21 in Fig. 5.4) for the relevant information before being forwarded to the Master computer.

Meteorological support data are provided by the *KNMI* (dutch: 'Koninklijk Nederlands Meteorologisch Instituut', english: 'Royal Netherlands Meteorological Institute', web: "http://www.knmi.nl/"). Reanalysis data from the *ECMWF* ('European Centre for Medium-Range Weather Forecasts', web. "http://www.ecmwf.int/") with a horizontal resolution of 1°×1°on a 6 hour time grid. These data are interpolated in space and time to the flight route of the CARIBIC aircraft, or more precisely, to vertical cross sections (profiles) along the longitudes and latitudes of the flight track. The parameters include potential vorticity (PV, cf. Sect. 2.1.2), equivalent potential temperature, isentropes, humidity, cloud cover, cloud water and ice contents and wind speed components. Furthermore, 5-day backward trajectories ending at the aircraft's position are created along the flight track, using the KNMI Climate Research trajectory model *TRAJKS*, cf. web "http://trajks.knmi.nl/", *Scheele et al.* (1996). These data including further information are available at "www.knmi.nl/samenw/campaign_support/CARIBIC/".

5.4. ARINC data at approach for a landing

In order to avoid a damage in the Master File Table on the memory card of the Master computer, the data files are stored only once in three minutes. With the weight-on-gear-signal at the landing, the power supply for the hole CARIBIC container is cut off and the current data file can not be closed any more, causing a data gap at the end of the flight between zero and three minutes. These missing data include the position (longitude, latitude, altitude) and velocity of the aircraft. For most other instruments, this data gap is not relevant because they are switched off below a certain altitude during descend. For the DOAS instrument, however, these data can be important like in the case of the descend of flight 393, where an SO_2 peak is observed just before landing, see Sect. 7.4. Therefore, in the following, a relatively simple linear approach is described to fill this data gap by extrapolating the ARINC data.

The basic assumption is that the speed changes linearly between the time t_{LA} of the **l**ast **A**RINC data and the **t**ouch-**d**own time t_{TD} of the aircraft. Let $y(t)$ be one component of the aircraft's coordinate (the latitude or the longitude) at time t, and $\dot{y} = \mathrm{d}y/\mathrm{d}t$ and $\ddot{y} = \mathrm{d}^2y/\mathrm{d}t^2$ it's first and second temporal derivatives (cf. speed, acceleration). Then this assumption means that $\ddot{y}$ is constant during the time span from t_{LA} to t_{TD}, while $\dot{y}$ changes linearly from $\dot{y}_{\mathrm{LA}}$ to $\dot{y}_{\mathrm{TD}}$. This results in the well-known

[4] ARINC is an abbreviation for the US company 'Aeronautical Radio Incorporated' ("www.arinc.com"), which has developed widespread used standards for avionic data bus systems.

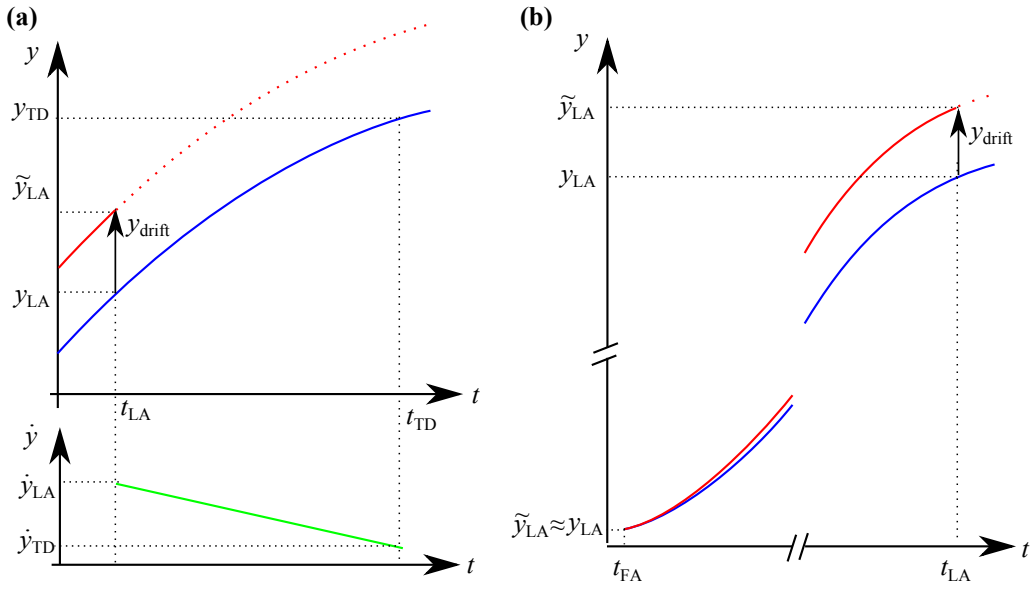

Figure 5.5.: Correction and extrapolation of the ARINC position data. y refers to one component, i.e. the longitude, the latitude or the altitude. (**a**) Time span between the last arinc time t_{LA} and touch-down t_{TD}. The solid red line shows the raw ARINC coordinates, ending at t_{LA}. Because of the drift, the extrapolated coordinates (dashed line) would not reach the airport (coord. y_{TD}). By forcing the y to reach y_{TD} at touch-down time t_{TD}, the blue (corrected) line is obtained. Therefore, $\dot{y}$ is assumed to decrease linearly (green line). (**b**) The mismatch between the given ARINC coordinates (red line) and the real data (blue line) is assumed to grow linearly with time for each component (longitude, latitude, altitude) during the flight.

equations for a uniform acceleration:

$$\ddot{y} = \frac{\dot{y}_{TD} - \dot{y}_{LA}}{t_{TD} - t_{LA}} = \text{const} \tag{5.1}$$

$$\dot{y}(t) = \dot{y}_{LA} + \ddot{y} \cdot (t - t_{LA}) \tag{5.2}$$

$$y(t) = y_{LA} + \dot{y}_{LA} \cdot (t - t_{LA}) + \frac{1}{2} \cdot \ddot{y} \cdot (t - t_{LA})^2 \tag{5.3}$$

With the touch-down, the power supply for the container is turned-off, including all instruments. Therefore, the touch-down time t_{TD} can be derived from the last recorded time of container instruments like the CO instrument. $\dot{y}_{LA}$ can be derived from the last stored velocity in the ARINC data and the flight direction at time t_{LA}. The flight direction itself is not part of the ARINC data files, and in general, it is not identical to the true heading of the aircraft. It could be calculated using the adjacent position data, but with limited accuracy due to the limited precision of the position data (only three decimal places). Instead, here, the assumption is made that the flight direction not changes any more until landing, so the direction of the runway is taken as a constant flight direction between t_{LA} and t_{TD}. For the landing position $y_{TD} = y(t_{TD})$, the coordinates of the runway are taken, assuming to get 'weight on gear' after one third of the runway. For a known position y_{LA}, only $\ddot{y}$ is unknown in (5.3) for $t = t_{TD}$, so the

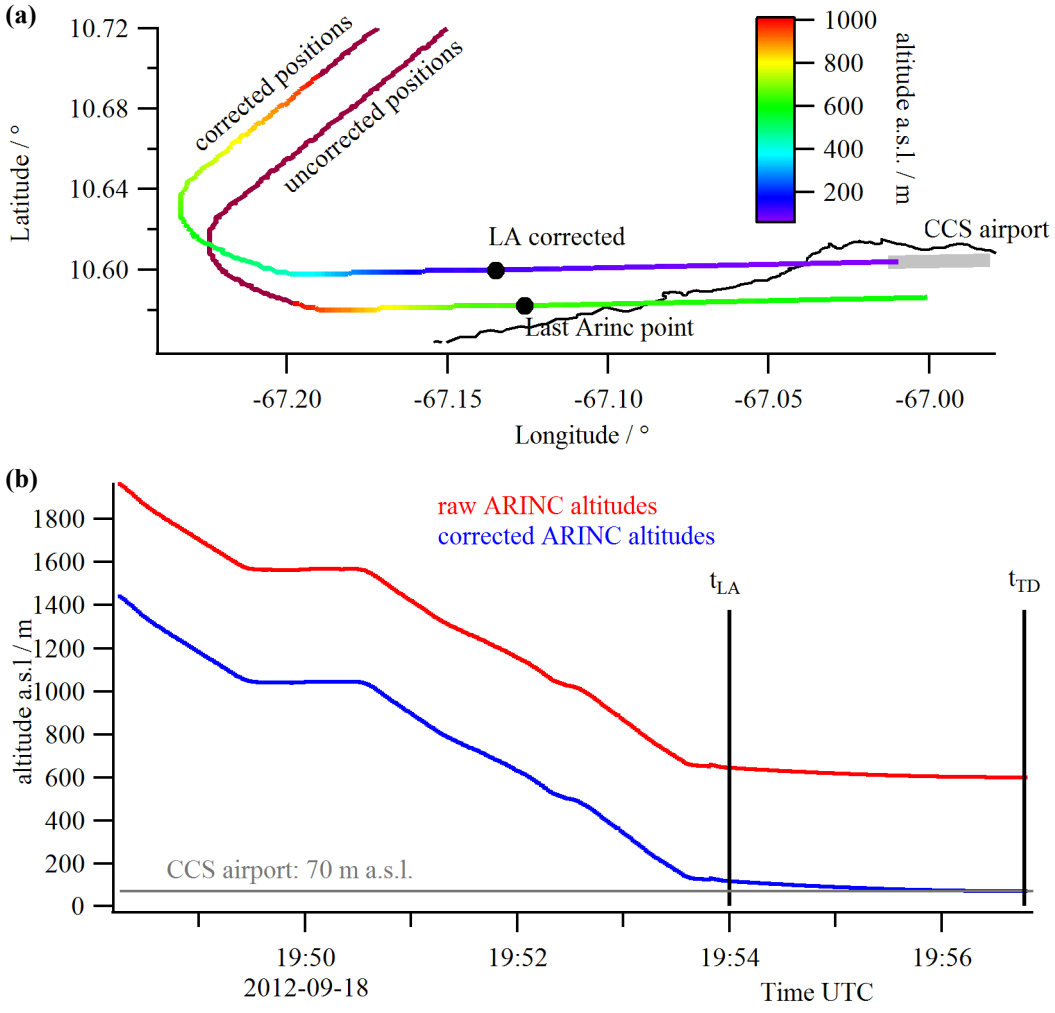

Figure 5.6.: Correction and extrapolation of the ARINC position data for the landing approach of flight 393 to Caracas airport. (**a**) Raw (uncorrected) and corrected position data from 19:50 to 19:57 UTC, color-coded with the altitude. The positions after 'Last Arinc point' and 'LA corrected' (time: 19:54 UTC) are extrapolated. The grey line depicts the runway. (**b**) Correction (blue line) of the altitude for descend of flight 393. Altitudes after t_{LA} are extrapolated. The runway is about 70 m a.s.l. (grey line).

equation could be resolved for $\ddot{y}$.

However, in fact, the real position y_{LA} is not known properly. The position actually given by the ARINC data – let it call $\tilde{y}_{\mathrm{LA}}$ – is not derived from a GPS signal but from a gyroscope inside the aircraft. The correct position is set before departure, but than the gyroscope based position data drift off in the course of time by several kilometers. To correct for that error, y_{LA} is calculated according to (5.3) using $\ddot{y}$ according to (5.1). But for that purpose, the component $\dot{y}_{\mathrm{TD}}$ of the landing velocity is needed. As this velocity is not known for that flight, it has to be guessed. With $\dot{y}_{\mathrm{TD}} = 70\,\mathrm{m/s}$, a typical landing value was chosen (e.g. *CLS*, 2006, p. 28). The difference $y_{\mathrm{drift}} = \tilde{y}_{\mathrm{LA}} - y_{\mathrm{LA}}$ can be used in order to perform a raw correction of the ARINC positions $\tilde{y}$ between the begin of the flight and t_{LA}, assuming a linear increase of the drift.[5]

$$y(t) = \tilde{y}(t) + y_{\mathrm{drift}} \cdot \frac{t - t_{\mathrm{FA}}}{t_{\mathrm{LA}} - t_{\mathrm{FA}}} \tag{5.4}$$

This method is applied on both coordinates (longitude and latitude) independently. The result for the landing approach of flight 393 to Caracas (cf. Fig. 5.4) is depicted in Fig. 5.6a. In that case, there is a data gap of nearly three minutes between the last stored ARINC files (19:54:00 UTC) and the touch-down at 19:56:47 UTC). The extrapolated route without correction would miss the runway, being ∼2 km too far south. By forcing the route to end at the airport according to the abovementioned approach, the corrected line is calculated. While the latitude is quite clear for that particular runway (oriented from west to east), the longitude of the touch-down position was guessed to be 300 m after the start of the runway. With that, the raw positions were shifted by 2.2 km northwestwards (cf. 'Last Arinc point' and 'LA corrected' in Fig. 5.6a).

This approach can also be applied for the altitude, where a mismatch between the pressure based ARINC altitude and the real altitude exists. While the horizontal speed was assumed to be 70 m/s, the vertical velocity at touch-down is set to zero, assuming a soft landing. However, the altitudes obtained with such an approach should be treated with sufficient care, because in reality, the decrease does not have such a quadratic behaviour. Figure 5.6b shows the raw altitudes (red line for $t < t_{\mathrm{LA}}$) and its extrapolation until t_{TD}, ending at an altitude of ∼600 m a.s.l. – in contrast to the runway's altitude of ∼70 m a.s.l. The blue line corrects for that mismatch, however, the assumed rate of decrease based on the decrease rate at time t_{LA} is quite small compared to the rate's occurring before t_{LA}. The reality might be somewhere between the blue and the red line.

[5] Especially for latitudes close to the poles, where the non-Cartesian behaviour of the spherical coordinates is pronounced, this simplified approach would not be suitable. Furthermore, assuming a more randomly aberration like in the case of a random walk (cf. diffusive motion of a molecule), a drift proportional to the square root of the time might be more accurate.

6. DOAS instrument, data acquisition and analysis

This chapter deals with the DOAS instrument as part of the CARIBIC project. After a description of the viewing geometry and the setup of the optical parts within the CARIBIC pylon and the aircraft, information about the parts of container instrument and results from laboratory tests are given.

6.1. DOAS onboard CARIBIC

Since CARIBIC phase 2, a DOAS instrument has been part of the CARIBIC, consisting of a telescope block within the CARIBIC pylon, an instrument within the CARIBIC container and quartz fibres in between. While the telescope block stayed unchanged throughout the years, the fibres had to be replaced several times. The first container instrument was replaced in 2010 by a successor which will be described in the following sections in more detail. Details about the telescope block and the former container instrument are given by *Dix* (2007), therefore they are only briefly discussed here.

Figure 6.1 shows the geometry (line of sights) of the three telescopes. The line of sights of all of them is directed to the right, when looking in flight direction. Two of them are close to the horizon – one telescope looks upwards (+10°) and one downward (−10°). A third line of sight has an angle of 82° to the horizon, or 8° to the nadir direction, thus it is referred to as −82° direction or 'nadir' direction. The reason for the mismatch of 8° between the viewing direction and real nadir can be seen in Fig. 5.3 p. 77 and Fig. 6.1. Because the complete pylon is tilted by 8°, a real nadir view is not possible with the current setup of the pylon. However, for the radiation transport like the length of the light path between the aircraft and the ground, this difference is rather low ($\cos 8° \approx 0.99$), and the horizontal offset (for example at the ground) can easily be accounted for, also including the tilt of the aircraft.

In principle, the flight attitude (pitch, yaw and roll angle) have to be taken into account for determining the real viewing direction; especially the roll angle changes during curves. Those data are included the ARINC data (Sect. 5.3), therefore such corrections are possible. However, during passenger flights, the number of turns are limited, therefore such calculations were not needed for the cases presented in Chap. 7.

The DOAS block is fixed on the inner side of the pylon's wall, on the left side in the

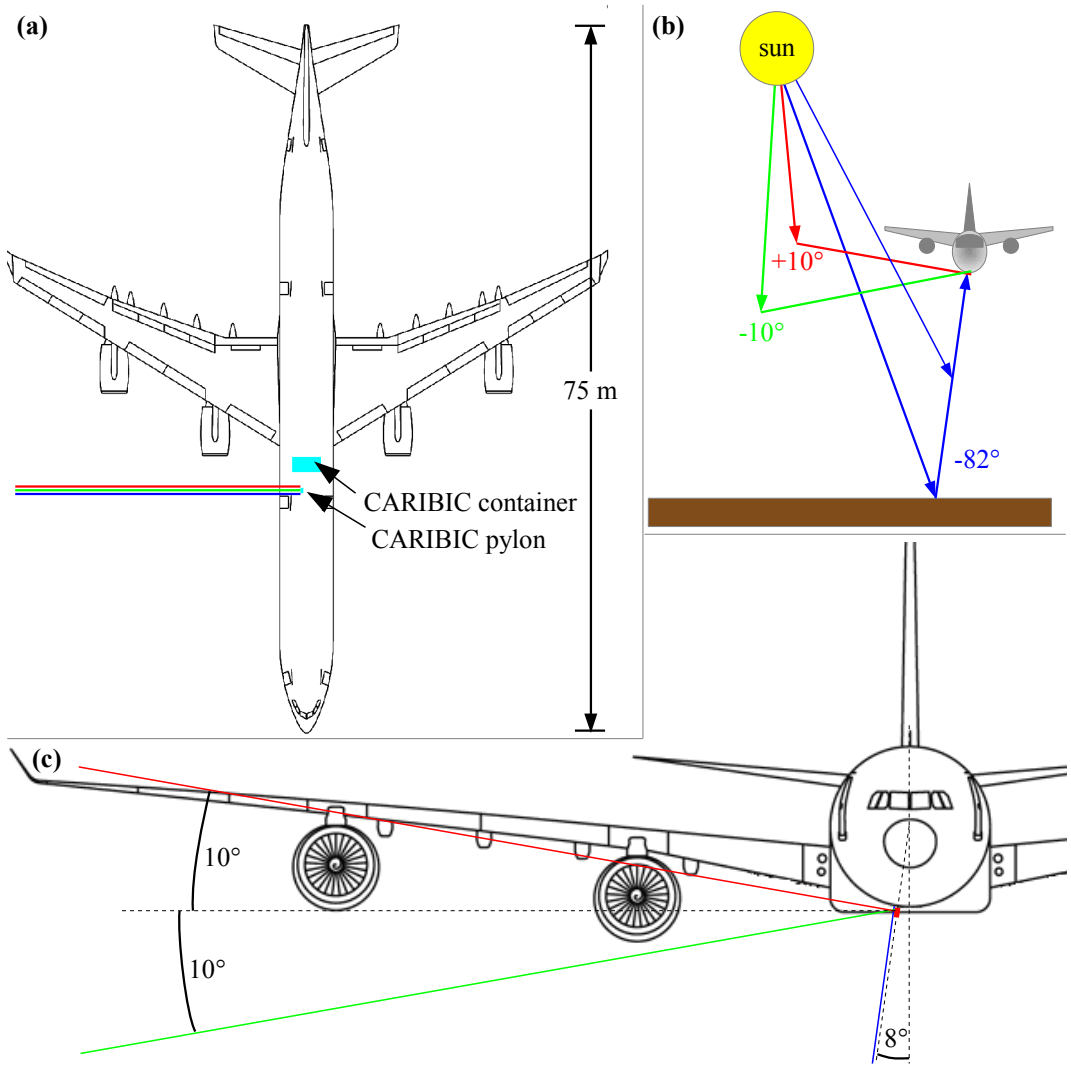

Figure 6.1.: Line of sights of the DOAS telescopes, seen from above (a) and looking against flight direction (b,c). The viewing directions are perpendicular to the flight direction. They are depicted in red (+10°), green(−10°) and blue(−82°). In (b), possible light paths from the sun to the telescopes are sketched. (Parts (a) and (c) are adapted from [Julien.scavini, own work, (CC-BY-SA-3.0 "http://creativecommons.org/licenses/by-sa/3.0"), accessed on 2012-12-21 via "http://commons.wikimedia.org/wiki/File%3AA346v1.0.png"].)

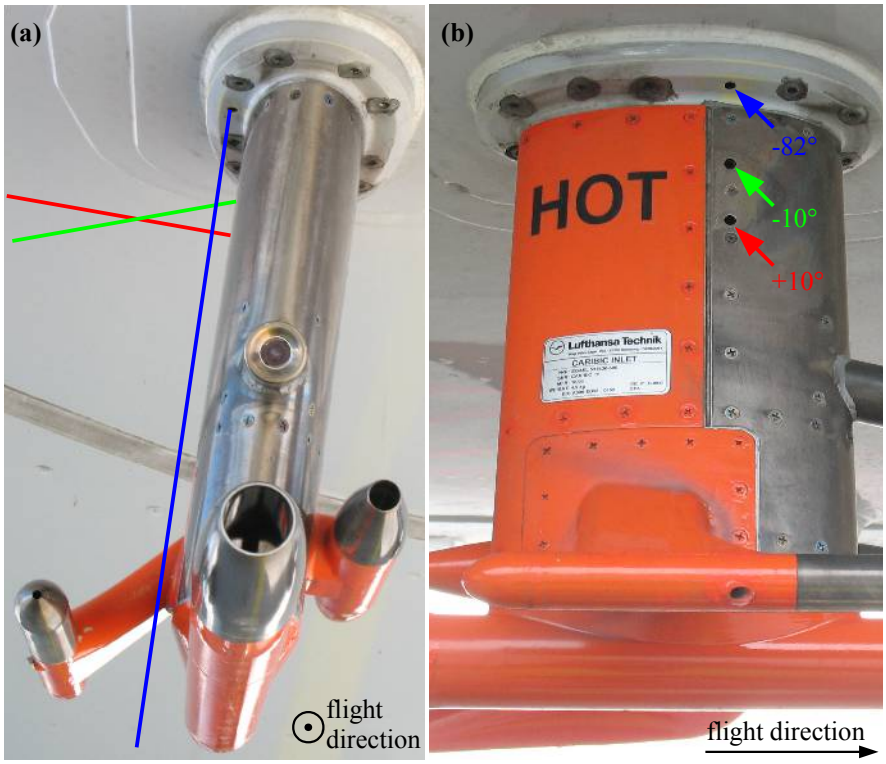

Figure 6.2.: Photographs of the CARIBIC pylon and the entrance holes for the impinging light. Like in Fig. 6.1, the viewing directions are depicted in red (+10°), green(−10°) and blue(−82°).

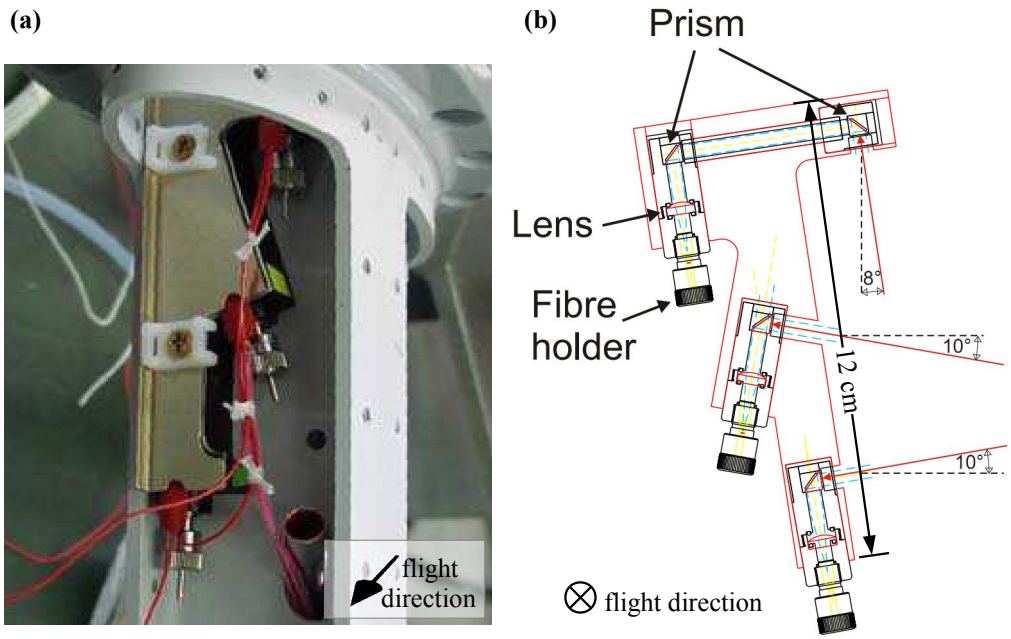

Figure 6.3.: Photograph and Sketch of the DOAS telescope block, which is fixed in the upper part of the CARIBIC pylon (From *Dix*, 2007, p. 80)

topmost part of the pylon when looking against flight direction (Fig. 6.3a). The three 1/4 inch holes in the pylon's wall allowing the light to enter can be seen in Fig. 6.2. These holes are covered with tape in order to protect the lenses of the telescopes, which is only removed for the monthly measurement flights. Figure 6.3b shows the construction of the DOAS block (a more detailed drawing can be found in *Dix* (2007, p. 181)). It is made of aluminium with the dimensions $120\times70\times15\,\mathrm{mm}^3$. The telescope for the 10° upward looking direction has the lowermost position within the block, because the line of sight shall not cross the belly of the aircraft. The three telescope units are fixed within the aluminium block. Each of them consists of a UV transmitting quartz glass lens for focusing and one (+10°, −10°) or two (−82°) prisms for deflecting the light. The telescope units are air tight sealed in order to prevent the entry and condensation of water. Furthermore, heating of the telescope block avoids water freezing on the outer part of the prisms. The lenses have a focal length of 15 mm, focusing incoming light onto the end of the fibre bundles (consisting of 4 fibres each, cf. Sect. 6.1.1). With a fibre diameter of 210 μm arranged in a square, the field of view is calculated to be 1.9° (cf. *Dix*, 2007, p. 81).

Originally, the telescope units contained optical filters (Schott UG5). They shielded light with wavelengths larger than 400 nm, which would have caused straylight within the spectrographs. Unfortunately, these filters broke into peaces, which caused a strong intensity reduction. For accessing the telescope block, the pylon has to be opened, which is a time-consuming attempt and therefore only possible during maintainance periods of the aircraft. Therefore, it took a longer time until the reason for the intensity loss could be found and resolved. To avoid the occurrence of the same problem again, there are no optical filters any more in the pylon. Instead, filters are installed inside the new instrument in the container (cf. Sect. 6.3.4).

6.1.1. Fibres

Before a set of flights (SoF), each telescope inside the pylon has to be connected with its corresponding spectrograph (inside the container instrument) with a quartz fibre bundle, which is sketched in Fig. 6.4. Such a bundle contains four 210 μm quartz fibres with a length of 5.60 m (+10°), 5.65 m (−10°) or 5.68 m (−82°). The fibre is fixed on one end (small metal bush, Fig. 6.4b) at the telescope. Inside the pylon, the bundle has to be bend with a radius of only ∼6 cm (cf. *Dix*, 2007, p. 82). Therefore the fibres are enclosed by a flexible plastic hose. The length of this part differs for the three viewing directions, namely 0.65 m for +10°, 0.70 m for −10° and 0.73 m for −82°. A 4.83 m long flexible steel tube protects the fibres from mechanical damages. Roughly 2.4 m of that part is lying beneath the floor panels of the aircraft's cargo compartment together with the tubings for the other CARIBIC instruments, cf. Sect. 5.2. Up to here, the fibre bundles are only touched or moved during maintainances of the aircraft. The remaining part, however, is used for spanning the last ∼2 m to the container instrument. The end of the fibre

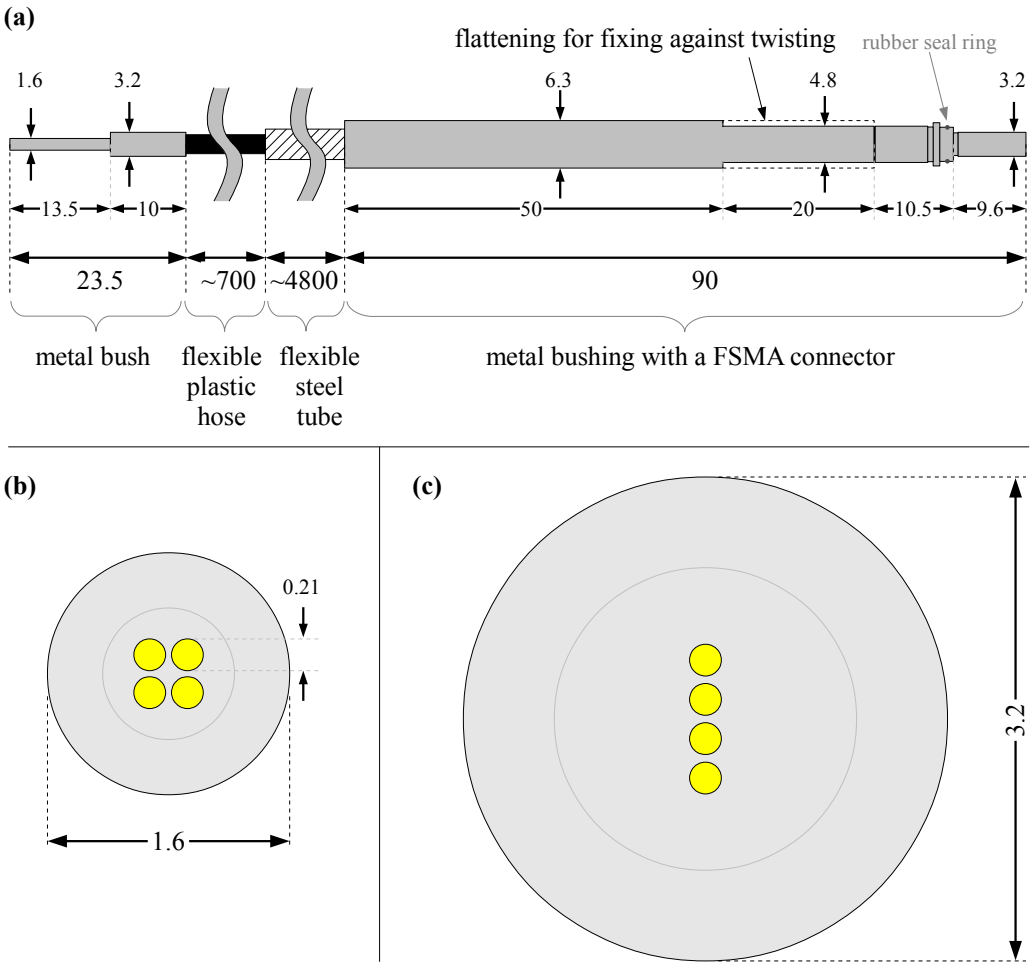

Figure 6.4.: Sketch of an optical cable with its fibre bundle, containing 4 quartz fibres. Lengths are given in millimeter. (**a**) from left to right: small metal bush for fixing the fibre at the telescope, flexible plastic sheath (inside the pylon), metallic protection tube (spiral tubing, under the floor panels), FSMA connector (at the spectrograph side); Scale 1:1 (**b**) fibre bundle end on the telescope side, fibres are arranged in a square; Scale 20:1 (**c**) End at the spectrograph side, fibres are arranged in a line; Scale 20:1

bundle consists of a metal bushing with a FSMA connector[1] which is connected to the entrance slit of the spectrograph during the measurement flights. Afterwards, all three fibre bundles are detached from the spectrograph and stored in the container connector bracket (CCB), a small box embedded in the floor of the cargo compartment. In order to fit inside the CCB, the three fibre bundles have to be rolled up with a diameter of ∼17 cm. Because the fibre bundles are moved regularly in that part, they are protected by an additional cloth jacket. Figure 6.4b shows the arrangement of the single fibres at the telescope end, which is in a quadratic shape in order to approximate the circular field of view of the telescope. The other end (Fig. 6.4c) adjoins the vertical entrance slit of the spectrograph, therefore the fibres are disposed in a line. The metal bushing contains a flat section for preventing a rotation of this line relative to the direction of the spectrograph's entrance slit. In the flexible part in between the two ends, the fibres are lying loose in the plastic tube. The fibre bundles were produced by 'LOPTEK Glasfasertechnik GmbH & Co. KG', Berlin, "www.loptek.de".

Since the start of CARIBIC, several cables had to be exchanged occasionally due to a lack of light reaching the detector. Because the fibre bundle in the pylon and beneath the floor panel can only be accessed during a maintainance period of the aircraft, it takes some time until the reason for such a light loss can be investigated and resolved. As mentioned above, broken UV filters caused this problem once. In another case, the metal bush at the end of the fibre got loose. Therefore, glue was used on several potentially critical points to secure the fibre bundles. In most cases, however, the fibres themselves got broken. Because the fibres are strongly bended within the pylon and because the have to endure strong temperature changes, this part of the fibre was presumed to be the most critical one. Therefore, fibre bundles with 6 thinner single fibres (150 μm diameter) were used, because such thinner fibres are able to stand a smaller bending radius. Also some of these fibres broke after some time, so afterwards, bundles with 4 fibres were used again. Presently, it is assumed, that the last meters on the other end are the most critical ones. The opening of an old fibre bundle after its replacement showed, that the fibres were broken within the metal bushing. At first glance this is quite surprising, because the fibres seem to be ideally protected inside the stiff metal bushing. But during the regular roll up and unroll of the spiral in the CCB before and after the flight, compression, tension and torque forces occur, probably especially the distortion is problematic. While the fibres can yield within the flexible part of the fibre bundle to some extend, they are fixed within the metal bushing.

To solve the problem, it is considered to replace each fibre bundle by two parts which are coupled together at the lead-trough between the cargo floor and the CCB. This allows an easy replacement of the flexible part directly before or after a set of flight. There are two possibilities for the handling of the flexible part: Like now, it can be

[1] FSMA, also 'F-SMA', for 'fiber sub-miniature assembly' is a connector type widely used in fibre applications.

stored in the CCB in between the flights, so the fibre coupling has only to be opened if a loss of light is observed. The other possibility is to decouple the flexible part after each flight and taking it back to Mainz. In that case, the critical roll up of the fibre can be avoided. On the other hand, it has to be considered that a fibre coupling causes a intensity loss, typically on the order of 10–40 %.

6.2. DOAS Container Instrument Overview

The first DOAS container instrument for CARIBIC was built by the IUP workshop, details see *Dix* (2007). The new instrument was custom-built by OMT ('omt – optische messtechnik gmbh', Ulm, Germany, "www.omt-instruments.com") in 2009 and is measuring since April 2010. It has the same position within the CARIBIC container (Fig. 5.4 p. 78) as the old instrument and therefore also nearly the same outside dimensions, namely $45 \times 36 \times 17.5$ cm (width × depth × height). The total instrument has a weight of 15 kg and therefore is the lightest instrument in the container. It is positioned in a standard 19" rack. According to the manufacturer, it is EMC conform, however, the edges are additionally covered by EMC tape to prevent electromagnetic radiation leaving the rack, cf. Sect. 6.5.1. A thermal isolated box (№ 3 in Fig. 6.5 and 6.6) within the rack houses three spectrographs produced by OMT (Fig. 6.5d). Each spectrograph with a cooled CCD sensor. The cooling of the single sensors is uncontrolled, but the spectrographs are fixed to a temperature controlled optical bench, cf. Sect. 6.4.3. The heat is disposed via a radiator located at the front side of the instrument (№ 1). Behind the spectrograph box, electronic cards control the detectors and the temperature regulation (№ 4). The regulation of the measurement procedure

№	Description
1	Front ventilator for cooling the optical bench
2	Inlet for FSMA fibre connector
3	Spectrograph box
4	Ventilator, below: Controlling electronics
5	Back ventilator for cooling the hole instrument
6	Power supply: DC/DC converter and EMC filter
7	Ethernet card for communication with Master PC
8	Embedded computer
9	Front plate for access to the memory card
10	Fuse switch
11	Connection for Ethernet
12	Connection for power supply

Table 6.1.: Description of the numbers depicted in Fig. 6.5 and Fig. 6.6.

Figure 6.5.: Photographs of the DOAS container instrument, cf. Table 6.1 concerning the depicted numbers. (**a**) top side (**b**) back side with blowhole for ventilator, edging taped with EMC tape (**c**) installed in the CARIBIC Container (cf. Fig. 5.4) (**d**) opened spectrograph box (**e**) old and new instrument (**f**) front side

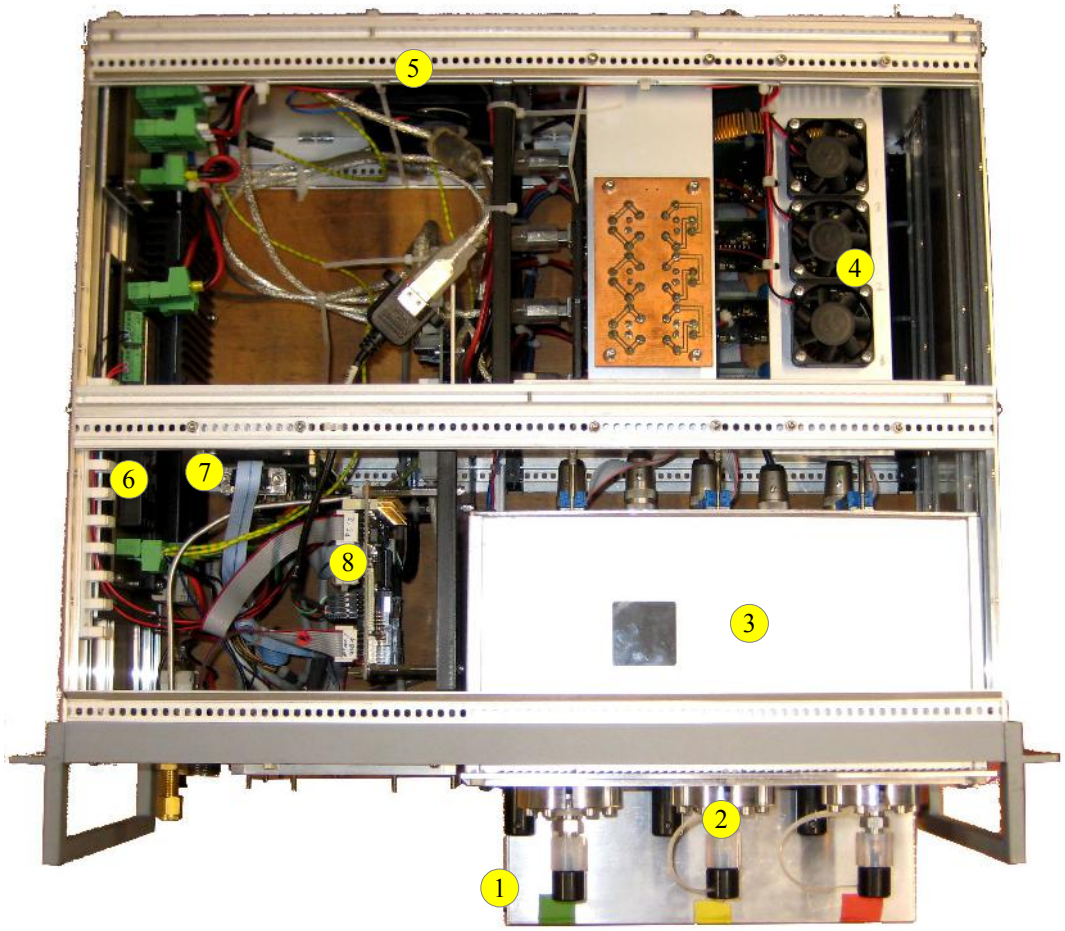

Figure 6.6.: Opened DOAS instrument (view from above). Cf. Table 6.1 concerning the depicted numbers

and the the data storage is performed by an embedded computer (№ 8) of the type 'Lippert Cool LiteRunner-LX800' ("http://www.adlinktech.com/rugged/index.php" or "http://www.lippertembedded.com/"), cf. Sect. 6.5.2. An ethernet card (№ 7) is used for the communication with the Master computer of the CARIBIC container, mainly for comparing the time signal, cf. Sect. 6.7.1. While the embedded computer and the electronic cards need a direct current (DC) of 12 V, the basic power supply (BPS) of the CARIBIC container delivers 24 V DC. Therefore, the DOAS instrument contains DC/DC converter and a filter to avoid disturbing frequencies in the voltage (№ 6).

Figure 6.5c shows the instrument when installed in the container (Fig. 5.4 p. 78). The front side is still accessible after the container is put into the cargo compartment of the aircraft, This is necessary to attach the fibre bundles to the the spectrographs via FSMA connection (№ 2). In Fig. 6.5f, the safety switch (№ 10) can be seen as well as the connection for the power supply (№ 12) and the connection for the ethernet communication (№ 11) with the Master computer. The front plate (№ 9) is closed during flight, afterwards it is opened to get access to the memory card for reading out the data. Behind that plate, there are also connections for a computer mouse, a keyboard, a monitor and a network cable. Therewith, the embedded computer can be accessed directly or using a Virtual Network Client (VNC) for testing purposes. Otherwise, the standard measurement routine automatically starts after boot up when the instrument gets power, cf. Sect. 6.6. Due to the rather low power consumption of about 50 W, the DOAS instrument does not have to wait for the permission signal from the Master computer.

6.3. Spectrographs

The instruments contains three identical spectrographs with nearly the same wavelength range of 285–421 nm (Spectrograph A), 286–423 nm (Spectrograph B) and 286–423 nm (Spectrograph C). See Sect. 6.3.3 for more details about the wavelength calibration.

6.3.1. Functionality

Table 6.2 contains characteristic numbers of the spectrographs, which are Czerny-Turner-type (*Czerny and Turner*, 1930). They contain a diffraction grating and two spherical mirrors for focusing the light beam. Figure 6.7 contains a sketch of the light path inside the spectrometer. Regarding the entrance slit as a point source (in a two-dimensional cross section of the spectrograph), the incident light (gray) is parallelized at the first mirror, than dispersed at the grating, indicated by the blue lines (short-wave, 286 nm) and the red lines (long-wave, 423 nm). By the second mirror, the light is focused on the detector.

In the following, the functionality of the grating is described.

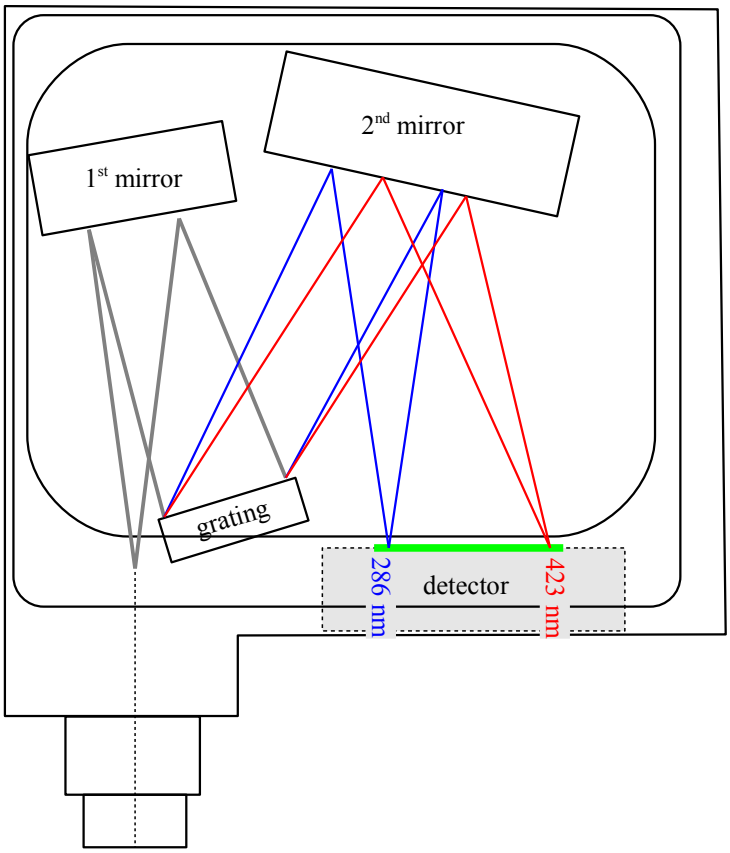

Figure 6.7.: Sketch showing the functional principle of the spectrographs. The dispersion of the polychromatic light takes places at the grating. The red and the blue line indicate the path and the impinging position at the detector for light with a wavelength of 286 nm and 423 nm.

Manufacturer	omt – optische messtechnik gmbh
Model	omt-ctf60
Serial Number	1321, 1322, 1323
focal length	60 mm
F-number	4
grating constant	2100 lines/mm
Blaze wavelength	350 nm
wavelength range	286–423 nm
FWHM	0.5 nm

Table 6.2.: Characteristic numbers of the spectrographs

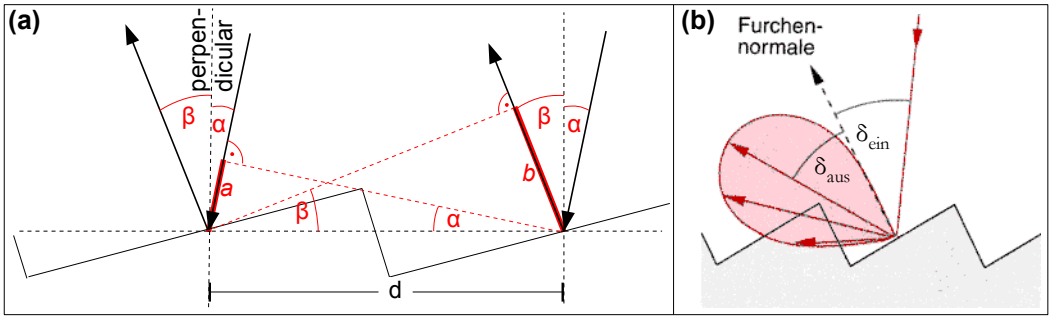

Figure 6.8.: (**a**) Interference of two incident rays at two adjacent grooves (**b**) radiation pattern of a groove. The angle with the highest radiance is the reflection angle, i.e. $\delta_{\text{ein}} = \delta_{\text{aus}}$. δ_{ein} and δ_{aus} describe the angle between the perpendicular of the groove surface and the incident or emergent ray, respectively. (Adapted from *Demtröder*, 2004)

Grating equation

Figure 6.8a shows the principle of a diffraction grating. Two incident parallel equiphase rays are reflected at two adjacent grooves at distance d (the *lattice spacing*). Afterwards there is a path difference Δs between them given by

$$\Delta s = a + b = d \cdot \sin\alpha + d \cdot \sin\beta = d \cdot (\sin\alpha + \sin\beta) \tag{6.1}$$

Here, the incident angle α is positive by convention; the emergent angle β is positive for the case that incident and emergent angle are on the same side of the perpendicular, and negative otherwise (which is the case for Fig. 6.8a). Constructive interference occurs, if the path difference Δs is an integer multiple of the wavelength λ, i.e. if the so-called *lattice equation* is fulfilled:

$$d \cdot (\sin\alpha + \sin\beta) = m \cdot \lambda \quad \text{with} \quad m \in \mathbb{Z} \tag{6.2}$$

The integer multiple m is called the *order* of the spectrum.

Dispersion

From (6.2) the dispersion $\mathrm{d}\beta/\mathrm{d}\lambda$ can be obtained (α is independent from λ):

$$\frac{\mathrm{d}\beta}{\mathrm{d}\lambda} = \frac{m}{d \cdot \cos\beta} \tag{6.3}$$

The *linear dispersion* between the position Λ at the detector (or the channel number n) and the wavelength can be approximated when multiplying with the focal length f, cf. *Palmer and Loewen* (2002):

$$\frac{\mathrm{d}\Lambda}{\mathrm{d}\lambda} = f \cdot \frac{|m|}{d \cdot \cos\beta} \tag{6.4}$$

With a focal length $f = 60\,\text{mm}$ and a grating constant of 2100 lines/mm ($\rightsquigarrow d \approx 480\,\text{nm}$), $m = 1$ (first order diffraction) and $\beta \approx 47°$ this results in

$$\frac{\mathrm{d}\Lambda}{\mathrm{d}\lambda} \approx 185 \cdot 10^3 \quad \text{or} \quad \frac{\mathrm{d}\lambda}{\mathrm{d}\Lambda} \approx 5.41 \cdot 10^{-6} \tag{6.5}$$

With a pixel with of $12\,\mu\text{m}$ (as it is the case for our detectors) this corresponds to

$$\frac{\mathrm{d}n}{\mathrm{d}\lambda} \approx 15.3 \frac{\text{Pixel}}{\text{nm}} \quad \text{or} \quad \frac{\mathrm{d}\lambda}{\mathrm{d}n} \approx 0.065 \frac{\text{nm}}{\text{Pixel}} \tag{6.6}$$

This dependency is only an approximation for the real wavelength-to-pixel-mapping (the so-called 'wavelength calibration'). However, the value of 0.065 nm/Pixel is in good agreement with the measured result (0.068 nm in the centre of the spectrograph's wavelength range), obtained by a wavelength calibration based on the Fraunhofer lines in the solar spectrum, cf. Sect. 6.3.3.

Blaze angle

In the above idealized consideration, light is assumed to be only reflected by the grating at discrete equidistant points of distance d. In fact, the grating consists of grooves of finite width, each acting like a plane mirror. Thus, the intensity distribution of the light after the grating can be interpreted as a combination of the inference of discrete points according to (6.2) and the reflection at the surface of each groove, which emphasizes angles δ_{aus} with $\delta_{\text{aus}} = \delta_{\text{aus}}$, see Fig. 6.8b. Because only the first order diffracted light is desired (other the light from other orders leads to undesired straylight, cf. Sect. 6.3.4), the surface of the grooves is inclined relative to the plane of the grating by the so-called *blaze angle* with the aim of overlaying the diffraction maximum with the reflection angle:

$$\gamma_{\text{blaze}} = \frac{\alpha + \beta}{2} \tag{6.7}$$

By choosing the blaze angle γ_{blaze} the grating is optimized for a certain wavelength range.

6.3.2. Instrument function

As described later in Sect. 4.3.1, the spectrally highly resolved cross section data for the absorbing species have to be convoluted with the instrument function. To determine the instrument function, a mercury lamp was used because of its sharp emission lines which can be treated as delta functions (the spectral with of such an emission line is small compared to the resolution of our spectrographs).

Figure 6.9a shows two instrument functions (derived from the 302.15 nm mercury line) for each spectrograph, taken on March 2010 and August 2011. The relative small differences show, that the spectrographs were stable in the course of time.

Indeed, both functions leave to similar results, which is illustrated in the scatterplot Fig. 6.9b for NO_2 SCD for flights 349 (July 2011): The values retrieved using cross

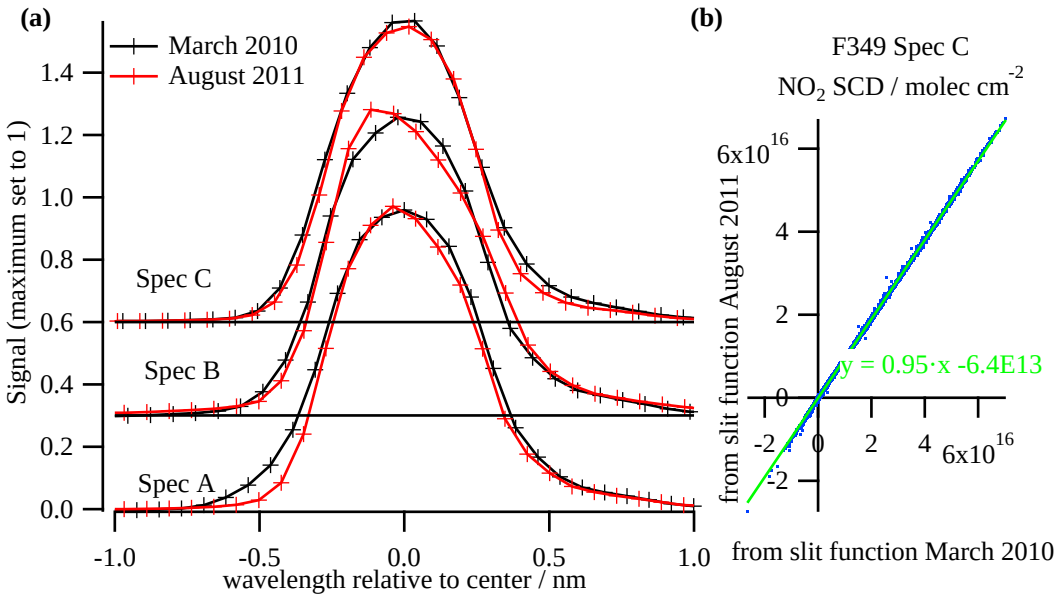

Figure 6.9.: (**a**) Instrument functions obtained from mercury spectrum, taken on 4 March 2010 (black line) and 3 August 2011 (red) (**b**) scatterplot for NO_2 SCD retrieved for flight 349, Spec C., using different slit functions for the convolution of the cross sections. x-axis: slit function of August 2011 used, y-axis: slit function of March 2010 used.

sections convoluted with the slit function of August 2011 are plotted against those based on a convolution with the slit function of March 2010.

The spectral resolution of the three spectrographs are similar, namely ∼0.5 nm FWHM, ranging from 0.51 nm (Spec C, cf. red curve in Fig. 6.9a for August 2011) to 0.58 nm (Spec A, black curve).[2]

6.3.3. Wavelength calibration

In (6.6), a linear approximation for the wavelength-to-pixel-mapping was given. The actual wavelength calibration is obtained by measuring a light source having a well-defined spectral shape. Spectral lamps provide sharp lines which can be used as calibration points. Mercury lamps are useful for a quick calibration, but this method is not very precise, because only a limited number of lines is available in the wavelength range of the spectrometer. A better lightsource for that purpose is solar light, containing many Fraunhofer lines at well-known wavelengths. Using the solar light for the calibration also has the advantage, that it is contained in every daylight spectrum anyway, whereas Hg-spectra cannot be taken during flight with our instrument.

In the following, the process of a manual calibration is described, afterwards the automated version provided by the WinDOAS program is mentioned.

[2]The FWHM ('Full Width at Half Maximum'), is the width F of a Gaussian approximation of the instrument function, taken at the half height, i.e. $F = 2 \cdot \sqrt{\ln 2} \cdot w$ for a Gaussian function $y = y_0 + y_{\max} \cdot \exp(-(\frac{x-x_0}{w})^2)$.

Manual calibration

Due to the limited spectral resolution of our spectrographs, not every Fraunhofer line can be resolved. In order to compare the spectrum measured by a CARIBIC DOAS spectrograph with a highly resolved solar spectrum (here referred to as 'Kurucz spectrum', cf. *Kurucz et al.* (1984)), the latter one has to be convoluted. The preferred way is to use the instrument function as convolution kernel, as done for this work, cf. section Sect. 6.3.2. Alternatively, a Gaussian function with a width corresponding to the spectrograph's resolution could be taken as an approximation for the slit function, but especially for the case of assymetric slit functions this method should be avoided. After the convolution, the measured and the convoluted Kurucz spectrum are compared by hand, resulting in a number of mapping points (channel|wavelength). Then, those points are interpolated by a polynomial, e.g. of third order:

$$\lambda(n) = (a_0 + a_1 \cdot n + a_2 \cdot n^2 + a_3 \cdot n^3) \cdot 1 \text{ nm} \tag{6.8}$$

Calibration with WinDOAS

The WinDOAS program provides an automated calibration routine. However, this routine needs a preliminary wavelength calibration like the manual calibration mentioned above. In this routine, a selectable section of the spectrum (e.g. 330–380 nm) is divided into N_{subw} sub-windows (here N_{subw}=8 was chosen). In each sub-window, the routine tries to approximate the measured spectrum with the Kurucz spectrum – the convolution of the Kurucz spectrum is done using a Gaussian, whose width is fitted for each sub-window independently. Furthermore, the spectrum can be shifted and stretched within each window. To improve the coincidence between the Kurucz spectrum and the measured spectrum, cross sections of gases and a Ring spectrum can be fitted. In case of success, for each sub-window, a value is calculated for correcting the preliminary calibration. At the end, a polynomial like in (6.8) is fitted. Further information about the calibration can be found in *Fayt and van Roozendael* (2001).

If the preliminary wavelength calibration is not precise enough, the routine usually fails. For CARIBIC, usually one reference spectrum was taken for a set of flights. For the calibration of the reference spectrum with the WinDOAS routine, typically the calibration of the previous set of flights was accurate enough for being used as preliminary wavelength calibration.

Figure 6.10a shows the wavelength calibration for SoF 325. The spectrographs B and C (green and blue line) have a quite similar mapping, whereas Spectrograph A is slightly shifted to shorter wavelengths. The unequal distances between the ticks at the coloured axes (one tick per 10 nm) clearly show the non-linear shape of the mapping. For the case of Spec B (SoF 325), the coefficients $a_0 = 286.5$, $a_1 = 7.9233 \cdot 10^{-2}$, $a_2 = -4.503 \cdot 10^{-6}$, $a_3 = -7.6526 \cdot 10^{-10}$ are obtained, cf. (6.8). In Fig. 6.10b, the measured spectrum is shown with the obtained calibration, together with the high resolution solar spectrum

after convolution with the instrument function. The differences in the broadband shape of the intensity is caused by different light paths (and therefore different scattering) and different spectral sensitivities.

The change of the wavelength-pixel-mapping in the course of time is illustrated in Fig. 6.10c, showing the wavelengths belonging to channel 250, 750 and 1250 for the flights 297–385. For Spectrograph A only calibration data for flights 325–356 are available because of the missing light during the other flights (cf. problems with broken fibres, Sect. 6.1.1).

Changes in the temperature and pressure cause slight distortions of the spectrographs body. Furthermore, the refraction index of the air inside the spectrograph is pressure dependent. Therefore, the mapping is not constant during a flight. In order to account for that and still avoiding to performing a new wavelength calibration for each spectrum, a shift and stretch coefficient is included in the DOAS fitting routine (cf. Sect. 4.3.4).

6.3.4. Straylight

In an idealized spectrograph, only light of the wavelength according to the dispersion function reaches the detector. As already mentioned in Sect. 4.3.1 and Sect. 6.3.2, the slit function has a finite width, so each pixel of the detector receives also light from adjacent wavelengths. But furthermore, so-called *straylight* from a quite different wavelength reaches the detector, caused by undesired lightpaths inside the spectrograph. In the IUP Heidelberg, strong straylight fractions have been observed with similar OMT spectrographs. By inserting blinds, this problem could be reduced. Thus, a similar approach was performed with the CARIBIC spectrographs in early 2012, using an extended time interval between the flights of January and February.

Figure 6.11 shows a sketch of possible light paths within a spectrograph. The magenta line corresponds to the desired light path (cf. Fig. 6.7 p. 97). But already the first mirror is probably missed by some part of the light, reflected at the mirror's frame (light blue line in Fig. 6.11) or the back board of the spectrograph, because both parts are not totally black. In the non modified version, this straylight can directly reach the detector. Beside the desired first order of diffraction, further orders occur (namely 0 and -1), again causing straylight. Order -1 reaches at the left board (pink line), from where it can directly reach the detector. Order 0 is reflected back into the direction of the first mirror and the surrounding frame. From the mirror itself it is reflected towards the region around the entrance slit. From the frame it is reflected into different directions. The second mirror is missed by a the light with higher wavelength than $\approx$423 nm, because first order diffraction occurs up to $\frac{1}{2100}$nm $\approx$ 476nm. The built-in color filter 'HOYA U-330' absorbs the biggest fraction of the light with $\lambda \gtrsim 400$nm (cf. Fig. 6.15), but nor completely – for 470 nm (blue line in Fig. 6.11), still $\approx$6 % of the light is transmitted according to the data sheet of the HOYA filter.

To visualize the straylight, a photo was taken with a digital camera and 30s exposure

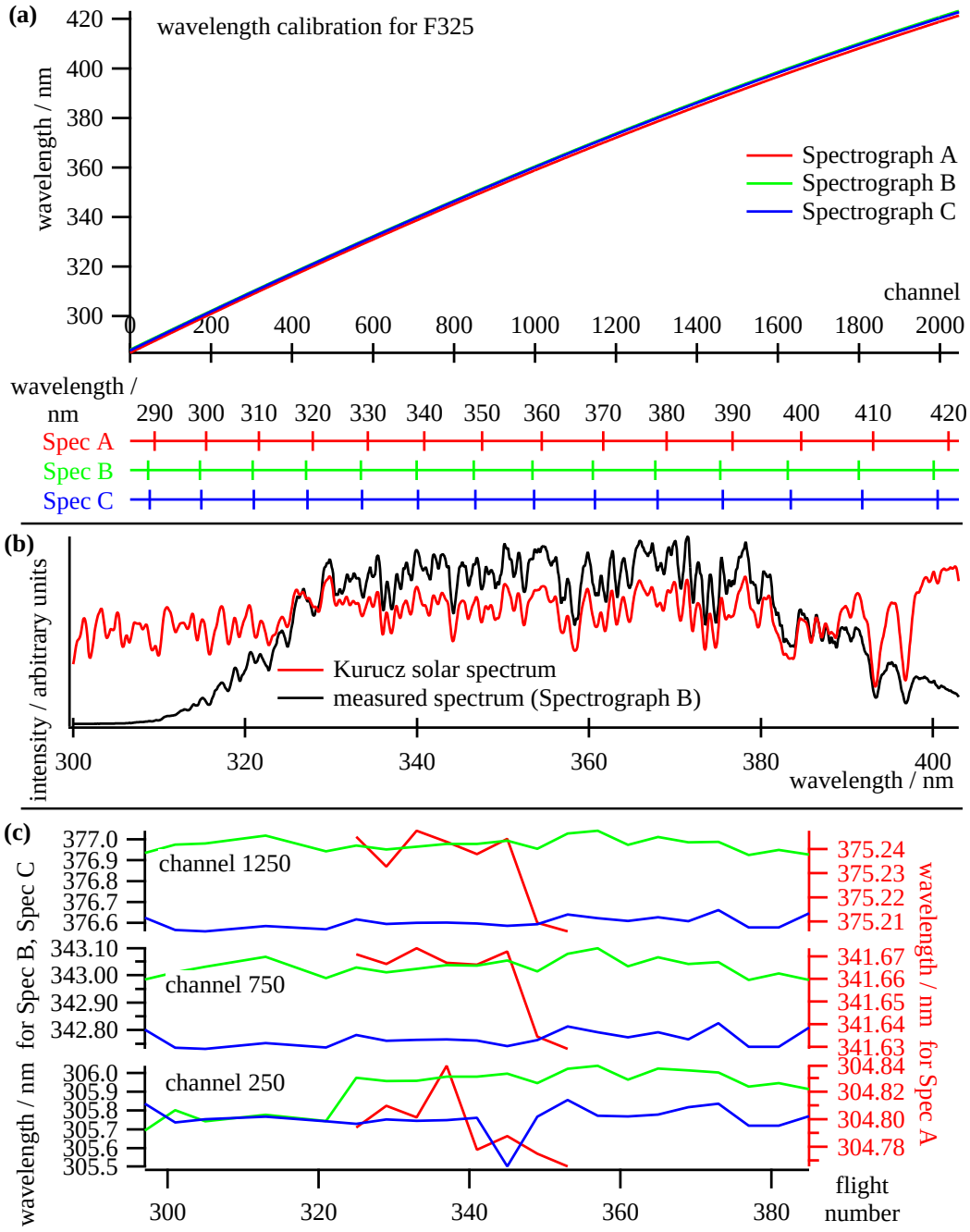

Figure 6.10.: Wavelength calibration (**a**) for SoF 325 (**b**) measured spectrum B0021755 (SoF 325, after offset and dark current correction), compared with a convoluted Kurucz spectrum (*Kurucz et al.*, 1984) (**c**) change in the course of time. Depicted are the wavelengths for three channels (250, 750, 1250). The left axis belongs to Spectrographs B and C, the right axis to Spectrograph A. The x-axis ranges from flights 297 (June 2010) till flights 385 (April 2012).

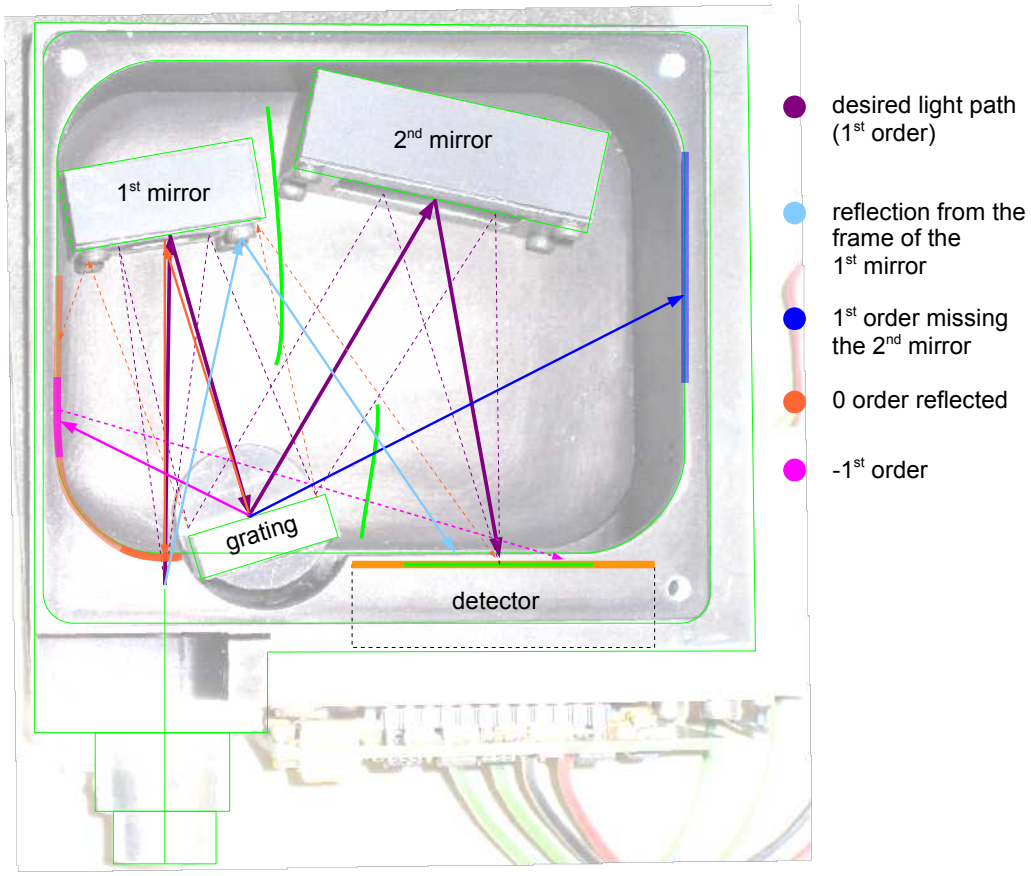

Figure 6.11.: Sketch of the spectrograph and possible light paths causing straylight

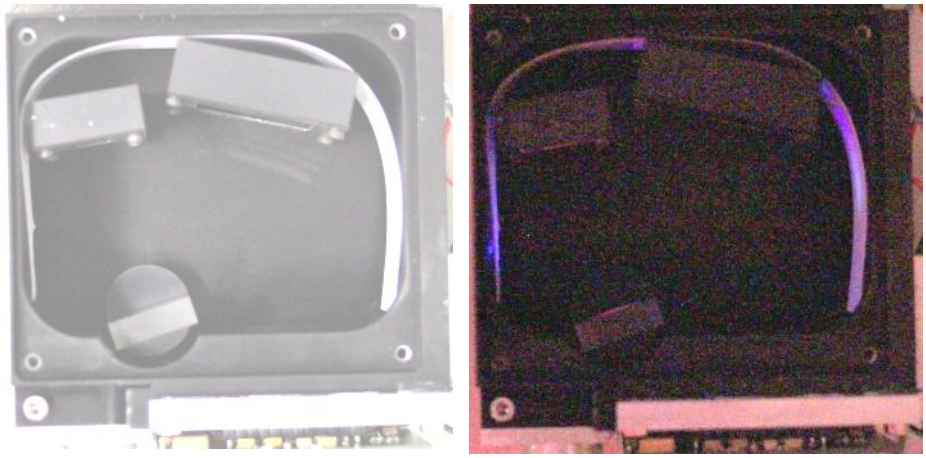

Figure 6.12.: (**a**) Photograph of the opened spectrograph (**b**) photograph of the straylight. To make it better visible, a white paper ribbon was inserted.

time (Fig. 6.12b), using the light of a halogen lamp. Because of the HOYA-filter, very little light could be observed with the camera. Therefore, a peace of white paper was put into the spectrograph for that test (Fig. 6.12a). The order -1 and 1 can be clearly seen on the left and right wall, respectively. Order zero could not clearly been observed, probably it is reflected by the first mirror, as mentioned above.

In order to block the direct line between the detector and the left part of the spectrograph, two blinds have been inserted (blue in Fig. 6.11). They consist of a thin metal sheet (painted with black metal varnish), which is glued to a T-shaped aluminium part (also black painted), built by the workshop according to equal blinds for other OMT spectrographs, cf. *Jurgschat* (2011). They were adjusted with the goal to minimize the straylight without significantly loosing intensity of the desired UV light. After the adjustment, the blinds were fixed by a adding a second cap.

Figure 6.13 contains photos of the tested modifications: In 6.13a and 6.13b, the cap with the T-shaped blinds is shown from above and from below, respectively. The detector array is surrounded by a gold-coloured reflecting metallic plate (Fig. 6.13c). In order to reduce the reflection, a blind made of black carton was fixed with double sided tape directly in front of the detector (Fig. 6.13c). A further peace of carton was fixed at the top and the left side of the grating.

With OMT spectrographs in the visible light, further improvements had been made by inserting a black carton on the walls and on the floor of the spectrograph (J. Lampel, pers. comm., 2012). Such cartons were tested with our spectrographs, too (Fig. 6.13e). However, in our case, no significant improvements could be observed with these pieces. A zigzag-shaped peace (Fig. 6.13f) with the intension to get a higher absorption was tested, also scratching lines into the carton with a cutter, again both without a large influence. Therefore, those add-ons were removed again, because every part inside the spectrograph could potentially damage the spectrograph if not fixed well enough.

Figure 6.14 shows the experimental setting. The light of a halogen lamp was coupled into the spectrograph via a quartz fibre. None or one of the following optical filter was inserted in the light path in order to discern between visible and infrared light: Schott GG 385 (blocking light with wavelengths smaller than 385 nm), Schott GG 475 (blocking $\lambda < 475\,\mathrm{nm}$) and Schott RG 665 (blocking $\lambda < 665\,\mathrm{nm}$). Their spectral transmittance is given in Fig. 6.15. Because the fixed HOYA filter blocks visible light between 400 nm and 700 nm, no light should be measured when inserting the filter GG 475 or RG 665.

Figure 6.16 shows for each spectrograph a spectrum of a halogen lamp, measured before adding blinds (solid lines) and afterwards (dashed lines). It is corrected for offset and dark current by subtracting a spectrum taken with the same exposure time. Without a filter in the light beam (except the built in HOYA filter), the black curve is measured. If this measurement would contain no straylight, the signal should disappear when inserting the filter GG 475, which is not the case (orange line). Roughly 20 000 counts are observed around channel 520 (corresponding to 326 nm according the wave-

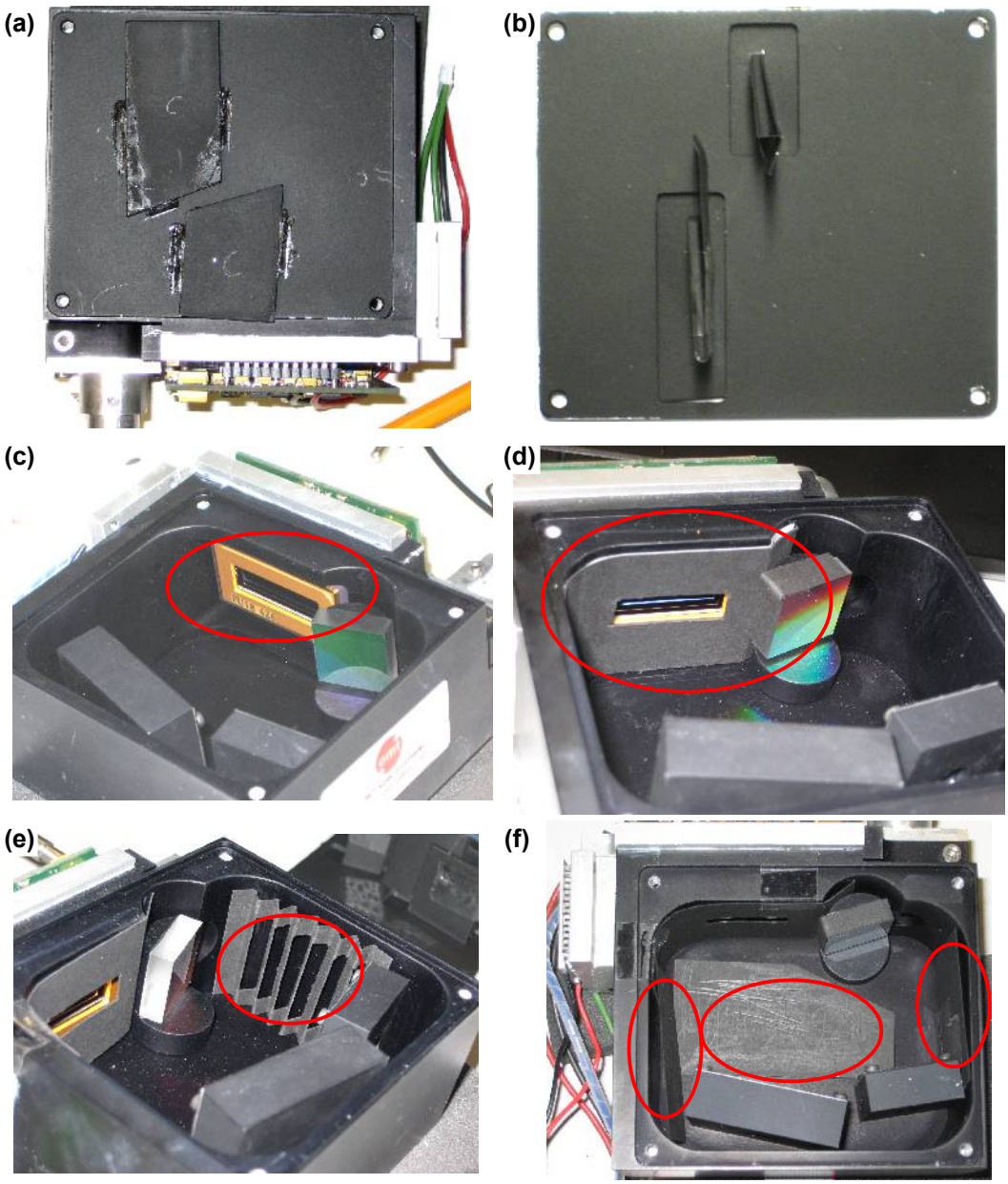

Figure 6.13.: Photos of the spectrograph with several tested modifications (**a**) closed spectrograph with blinds in the coverplate (**b**) coverplate with blinds, seen from below ('from inside the spectrograph') (**c**) reflecting metallic plate around detector array (**d**) black carton fixed before that reflecting plate (**e**) tested but finally not used black carton at the wall for absorbing light (**f**) further tested positions for black carton

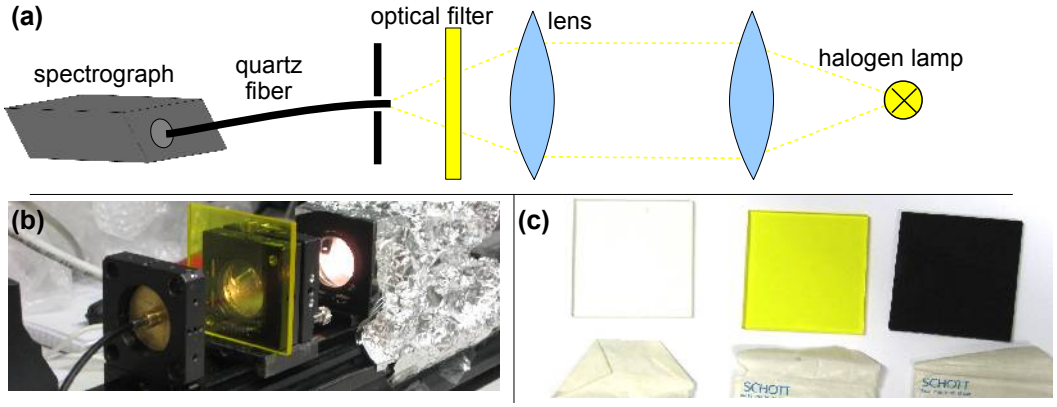

Figure 6.14.: Measurement setup (a), (b) and photo of the used optical filters (c)

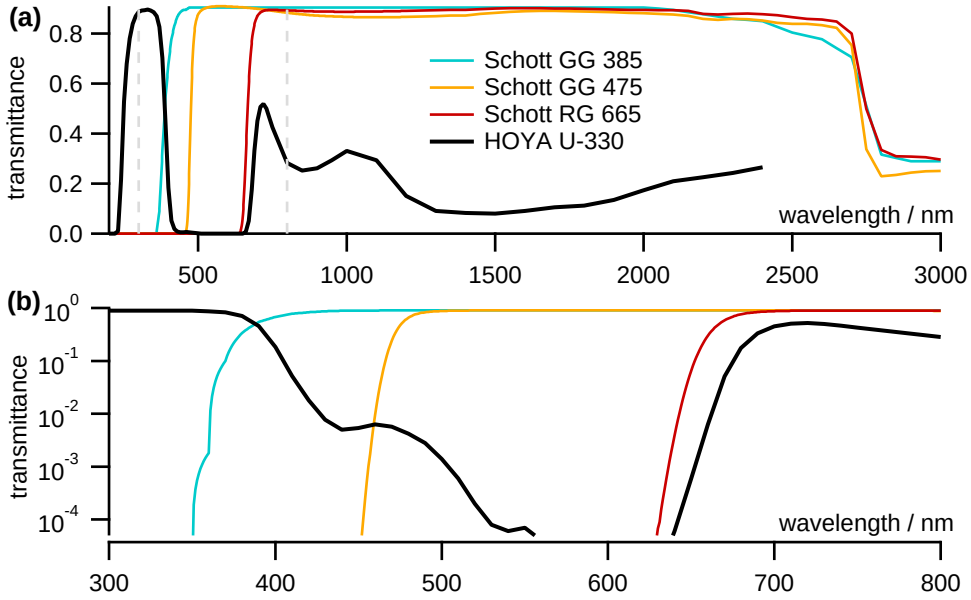

Figure 6.15.: Spectral transmittance of the HOYA and Schott filters according to their data sheet (**a**) linear axes (**b**) section 300–800 nm with logarithmic y-axis

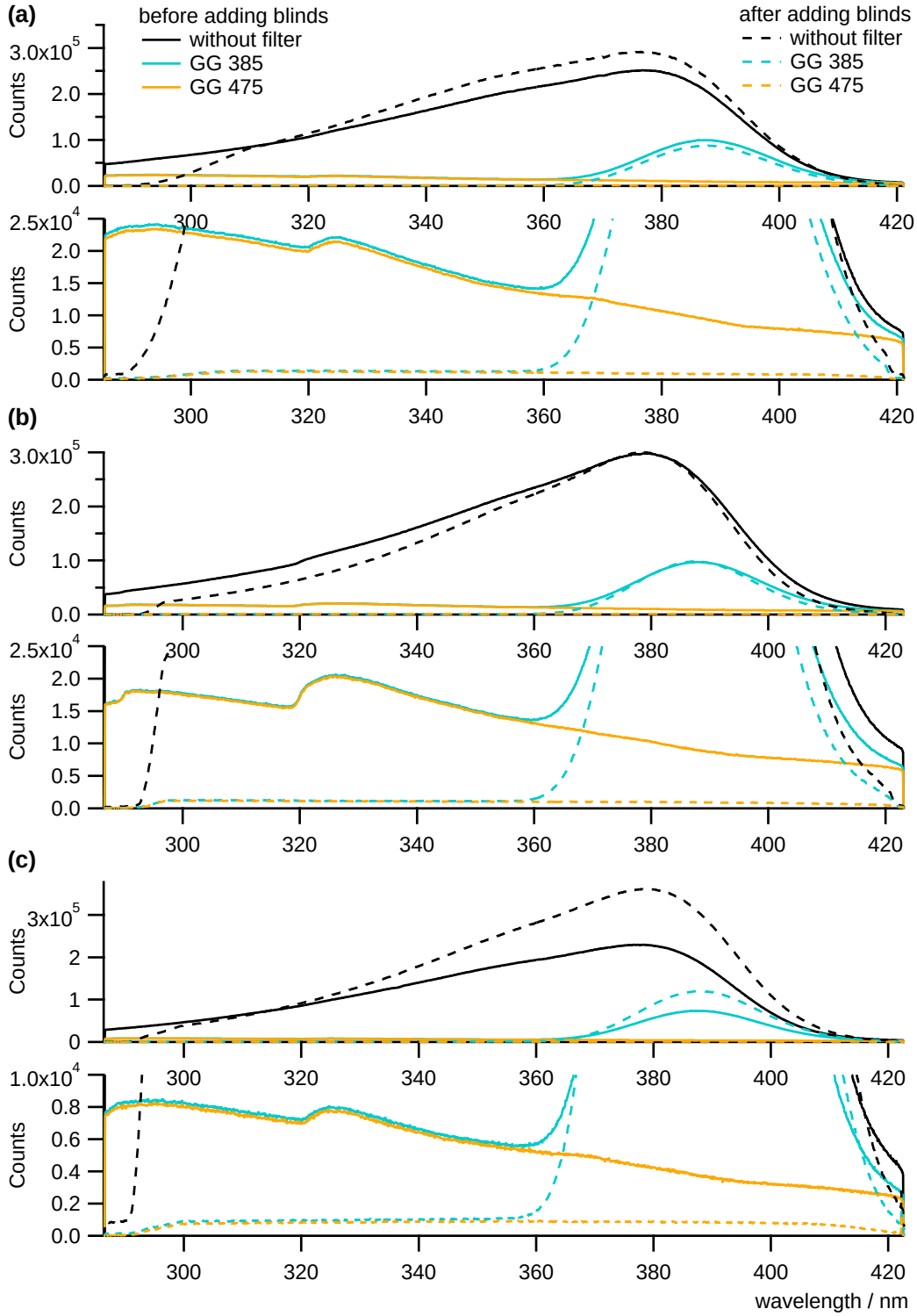

Figure 6.16.: Spectrum of a halogen lamp, measured before adding blinds (solid lines) and afterwards (dashed lines). The lower part is a detail of the upper part. (**a**) spectrograph A (**b**) spectrograph B (**c**) spectrograph C

length calibration). In the region $\lambda \gtrsim 360$nm nearly the same count rates are obtained when replacing the filter GG 475 by GG 385 (blue line). Therefore, that signal must predominantly caused by light being transmitted by GG 475 and GG 385. Taking also the transmission curve of the built in HOYA filter into account, infrared light with $\lambda \gtrsim 650$nm can be regarded as the main cause for that straylight signal. Beside the amount of straylight, also the shape of the 'straylight spectrum' (solid orange or blue line) causes a problem. The sharp 'edge' at ~320 nm can be compensated neither by the DOAS polynomial nor by the additional offset polynomial. Thanks to the inserted blinds, the straylight signal could be extensively reduced. The maximum of the corresponding dashed orange and blue lines is around 305 nm with roughly 1200 counts, which means, that the straylight could be reduced by more than 90 %. Furthermore, the residual straylight has a smooth shape – the edge at ~300 nm is unproblematic because it is outside the DOAS fit range.

It has to be mentioned, that the blinds also lead a small loss of desired UV light. The overall intensities between the dashed and the solid blue and black lines also differ, because the instrumental setup including the halogen lamp did not allow reproducible absolute intensities. For the tests with the halogen lamp, the straylight problem before adding the blinds appears to be dramatic. However, during CARIBIC flights, scattered sunlight is observed which contains a much lower fraction of infrared light than a halogen lamp.

6.4. Detectors

In this section, the function principle and the characteristics like offset, dark current and the temperature stabilisation of the detectors are described. An overview over the detector's specifications is given in Table 6.3.

6.4.1. Functionality

As described in Sect. 6.2, the diffracted light reaches the detector on different positions depending on the wavelength. The aim of the detector is to convert the light intensity into an electrical signal, in this case a digital signal. In the CARIBIC DOAS instrument,

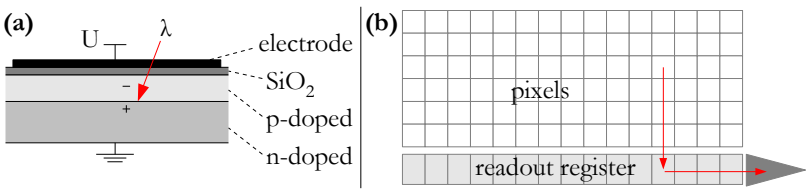

Figure 6.17.: (**a**) Schematic sketch of CCD pixel (Adapted from *Walter*, 2008) (**b**) read out of the CCD chip. The stored charges are shifted to the readout register, then from the readout register to the ADC.

Manufacturer	Hamamatsu
Model	S10141-1107S
Sensor type	back-thinned CCD
Number of rows	122
Number of columns	2048
Pixel size	12 μm × 12 μm
Detector area (W×H)	24.58 mm × 1.464 mm
Signal output frequency	250 kHz
Readout noise at -50 °C	4 e^- RMS, max. 18 e^- RMS
Dark current at 0 °C, 25 °C	5 e^-/Pixel/s, 100 e^-/Pixel/s
Analog Digital Converter	16 bit
Saturation signal	65 535 Counts
Charge transfer efficiency (CTE)	0.99999
Full well capacity (horizontal)	150 000 e^-

Table 6.3.: Product specifications of the Hamamatsu detectors according to data sheet (*Hamamatsu*, 2011)

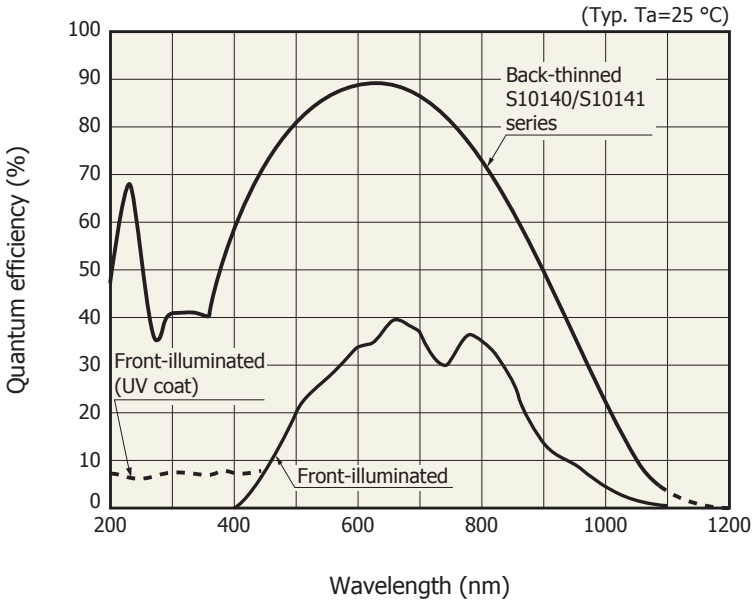

Figure 6.18.: Quantum efficiency of the Hamamatsu detectors. The thick line ('Back-thinned') applies for our exemplars. From the data sheet of the detector (*Hamamatsu*, 2011).

three charge-coupled device (CCD) detectors are used.

A CCD consists of an array of M rows and N columns (called 'channels') and therefore $M \cdot N$ picture points, the so-called 'pixels'. Figure 6.17a shows a systematic sketch of a pixel, essentially consisting of an n-doped and a p-doped silicon layer, an SiO_2 insulating layer and an electrode. This structure is called a 'Metal Oxide Semiconductor' or 'MOS capacitors'. Photons reaching the so-called 'depletion region' between the n- and the p-doped layer can create an electron-hole pair if their energy is larger than the bandgap of the semiconductor. For silicon at 300 Kelvin, this band gap is 1.17 eV, which corresponds to a wavelength of 1.1 μm according to $E = h \cdot \nu = h \cdot c/\lambda$. Therefore photons with larger wavelength cannot be detected. The free electrons are attracted by the positive electrode but stopped by the insulating SiO_2 layer, therefore stored in the p-doted layer until the read-out of the CCD. The storage capacity ('full-well capacity') of one pixel as well as the capacity of the shift register are limited, therefore limiting the exposure time for a given light intensity.

As long as no saturation effects occur, the number n_e of the created free electrons is proportional to the number n_ph of the incident photons. The ratio Q_eff is called 'quantum efficiency':

$$Q_\mathrm{eff} := \frac{n_\mathrm{e}}{n_\mathrm{ph}} \tag{6.9}$$

The quantum efficiency is wavelength dependent, see Fig. 6.18 from the detector's data sheet. In the wavelength range of the DOAS retrieval ($\sim$310–370 nm), Q_eff is around 40 %.

After the exposure, the CCD is read out. To obtain a two-dimensional picture, the detector is read out line by line: In a first step, the stored charges (electrons) of all pixel are shifted one row downward; those charges of the lowest line are shifted to the shift register. In a second step, the charges on the shift register are subsequently moved to the amplifier. A 16 bit analog-to-digital converter (ADC) converts the signal into an integer number (the 'counts') from 0 to 65535. This has to be repeated for every row.

Alternatively, the pixels can be vertically binned to obtain a one-dimensional picture (spectrum). Here, the charges of all pixel rows are transferred into the shift register in the first step. The second step is like in the two-dimensional mode but has to performed only once per spectrum. For the case of the CARIBIC instrument, this binned mode is used, meaning that the counts of the 122 pixels of each column are summed up to one signal per channel. This has the advantage of a significantly lower readout time, which is important when using the detector without a shutter, because new light is reaching the detector during the readout process.

The charge of one pixel has to be transferred several times during the readout process, depending of the pixel's position. For the 'worst case position', the charge has to be moved $M + N = 122 + 2048$ times to reach the amplifier. During that process, some electrons can get lost, which is described by the 'charge transfer efficiency' (CTE),

which is 0.99999 for the case of our detectors according to the data sheet (*Hamamatsu*, 2011). Therefore, for the 'worst case position', ∼2 % of the charge will be lost.

The amplification and conversion of the charge into the digital signal is described by the ratio Q_S between the number n_e of the photoelectrons and the number $I^\times$ of counts:

$$Q_S = \frac{n_e}{I^\times} \tag{6.10}$$

Together with the quantum efficiency (6.9) this leads to

$$I^\times = \frac{n_e}{Q_S} = \frac{Q_{eff}}{Q_S} \cdot n_{ph} \tag{6.11}$$

6.4.2. Offset and Dark Current, Noise

The creation of electron-hole pair does not only occur by photons, but also due to thermal excitation. Because this additional signal also occurs without incident radiation, it is called 'dark current'. The dark current signal is (almost) proportional to the exposure time and independent of the impinging radiation[3]. The dark current is temperature dependent – it is proportional to the Boltzmann factor $\exp(\frac{-\Delta E}{k_B \cdot T})$ with Boltzmann constant k_B, band gap ΔE of the silicium and the absolute temperature T.

Noise effects during the signal processing in the analog-digital-converter could lead to negative values. To avoid these, an electronical offset signal is added. For the analysis of the spectra, this offset signal has to be subtracted. To retrieve this offset signal, a spectrum is taken with a minimum exposure time (to minimize the effects of the dark current) in the darkness. To minimize statistical variations of the offset signal (noise), many scans are taken for determining the offset signal.

Figure 6.19 shows an offset spectrum with 400 scans and 20 ms exposure time per scan, and a dark current spectrum (1 scan, 8 seconds). There are striking peaks with a particular high dark current in between, called 'Hot Pixel'. Like 'dead pixels' (light insensitive pixels), such defective pixels occur already in new detector chips, but they can also be created due to cosmic radiation and probably further processes, cf. *Theuwissen* (2005).

The total noise σ_{tot} is composed of the photon noise σ_{ph}, the readout noise σ_{read}, the dark current noise σ_{darkc}, the amplifier noise σ_{amp} and the noise σ_{adc} of the analog-digital-converter. These noise sources can be considered to be independent from each other, therefore σ_{tot} can be calculated by

$$\sigma_{tot} = \sqrt{\sigma_{ph}^2 + \sigma_{read}^2 + \sigma_{darkc}^2 + \sigma_{amp}^2 + \sigma_{adc}^2} \tag{6.12}$$

The emission and scattering of light is a statistical process. The number of photons reaching the detector during a given time interval (here the exposure time) is described

[3]This is not exactly the case, because the free electrons in the semiconductor layer influence the electric potential to some extend. Furthermore, the readout process slightly warms the detector.

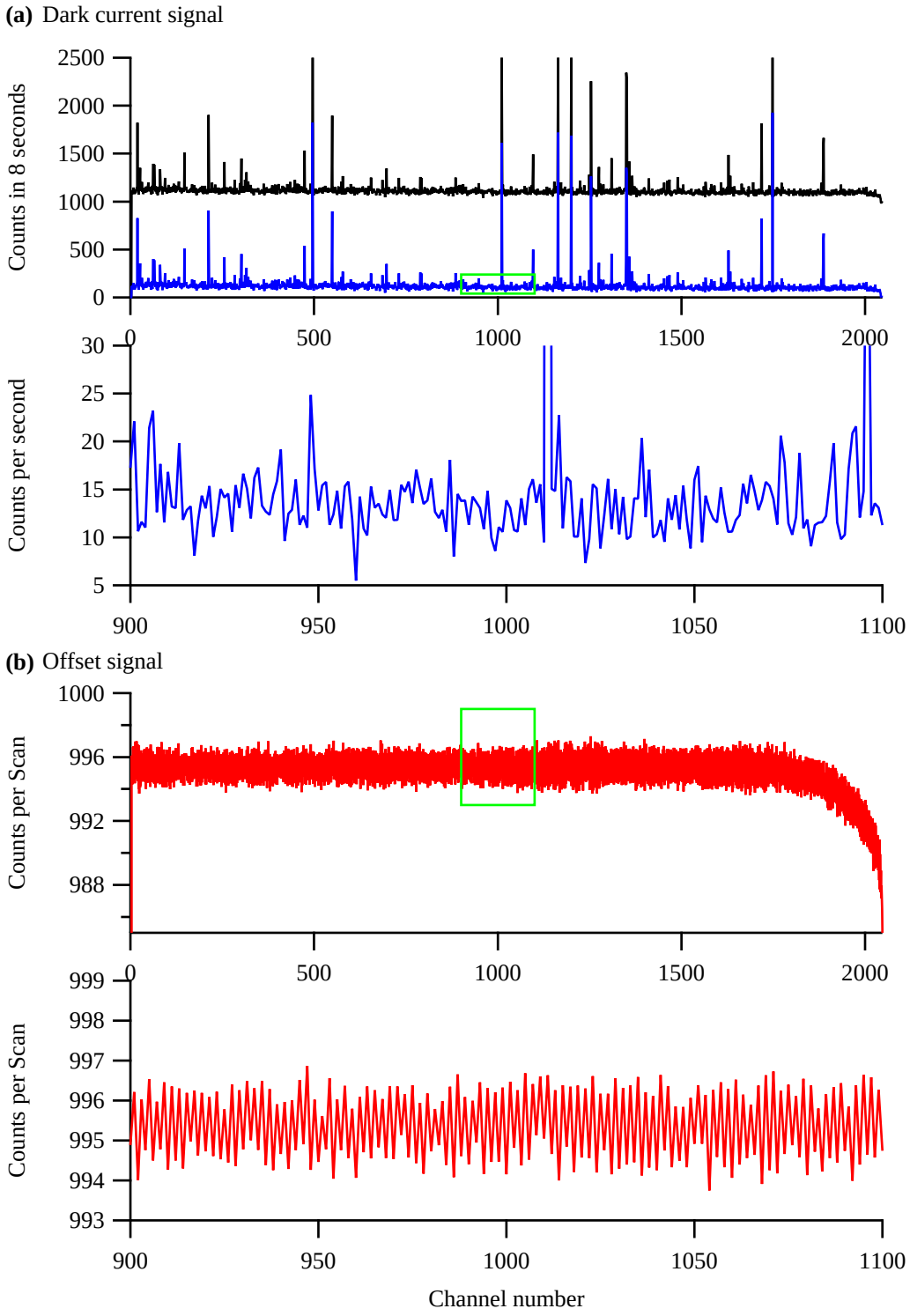

Figure 6.19.: Offset and dark current spectrum of Spectrograph A, taken during SoF 401. (**a**) Dark current spectrum A0010010, containing one scan. The blue line shows the offset corrected version of the raw spectrum (black line). The lower part is a section of the upper part, divided by the exposure time of 8 seconds. (**b**) Offset spectrum A0010020. The lower part is a section of the upper part (cf. green rectangle). The odd-even structure depicted in this raw spectrum is a systematic feature.

by a Poisson statistic, cf. *Stutz and Platt* (1996). In the Gaussian approximation, the photon noise is given by the square root of the number n_{ph} of the impinging photons: $\sigma_{\mathrm{ph}} = \sqrt{n_{\mathrm{ph}}}$. According to the values given in (*Hamamatsu*, 2011), cf. Table 6.3, the Full well capacity amounts to 150 000 electrons which corresponds to roughly 400 000 photons for a quantum efficiency $Q_{\mathrm{eff}} \approx 0.4$ (cf. Fig. 6.18 for 300–400 nm). Assuming a saturation of 30 % (averaged over the spectrum), ∼120 000 photons reach the pixels of one channel. This leads to $\sigma_{\mathrm{ph}} \approx \sqrt{120000} \approx 350$. Without other noise sources, this is equal to the signal to noise ratio $\frac{\sqrt{n_{\mathrm{ph}}}}{\sigma_{\mathrm{ph}}} \approx 350$. Actually, the photon noise is the dominant contributor to the total noise. The readout noise σ_{read} is only on the order of 10 electrons (Table 6.3), the dark current noise is also on that order of magnitude. Also the amplifier noise and the noise of the analog-digital-converter (ADC) are usually rather small. However, the ADC limits the signal to noise ratio according to the number of bits. For a 16-bit ADC with 65536 possible output signals, this is of minor importance.

To improve the signal-to-noise ratio, the exposure time per scan or the number of scans per spectrum can be extended. For the CARIBIC DOAS instrument, the exposure time is limited to 8 s. In order to obtain a synchronous numbering of the spectra between the three spectrographs, the total exposure time of a spectrum is set to 8 s, and the number of scans are adapted according the light intensity, cf. Sect. 6.6. Furthermore, spectra can be added for the analysis in order to further increase the signal-to-noise ratio.

6.4.3. Temperature Stabilisation

As mentioned above, the dark current is temperature dependent. Also the wavelength to pixel mapping is influenced by the temperature due to mechanic expansion and a changing refraction index. Therefore a stable temperature is desired. In our instrument, each detector is cooled with an unregulated Peltier element. Those three Peltier elements are connected to the optical bench which is also cooled, but regulated by a software implemented proportional-integral-controller (PI) as part of the measurement script: After each acquisition of three spectra (one per spectrograph), the observed Celsius temperature θ_{ob} is compared with the setpoint value θ_{set}. Then the current is adapted according to following equation.

$$C_{\mathrm{new}} = P_{\mathrm{new}} + I_{\mathrm{new}} \tag{6.13}$$

with

$$P_{\mathrm{new}} = C_{\mathrm{P}} \cdot (\theta_{\mathrm{ob}} - \theta_{\mathrm{set}}) \tag{6.14}$$

$$I_{\mathrm{new}} = I_{\mathrm{old}} + C_{\mathrm{I}} \cdot (\theta_{\mathrm{ob}} - \theta_{\mathrm{set}}) \cdot t_{\mathrm{diff}} \tag{6.15}$$

P_{new} is called ‘proportional part’, because P_{new} is proportional to the mismatch $\theta_{\mathrm{ob}} - \theta_{\mathrm{set}}$ between the actual temperature θ_{ob} and the desired setpoint temperature θ_{set}, weighted

by a constant factor C_P. The 'integral part' I_new depends on the previous value I_old, to which the temperature mismatch is added, weighted by the constant C_I and the time difference t_diff since the previous acquisition.

The two constants C_P and C_I have to be chosen in a way that the temperature regulation reacts fast but without overshooting to much. The proportional part P_new reacts quickly to changes while the integral part I_new reacts more inert. Tests in the laboratory showed a good balance for $C_\mathrm{P} = 30$ and $C_\mathrm{I} = 0.3$.

Sometimes, a third summand is added, called 'differential part' (leading to a PID-controller), which is proportional to the change of the temperature mismatch per time: $D_\mathrm{new} = C_\mathrm{D} \cdot (\theta_\mathrm{ob} - \theta_\mathrm{set})/t_\mathrm{diff}$. This part shall push up the reaction to changes. However, in the performed tests, this differential part did not improve the results, therefore it was omitted.

In order to avoid the damage of the instrument, C_new was restricted to be between 0 and 100. The setpoint value θ_set was set to 25 °C, later to 22 °C. While the regulation itself worked well, the cooling capacity was not always large enough when high ambient temperatures in the cargo compartment and therefore also in the CARIBIC container occurred. On the other hand, sometimes the ambient temperature was lower than the setpoint, especially at the beginning of some flights in winter.

Figure 6.20 gives an overview over the temperature sequence for flights 373–376. The black line shows the Celsius temperature θ_ob regulated by the PI control routine. In the case of flights 373 and 375, the setpoint temperature of 25 °C is reached after the ambient air's temperature inside the container had increased (gray line). The cooling current C_new is successfully adapted to prevent a higher θ_ob. During flights 375 and 376 however, the ambient air decreases during the flight. C_new sinks to compensate but after reaching zero, the temperature θ_ob sinks below 25 °C. In order to avoid such situations, for the following flights, the setpoint temperature was decreased to 22 °C.

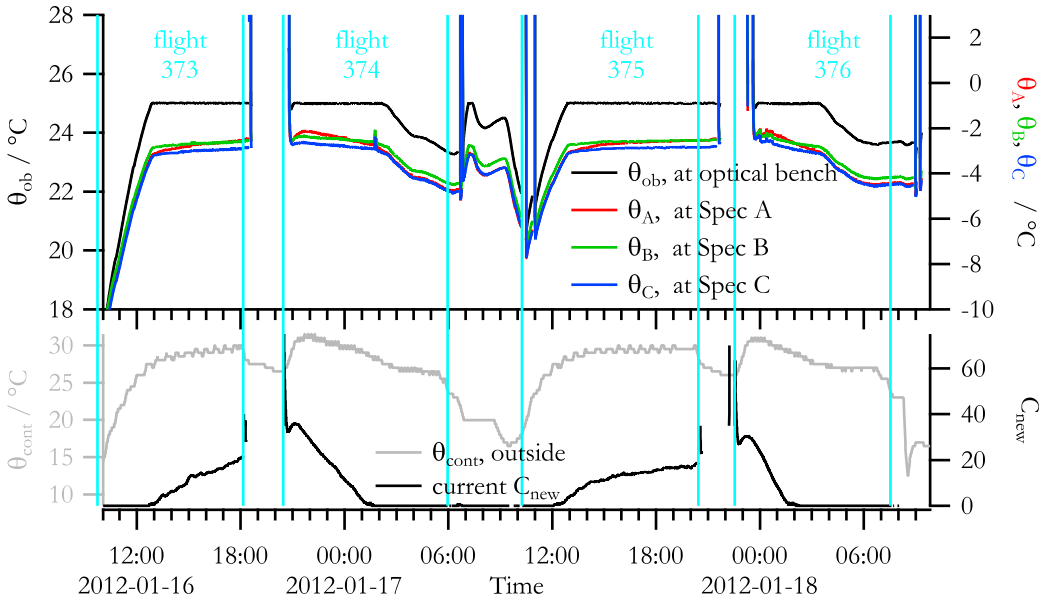

Figure 6.20.: Temperature and cooling current during set of flights 373–376. In the upper part, the temperature θ_{ob} of the optical bench (left axis) and the temperatures θ_A, θ_B, θ_C at the spectrograph's detectors (right axis) are shown. The temperature θ_{cont} in the CARIBIC container measured outside the instrument and the cooling current C_{new} (in arbitrary units) are depicted in the lower part.

6.5. Further technical issues

6.5.1. EMC Test

Following the Maxwell's laws, changing electric current and voltages in an instrument cause electromagnetic radiation leaving the instrument. For aviation security reasons, this radiation has to be below certain wavelength dependent threshold values in order to ensure, that the aircraft's instruments or the communication of the aircraft is not disturbed.

After the modifications of the CARIBIC container in 2009, the completely equipped container had to be tested in a test chamber in Ottobrunn (near Munich) for its electromagnetic compatibility (EMC). During the first test in December 2009, the threshold values were exceeded for some frequencies. Therefore, the instruments inside the container as well as the electromagnetic shielding of the container itself hat to be revised. Although the housing of the DOAS instrument is presumed to be electromagnetic compatible, tests with a electromagnetic detector showed a emission peak for 192 MHz. After all edges were sealed with electromagnetic shielding tape, and longer slits were replaced by a lattice, this peak largely disappeared. With similar modifications also in the other instruments, the container was successfully tested in February 2010.

6.5.2. Difficulties with the embedded computer

As mentioned in Sect. 6.2, the instrument is controlled by an embedded PC, namely a 'Lippert Cool LiteRunner-LX800'. The time keeping of the first such unit used elapsed faster than the real time. More precisely, the time elapsed in normal speed but jumps occurred. Those jumps also occurred without connecting the spectrograph to electronics of the spectrographs.

The reason for those jumps are still unclear, but they might have been caused by an interaction between the DOS clock and the real time clock (RTC). The DOS-clock is a timer used to generate the regular ticks, here referred to as 'tickcounts', counting the milliseconds starting with the booting of the computer. This clock has a high temporal resolution but usually a low accuracy (*Becker*, 1992). The RTC is an independent clock with a lower temporal resolution (typically one second). While the DOS clock is reset after a power interrupt, the RTC is powered by a battery when the system is not operating, and it should be more accurate than the DOS clock. While no clear regularity for those jumps was found for the first tests, in later tests, the jumps occurred when the tickcount time exceeded an integer multiple of 3 600 000, which is once per hour. The system time followed the DOS clock (tickcounts) for one hour, but then was changed, probably according to the RTC. However, the RTC elapsed in normal speed while the instrument was off.

In order to remedy that problem, the computer was send to the manufacturing company for repair – without success: While previously the computer had jumped by roughly 15 minutes each hour, the 'repaired' instrument jumped by several hours. Now, the company offered a new unit. With this, the jumps still occur, but 'only' by ~2 minutes. In order to avoid the risk of missing a flight because of further repairs or exchanges of the computer, and based on the experience of the previous 'repair', this unit has been kept until now, as the recorded times of the spectra can be corrected after flight (see Sect. 6.7.1).

A further problem occurred after switching power on: For the fraction of a millisecond, the power consumption of the computer increased so strongly, that the power supply of the instrument was not able to keep the voltage stable enough. As a result, the computer was not able to boot. This problem was compensated by installing a 3300 μF capacitor in the power supply line.

6.6. Data acquisition

Because the DOAS instrument has a low power consumption and because it can not be contaminated with boundary layer air (in contrast to some in-situ instruments), it is allowed to start the measurements as soon as the CARIBIC container is supplied with energy. After the boot process, the connection to the Master is built up and the measurement program is started. Furthermore, a batch file is started as 'watchdog':

Every two minutes, the logfile 'LogSpec.log' (see below) is checked for changes. If no change has happened, the measurement program is assumed to have crashed, and the computer is rebooted. Until May 2013, during all flights such a case only occurred once. However, it has to be mentioned, that the watchdog can only work if the operating system itself is working correctly.

As measurement program, 'MS-DOAS' is used, which has been developed by U. Frieß at the IUP Heidelberg, providing a scripting language for customizing the process. The routine is a endless loop between measuring, saving the spectra and temperature regulation. The three spectrographs record one spectrum each simultaneously, which takes about 8 seconds. Afterwards the spectra are saved on the memory chip, the temperature is regulated (Sect. 6.4.3) and two log files 'LogSpec.log' and 'LogPid.log' are written, containing information about the measurement mode (see below), spectrum number, time, average counts and temperature data.

There are two modes – a daylight mode and a night mode. For the retrieval of the trace gases, daylight is needed and therefore only the spectra of the daylight mode are usable. The night mode shall provide offset and dark current spectra. The program starts in the daylight mode. After each acquisition, the averaged count numbers of the spectra are checked. If that number is below a certain value for all spectrographs for three following spectra, the night mode is entered. Here, 10 offset and 10 dark current spectra are taken. Each offset spectrum contains 400 scans with an exposure time of only 20 ms, while a dark current spectrum contains one scan with an exposure time of 8 s. Afterwards the light is checked again based on the average counts. If at least one spectrograph has a higher value than the threshold value in at least five of the dark current spectra, the daylight mode is entered again.

In order to reduce the computational demand from the embedded computer and the number of spectra to be stored on the flash card, and in order to get synchronous spectra numbers between the three spectrographs, several single scans are added into one spectrum. While the total acquisition time for a spectrum is set to 8 s, the exposure time of a single scan and the number of scans in daylight mode are adapted to the light intensity for each spectrograph independently in order to get a spectrum with a good saturation degree. This is done after the storage of each spectrum $I^{\times}$. Oversaturated spectra have to be avoided (non linearity) as well as undersaturated spectra, which have a bad signal-to-noise ratio.

The average value of the counts, $I^{\times}_{\mathrm{avg}}$, emerged to be a good proxy for the saturation. The desired value for $I^{\times}_{\mathrm{avg}}$ varies with the shape of a typical spectrum which mainly depends on the measurement geometry and the instrument setup (wavelength range, sensitivity of the detector, optical filter). For the CARIBIC flights, roughly 17 000 is taken as setpoint value[4]. Based on $I^{\times}_{\mathrm{avg}}$ of the previous spectrum and the setpoint value, the new exposure time is calculated. In order to avoid a too frequent change

[4]In order to take the offset signal into account, this value slightly depends of the number of scans.

of the exposure time, a certain difference between the measured $I^{\times}_{\mathrm{avg}}$ and the setpoint value is allowed. The maximum exposure time provided by the instrument is 8 seconds. If the calculated exposure time is small enough, two or more scans are taken for one spectrum.

Due to the simultaneous measurements, the spectrum numbers of the three spectrographs are identical offering an easy comparison. In a few exceptions, the numbers between the spectrographs differed due to a power cut-off (e.g. after landing) while one spectrograph was still in acquisition while the others already were finished. The spectra are stored in the mfc file format, each having a size of about 8 kilobytes. During a set of four flights, roughly $3 \cdot 20\,000 = 60\,000$ spectra are taken which corresponds to 480 megabyte.

6.7. Data analysis

6.7.1. Times: DOAS, Master, CARIBIC, ARINC

Especially for temporally high resolved measurements, the accuracy of the time-stamp is important. Therefore the Master computer sends its own time (the so-called 'Master time') to each instrument every 10 seconds, and each instrument has to answer with its computer time. Furthermore, the Master receives the 'ARINC time' (cf. Sect. 5.3), which is supposed to be virtually correct, i.e. identical to UTC (Coordinated Universal Time).

Because normally the difference between the Master time and the ARINC time is below ten seconds, and because the ARINC data are not always available, the convention has been set up to use the Master time instead of the ARINC time as common reference time – the 'CARIBIC time'. Only for a few flights, the mismatch between the Master time and the ARINC time was too large to be ignored. Up to now, in all those cases, this mismatch was nearly constant during the flight. Therefore, the CARIBIC time series were created by shifting the Master time series by a constant offset to match the ARINC time: $t_{\mathrm{CARIBIC}} = t_{\mathrm{master}} + t_{\mathrm{offset}}$.

In the CARIBIC database, all the instrument's results shall contain the CARIBIC time. Especially for the case of the DOAS instrument, this correction is important because of the inaccurate clock of the DOAS computer, which performs time jumps once per hour (cf. Sect. 6.5.2). Figure 6.21 shows an example for flight 373. Delays in the logging of the communication with the Master computer lead to further temporal discrepancies in the order of several seconds, which make the time correction more difficult. However, combining the log file stored by the DOAS computer with that of the Master computer allows a correction with an accuracy of around 1 second. This is precise enough considering the typical integration time of 8 seconds for a spectrum and the accuracy of the CARIBIC time.

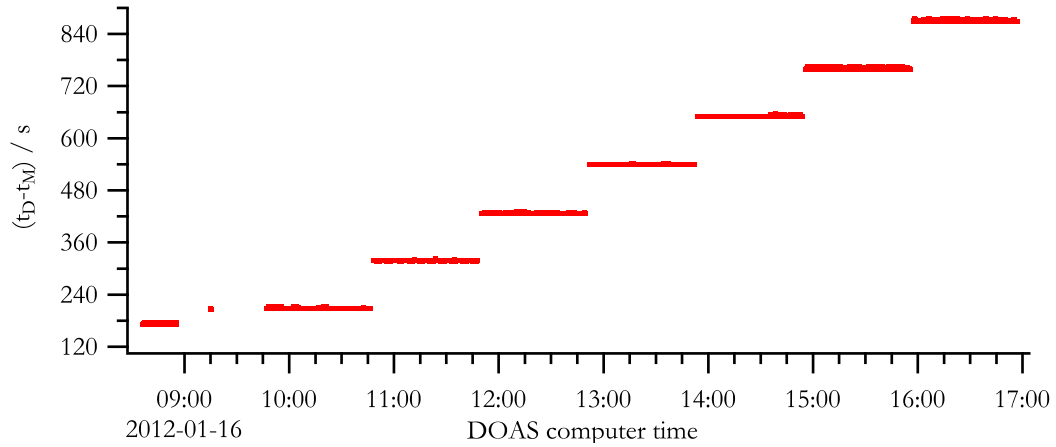

Figure 6.21.: Difference between the DOAS computer time and the CARIBIC time (here equal to the Master time) for flight 373, given in seconds. Once per hour, a jump of the DOAS computer time by nearly 2 minutes occurs. In case of power interrupt (here after 09:15), typically smaller jumps occur.

6.7.2. Correction for offset and dark current and straylight

As mentioned in Sect. 6.3.4 and Sect. 6.4.2, the measured digital spectrum $I^{\times}$ contains straylight and a structured offset and dark current signal, influencing $I^{\times}$ as described in Sect. 4.3.1, cf. (4.44) p. 62.

$$I^{\times} = I^{\times[\text{real}]} + I^{\times[\text{s}]} + I^{\times[\text{o}]} + I^{\times[\text{d}]} \tag{6.16}$$

In the DOAS retrieval, the straylight contribution $I^{\times[\text{S}]}$ is approximated by a second order offset polynomial (cf. Sect. 4.3.3).

For the correction of the offset and the dark current signal, spectra taken during the night mode (Sect. 6.6) are taken. Because the instrument has no shutter, it cannot be guaranteed that those spectra are completely dark. Alternatively, they could be taken within a dark laboratory between the flights. However, inflight measurements are preferred, because the time and the conditions (e.g. temperature) of their acquisition is closer to the time and conditions for the daylight measurements than it would be the case for spectra taken in the laboratory.

6.7.3. Reference and Ring spectrum, cross sections

For each spectrograph a daylight spectrum is taken as FRS (Sect. 4.2.6), usually with the same spectrum number (being observed at the same time and location) for each spectrograph. An indicators for a suitable spectrum is the degree of saturation – over-saturated spectra as well as spectra with too low light are avoided. Furthermore clouds are problematic due to different light paths caused by multiple scattering. For detecting such clouds, the movie of the pylon camera can help as well as the retrieved column of the oxygen dimer O_4 and the Ring signal. Also frequently changing scan numbers and

NO_2	*Vandaele et al.* (1996), 294 K
SO_2	*Bogumil et al.* (2003), 223 K or 243 K,
BrO	*Wilmouth et al.* (1999), 228 K
O_3	*Voigt et al.* (2001), 223 K
O_4	*Greenblatt et al.* (1990), 296 K
HCHO	*Meller and Moortgat* (2000), 298 K
HONO	*Stutz et al.* (2000), 298 K
OClO	*Kromminga et al.*, 233 K

Table 6.4.: Cross sections used in the DOAS analysis together with reference and temperature.

exposure are usually connected to changing cloudiness. For detecting striking features like peaks in NO_2 or SO_2 due to local emissions (cities or large industrial facilities), one FRS for a complete set of flight is often sufficient. However, to look closer to such an event, a spectrum rather close to the peak has to be taken at a similar flight altitude (pressure dependency of the wavelength calibration, cf. Sect. 6.3.3) and a similar temperature. Also the sun's position changes with time, leading to a different length of the light path and therefore to a changing stratospheric signal (Sect. 4.2). Furthermore the reference spectrum should be taken over a relative pristine area, otherwise negative values (e.g. of NO_2) are retrieved.

For the calculation of the Ring spectrum, the offset and dark current corrected reference spectrum and the standard Ring calculation routine of the DOASIS program is used. The obtained spectrum than is included in the DOAS fitting setup like a cross section.

The cross sections of the trace gases are taken from literature (cf. Table 6.4) after folding them with the instrument's slit function. Three different wavelength ranges ('fitting windows') were chosen to retrieve the species, one focused on SO_2 (311.6–327 nm), one for BrO (320–342 nm or 336–360 nm) and one for NO_2 (337.5–371 nm).

The fit result shown in Fig. 6.22 belongs to the SO_2 peak of flight 316 close to Norilsk, cf. Sect. 7.5. Figure 6.23 belongs to the BrO observation over Canada during flight 339, cf. Sect. 7.3.

6.7.4. Coadded spectra

By default, each daylight spectrum was evaluated separately. However, in order to improve the signal-to-noise ratio and therewith reducing the measurement error, in some cases, ten spectra were coadded. This leads to a lower temporal and spatial resolution along the flight track. For a typical ground speed of roughly 250 m/s and a exposure time of 8 seconds, the aircraft moves by 2 km, which increases to 20 km for 10 coadded scans.

Coadding spectra increases the risk of problems due to oversaturation. Already a sin-

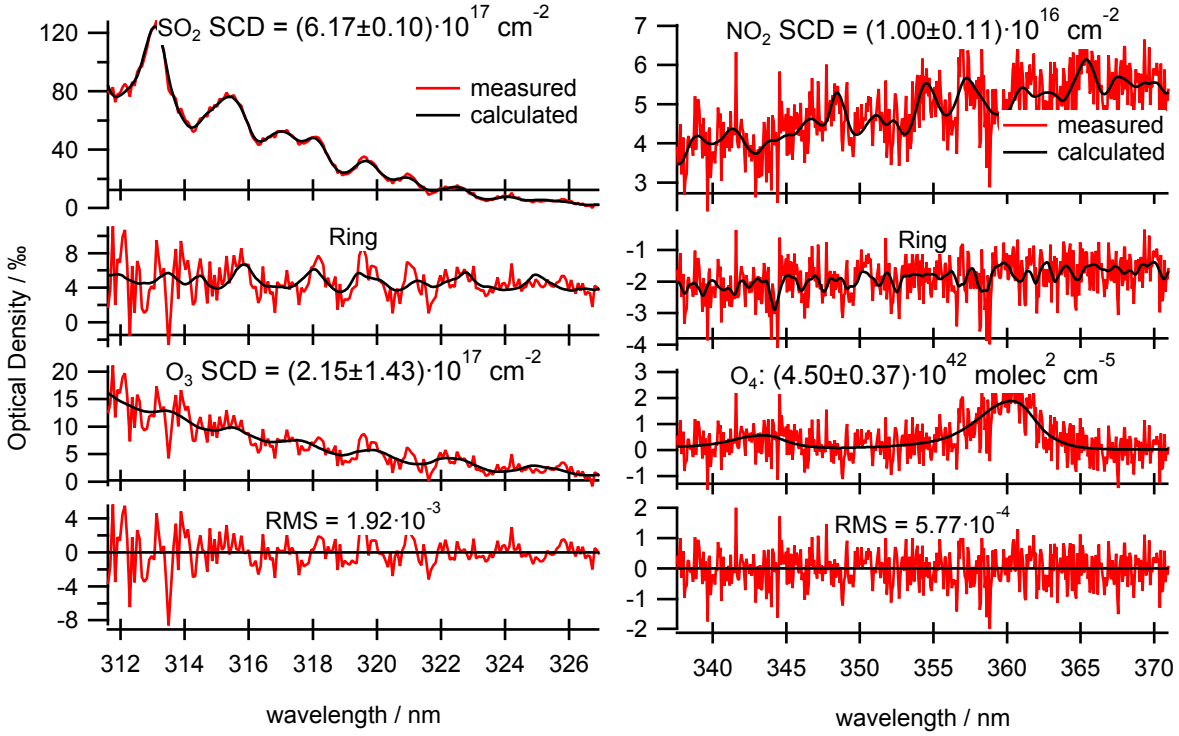

Figure 6.22.: Fit for the 'peak spectrum' of flight 316 on 2010-10-22. The fit result of the co-added spectrum taken between 07:15:06 and 07:16:26 UTC are depicted, cf. maximum SO_2 value in Fig. 7.22. Left: Fitting window for SO_2 retrieval (311.6–327 nm) Right: Fitting window for NO_2 retrieval (337.5–371 nm). From *Walter et al.* (2012)

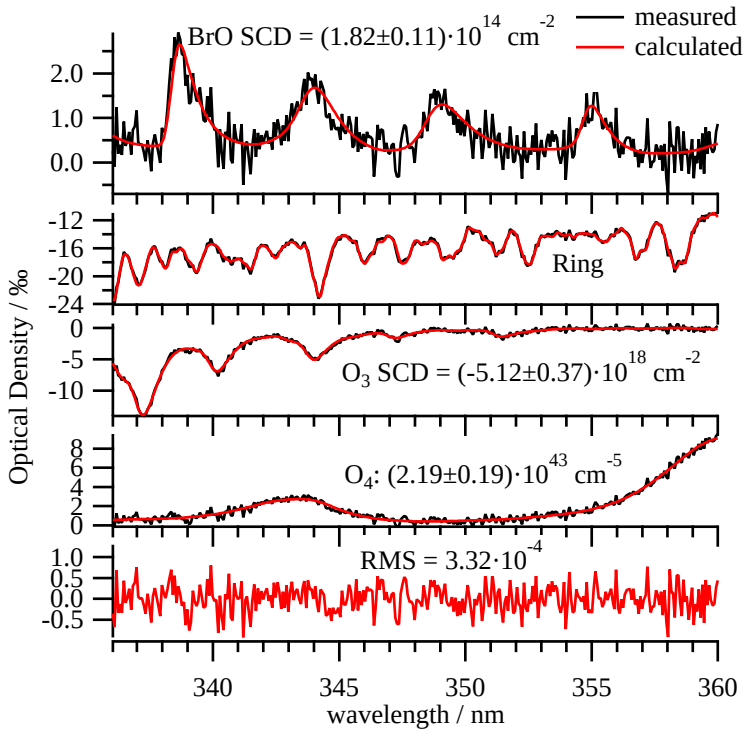

Figure 6.23.: Fit for the 'BrO peak spectrum' of flight 339 on 2011-04-19. The fit result of the co-added spectrum taken between 17:57:25 and 17:58:48 UTC is depicted, cf. maximum BrO value of Spectrograph C in Fig. 7.10. Fitting window: 336–360 nm

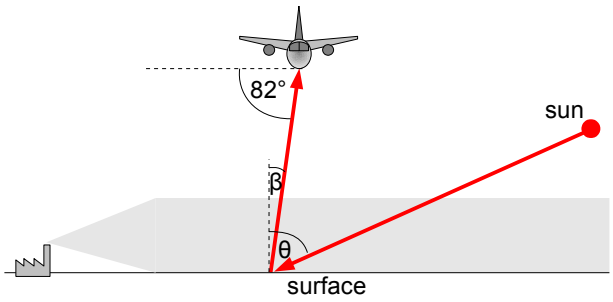

Figure 6.24.: Geometric light path for direct sunlight. The light passes through the plume twice. In relation to the plume's height, the light path is stretched by a factor $1/\cos\theta$ before and by $1/\cos\beta$ after the reflection at the ground.

gle oversaturated strongly affects the coadded spectrum. To avoid such problems, first each spectrum was evaluated independently. Then, only those spectra were considered for coadding having a RMS value below a certain threshold.

6.7.5. Geometric AMF for the nadir instrument

In Sect. 4.2.1, the geometric AMF for a direct light path from the sun to the instrument was given as $A_j = 1/\cos(\theta)$, cf. (4.17) p. 51 and Fig. 4.1a. The analogous geometric light path for the nadir instrument of CARIBIC is depicted in Fig. 6.24. Sunlight passes through the atmosphere until it reaches the ground, where it is reflected towards the telescope. Therefore the received light has passed the atmosphere twice, so the geometric AMF is the sum of both parts, namely

$$A = \frac{S}{V} = \frac{1}{\cos\theta} + \frac{1}{\cos\beta} \tag{6.17}$$

with $\beta = 90° - 82° = 8°$ for the nadir telescope (80° for the −10° telescope) and SZA θ. However, the longer the light is, the higher the fraction of scattered light is, therefore the geometric AMF is only a feasible approximation for small SZA and a cloud-free sky. Especially for the −10° instrument, the geometric approximation is not reasonable any more, because for a cruise altitude of ∼11 km, the slant distance between ground and telescope is over 60 km. The VCDs calculated in Sect. 7.5 and Sect. 7.6 for Norilsk and Paris use Box-AMF obtained by the McArtim radiative transfer model (Sect. 4.2.3).

6.8. Exchange of fibres between Spectrographs A and B

Usually the fibre bundles are always connected to the same spectrographs (therefor the fibres are label with three different colours): The green marked fibre with viewing direction +10° is connected to spectrograph A, the yellow one (−10°) to spectrograph B and the red one (−82°) to spectrograph C, cf. corresponding marks at the instrument, Fig. 6.5d p. 94. However, during flight 393 (cf. Fig. 7.4), the green and the yellow fibres

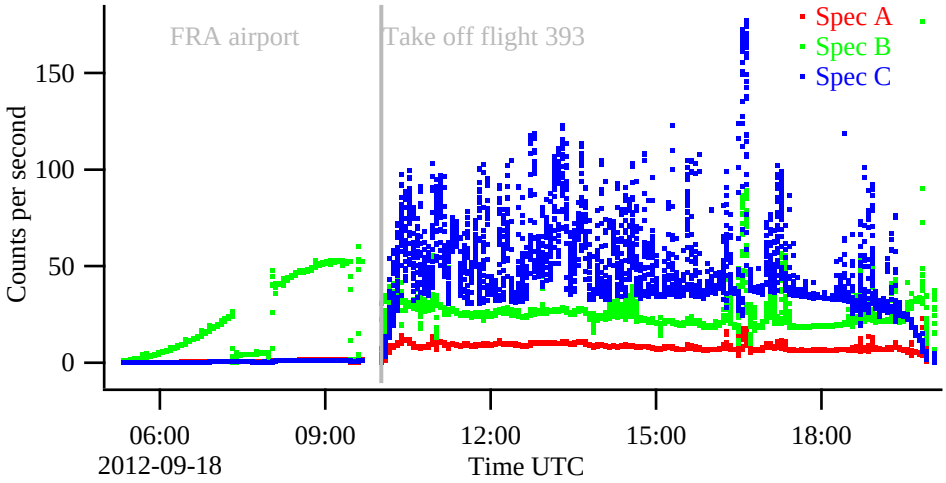

Figure 6.25.: Light intensity of the three spectrographs before and during flight 393. On the y-axes, the average count number per second is given (raw data without offset or dark current correction). The grey vertical line marks the take-off time of flight 393. Before that, the aircraft was at the Frankfurt airport.

were mixed up, leading spectrograph A to get light from −10° and spectrograph B from +10°. The suspicion for that mixing up arised when looking at the light intensity measured by the spectrographs at the airport. As usual, spectrograph C (−82°) got very little light reflected from the dark asphalt below the plane. But spectrograph B got much more light than spectrograph A, which is a clear indication, that B was connected with the upward looking telescope (+10°), while A was connected with the downward looking telescope – in mixed order compared to other flights. The intensities during flight 393 and at Frankfurt airport before the flight are depicted in Fig. 6.25. At the airport, the red and the blue curve belonging to spectrographs A and C nearly overlap each other, the light signal is close to zero. Spectrograph B gets a much stronger signal, increasing with the solar insolation. The break-in of the intensity between 7:20 and 8:02 UTC could be caused by a vehicle being parked close to the aircraft in the line of sight of Spectrograph B, which has been observed several times. Another indication for the mixing up of the fibres is the O_4 signal, when comparing with the SCD of the previous or the successive set of flights (389–392 or 397–400). Because the aircraft usually flies above clouds, the change in the length of the light path and therefore in the O_4 signal on average is smaller in the +10° direction than in the −10° direction. For flight 393, stronger variation was observed for spectrograph A, indicating that A was looking downwards.

The fact that the spectra were of comparable quality with respect to the received light and the residual structures in the DOAS fit shows that such an exchange is unproblematic with the currently installed fibres. This can be helpful for the case of a damage in one of the fibres or a spectrograph.

7. Measurements and Results

In Sect. 7.1, an overview over the performed flights are given. The next sections shows results from special mission flights to investigate the plume of the Eyjafjallajökull volcano during its eruption in 2010. The observation of bromine monoxide over northern Canada in April 2011 are presented in Sect. 7.3. As shown in Sect. 7.4, the plume of a power station was measured during the descent to Caracas airport. Sections 7.5 and 7.6 are focused on the retrieval of emissions based on flux measurements, here performed for the case of SO_2 from the Siberian nickel smelter of Norilsk and for the NO_2 emission from the city of Paris (France).

7.1. Flight Overview

In April and June 2010, the first flights after the renovation of the container, including the new DOAS instrument onboard, took place. These were special mission flights to investigate the plume of the Eyjafjallajökull volcano, see Sect. 7.2 or *Heue et al.* (2011) for more details.

Since June 2010, CARIBIC has been flying on a regular basis. In Appendix A, a table of these flights and a graphical overview are given. With some exceptions, one set of flight (SoF) was performed once per month. Each SoF consisted of four subsequent flights, except SoF 385 and SoF 387 with only two flights each, and SoF 389 with four flights but three of them without power supply for the container.

During the first of these flights (SoF 297–321), only two viewing directions were available, namely $-10°$ and $-82°$ ('nadir'), whereas the fibre bundle for the upward looking instrument ($+10°$) was broken, cf. Sect. 6.1.1. Measurements over South Korea and China during SoF 297 (June 2010) are shown in Sect. 7.1.1; the observation of the Siberian nickel smelter in October 2010 is presented in Sect. 7.5.

A maintainance period of the aircraft in Dezember 2010 offered the possibility to install new fibres. Therefore, all three viewing directions were available from January 2011 (SoF 326) to August 2011 (SoF 353). During SoF 333 (March 2011), the downwind of Paris was measured, cf. Sect. 7.6. Bromine monoxide was found one month later (April 2011, SoF 337) over Northern Canada, cf. Sect. 7.3. Formaldehyde and nitrous acid could be measured in August 2011 (SoF 353) due to the enhanced light path within a large convective cloud, cf. *Heue et al.* (2013). Afterwards, the fibre bundle for the $+10°$ was broken again. In November 2011 (SoF 365), several NO_2 sources were

observed in the Czech Republik, cf. Sect. 7.1.2.

During SoF 387 (May 2012), light was only received in the −10° direction. Fortunately, a maintainance check of the aircraft followed; again, all fibres were replaced. Up to now (May 2013), all viewing directions have been availble since that change. In August 2012 (SoF 389), the plume of a power plant was observed during descent to Caracas, cf. Sect. 7.4.

7.1.1. Flight over South Korea and China, Biomass Buring

The first regular flights (SoF 297) took place in June 2010, from Frankfurt to Caracas and back, than to Osaka (Japan) and back. During the last of these four flights, namely flight 300, several NO_2 enhancements were found in the first flight hours, cf. Fig. 7.1. Peak № 1 is observed directly after the start in Osaka in both directions, −10° and nadir (the fibre bundle of the +10° direction was broken). The higher signal in the −10° can be explained with the high sensitivity towards air masses in the flight altitude, which increased from ground level to ∼2 km between the start at 2010-06-24 01:47 and 01:52 UTC (end of peak № 1). The second peak was obsverved over the city of Okayama, which is surrounded by further large cities. SCDs of nearly $3 \cdot 10^{16}$ molec/cm^2 were measured (№ 3) with the nadir instrument when the aircraft flew rougly 20 km southwest of the center of Seoul, a megacity with over 10 million inhabitants and over 25 million people in the metropolitan area[1]. Actually, the nadir instrument targeted by 2.8 km towards the right (with respect to the flight route) and therefore closer to the city, because is tilted by 8° (Fig. 6.1 p. 88) and the aircraft turned left at that time with a roll-angle of ≈8°. At 03:52 UTC, the aircraft flew straight over Tianjin, a Chinese city with over 10 million people in its urban agglomeration[1], cf. № 4. Shortly afterwards, at 04:00, the flightroute passed the Chinese capital Beijing by ∼40 km to the east, cf. № 5.

While these findings are explained by the high emissions expected in such agglomerations, peak № 6 in NO_2 and SO_2 is surprising, because no larger city or industrial plant could be found in the near surrounding. In that month, there was a rather high biomass burning activity. In Fig. 7.1a, the orange dots show fire sources observed by the 'Fire Information for Resource Management System' (FIRMS)[2] during that day. The next fire activity depicted in that dataset is about 130 km northeast of the flightroute. HYSPLIT backward trajectories ending at the flight track (cf. Fig. 7.2) show that the wind actually came from that direction, however, it is difficult to explain such a narrow peak with sources of that large distance. Furthermore, a signal in the −10° would be expected in that case as well, which was not observed. On the other hand, the resolution and sensitivity of such satellite based firemappers are too low to resolve smaller fires. In contrast to that, clear fire activity is reported by the firemapper close to the flight route between Tianjin (№ 3) and Beijin (№ 4), cf. SO_2 enhancement observed between 03:40 and 03:55.

[1] Source: "www.wikipedia.org"

[2] webpage: "http://firms.modaps.eosdis.nasa.gov/firemap/"

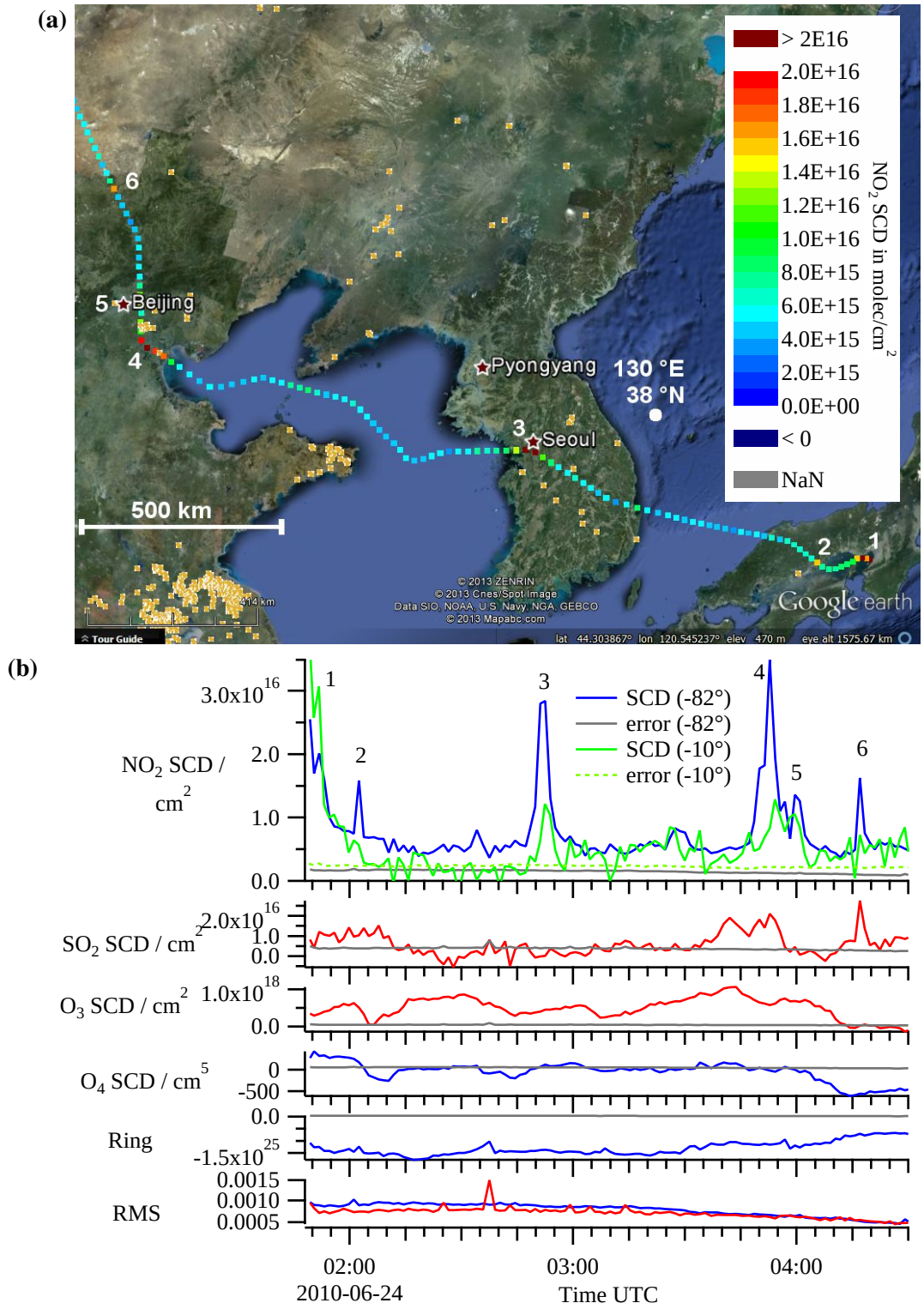

Figure 7.1.: First part of flight 300 from Osaka to Frankfurt on 24 June 2010 (**a**) flight route colour-couded with NO_2 (**b**) time series of NO_2, SO_2, O_3 and O_4, Ring and RMS. Except the green lines in the upper part, all traces belong to the nadir instrument. The red traces result from the fit window 311.6–327 nm, blue lines from 337.5–371 nm, the statistical fit errors are gray (or dashesd green line for the −10° direction).

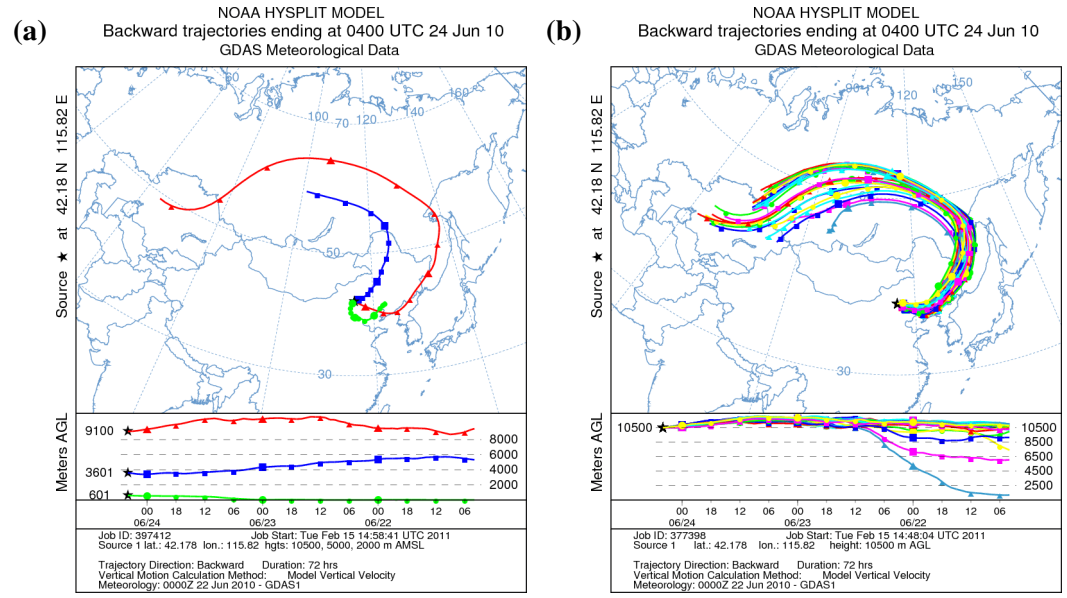

Figure 7.2.: HYSPLIT backward trajectories ending at the observation position of NO_2 peak № 5 (**a**) trajectories for three different altitudes (0.6 km, 3.6 km and 9.1 km a.g.l.) (**b**) ensemble run for 10.5 km altitude (flight alitude)

7.1.2. Flight over Czech Republic

Figure 7.3b shows a part of the route of flight 365 from Frankfurt to Chennai (India) on 15 November 2011, colour-coded by the NO_2 SCD, cf. corresponding time series in Fig. 7.3a. The large NO_2 enhancement at the begin of the flight (№ 1, 2) in both directions ($-10°$ and $-82°$; the $+10°$ fibre bundle was broken) was observed during ascend from Frankfurt. The dip between № 1 and 2 is probably an artefact, cf. enhancement in the error and the RMS. At 10:17 UTC, the city of Prague (Czech Republic) was overflown, just ∼4 km to the south of the centre of the city, cf. large NO_2 peak № 3 of the nadir instrument. As expected, no signifcant enhancement was observed in the other viewing direction. Only 5 minutes later, at 10:22, a peak (№ 4) is observed in the nadir instrument, accompanied by a SO_2 spike. At that time, the aicraft flew directly over the 'Chvaletice Power Station', a coal-fired power plant with a total installed power output of 800 MW near the city of Chvaletice.[3]

A further large peak (№ 5) in the nadir NO_2 was observed at 10:37, together with small enhancements in the nadir SO_2 and in the $-10°$ NO_2. In that case, Ostrava was overflown, a city with over 300 000 inhabitants and more than 1 million people in its larger urban zone.[1]. According to *Zdeňka et al.* (2013), this region is the most air-polluted in the country: "Industrial sources, emissions from road vehicles and local heating are the main causes of degraded air quality". One of the main industrial polluters mentioned in that study are the steel facilities of 'ArcelorMittal Ostrava a.s.' (formerly

[3]Source: "http://www.cez.cz/en/power-plants-and-environment/coal-fired-power-plants/cr/chvaletice.html", accessed on 2013-05-24.

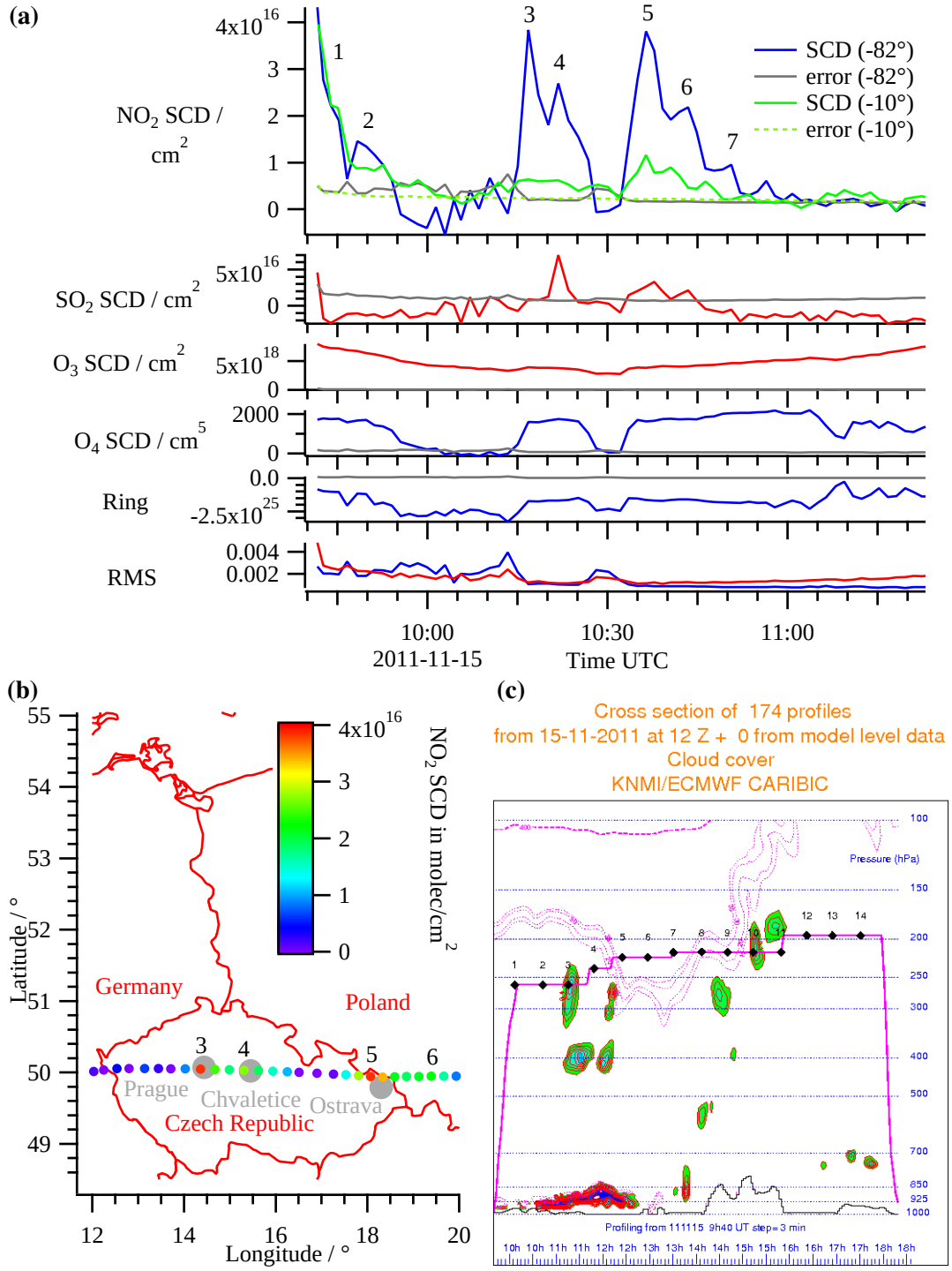

Figure 7.3.: First part of flight 365 Frankfurt to Chennai on 15 November 2011 (**a**) time series of NO_2, SO_2, O_3 and O_4, Ring and RMS. Except the green lines in the upper part, all traces belong to the nadir instrument. The red traces result from the fit window 311.6–327 nm, blue lines from 337.5–371 nm, the statistical fit errors are gray (or dashesd green line for the −10° direction). (**b**) flight route colour-couded with NO_2 (**c**) cloud coverage during flight 365 (from P. van Velthoven, "http://www.knmi.nl/samenw/campaign_support/CARIBIC/151111a/tsecCC11111512.gif", accessed on 2013-05-24)

known as 'Nova Hut', "http://www.arcelormittal.com/ostrava/index_en.html").

No obvious candidates for the smaller peaks № 6 and 7 (over Poland) have been found. While № 6, was surrounded by several towns of medium size, № 7 was recorded over a rather rural area.

However, also the events № 1–5 have to be treated with care, because there is a strong correlation with the oxygen dimer O_4 (Fig. 7.3a). In № 3 the NO_2 peak coincides with an increase of O_4, the same applies for № 5. Figure 7.3c shows a vertical profile of the cloud coverage along the flight route (the pink line depicts the flight altitude, given in terms of pressure), calculated by P. van Velthoven with the KNMI TRAJKS model based on ECMWF data. Especially after 10:32 UTC, a thick cloud cover close to ground is calculated. Also before, smaller clouds are indicated, especially above areas with low surface altitude (black line). Also the record of the video camera of the CARIBIC pylon shows a thick cover of deep clouds between 10:14 and 10:26 and after 10:32, in good agreement with the O_4 data. Because the albedo of clouds is higher than the albedo of the ground, the fraction of reflected light is higher (in relation to the light scattered in higher altitudes). Therefore the average light path over clouded areas is longer than over the 'dark ground', if the clouds are close to the ground.[4] Multiple scattering inside the cloud enhances the light path further and increases the sensitivity for O_4 and other gases (here NO_2, SO_2). Therefore, also the NO_2 observations are a result of both, enhanced lightpaths (from 10:14 to 10:27 and after 10:32) and local emission sources.

7.2. Eruption of Eyjafjallajökull

In the following, CARIBIC DOAS measurements of the plume of the Eyjafjallajökull volcano after its eruption in 2010 is described. An overview over the measurements performed by the CARIBIC container is given by *Rauthe-Schöch et al.* (2012). A more detailed analysis of the DOAS measurements is given by *Heue et al.* (2011).

Eyjafjallajökull (in literature also denoted as 'Eyjafjalla' or 'Eyjafjöll') is a volcano with a height of 1 666 m a.s.l. in the southern part of Iceland (coordinates: 19.63° W, 63.63° N), covered by an ice cap. Four comparatively small eruptions of Eyjafjallajökull took place in the last 1500 years before 2010. The last eruption was in 1821 and lasted for more than one year (*Gudmundsson et al.*, 2010). Enhanced activity of the volcano has been observed since nearly 20 years, like earthquakes in 1994, 1999, 2009 and 2010. Therefore, a forewarn system was installed for protecting the surrounding population. On 20 March 2010, a small eruption began but with negligible ash production (*Petersen*, 2010).

However, the strong eruptions started in the middle of April. The ongoing eruption ceased on 12 April, but two days later explosive eruptions started. According to *Gud-*

[4] In case of high clouds (still below the aircraft), the opposite is usually the case, because than, the light path of the reflected light is shorter.

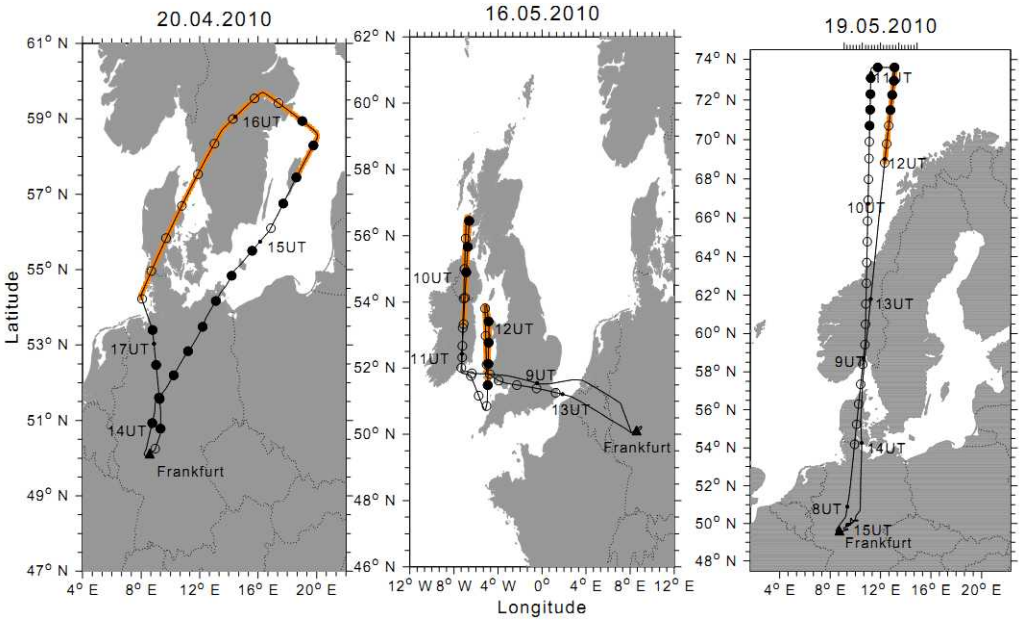

Figure 7.4.: Eyjafjallajökull flight routes of CARIBIC on 20 April (left), 16 May (middle) and 19 May (right). The orange part of the route corresponds to airsamples indicating volcanic origin. (From *Rauthe-Schöch et al.*, 2012)

mundsson et al. (2010), the Icelandic Meteorological Office (IMO) was alerted by the seismic system at 23:00 UTC on 13 April 2010; a few hours later, a visible eruption plume was observed. In the following days, large amounts of fine-grained silicic ash were emitted into the atmosphere. Due to northwesterly winds over Iceland, the plume was transported southeastwards. The ice cap of the volcano was melted by the magma, leading to explosive eruptions, mainly from 14 to 17 April where the plume reached a height of 9.5 km (14 April), than decreasing to 5–7 km. The production of ash and tephra in the most explosive phase is estimated to be around 750 tons per second (*Petersen*, 2010).

Volcanic ash can damage the aircraft's engines, cf. *Casadevall* (1993), *Prata and Tupper* (2009). In contrast to desert dust, the melting point of volcanic ash is lower, leading to a stronger danger of glazing. Although the volcanic hazards on aviation are increasingly discussed since the 1980s, up to now, there is no satisfying knowledge about the critical amount of ash being dangerous for aircrafts, because the risk depends on several factors like the size distribution and the composition of the volcanic ash, the exposure time of the aircraft and the construction of the engines. Furthermore, such parameters are not well-known for the large diversity of volcanic eruptions. Numerical models help to estimate the dispersion of the plume, but the source term (the amount, composition and size distribution of the emission) is a major uncertainty factor.

However, the aviation authorities had to make concrete decision for guaranteeing safety. On the evening of 14 April, Scottish and Norwegian airspace was restricted

(*Budd et al.*, 2011). With the spread of the plume south and east, the restricted areas was expanded over Ireland, the Netherlands, Belgium and Sweden and further European countries (e.g. Germany between 16 and 21 April).[5] This resulted in the cancellation of more than 100 000 flights, affecting about 10 million passengers, causing costs in the billions (*Budd et al.*, 2011). While the major shutdown over northern Europe was from 15 to 23 April, several shorter and more regional flight restrictions were made until the middle of May. A concentration of 0.2 milligrams of ash per cubic meter was taken as a threshold value below which aircraft may fly without special attention, while flights in areas with concentrations higher than 2 mg/m^3 had to be avoided (*Schumann et al.*, 2011). Estimates of the concentration were mainly based on the dispersion model of the Volcanic Ash Advisory Center (VAAC), London.

The eruption was observed based on a large variety of measurement techniques like seismic monitoring, GPS monitoring, weather radar, web cameras, ozone soundings etc. Within the ceilometer network of the German Meteorological Service (DWD), Lidar ceilometers were used for detecting the aerosol and obtaining the plume height. The DWD also performed in-situ measurements of aerosols and gases (e.g. SO_2) at the Global Atmospheric Watch (GAW) stations at Zugspitze and Hohenpeissenberg (Germany), cf. *Flentje et al.* (2010). Satellite instruments offered a global view on the plume. Furthermore, measurements with research aircraft took place, among them 17 flights by the Falcon aircraft of the German Aerospace Center (DLR), cf. *Schumann et al.* (2011).

Due to the aforementioned airspace closure, also the regular flights of the CARIBIC aircraft were cancelled. Therefore the aircraft was available for performing three special mission flights without passengers on board, equipped with the CARIBIC container, just after its retrofitting with new instruments.

The first flight started on 20 April 2010 at 13:47 UTC, taking off at Frankfurt Airport, flying over Denmark and Sweden, landing in Frankfurt at 17:33 UTC. The flight route is shown in Fig. 7.4. The presence of volcanic ash particles was indicated by the collected air samples and the change in the elemental composition, retrieved from the aerosol impacter samples. Also enhanced particle concentrations by the OPC were found. As mentioned in Sect. 2.3.7, volcanoes typically emit SO_2, which in some cases can be used as indicator for imminent eruptions. However, in the case of the 2010 Eyjafjallajökull eruptions, larger SO_2 emissions were mainly observed after 19 April 2010. Accordingly, in the area probed by CARIBIC on 20 April (more than 1 500 km away from the eruption), no clear SO_2 signal could be found by the DOAS instrument. Figure 7.5 shows the time series for that flight. Enhanced SO_2 values can be observed around 15:15 UTC, however this enhancement is close to the detection limit and the obtained SCD depend

[5] Source: Wikipedia article 'Air travel disruption after the 2010 Eyjafjallajökull eruption', "http://en.wikipedia.org/w/index.php?title=Air_travel_disruption_after_the_2010_Eyjafjallaj%C3%B6kull_eruption&oldid=501852245", accessed on 2010-12-28.

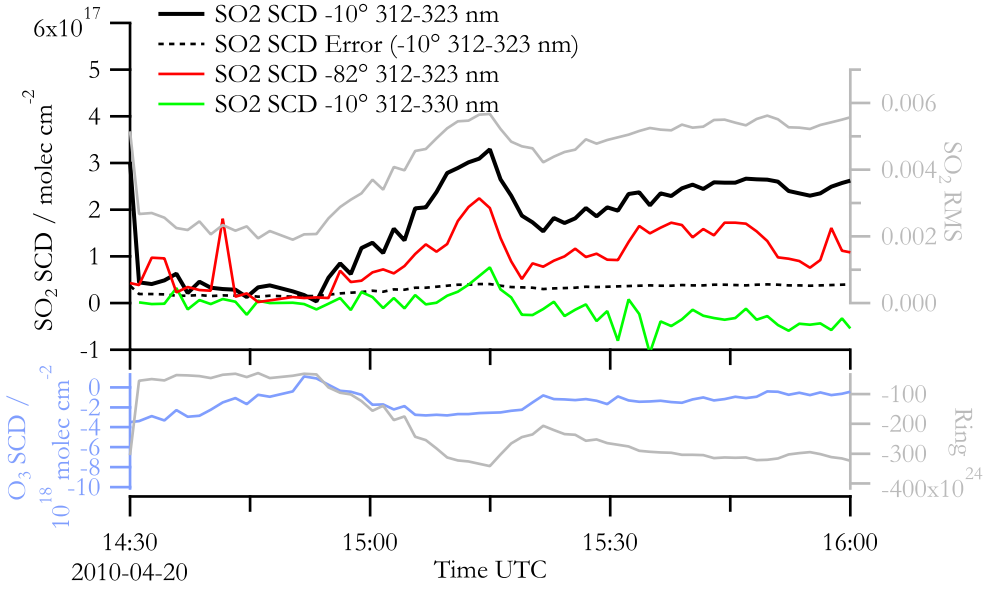

Figure 7.5.: Section of the time series for volcano flight F294 on 20 April 2012. The thick black line (top left axis) depicts the retrieved SO_2 SCD for the fitting window 312–323 nm for the 10° downward looking instrument. The dashed line shows the corresponding statistical retrieval error, the grey line (top right axis) contains the RMS. Furthermore, the SO_2 SCD for a different fitting window is shown (312–330 nm, green line) as well as the SCD of the nadir instrument (red line). In the lower part, the O_3 SCD and the Ring effect are depicted ($-10°$ direction).

too much on the retrieval settings (wavelength range etc.) to clearly indicate the volcanic plume: For the fitting window 312–323 nm, the plume seems to be clearly above the detection limit (black line in Fig. 7.5), but for 312–330 nm the peak nearly disappears. Also other observations showed only low amounts of SO_2 in this early stage of the eruption, e.g. *Thomas and Prata* (2011).

The volcanic eruptions continued with adherent temporally air traffic disturbances. Therefore, a second flight took place on Sunday, 16 May 2010, taking off at 08:08 UTC and landing at 13:49 UTC, cf. Fig. 7.4. Based on the forecasts (cf. Fig. 7.6), provided by the British Met Office), the flight route was chosen with the aim for probing the volcanic plume, without getting to deep into the ash cloud in order to avoid damages of the aircraft. Therefore the aircraft flew over Ireland and made a U-turn in the east of Scotland; later it flew a second time northwards between Ireland and England, than back to Frankfurt.

Figure 7.7 shows the time series of the SO_2 and BrO measured by the DOAS instruments for the directions $-10°$ and $-82°$. Furthermore, the particle number concentrations measured by the CPC (Condensation Particle Counter, Sect. 5.2.2) are depicted. In the SO_2 time series of the nadir and the 10° downward looking instrument, three peaks can be seen at around 10:10, 10:20 and 12:00 UTC, with peak SCDs of $5.1 \cdot 10^{17}$, $7.3 \cdot 10^{17}$ and $1.1 \cdot 10^{17}$ molec/cm^2 for the nadir instrument and $3.0 \cdot 10^{17}$, $9.2 \cdot 10^{17}$

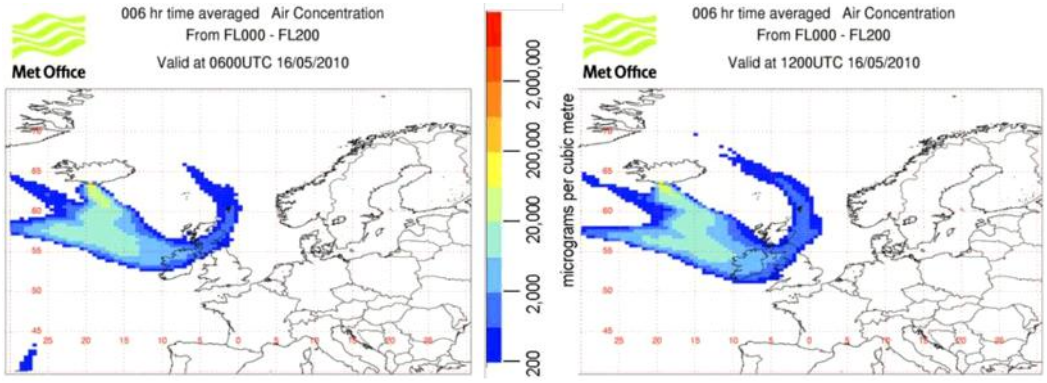

Figure 7.6.: Forecast for the dispersion of the Eyjafjallajökull's ash plume on 16 May 2010, 06:00 UTC (left) and 12:00 UTC (right), provided by the British Met Office ("http://www.metoffice.gov.uk/"). (From *Heue et al.*, 2011)

and $2.5 \cdot 10^{17}$ molec/cm^2 for the $-10°$ direction. As depicted in Fig. 7.8, the first two peaks were found shorty before and after the U-turn, while the third one was observed between Ireland and England, close to the Isle of Man. While in the nadir direction, both maxima in the north of Ireland have similar height, the second maxima is clearly stronger than the first one in the 10° downward direction. This can indicate that the aircraft flies above the plume before the U-turn. In that case, the $-10°$ instrument 'looks over the plume' and therefore is not very sensitive to it, while the nadir instrument looks through the plume. After the U-turn, the aircraft flies at a lower altitude than before (cf. top part of Fig. 7.7).[6] Now, the large maximum at 10:20 is measured in both spectrographs, an indication for the aircraft to be inside the plume. This coincides with enhanced particle number concentrations measured by the CPC, although that maximum is observed slightly before the SO_2 maximum. However, the CPC data also show two spikes before and during the first SO_2 peak around 10:00. Apparently in contradiction to the abovementioned assumption this could be an indication that the aircraft was already inside the plume. It can also be, that these spikes belong to a small streak of the plume reaching higher or to remains of an older plume (cf. *Heue et al.*, 2011). It also has to be considered, that high particle concentrations in general not directly concur with high SO_2 concentrations because of changes in the composition of the volcano's output and the separation during the transport. The third SO_2 maximum between Ireland and England is mainly observed in the $-10°$ direction. A comparison with satellite data show that it probably belongs to the edge of a plume reaching further north. See *Heue et al.* (2011) for a more detailed analysis of the DOAS results, including comparisons with satellite data.

A third volcanic flight took place on 19 May 2010. Unfortunately, a bug in the acquisition routine caused an error which stopped the measurement program; therefore no DOAS data are available for this flight 296.

[6] According to the ARINC data, the altitude was 7.6 km a.s.l. before the U-turn and 4.6 km a.s.l. afterwards.

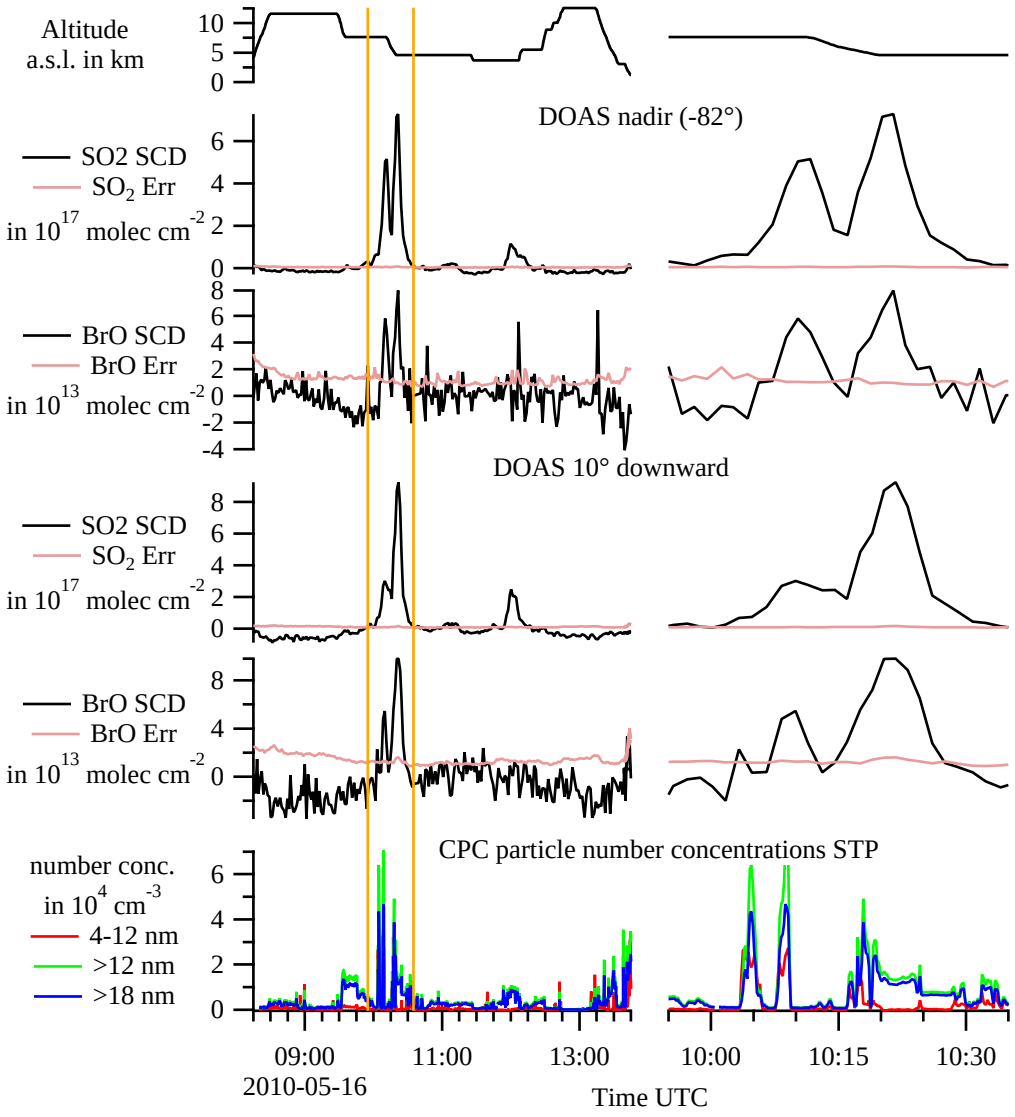

Figure 7.7.: Time series for the second Eyjafjallajökull flight on 16 May 2010. The right part is a section of the left part for the time interval from 9:55 to 10:35, in which the maxima in the north of Ireland were found. On top, the aircraft's altitude is depicted. Below, the SCD of SO_2 and BrO are shown for both viewing directions. Ten spectra were coadded for the retrieval. The lowermost graph contains particle number concentrations (normalized to standard pressure) measured by the Condensation Particle Counter onboard the CARIBIC container.

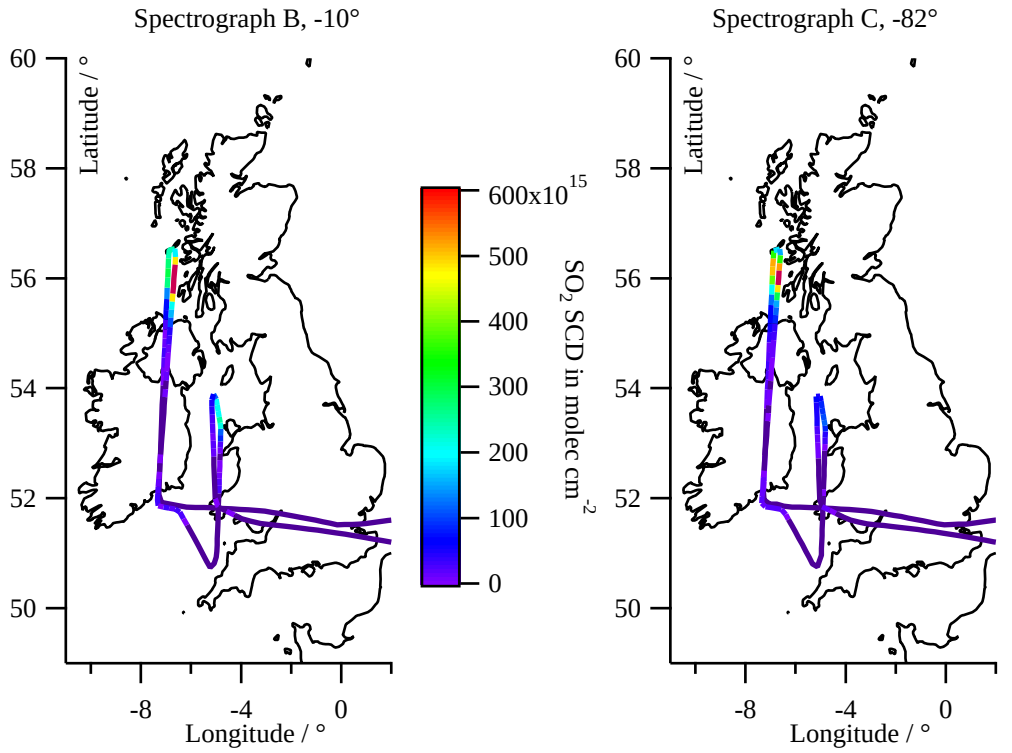

Figure 7.8.: Flight route of 16 May 2012 color-coded with the SCD of SO_2 measured by the 10° downward looking instrument (left) and the nadir instrument (right).

7.3. Bromine Oxide over Canada in April 2011

In April 2011, flights 337 to 340 were performed to Caracas and to Vancouver. The third of them, flight 339, took place on 19 April, starting at 12:09 UTC in Frankfurt and landing at 21:44 UTC in Vancouver (Canada). On the way, Greenland and the northern part of Canada was crossed, cf. Fig. 7.9. There, BrO was found by the CARIBIC instrument. In Sect. 7.3.2, the CARIBIC data are compared with VCDs from GOME-2, which were evaluated by H. Sihler.

7.3.1. CARIBIC Observation

Figure 7.10a shows the time series of BrO for the three spectrographs and the solar zenith angle (SZA). These are SCDs relative to the FRS taken at 16:52 UTC (blue vertical line). A wavelength range of 336–360 nm was used like it was taken by *Sihler et al.* (2012) for the analysis of GOME-2 spectra.

Amongst some smaller enhancements close to the detection limit, BrO was detected shortly before flying over Greenland, and a stronger BrO-Peak was observed between 17:30 and 18:15 UTC, cf. Fig. 7.10. In both cases, BrO was found by all spectrographs, with the strongest enhancement in the nadir direction and the weakest in the 10° upward direction.

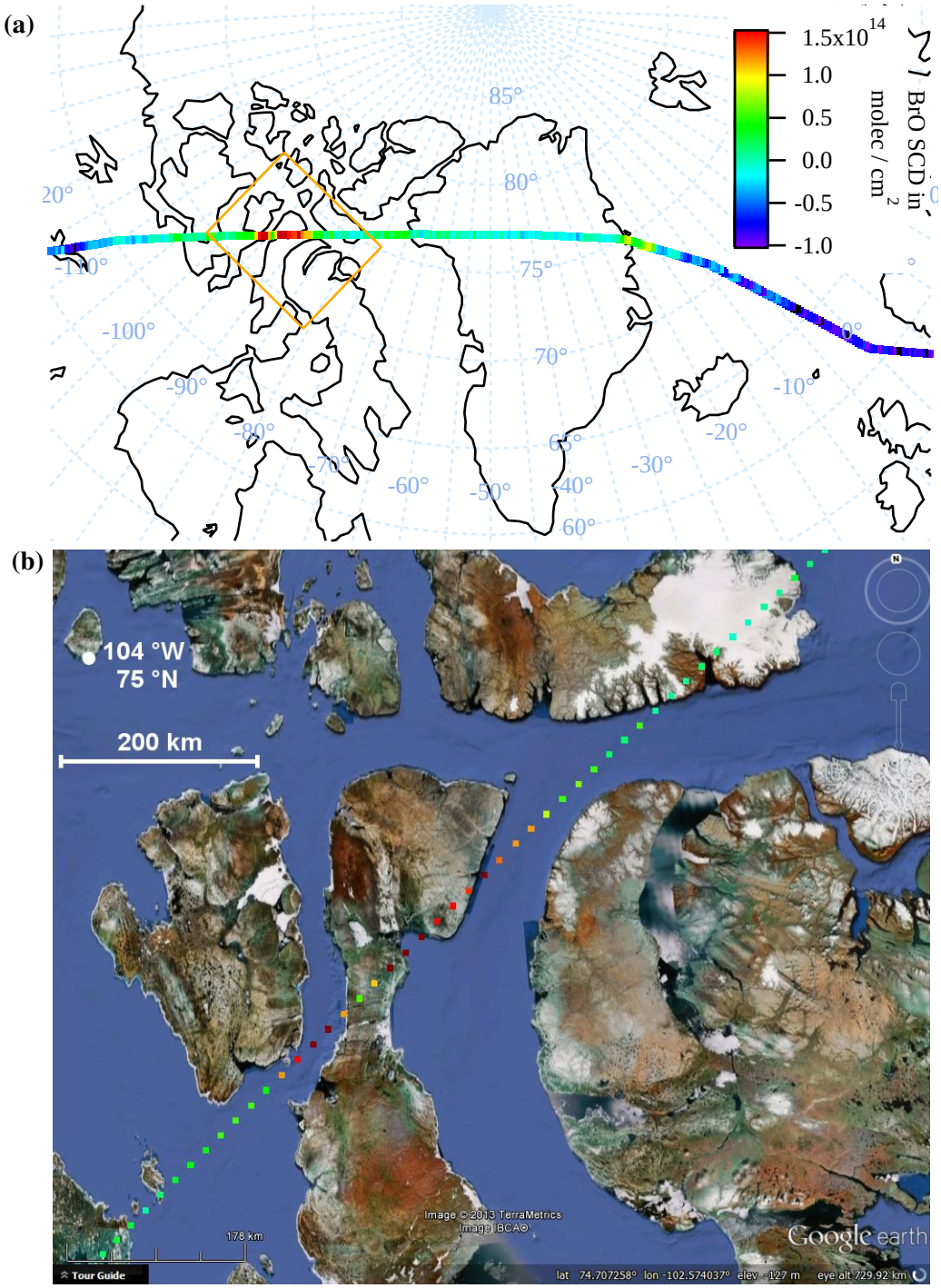

Figure 7.9.: Section of flight 339 from Frankfurt to Vancouver on 19 April 2011, flight route colour-coded with the SCD of bromine oxide. Part (b) is a section of (a), indicated by the orange rectangle over northern Canada.

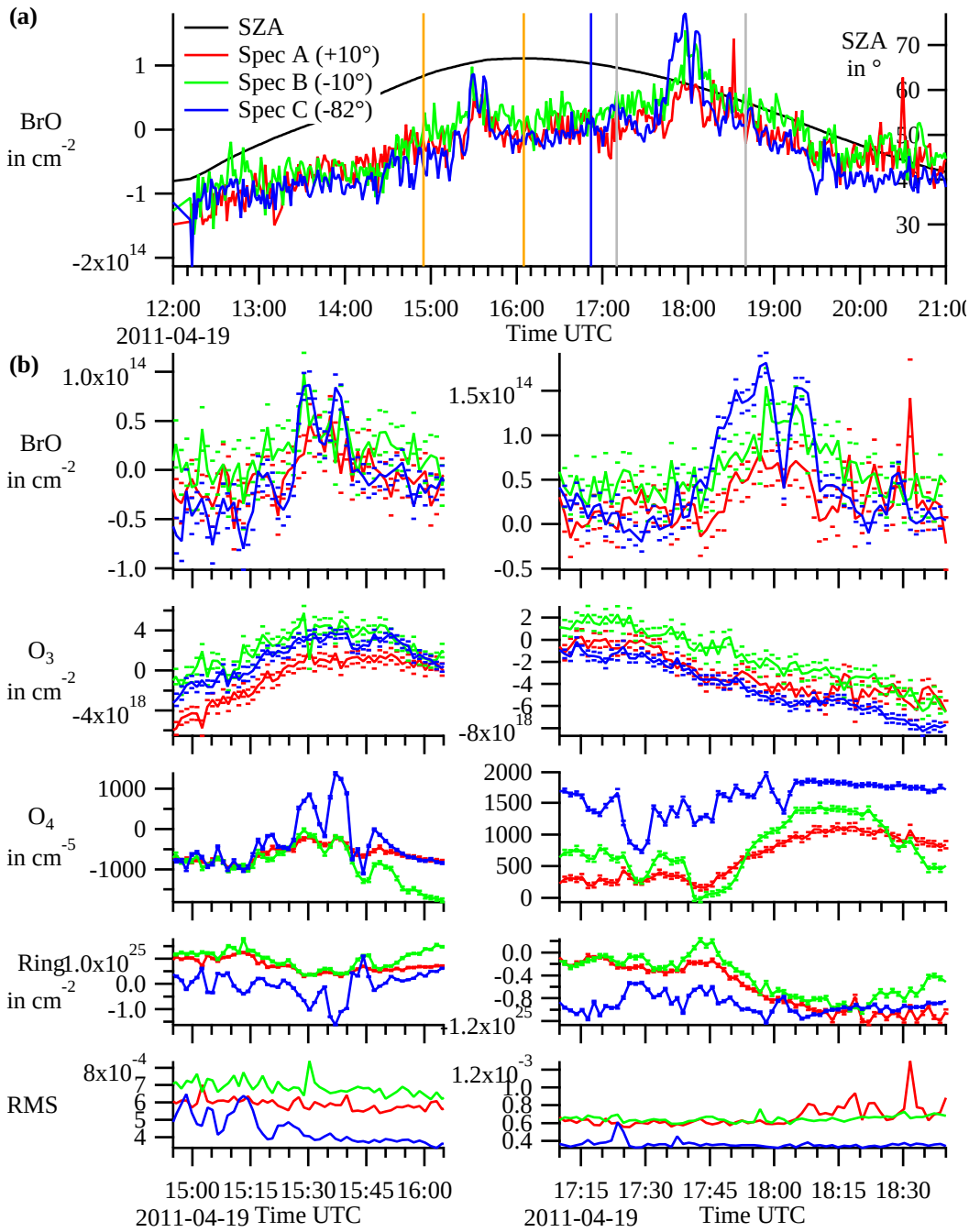

Figure 7.10.: Time series for Flight 339 from Frankfurt to Vancouver on 19 April 2011. The graphs in (b) belong to the time intervals of the BrO observations, which are indicated by the orange and grey vertical lines in (a).

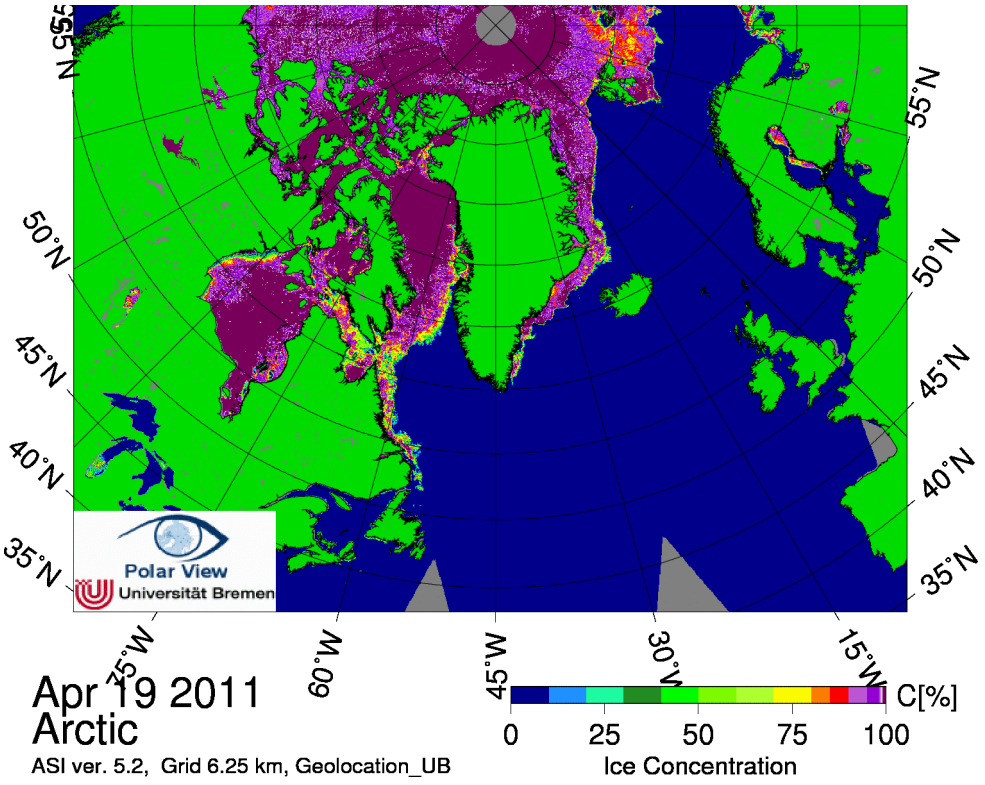

Figure 7.11.: Arctic Sea Ice Coverage on 19 April 2011 from AMSR-E data. (From 'Polar View', Universität Bremen, "http://iup.physik.uni-bremen.de:8084/amsr/amsre.html", direct link "http://www.iup.uni-bremen.de/seaice/amsredata/asi_daygrid_swath/l1a/n6250/2011/apr/asi-n6250-20110419-v5_nic.png", accessed on 2013-03-26)

The double peak around 15:30 UTC (left side of Fig. 7.10) has to be treated with caution, because a clear correlation of BrO with the oxygen dimer O_4 is observed, which also shows a strong double peak. This change in the O_4 signal, especially in the nadir direction (blue line), denotes an enhanced light path. Such an enhancement can be caused by a change in the surface albedo or a cloud. Also the Ring signal shows enhanced variations in that time interval. Indeed, the video camera included in the CARIBIC pylon showed a partial cloud coverage in that region (although the pictures were already overexposed and therefore not very conclusive). The BrO peak is not expected to be an artefact based on a cross correlation with O_4, because the shapes of the BrO and the O_4 cross sections are clearly distinct. Also cross correlations with other trace gases like ozone, OClO or HCHO are improbable, because the BrO peak remains when changing the wavelength interval of the DOAS retrieval. Therefore the BrO signal is believed to be real, but it can not be clearly discerned whether this signal is only caused by longer light path through the BrO containing atmosphere or by locally enhanced BrO concentrations.

The even stronger BrO signal around 18:00 UTC (right side of Fig. 7.10) also consists of a double peak particularly in the nadir instrument – a first one at 17:58 with a SCD

of $1.8 \cdot 10^{14}$ molec/cm^2 (cf. Fig. 6.23 p. 122) and a second one at 18:06 with about $1.5 \cdot 10^{14}$ molec/cm^2 (nadir instrument). In between the SCD decreases to about $0.4 \cdot 10^{14}$ molec/cm^2 at 18:02. The statistical error value of about $1.5 \cdot 10^{13}$ molec/cm^2 given by the WinDOAS program underestimates the total error: The results from the usage of other wavelength ranges vary on the order of 30 %, e.g. $2.4 \cdot 10^{14}$ molec/cm^2 are obtained at a fitting window of 324–354 nm as used by *Heue et al.* (2011) for detecting BrO in the Eyjafjallajökull plume, cf. Sect. 7.2.

Also for this double peak over northern Canada, the O_4 signal shows clear variations, but less than in the aforementioned case before Greenland; also the correlation between the BrO and and the O_4 signal is rather low (except the dip at 18:02), cf. right side of Fig. 7.10. Therefore, here a clearly enhanced abundance of BrO can be concluded from the nadir observation. As depicted in Fig. 7.9b, the BrO dip at 18:02 UTC occurred while flying over land whereas the peaks directly before and afterwards were over the sea. This dip correlates with a decrease of the O_4 SCD. Like mentioned above, clouds in that region or a change in the surface albedo can be one explanation for this decrease of both signals. Unfortunately, the pictures of the video camera where overexposed (everything below the aircraft was virtually homogeneously white with a blue sky above) due to the bright surface, so neither clouds nor land masses could be seen therein.

The most supposable reasons for this BrO observation are stratospheric BrO or a bromine explosion as mentioned in Sect. 2.3.5. In general, high BrO concentrations are found in the stratosphere. Due to a tropopause fold or a tropospheric deep pressure system, the stratospheric BrO column could increase. However, in that case, it is hard to explain why this enhancement is mainly observed in the nadir instrument: According to typical vertical BrO profiles found in literature (e.g. *Pundt et al.* (2002)), the highest BrO concentrations are found above 15 km altitude, the maximum mixing ratio further above, much higher than the flight altitude of 11 km. Therefore, an extension of this layer should be even more pronounced in the $+10°$ and $-10°$ direction than in the nadir direction.

The other explanation, a BrO activation ('bromine explosion') in the arctic spring, fits much better to the observations: The fact that the strongest BrO signal has been observed by the nadir instrument suggests that the BrO was located close to the ground, where the nadir instrument has a significantly higher sensitivity than the other directions. For the case of the $-10°$ direction, the distance between the ground and the DOAS telescope would be ∼60 km in a geometrical light path[7], so a large fraction of the light received by the $-10°$ instrument has been scattered in the higher troposphere and the lowermost stratosphere. The 10° upward looking instrument would not be sensitive to BrO below the flight altitude at all if it would merely get light having been scattered only once. But due to the high surface albedo close to 1 (the surrounding area was covered by sea-ice and snow, cf. Fig. 7.11), a considerably fraction of the light

[7]Light from the sun to the ground and than into the telescope without any scattering

has reached the ground before being scattered into the viewing direction of the upward looking telescope.

7.3.2. Satellite Observation

GOME-2 ('Second Global Ozone Monitoring Experiment') is a nadir scanning spectrometer aboard the 'Meteorological Operational satellite' MetOp-A, which was launched in 2006. The satellite has a sun-synchronous polar orbit at 800 km altitude and crosses the equator at 09:30 local time. The GOME-2 instrument contains four channels for covering the wavelength range from 240 to 790 nm with a ground-pixel size of $\sim 80 \times 40\,\mathrm{km}^2$, cf. *Callies et al.* (2004), *Munro et al.* (2006).

For both BrO findings, there is a good temporal concurrence between the overpass times of CARIBIC and the GOME-2. In first case, CARIBIC crossed the northeastern coast of Greenland around 15:30 UTC, just 15 minutes after GOME-2 (15:14). In the second case, CARIBIC found BrO over Canada at 18:00, about half an hour before GOME-2. The GOME-2 VCDs are depicted in Fig. 7.12a and Fig. 7.13; the black line shows the CARIBIC flight route, which is also depicted in Fig. 7.12b for comparison.

The shapes of both measurements agree well with each other. Both instruments observe an increase on the eastern cost of Greenland, lower amounts over the middle of Greenland, afterwards an increase again of the sea and the strong Peak over Canada (roughly 95° W, 73° N). The absolute amounts can not be directly compared, because the satellite VCDs contain both, tropospheric and stratospheric BrO, while for the CARIBIC results, the stratospheric signal is widely removed due to the FRS (as long as the stratospheric influence does not change, cf. discussion in Sect. 7.3.1 about the possibility of having observed stratospheric BrO).

In contrast to Fig. 7.13a, only the tropospheric VCD is depicted in Fig. 7.13b. They were retrieved using an algorithm described in *Sihler et al.* (2012) and *Sihler* (2012). According to this algorithm, the BrO peak observed by both instruments is clearly attributed to tropospheric BrO, confirming the considerations of Sect. 7.3.1.

To compare the absolute values between GOME-2 CARIBIC, the SCD's of the CARIBIC nadir instrument have to be converted into VCDs. Due to the high albedo and the moderate SZA, the geometric approximation for the AMF can be used for approximation, cf. (6.17) p. 123. With $\beta = 90° - 82° = 8°$ for the nadir telescope and an SZA of $\theta = 61°$ (at 18:00 UTC), an AMF of 3.1 is calculated. For the peak SCD of $1.8 \cdot 10^{14}\,\mathrm{molec/cm}^2$ (at 17:58, cf. Fig. 7.10), this leads to a VCD of $5.8 \cdot 10^{13}\,\mathrm{molec/cm}^2$. The corresponding satellite pixels show lower tropospheric VCDs around $3 \cdot 10^{13}\,\mathrm{molec/cm}^2$, but higher total VCDs around (slightly above $10 \cdot 10^{13}\,\mathrm{molec/cm}^2$), cf. Fig. 7.13. The fact that the CARIBIC VCD is closer to the tropospheric than to the total GOME-2 column is a further indication that we observed a tropospheric plume.

It has also be be mentioned that the instruments have a different spatial resolution, especially perpendicular to the flight path, CARIBIC's resolution is much higher than

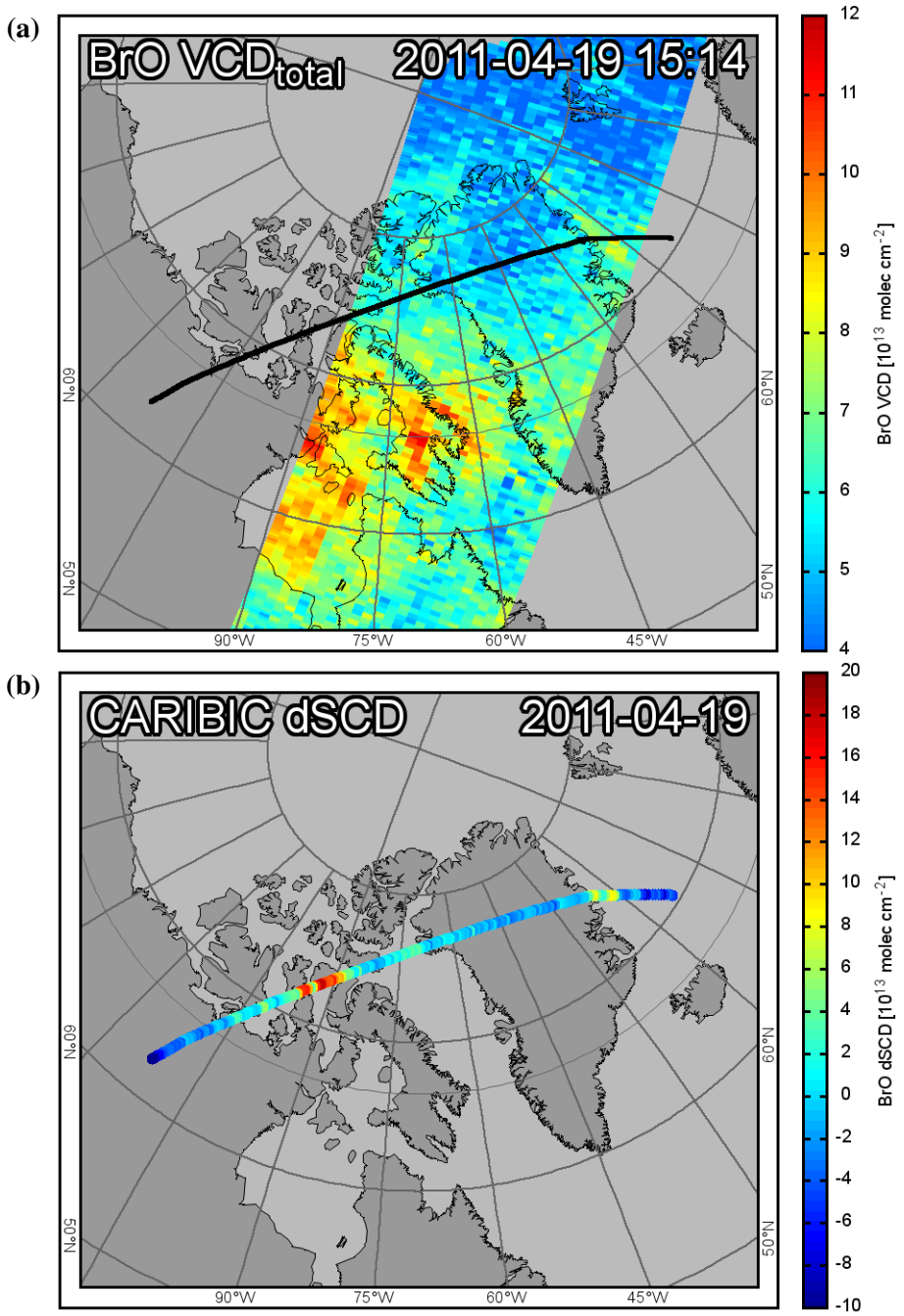

Figure 7.12.: (**a**) BrO total VCD from GOME-2 overpass at 15:14 UTC, ≈15 minutes before CARIBIC observed the peak at the eastern coast of Greenland. (From H. Sihler, Satellite Group of the Max Planck Institute for Chemistry) (**b**) CARIBIC flight route from 15:00 to 19:30 UTC, color-coded with the CARIBIC nadir SCD, like in Fig. 7.9, cf. blue line in Fig. 7.10. (Graph created by H. Sihler)

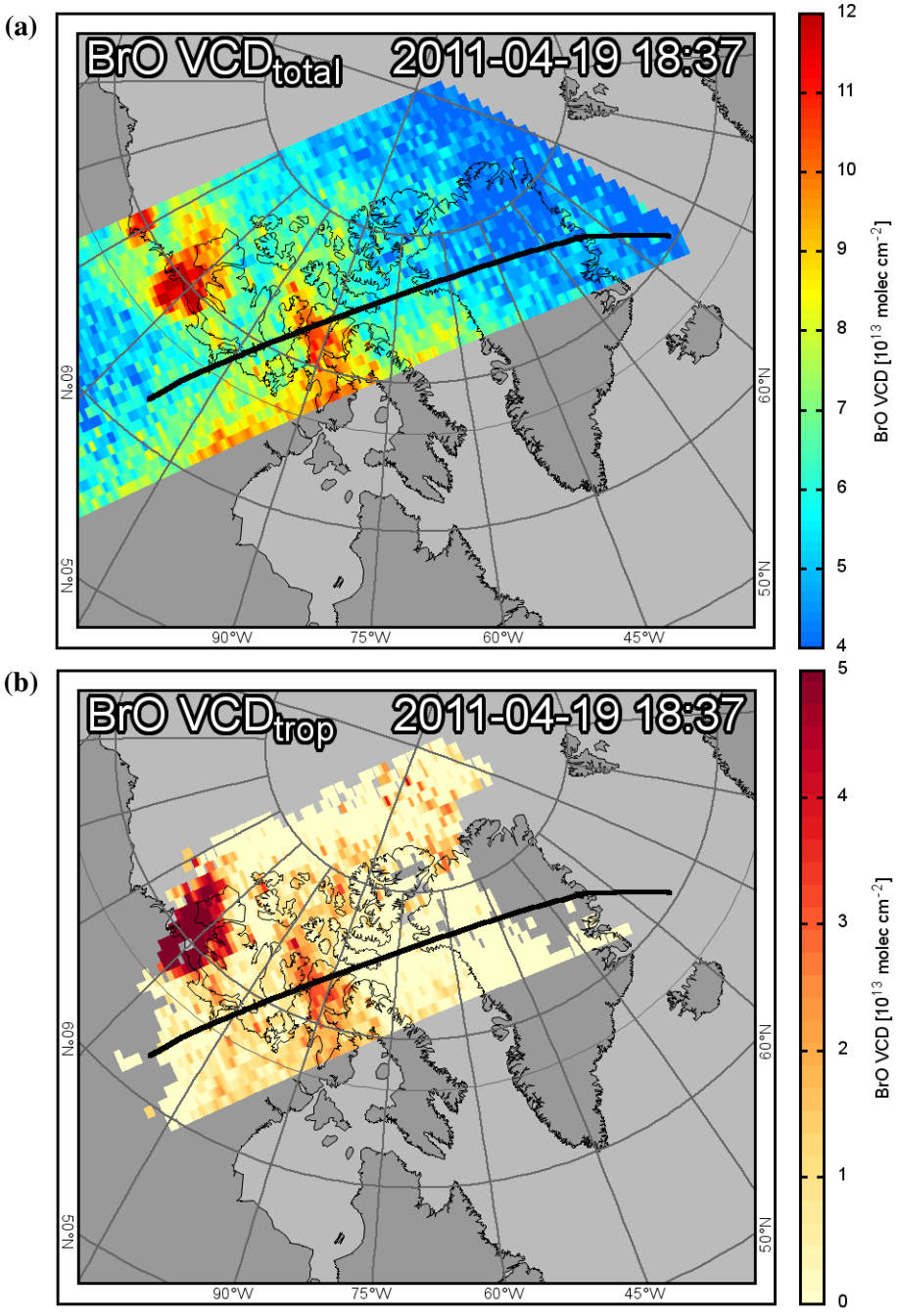

Figure 7.13.: GOME-2 overpass at 18:37 UTC, ≈35 minutes after CARIBIC observed the peak over norther Canada. (From H. Sihler, Satellite Group of the Max Planck Institute for Chemistry) (**a**) BrO total VCD (**b**) BrO tropospheric VCD

those of GOME-2. This can be a reason why CARIBIC observed a double peak (17:58 and 18:05 UTC), while one peak can by seen by GOME-2.

A graph with tropospheric GOME-2 BrO columns analogous to Fig. 7.13b for the 15:14 overpass is not depicted here, because the abovementioned algorithm was not able to perform a reliable distinction between stratospheric and tropospheric columns for the enhancement at the east coast of Greenland. This confirms the doubts mentioned in Sect. 7.3.1 about the origin of the first BrO peak.

To conclude, the CARIBIC measurements agree well with GOME-2 observations. In coincidence, both data show strong evidence for a bromine explosion over northern Canada.

7.4. SO_2 before landing in Caracas

CARIBIC flight 393 took place on 18 September 2012 between Frankfurt and Caracas, arriving at 19:57 UTC. During the descend, just two minutes before touch-down, a clear SO_2 peak concurrent with an NO_2 peak and was observed in two directions, namely in the $+10°$ and the $-10°$ direction, cf. Fig. 7.14. Only a small enhancement close to the detection limit was found in the nadir direction. As the aircraft descended, such a peak could be caused by a horizontally quite homogeneous but vertically thin layer or by a horizontally limited plume. The temporal match of the maxima of both viewing directions are an indication for the latter case, because in the first case, the layer should have been detected by the 10° downward looking instrument before the other, as depicted in Fig. 7.15.

Besides the airport and the city of Caracas, several industries are located in that area. For the identification of the possible source, the position and viewing direction of the aircraft during the observation is needed. Unfortunately, the ARINC data are missing for the last minutes of the flight. However, by using the airport's coordinates, the flight route could be extrapolated, which is described in Sect. 5.4. The result of that extrapolation is depicted in Fig. 7.16a, including the most apparent candidates for the source of the plume, namely the city of Caracas, the airport of Caracas and a power plant close to the flight route. The geometry is sketched in Fig. 7.16b from above and in Fig. 7.16c seen when looking westwards against the flight direction. The line of sight of the $-10°$ instrument reaches the surface over water, assuming the roll angle of the plane to be zero and the altitude to be below 240 m during the observation of the peak. Actually, the altitude at that time might have been around 85 m a.s.l. (cf. Sect. 5.4). For that case, the intersection point of the line of sight and the water surface is indicated by the orange arrow in Fig. 7.16c. That arrow also represents the direction of the light coming directly from the sun – the solar azimuth angle (SAA) amounts to $-96°$ and the SZA to 54°.

The light path and the close vicinity already suggests the power plant 'Ricardo Zu-

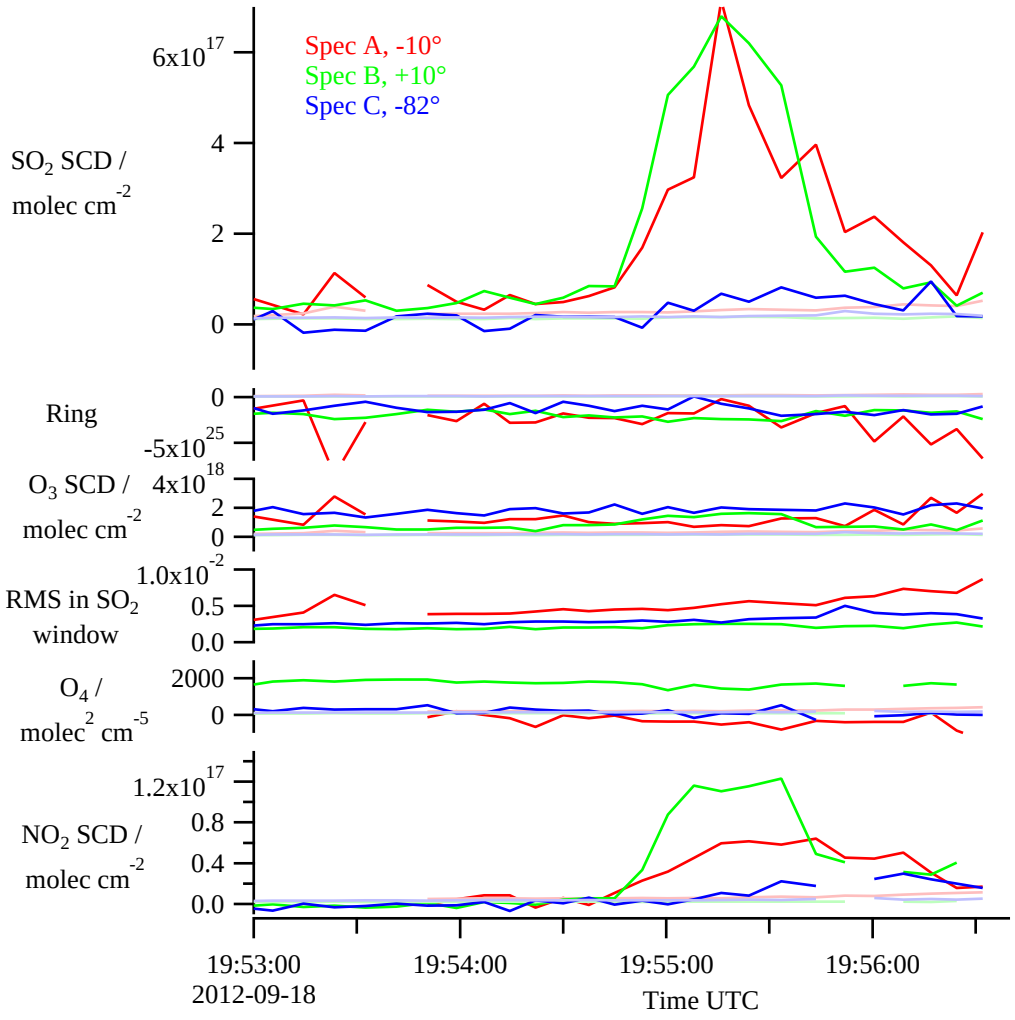

Figure 7.14.: Time series for flight 393 shortly before arriving at Caracas airport. The SCDs of SO_2 and NO_2 are depicted in the topmost and the lowermost part, containing a quite narrow peak at 19:55 UTC in the $+10°$ viewing direction (green) and the $-10°$ direction (red). Other retrieved quantities like Ring, O_3 (here shown for the SO_2 analysis window) and O_4 don't show a correlation, so interference artefacts should not influence the SO_2 result significantly. The pale lines depict correspondig the fit errors.

loaga' in the southeast of the aircraft's position to be the source of the SO_2 peak. Trajectories produced with the web interface of the HYSPLIT model (*Draxler and Rolph*, 2011) were looked at to approve the suggestion. Forward trajectories for Caracas airport and the power station are depicted in Fig. 7.17a and b, starting at 18:00 UTC (CCS airport) or 19:00 UTC (power station). Several adjacent trajectories were calculated (Ensemble mode) in order to get an estimation of the spread of the trajectories which can be caused due to the limited resolution and precession in the model and its underlying data, but also in reality, turbulences can lead to strongly diverging trajectories escpecially in the lower altitudes. The trajectories are combined in Fig. 7.17c, together

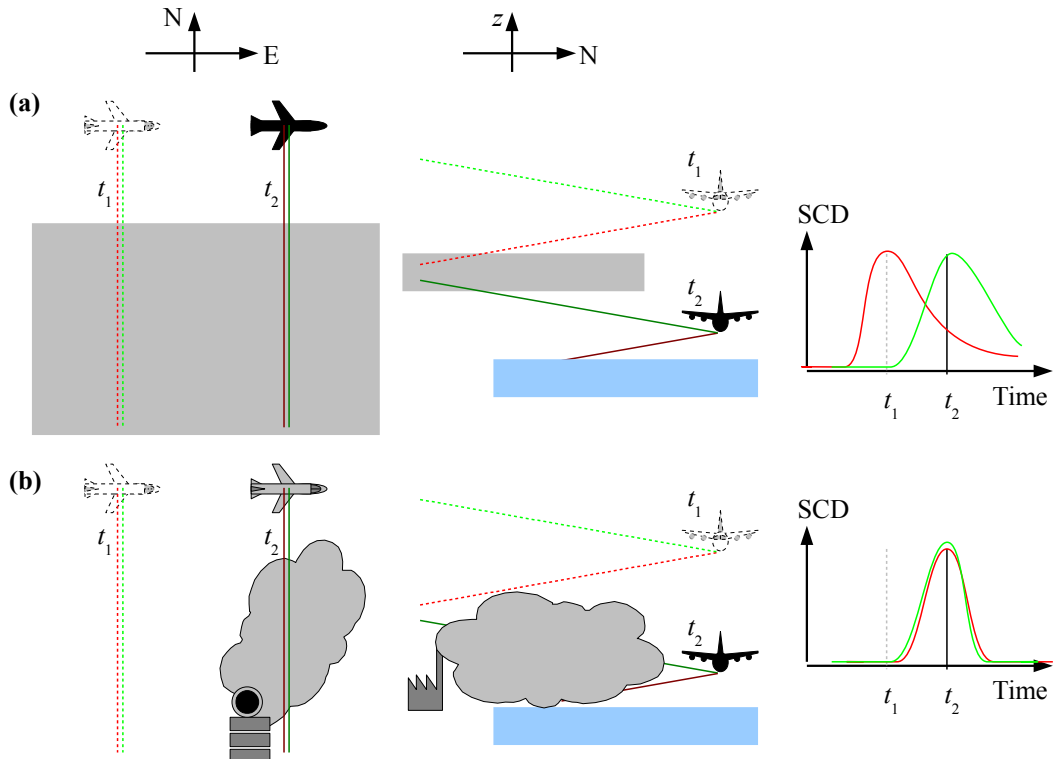

Figure 7.15.: Sketch of two potential shapes of the SO_2 plume and the expected time series of the SO_2 SCD for the $+10°$ and the $-10°$ viewing direction (**a**) For the case for a rather thin but horizontally quite extended layer, spectrograph A detects the plume earlier than spectrograph B. (**b**) A local (horizontally limited) plume is observed by both instruments at the same time.

with those starting at two positions in the area of the city of Caracas, one point in the center and one point at the northeastern outskirts of the city. Also the altitude of the injection of the air parcel plays an important role (here only the trajectories for one emission altitude per candidate is depicted). The vertical mixing, which is enhanced due to heat production, further increases the spread in the direction of the air movement.

Except for the case of the power plant, the sources are too far away to produce a quite narrow plume as observed during the descend. Therefore, the power plant can be clearly attributed to be the (main) originator of the observed plume. This coincides well with the backward trajectories starting in three different heights (50 m, 150 m, 300 m a.g.l.) in an area between the aircraft and the power plant, see Fig. 7.18. That area was chosen, because in that volume the highest sensitivity is given considering the light paths for the instruments.

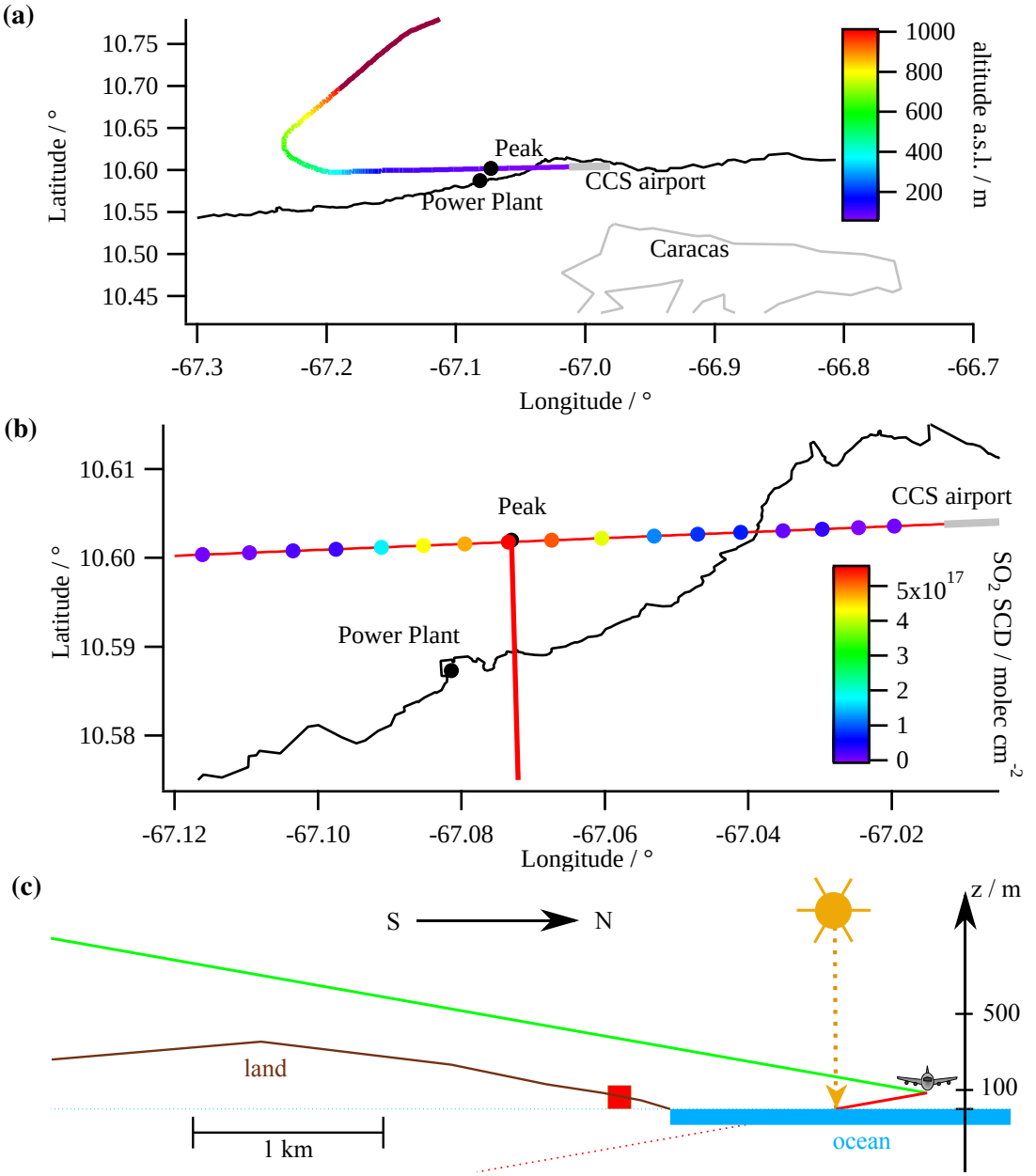

Figure 7.16.: Section of flight route (flight 393) on 18 September 2012, shortly before landing at CARACAS airport (**a**) flight track between 19:49:05 and 19:56:45 UTC, color-coded with altitude (**b**) flight track between 19:54:22 and 19:56:45 UTC, color-coded with SO_2 SCD (**c**) sectional view, looking westwards against flight direction. The red square indicates the position of the power plant.

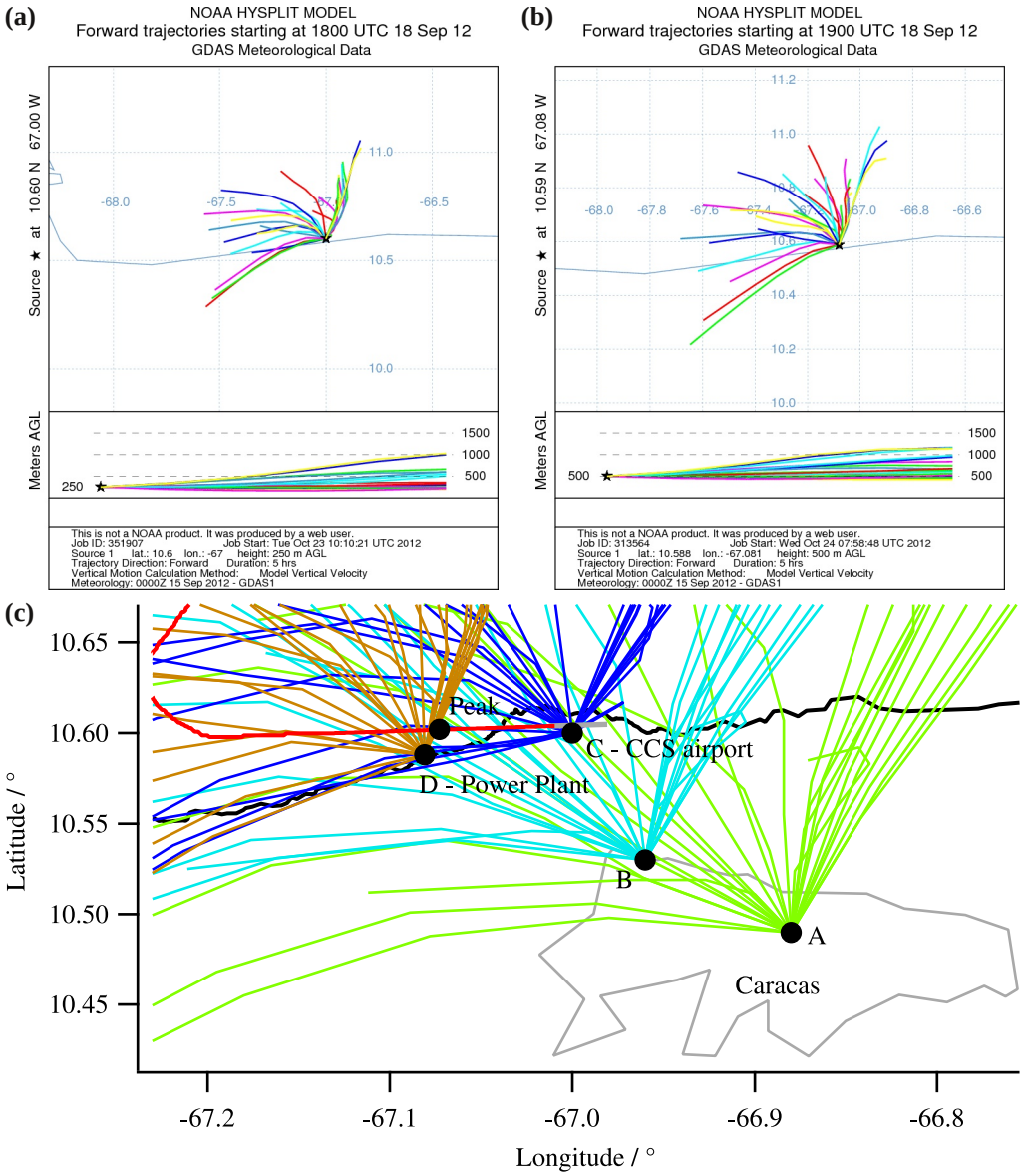

Figure 7.17.: Forward trajectories (ensemble run) calculated by the HYSPLIT trajectory model for 18 September 2012, duration time: 5 hours (**a**) trajectories starting at 18:00 UTC at Caracas airport (88.2° E, 69.32° N) (**b**) trajectories starting at 19:00 UTC at the power plant 'Ricardo Zuloaga' (88.2° E, 69.32° N) (**c**) combined plot of trajectories starting at two places within the city of Caracas (A, green lines, and B, light blue), Caracas airport (C, dark blue), and the power plant (D, ochre). The red curve marks the flight route.

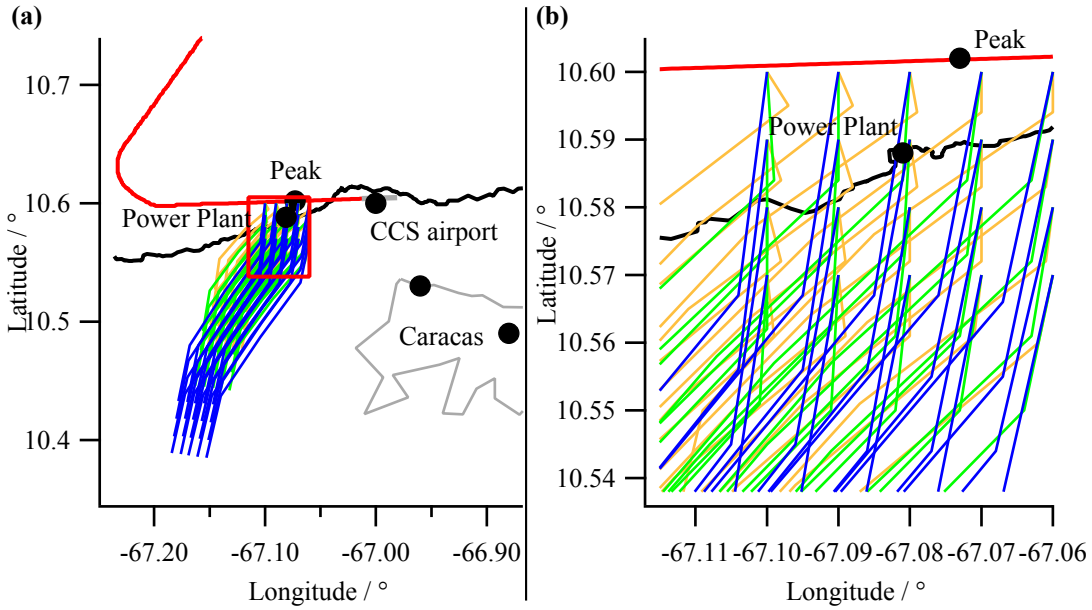

Figure 7.18.: HYSPLIT backward trajectories (matrix run) for an area between the aircraft's position when observing the peak and the power station. The altitudes of the endpoints are 50 m (ocher lines), 150 m (green) and 300 m (blue) a.g.l. The trajectories start at 16:00 UTC and end on 20:00 UTC. Part (b) is a section of part (a).

7.5. Norilsk

On 22 October 2010, during the flight from Osaka to Frankfurt, the aircraft flew close to a large Siberian Nickel smelter, offering DOAS SO_2 and NO_2 measurements of the plume. In the following, the result of an SO_2 flux estimation of the mining plant will been given and discussed, using the DOAS results and meteorological data for the wind field. See also Sect. 4.5 for the theoretical background. This section is an extended version of *Walter et al.* (2012), where also most of the graphs of this section can be found.

7.5.1. Norilsk Nickel

Norilsk is a Russian city in the continuous permafrost zone in Siberia, located in the south of the Taimyr Pensinsula, cf. Fig. 7.19. With about 134 000 inhabitants[8] Norilsk is the northernmost city on the planet to have a population over 100 000. The region around Norilsk contains large amounts of natural resources like anthracite coal and ores of copper, cobalt, platinum and palladium. The nickel deposits are among the largest's ones worldwide. These natural resources have been the main reason for the growth of the city which was founded by the end of the 1920s and the 1930s. After a resolution of the Council of People's Commissars of the USSR in 1935, the mining and

[8] in 2002; source: Wikipedia article 'Norilsk', accessed on 2010-12-28, "http://en.wikipedia.org/w/index.php?title=Norilsk&oldid=397205294"

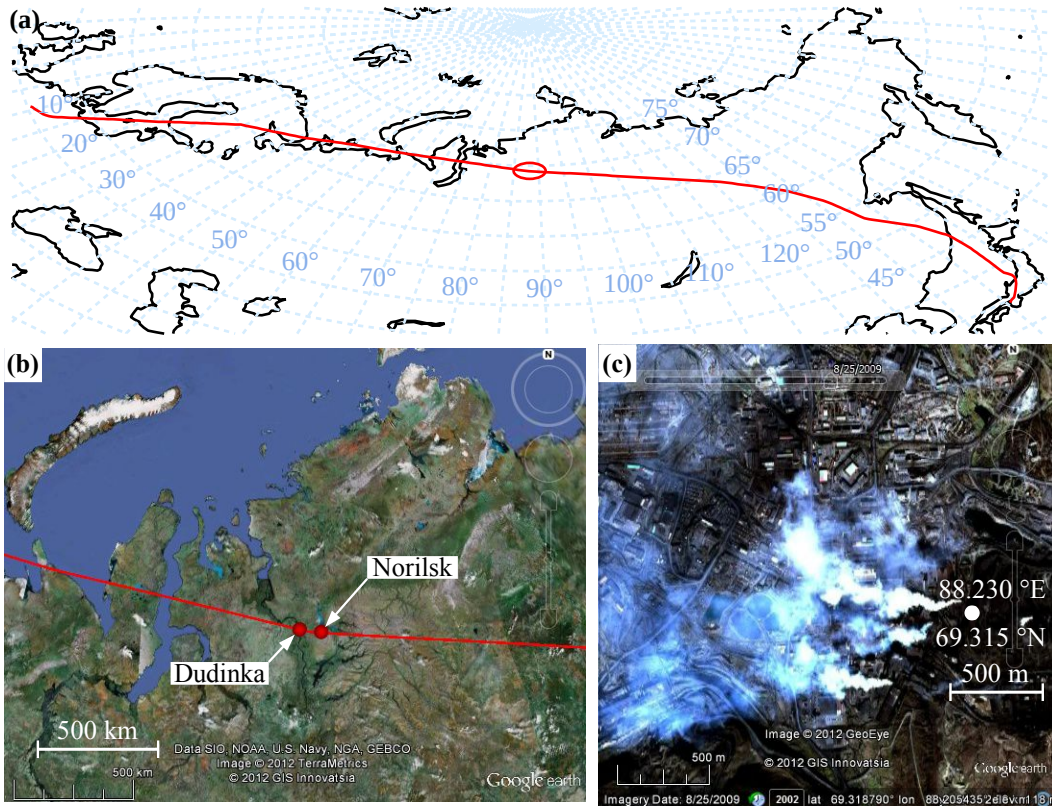

Figure 7.19.: Geographical position of the city of Norilsk and the facilities of MMC Norilsk Nickel. Coordinates of Norilsk: 88.2° E, 69.32° N (**a**) flight route from Osaka to Frankfurt (**b**) section of (a) in the Norilsk region (**c**) small detail of of (b), showing the industrial plant of Norilsk Nickel

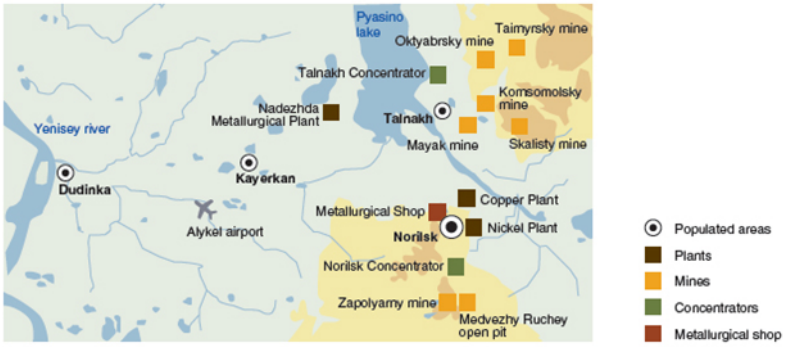

Figure 7.20.: Overview over Norilsk and surroundings, with facilities of MMC Norilsk Nickel. From Norilsk Nickel website “http://www.nornik.ru/en/”, 2011-07-23.

metallurgical complex was built up. Four years later, the first copper-nickel mattes were produced (*MMC*, 2012). Soon, the Norilsk copper and nickel plant have been belonging to the largest of their kind worldwide, being the principal employer in the Norilsk area. After several reorganisations they are part of the OJS Company "MMC "NORILSK NICKEL"[9], which is copper, nickel and palladium mining and smelting company with facilities in Russia, Australia, Botswana, Finland and South Africa. Figure 7.20 shows a map of the facilities in the Norilsk region.

The mining and refining processes cause a strong negative impact on the environment. In the surrounding area, enrichments of the aforementioned metals as well as iron and manganese are found. According to *Yakovlev et al.* (2008), the territory around Norilsk is characterized by high concentrations of heavy metals, the absence of trees, and the disturbance of organic matter mineralization. Not only the vegetation is affected by the pollution, but also the population in and around Norilsk. According to *Leder et al.* (2009), "emissions have caused death or significant damage to vegetation up to 200 km from the operations". Because of that, Norilsk is regarded to be one of the most polluted cities in the world (e.g. *Blacksmith Instititute*, 2007).

Beside metallic compounds, several trace gases are emitted, amongst them NO_2 and SO_2. Both substances have been routinely observed by UV-spectroscopy using satellite instruments like OMI, SCIAMACHY, GOME and GOME-2, cf. *Hörmann* (2013). Because of the big amount, the SO_2 emitted from Norilsk can be observed by satellites regularly, cf. dark red dot over Siberia in Fig. 2.5 p. 27.

7.5.2. Observations

On Friday, 22 October 2010, the aircraft flew from Osaka to Frankfurt (CARIBIC flight 316), taking a route far north which passed about 6 km south of Norilsk (Fig. 7.21) at ∼07:15 UTC, which corresponds to 15:15 local time (UTC+8) or 13:08 solar time (88.2° E). Taking into account that the viewing direction of the 'nadir' telescope is 8° to the right (in flight direction, cf. Fig. 6.1), the closest distance to the stacks of Norilsk Nickel was roughly 5 km. The aircraft's altitude was 10.6 km above sea level.

While the flight route was from east to west, the wind came from the north. Therefore, the aircraft flew over the plume of Norilsk industries which could be clearly detected by the nadir instrument (Fig. 7.21, Fig. 7.22). Because there was little sunlight (the Solar Zenith Angle was around 81.5°), 10 spectra were co-added to increase the signal-to-noise-ratio, resulting in a maximum SCD of $6.2 \cdot 10^{17}$ molec/cm^2. This value was retrieved using a DOAS fit in the wavelength range 311.6–327 nm. The fit result is depicted in Fig. 6.22 p. 122. In Fig. 7.22, the retrieved NO_2 SCD is also shown with a clear peak at 07:15 UTC. A second NO_2 peak is observed around 07:23 UTC. At that time, the aircraft flew over 'Dudinka', a town with a seaport used by Norilsk Nickel. A

[9] Full name: 'Open Joint Stock Company "Mining and Metallurgical Company "Norilsk Nickel"'

Figure 7.21.: Flight path close to Norilsk, color-coded with SO_2 SCD for the nadir direction. The section depicts the flight route between 07:10 UTC (right image border) and 07:20 UTC (left border). The closest distance to Norilsk was at 07:15 UTC, where the highest SO_2 SCD were observed.

FRS at 07:10 UTC was taken (coordinates: 90.3° E, 69.2° N), just five minutes or 75 km before the plume's maximum. Therefore, the stratospheric contribution – especially concerning ozone – is removed automatically.

In the −10° direction no clear enhancement was observed. This fact supports the assumption that the plume was moving in lower altitudes southwards, cf. Fig. 7.23. The geometrical light path (green line) for that viewing direction hits the ground ∼60 km north of the flight route; it's hight at the position of the Norilsk stacks amounts to roughly 8 km (before reaching the ground) and 9.5 km (after the reflection at the ground). However, the SO_2 signal in that direction is not smooth but indicates some enhancement. This might be explained with multiple scattering: Also SO_2 not being in located in the geometrical light path influences the retrieved SCD, cf. dashed orange line in Fig. 7.23.

7.5.3. Emission Estimate of Norilsk Nickel

In section Sect. 4.5, the equations and underlying assumptions have been given. The wind speed $v_{i,j}$ needed for (4.59) p. 72, is obtained using a FLEXPART interpolation (Version 8.2, *Stohl et al.* (2005)) based on 3 hourly $1° \times 1°$ ECMWF data, see Fig. 7.24. Together with $c_{i,j}$ from (4.63) p. 73, the desired flux can be calculated.

In the standard scenario (№ 1, cf. Table 7.1), the concentration is assumed to be vertically constant within the lowermost ∼1.5 km, and zero above, giving a box-profile for the (relative) concentration, cf. Fig. 7.25b. The idea behind that shape is that the plume might be vertically well-mixed within the boundary layer with a boundary layer height of 1.5 km. That value was estimated by regarding the ECMWF wind field (which increased significantly above 1.5 km) and the potential temperature from radio soundings. Because those soundings were taken ∼400 km away from Norilsk, the value 1.5 km

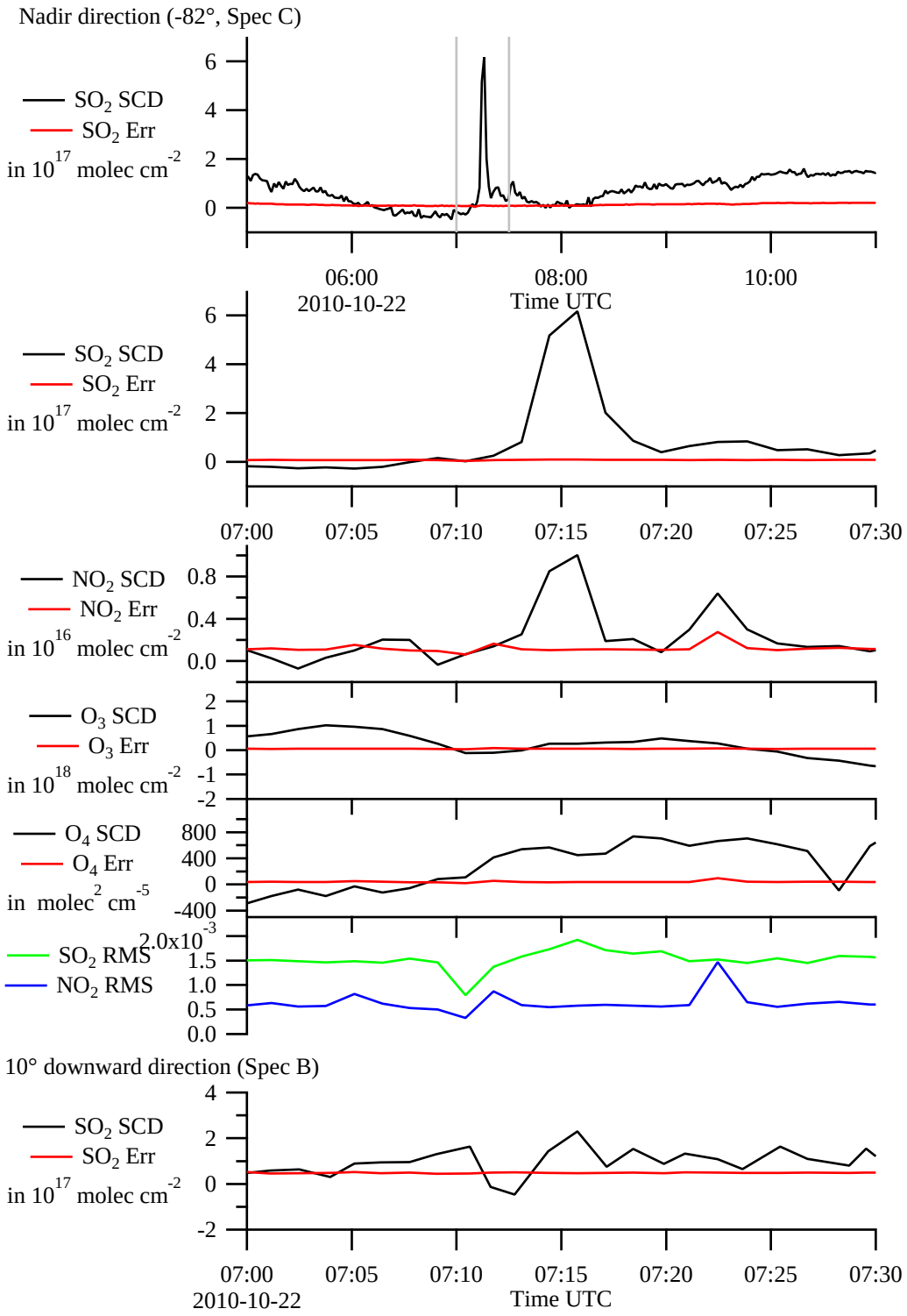

Figure 7.22.: Time series for flight 316, co-added spectra. The grey lines in the topmost graph indicate the section from 07:00 to 07:30 UTC, which is depicted by the graphs below. The FRS was taken at 07:10 UTC. Except for the lowermost graph, the results of the nadir instrument are depicted.

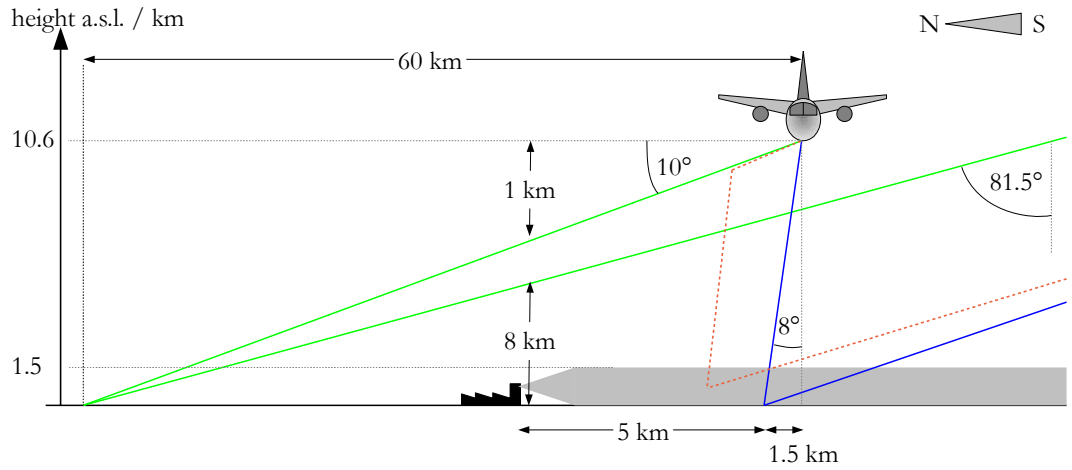

Figure 7.23.: Observation Geometry. The sketch (not true to scale) shows the observation geometry for the Norilsk plume looking eastwards and therefore against the flight direction. The green and the blue line indicate the geometric light paths for Spectrographs B and C (−10° direction and nadir direction). The dashed orange line depicts a possible 'non-geometric' light path, where light reaches Spectrograph B after having passed the plume. The ground height is on the order of 100 m a.s.l. and therefore neglected. The sun is located in the southern direction (Solar Azimuth Angle -160°).

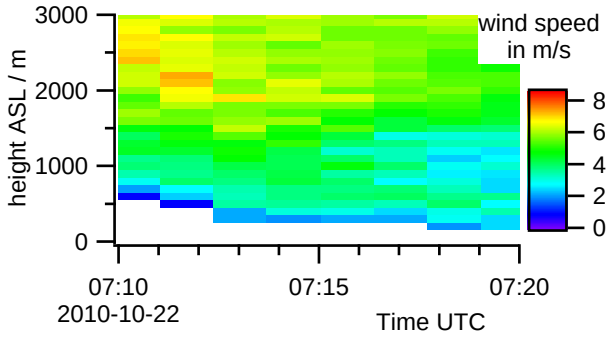

Figure 7.24.: Wind speed below the flight trajectory based on ECMWF data. The time period of 10 minutes corresponds to a distance of about 140 km. The wind came approximately from the north.

is only a rough estimate, cf. Sect. 7.5.4.

Combining the measured SCD (Fig. 7.22) with the assumed relative concentration (Fig. 7.25b), the concentration profile, $c_{i,j}$, is calculated according to (4.63). It is depicted in Fig. 7.25a in terms of a mixing ratio (for a pressure of 10^5 Pa). Multiplying the concentration by the wind speed $v_{i,j}$ (Fig. 7.24) and considering the wind direction $\beta_{i,j}$ according to (4.59) leads to the flux pattern illustrated in Fig. 7.25c.

The desired total flux is the sum of all pixels, being $2.75 \cdot 10^{26}$ molecules per second. With a molar mass of 64.1 g for SO_2, this corresponds to an SO_2 emission of 29.3 kg/s. Extrapolated to a whole year this leads to an integrated annual output of 0.92 Mt SO_2, assuming this single measurement to be representative, cf. discussion.

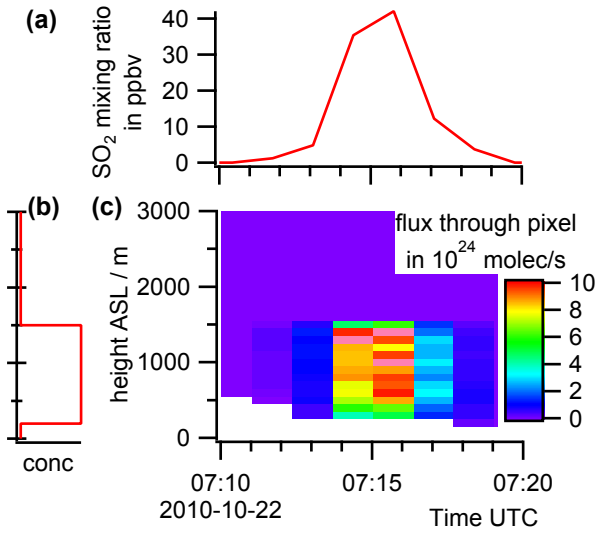

Figure 7.25.: Flux calculation (**a**) derived mixing ratio in the lowermost 1.5 km (**b**) assumed relative concentration profile: constant until 1.5 km altitude, zero above (**c**) flux pixel calculated from the SCD, relative concentration profile and wind data

7.5.4. Discussion of the Accuracy

In the following, the assumptions for the flux calculation are discussed as well as the Radiative Transfer Calculation and the chosen relative concentration profile. A quantitative error estimation can not be given due to the uncertainty of the various parameters, therefore several calculations with alternative parameters are given, here denoted as 'scenarios'. An overview over those scenarios is given in Table 7.1.

Flux calculation – Assumption 1: $Q_{\text{net}} = Q$

The wind is coming from the north (Arctic Ocean, Kara Sea), passing about 600 km of Northern Siberia before it blows over Norilsk. In that area, the population density is very low and there are no big industrial activities. Hence Norilsk can be considered to be the only SO_2 source for the measured plume. Even if there would be a large-scale background of SO_2 from other continents, this would be widely compensated for due to the reference spectrum taken only ∼75 km before the maximum.

To take sinks into account, the loss by oxidation of SO_2 has to be considered. The atmospheric lifetime of SO_2 is typically on the order of one day. The distance from the industrial plant to the flight track is between 5 and 10 km. With a wind speed in the range of 2 to 5 m/s this corresponds to a residence time between the emission and the detection of less than one hour. For an exponential decay $N(t) = N_0 \cdot e^{-t/\tau}$, this means that the amount of SO_2 has been reduced by ∼4 % (for $t = 1$ h and $\tau = 24$ h). Taking this decay into account, the estimated source strength would slightly increase to $2.87 \cdot 10^{26}$ molec/s or 0.96 Mt/year (Table 7.1 № 2). A longer lifetime would lead to

results closer to the standard scenario (№ 1). Therefore sinks could only change the result significantly if they would lead to a much shorter lifetime.

Flux calculation – Assumption 2: The amount of SO_2 inside the volume remains constant, assuming a steady state situation.

For this, first of all, the source strength has to be constant. For smaller industrial plants and for cities, this would probably not be the case due to diurnal, weekly and seasonal cycles. In our case this should be fulfilled, as smelting furnaces usually run 24 hours a day and 7 days per week. However, at least the extrapolation to the annual output has to be treated with caution.

To ensure a steady state, also the wind has to be constant in the time interval of ∼1 hour between emission and detection. To get an estimate of the variability of the wind, the wind along the flight route was re-calculated for ≈6:15 UTC instead of ≈7:15 UTC. The difference of the wind speed between the two wind fields was ∼5 %. A wind change in that time interval does not necessarily change the obtained result significantly, as only the wind up to the maximum plume height at the time of observation is used in the calculation of the flux. Indeed, the result of the flux calculation hardly changed when using the 6:15-wind-data (less than 1 %, cf. Table 7.1 № 3).

On the other hand, quite local changes in the wind field close to the stacks could effect the result significantly. For example, in a time period of low wind speed, SO_2 accumulates around the stack. If the wind increases afterwards, the SO_2 is transported in an agglomeration, which would lead to exaggerated results. Such short term temporal and small-scale spatial variability of the wind (over seconds to minutes or several kilometers respectively) is averaged out by the model. From a single measurement it is not possible to determine this error. Repeated measurements would help to reduce that problem, therefore such fluctuations can be interpreted as a statistical error source.

Additionally it has to be mentioned, that the wind data based on ECMWF contain systematic errors as well. At least in the lower altitudes close to the ground, the values contain significant uncertainties due to small-scale convection which cannot be resolved in the model.

Apart from the FLEXPART based interpolation, also ECMWF raw data were used, applying a linear interpolation in space and time for the relevant coordinates. With that, the result increased by 18 % (cf. Table 7.1 № 4), which can be explained by large errors due to the simplistic interpolation approach compared to the one used in the FLEXPART model. Also different handling of the boundary conditions (surface height) and the choose of the grid resolution for the interpolation lead to discrepancies.

Flux calculation – Assumption 3: The flight path of the aircraft crosses over the whole plume.

As the aircraft's altitude is more than 10 km a.s.l. and the aircraft was flying straight across the plume, this assumption can be deemed to be fulfilled. This is confirmed by the fact that the plume was not detected in the $-10°$ looking channel. However, it has to be mentioned, that the plume could have been partly obscured by a cloud between the SO_2 plume and the aircraft's altitude. But in that case the length of the light path would have changed due to changes in the scattering inside the cloud. This was not observed, the O_4 signal does not change strongly within the period of the plume's observation.

SCD, Radiative Transfer

The statistical DOAS retrieval error in the time interval used for the flux calculation is on the order of 3 %, which is negligible relative to the other uncertainties. However, the retrieved SCD shows some dependency on the wavelength range selected for the fit, and cross sensitivities, mainly to ozone, increase the uncertainties (cf. Table 7.1 № 5).

The retrieval of the Box-AMF depends on several factors: A ground albedo of 0.9 was used for the calculation in the 'standard' scenario (№ 1). For that value, a snow coverage of that area was assumed, which is typical for that season in Siberia. However, the snow might be dirty, e.g. due to the aerosols emitted by Norilsk. Also steep rocks and plants decrease the albedo. Changing the albedo from 0.9 to 0.6 causes a decrease of the AMF from 3.46 to 2.37, as the fraction of light reflected from the surface decreases. This results in larger VCDs and concentrations and thus in an increase in the flux calculation of 47 % to 1.35 Mt/year (№ 6).

Due to the wavelength dependent scattering properties of air, also the AMF contains some wavelength dependency (cf. Sect. 4.2.2). However, the used RTM 'McArtim' uses one single wavelength for the simulation. Changing the wavelength for the radiative transfer simulation from 315 nm to 325 nm leads to an AMF of 3.87 and a decrease of the flux calculation of 11 %, giving 0.83 Mt/year (scenario № 7).

A strong influence is given by aerosols (scattering). While in scenario № 1, no aerosols are included in the RTM simulation, in № 8, an aerosol extinction coefficient of 0.4/km is taken for the boundary layer (1.5 km). This leads to a much smaller AMF (2.2) and therefore to a larger flux (1.5 Mt/year).

The geometrical AMF for the geometrical light path is calculated according to (6.17) p. 123. With $\beta = 90° - 82° = 8°$ for the nadir telescope and Solar Zenith Angle $\theta = 81.5°$ this results in $A = 7.78$. The usage of the geometrical AMF results in an emission of 0.41 Mt/year (№ 9). This result has to be regarded as a lower (but unrealistic) limit for the radiative transfer, as it describes the unrealistic case, in which no light would have been scattered in the atmosphere.

Scenario	total AMF	Result molec/s	Result Mt/year	Rel. Diff.[a]	Notes
№ 1: 'standard'	3.46	2.75E+26	0.92	0 %	
№ 2: decay of SO_2	3.46	2.87E+26	0.96	+4 %	SO_2 lifetime: 1 day
№ 3: wind for 6:15	3.46	2.74E+26	0.92	−0.3 %	
№ 4: raw wind data	3.41	3.25E+26	1.09	+18 %	simplistic interpolation of ECMWF wind data
№ 5: other λ range	3.99	3.34E+26	1.12	+22 %	fitting window 320–342 nm, McArtim simulation at 330 nm
№ 6: ground albedo: 0.6	2.37	4.03E+26	1.35	+47 %	
№ 7: McArtim 325 nm	3.87	2.46E+26	0.83	−11 %	
№ 8: aerosol extinction	2.19	4.34E+26	1.46	+58 %	aerosol extinction coeff. 0.4/km
№ 9: geometric AMF	7.78	1.23E+26	0.41	−55 %	no scattering, unrealistic
№ 10: pl. height 2 km	3.40	3.07E+26	1.03	+12 %	plume height 2 km instead of 1.5 km
№ 11: pl. height 1 km	3.50	2.51E+26	0.84	−9 %	plume height 1 km instead of 1.5 km
№ 12: pl. height 0.6 km	3.42	2.15E+26	0.72	−22 %	plume height 0.6 km instead of 1.5 km
№ 13: exp. conc. profile	3.46	2.73E+26	0.92	−0.6 %	constant mixing ratio instead of constant concentration

[a] relative difference compared to № 1

Table 7.1.: Overview over the different scenarios.
Scenario № 1 is the 'standard' scenario. The other scenarios are based on № 1 but with certain differences.

Vertical Profile

The relative vertical profile of the plume is a further uncertainty. Firstly, it influences the calculation of the AMF. Secondly, it can be interpreted as a weighting function for the wind speed (cf. (4.59) and Fig. 7.25): In a high plume, the strong wind yields a strong contribution to the total flux, resulting in a higher flux estimation. In the case of our Norilsk observation, the sensitivity of the result with respect to the plume height was rather low. If the box height was not 1.5 km (like in № 1) but 2 km, the result would increase by 12 % to 1.03 Mt/year (№ 10). For a height of 1 km (№ 11), it would decrease by 9 % to 0.84 Mt/year. Therefore it can be supposed that also the unknown real profile would lead to a similar result. However, in case of an upper plume height of 0.6 km, only 0.72 Mt/year would be calculated.

The flux calculation according to (4.59) also allows the assumption of non-constant profiles. For a well-mixed boundary layer, a constant mixing ratio instead of a constant concentration is more realistic, leading to an exponential conc. profile (Barometric formula). Here, this difference is quite small (№ 13), because the pressure decreases by only ∼15 % in the lowermost 1.5 km.

7.5.5. Comparison with GOME 1996-2002 literature value

The Global Ozone Monitoring Experiment (GOME) is a spectrographic instrument aboard the European Remote Sensing Satellite (ERS-2), which was launched in 1995. GOME has a spectral range of 240–790 nm at a spectral resolution between 0.2 and 0.4 nm. The ERS-2 satellite has a near-polar sun-synchronous orbit at an altitude of 795 km with a local equator crossing time at 10:30 (*Burrows et al.*, 1999). Within three days, a global ground coverage (at the equator) is obtained from the 960 km across-track swath.

The recorded spectra are analyzed based on DOAS to retrieve SCDs of several trace gases like O_3, SO_2, NO_2 and BrO. In *Khokhar et al.* (2008), the retrieval of the SO_2 output of several industries is described, amongst them the Norilsk Nickel Company and other smelters, using data from the years 1996–2002. For their SO_2 evaluation, a spectral range of about 312 nm to 327 nm was chosen. To convert the SCD into VCD, the Radiative Transfer Model Tracy-II (*Deutschmann and Wagner*, 2007) was used, which is the predecessor of the McArtim model used in this study.

The emission was estimated by integrating the SO_2 VCD over an area around the source and assuming an average atmospheric lifetime τ. A region around Norilsk (85–92 °E, 68–72 °N) was evaluated, considering Norilsk Nickel to be the only source accounting for SO_2 in that area (see Sect. 7.5.4).

The annual emission E_{annual} was calculated using the following equation:

$$E_{\text{annual}} = \frac{\int V \cdot \mathrm{d}A_{\text{area}}}{\tau} \cdot 365\,\text{days} \tag{7.1}$$

V is the SO_2 Vertical Column Density, τ the atmospheric lifetime of SO_2. This lifetime is highly variable (cf. Sect. 2.3.7 p. 29). For their calculation, Khokhar et al. chose a lifetime of one day. They obtained an emission estimate for Norilsk of 1.685 ± 0.3 Mt SO_2 per year in 1996–2002. For an SO_2 lifetime of 2 days, half the emission would be calculated.

7.5.6. Comparison with OMI SO2 for 2012-10-22

The Ozone Monitoring Instrument (OMI) is a spectrographic instrument aboard the 'Aura' satellite launched in July 2004 (*Levelt et al.*, 2006). It has a spectral range from 264 nm to 504 nm with a spectral resolution of about 0.5 nm. In contrast to GOME, no scanning mirror is used to obtain spatial information perpendicular to the flight track, but rather, it uses a two-dimensional CCD detector. OMI has a swath width of 2600 km. As OMI performs 14 orbits a day, a daily global coverage can be provided. The spatial resolution is 13 km by 24 km (48 km for the UV-1 channel) at nadir position, becoming broader towards the outer swath-angle of 57°.

The Sulfur Dioxide Group evaluates and validates SO_2 column densities (e.g. *Carn and Lopez*, 2011). Due to the large solar angles in Siberia during October, the lack of

sufficient sunlight makes satellite SO_2 retrievals difficult and imprecise. Nevertheless, for 22 October 2010 data is available from an OMI overpass at 05:38 UTC, about 1.5 hours prior to CARIBIC's overpass time (see Fig. 7.26a).

A similar approach as mentioned above (Sect. 7.5.5) can be used to estimate the source strength for that particular day. Therefore, the SO_2 emitted within 24 hours before the overpass of OMI is assumed to be within a circle of 111 km radius (1° of latitude) around the estimated centre of the plume. To remove the background signal, an offset is subtracted in a way that the average of the pixel's values outside the circle vanishes (Fig. 7.26c). Summing up all the values inside the circle equals to about $1.7 \cdot 10^{31}$ molecules. This value depends on the chosen radius. Taking too small a radius leads to an underestimated value because the complete plume is not inside, whereas too large a radius contains too much noise from the background. Forward trajectories from HYSPLIT (*Draxler and Rolph*, 2011) indicate that it might be reasonable to vary the circle between 80 and 160 km (Fig. 7.26d). This results in values from $1.5 \cdot 10^{31}$ to $2.3 \cdot 10^{31}$ molecules. Using an SO_2 lifetime of one day leads to an SO_2 output of $\approx 2 \cdot 10^{26}$ molec/s ($1.7 \cdot 10^{26}$ to $2.7 \cdot 10^{26}$ molec/s respectively), corresponding to an annual output of 0.7 Megatons (0.6 to 0.9 Mt), which is in agreement with the results from the CARIBIC measurements, considering the uncertainties of both approaches. Again, the SO_2 lifetime is a critical parameter, cf. Sect. 7.5.5.

7.5.7. Miscellaneous literature values

According to the EDGAR database ("edgar.jrc.ec.europa.eu/", 2011-09-02), the production of metals in the Russian Federation caused about 2.5 Mt of SO_2 emission in the year 2005. This database also contains emission maps, one of them called "Industry combustion and process emissions". Summing up the SO_2 emission in that map in a grid box around Norilsk (87.7–88.4 °E, 68.9–69.6 °N) leads to annual emission estimates between 0.63 Mt and 0.73 Mt in the years 1995 to 2005.

In the report "The World's Worst Polluted Places" of the *Blacksmith Instititute* (2007), an annual SO_2 emission of 2 Mt is reported for the Norilsk emissions. Also according to *Carn et al.* (2004), the emission is "variously reported as being on the order of 2–3 Megatons (Mt) per year". According to the report "Commitment to Environmental Protection" of the Norilsk Nickel Company (*Norilsk Nickel*, 2009), the SO_2 emission of the "Group's Operations in the Russian Federation" is about 2.1 Mt for the years 2007–2009. However, it is not mentioned, which fraction of that amount is related to the 'Taimyr Peninsula' (Norilsk). In a recommendation of the Norwegian 'Council on Ethics' (*Leder et al.*, 2009), also around 2 Mt are mentioned (1.94 Mt for 2006 and 2007). The same report mentions a plan of Norilsk Nickel to reduce the SO_2 emission levels by 70 % by 2010, but it also says that "SO_2 emission levels are nearly unchanged" and "The company's plans to significantly reduce emissions have so far not been implemented."

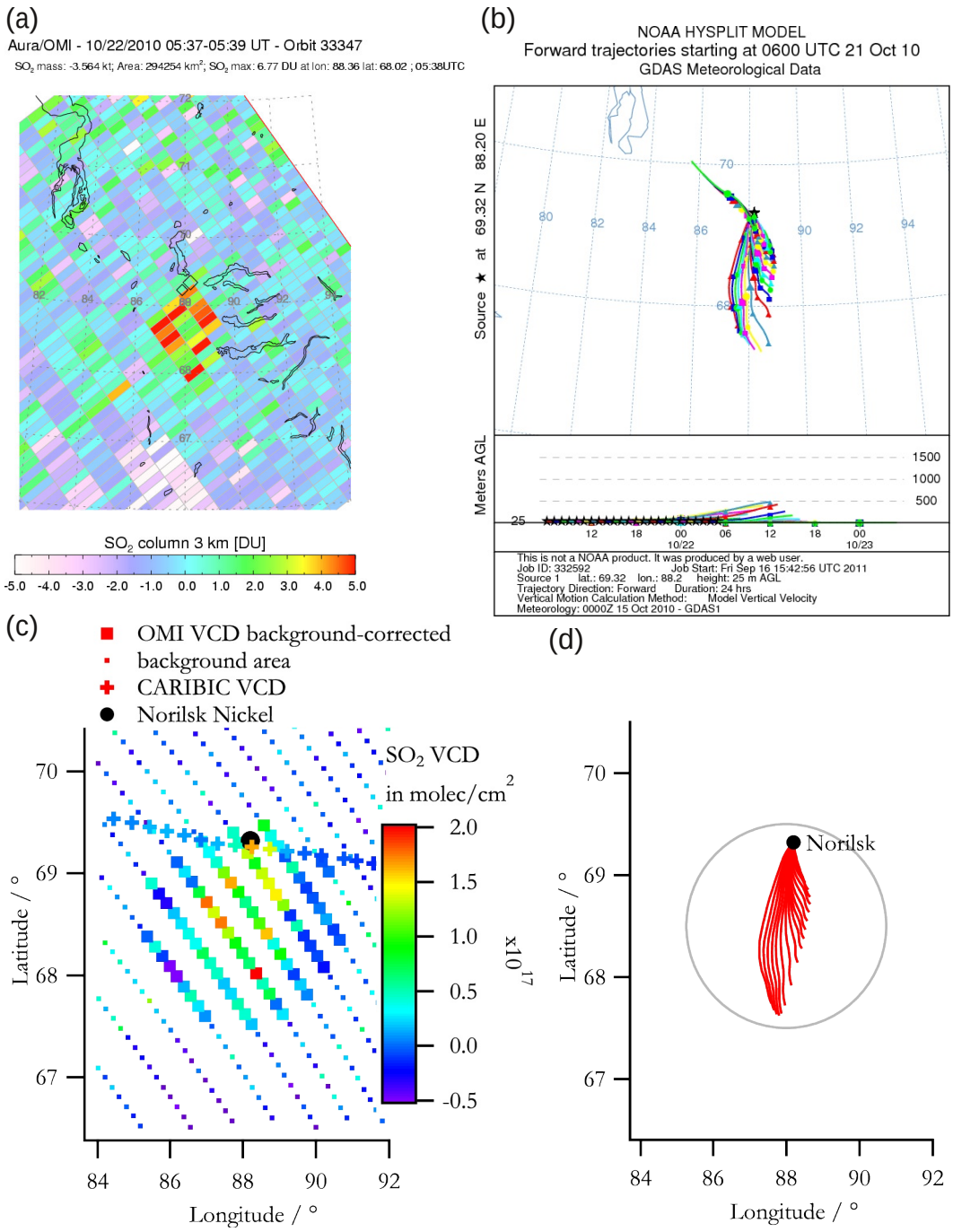

Figure 7.26.: (**a**) OMI SO_2 data from the Sulfur Dioxide Group (NASA/Goddard Space Flight Center, Greenbelt, USA; Web: "http://so2.gsfc.nasa.gov/". $1\text{DU} = 2.69 \cdot 10^{16}\,\text{molec/cm}^2$ (**b**) forward trajectory starting at the Norilsk facilities between 2010-10-21 06:00 and 2012-10-22 05:00, each of them calculated for 24 hours. From NOAA HYSPLIT Web interface "http://ready.arl.noaa.gov/HYSPLIT.php", accessed on 2011-09-16 (**c**) detail of (a): OMI measurements (squares) compared to CARIBIC (crosses). The big squares are used for the calculation of the amount of SO_2 in the plume. (**d**) forward trajectories from (b), but ending at 2012-10-22 06:00 UTC. The grey circle (radius 111 km) refers to the thick squares in (c).

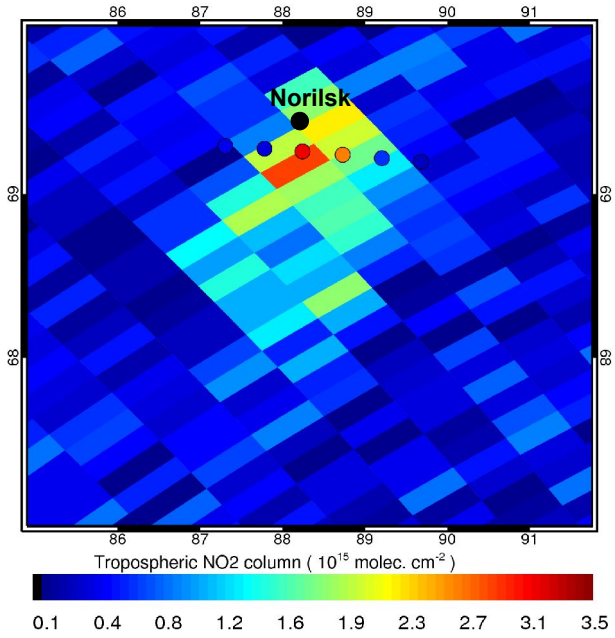

Figure 7.27.: NO_2 VCD of OMI (rectangles, 05:38 UTC) and CARIBIC (circles, 07:10–07:20 UTC, assumed surface albedo: 0.6). (From *Walter et al.*, 2012)

7.5.8. Comparison with OMI NO2 for 2012-10-22

As depicted in Fig. 7.22, also NO_2 was observed by the CARIBIC DOAS instrument. The same is true for the OMI measurement that took place at 05:38 UTC (cf. Sect. 7.5.6). For comparison, the VCD are plotted in Fig. 7.27. In the OMI retrieval, the total VCD is separated into a stratospheric and a tropospheric part (which is depicted here). For CARIBIC, a reference spectrum taken shortly before 07:10 UTC is used, so the stratospheric part is removed automatically. For the conversion from SCD to VCD, a box profile of 1.5 km height was assumed like in the case of SO_2 (Fig. 7.25b). The VCD depends on the assumed surface reflectance: For an albedo of 0.9, the maximum NO_2 VCD of CARIBIC is $2.31 \cdot 10^{15}$ molec/cm^2; for an albedo of 0.6, this value increases by 35 % to $3.13 \cdot 10^{15}$ molec/cm^2. For the OMI data, a surface reflectance database is used with a snow albedo of 0.6. Using an albedo of 0.6, the CARIBIC and OMI results compare reasonably well, considering several differences between the two measurements. As already discussed for SO_2, there is a time difference between OMI and CARIBIC of ∼1.5 hours and the spatial resolution of the two instruments is vastly different.

An emission estimate for NO_2 based on the OMI data like in Sect. 7.5.5 and 7.5.6 was not performed, because there is no 'constant lifetime' of NO_2, cf. (7.1). A flux calculation based on the CARIBIC data and (4.59) results in $3.7 \cdot 10^{24}$ molec/s (albedo 0.9) or $5.0 \cdot 10^{24}$ molec/s (albedo 0.6). This value does not represent the real amount of NO_2 emissions of Norilsk Nickel, as chemical reactions take place between emission and observation. However, the NO_2 emission probably represents 80 % or more of the

total NO_x emission, which can be estimated from the Leighton ratio (*Leighton*, 1961):

$$L_{\text{Leighton}} := \frac{[\text{NO}]}{[\text{NO}_2]} = \frac{J_{\text{NO}_2}}{k_2 \cdot [\text{O}_3]} \tag{7.2}$$

For a photolysis frequency $J_{\text{NO}_2} = 1.5{\cdot}10^{-3}\text{s}^{-1}$, a reaction constant $k_2 = 1{\cdot}10^{-14}\text{cm}^3\text{s}^{-1}$ (see *Atkinson et al.* (2004), reaction between NO and O_3 for 265 K) and a ozone concentration of $5.4 \cdot 10^{11}\text{cm}^{-3}$ (20 ppb) it calculates to $L_{\text{Leighton}} \approx 0.2$. The value for the photolysis frequency is a rough estimate for clear viewing conditions (cf. *Koepke et al.*, 2010), the actual one might be lower, which would lead to an even lower L_{Leighton}, meaning less NO and therefore also less NO_x emission.

7.6. Paris

In March 2011, the aircraft flew downwind of Paris, during which NO_2 was observed. Like in the previous section for Norilsk, flux calculations are performed; here the problem arising from a wind field exhibiting significant vertical variation is highlighted. Again, the result is compared to other measurements.

7.6.1. Observations

During flights in March 2011 (SoF 333), the CARIBIC aircraft traversed France twice – in the north of Paris during flight 335 (from Frankfurt to Bogota) and in the south of Paris during flight 336 (back from Bogota to Frankfurt), cf. Fig. 7.28. While no clear enhancement in the gases measured by the DOAS instrument was observed in the first leg (north of Paris), a large and broad NO_2 peak was observed in the return flight on 23 March 2011 between 12:00 and 12:15 UTC, cf. Fig. 7.29.

A potential increase in other gases like SO_2 was below the detection limit. A slow increase in O_3 and O_4 is retrieved within the half hour depicted in Fig. 7.29, which can be attributed to a slightly changing light path. However, this increase does not coincide with the more narrow NO_2 peak, therefore, there is no indication for this peak to be an artefact of cross sensitivity in the retrieval or significantly changing light path due to clouds. In the 10° downward direction, a broad but small NO_2 enhancement was observed at the detection limit.

7.6.2. Flux calculation

The prevailing wind direction was northeast in the lowermost kilometer, which coincides with the fact, that the highest NO_2 SCD were found in the southwest of Paris at 12:08 UTC. This suggests a flux estimation for the city of Paris analogously to the previous section (Norilsk). Due to the wind conditions changing with altitude, the assumption about the relative concentration profile is even more critical for this case than for the case of the Norilsk flux (Sect. 7.5). Therefore the results for several plume

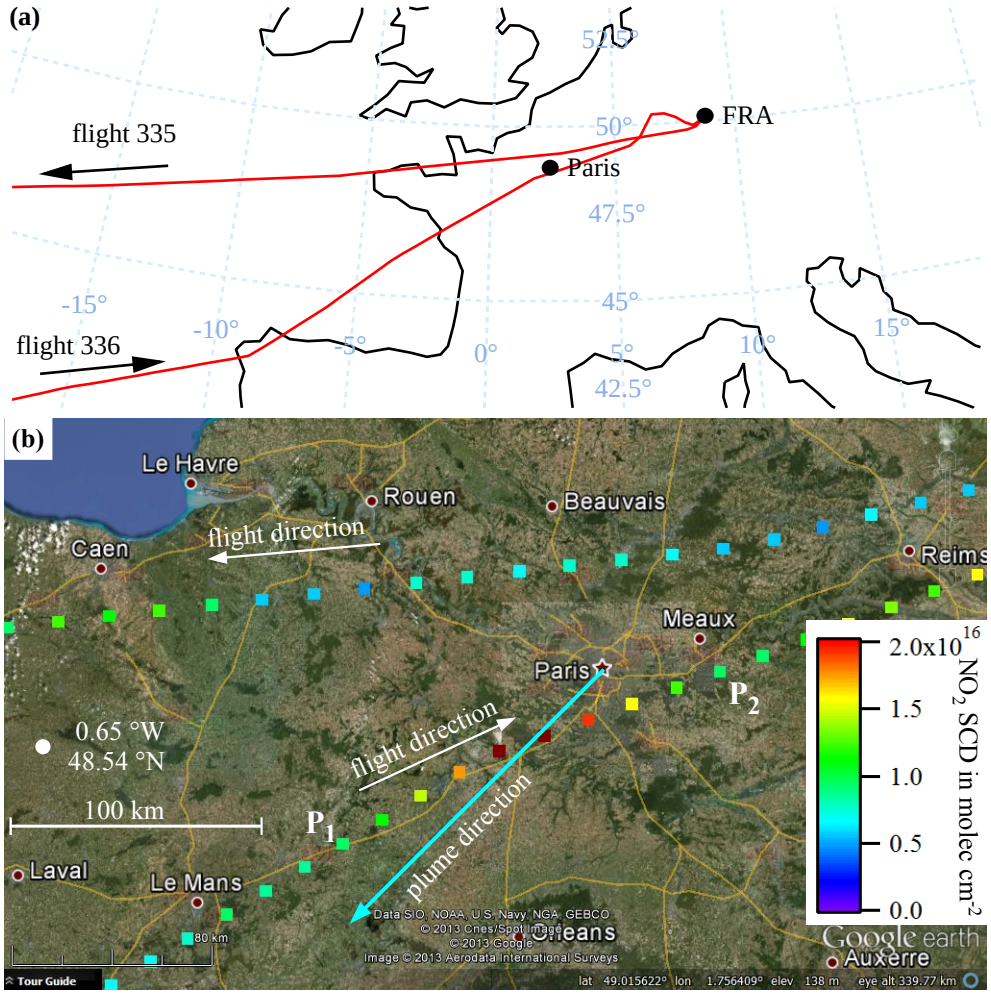

Figure 7.28.: Paris and surrounding cities. Coordinates of Paris (Ile de la Cité): 2.35° E, 48.85° N (**a**) flight route from Frankfurt to Bogota (north of Paris) and back (south of Paris) (**b**) section of (a) around Paris. The cyan-blue arrow is directing from the center of Paris to the observed NO_2 maximum.

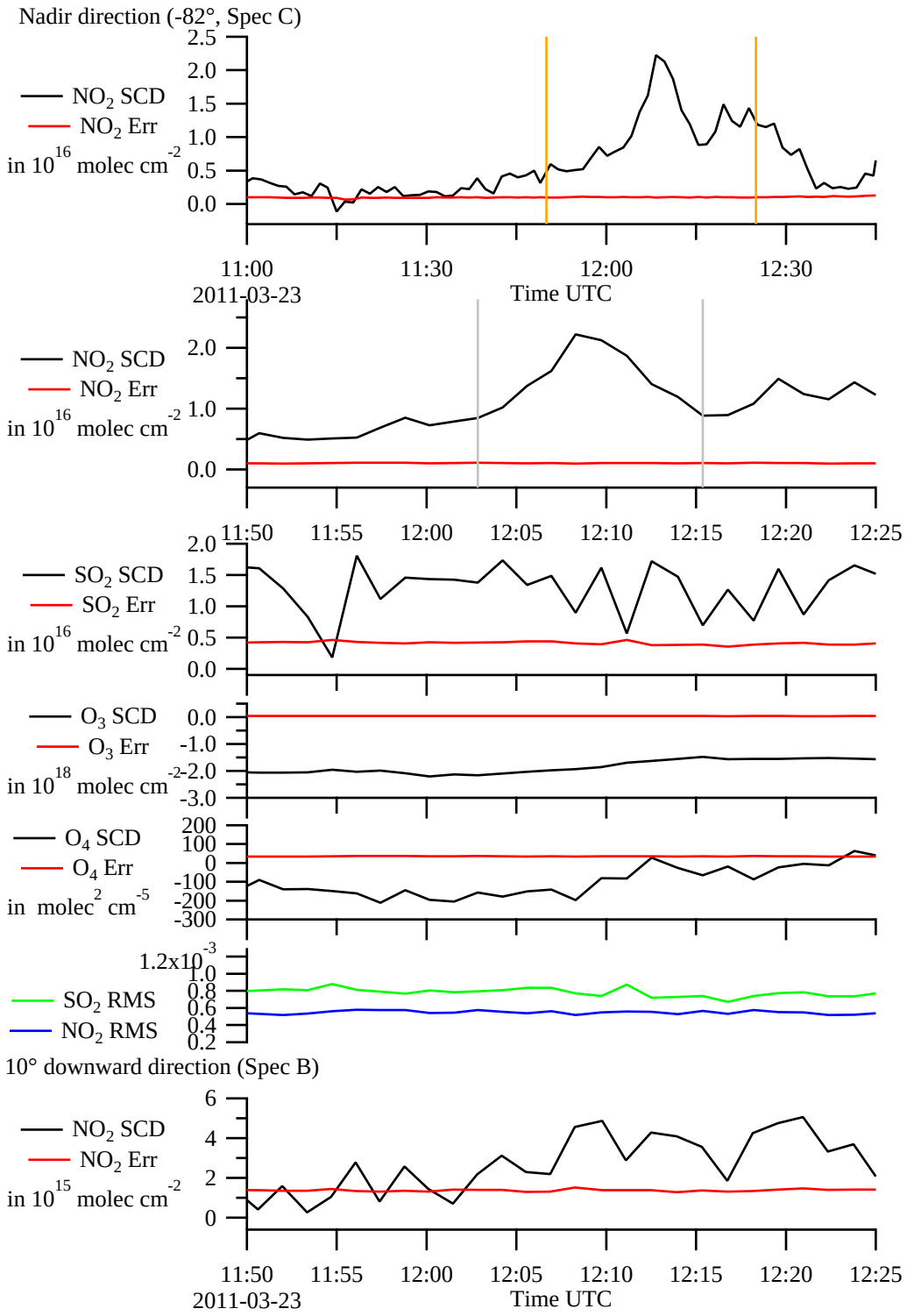

Figure 7.29.: Time series for flight 336, co-added spectra. The orange vertical lines in the topmost graph indicate the section from 11:50 to 12:25 UTC which is depicted by the graphs below. The grey vertical lines below indicate the section used for the flux calculation, cf. Fig. 7.30b. Except for the lowermost graph, the results of the nadir instrument are depicted.

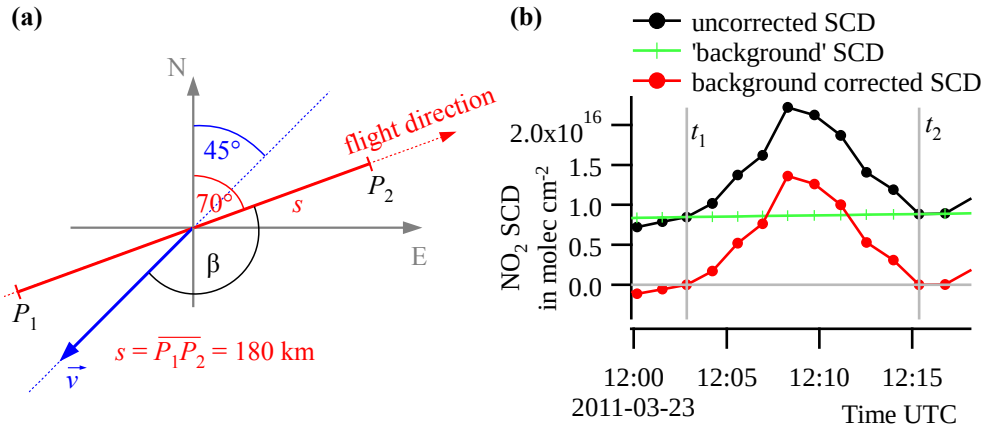

Figure 7.30.: (**a**) Sketch of the flux calculation for the simplistic case of only one wind speed v and wind direction (45°) along the flight path from P_1 to P_2 and for all heights (**b**) Background correction of the SCD based on a linear interpolation between the times t_1 and t_2, which correspond to the positions P_1 and P_2

heights and shapes are given below, using ECMWF based wind data or wind data from a sounding station respectively. Before that, the calculation is explicitly demonstrated and discussed for the simplistic case of a horizontally and vertically constant wind field.

Neglecting any non constant parameters in the flux calculation, (4.59) p. 72 can be simplified to

$$Q = s \cdot h \cdot \bar{c} \cdot v \cdot \sin(\beta) \tag{7.3}$$

Here, only one single wind speed v and one wind direction (and therefore one angle β between the wind vector and the flight direction) was used; $\bar{c}$ shall be the averaged concentration in the plume of height h and length s, cf. Fig. 7.30a. According to (4.15) p. 50 and (4.16) p. 51, the product $h \cdot \bar{c}$ can be replaced by the averaged VCD $\bar{V}$ or by $\bar{S}/A$ with total AMF A and averaged SCD $\bar{S}$:

$$Q = s \cdot \frac{\bar{S}}{A} \cdot v \cdot \sin(\beta) \tag{7.4}$$

For $s = 180\,\text{km}$, $\bar{S} = 5.9 \cdot 10^{15}\,\text{cm}^{-2}$, $A = 0.65$, $v = 5\,\text{m/s}$ and $\beta = 155°$, this results in an NO_2 flux of $3.2 \cdot 10^{25}$ molecules per second. This wind speed and direction was chosen based on data from a sounding for the lowermost altitudes, cf. Fig. 7.31a. The AMF A was gained based on Box-AMFs (retrieved by the McArtim model, cf. Sect. 4.2.3) and a plume height of ∼0.8 km. The horizontal distance s is depicted in Fig. 7.30a, which corresponds to the time interval from t_1 (12:03 UTC) to t_2 (12:15 UTC), cf. Fig. 7.30b. Within this period, the SCDs were averaged to $\bar{S}$ after a correction of the 'background SCD': The first and the last point of the mentioned time interval are assumed to be outside the plume, therefore their SCD is shifted to zero, with linear interpolation in between (Fig. 7.30b). The choice of this interval is arbitrary to some extend, leading to uncertainties in the result.

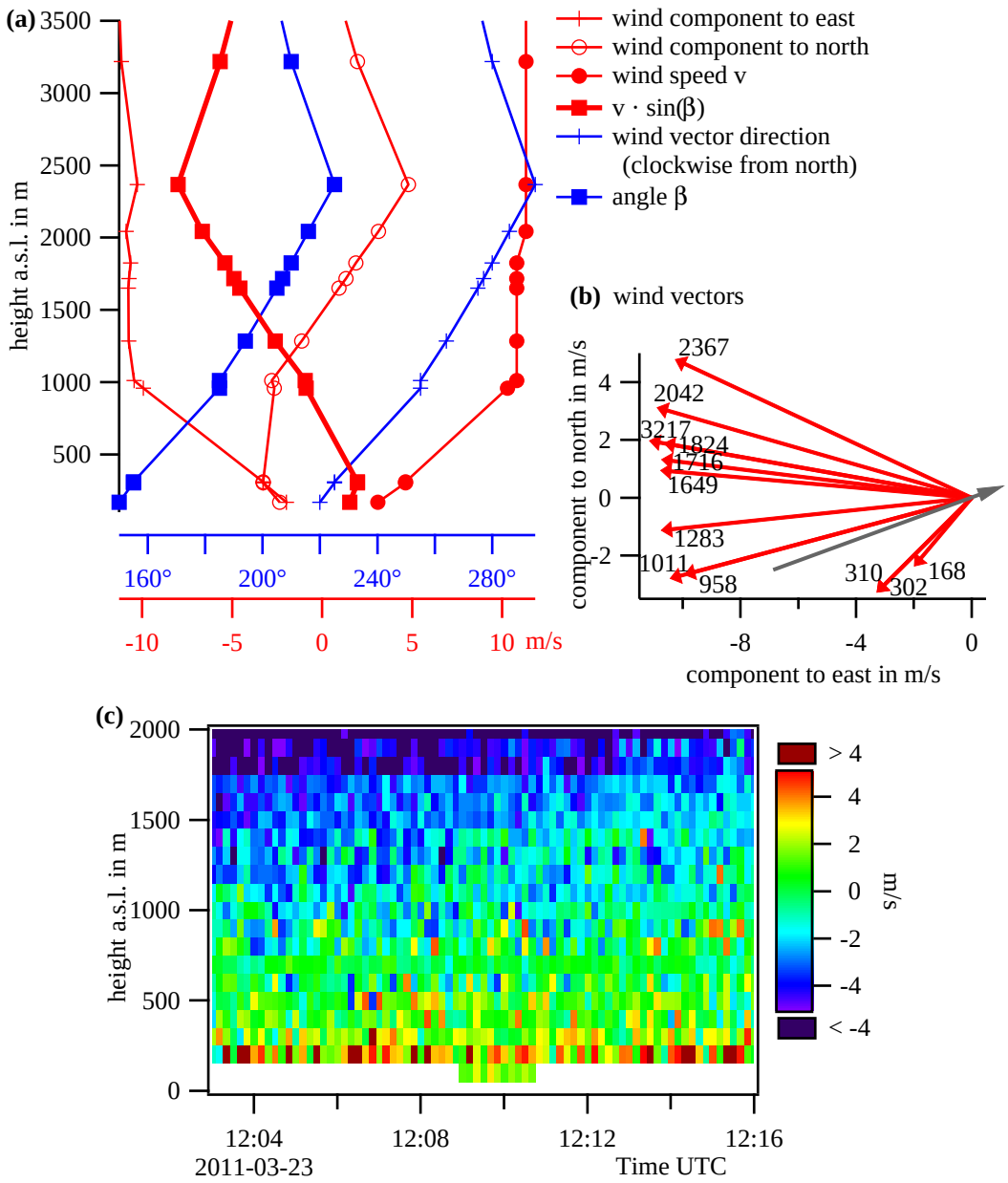

Figure 7.31.: Wind data from sounding measurement (a),(b) and ECMWF data (c). (**a**) Vertical wind profile. The red curves belong to the red axis and contain the components of the wind vectors to east and north, the wind speed and $v \cdot \sin(\beta)$; the blue lines contain the wind vector direction and the difference β between the wind vector direction and the flight direction. (**b**) Wind vector diagram of (a). The numbers attached to the arrows represent the height of the measurement in Meter a.s.l. The grey arrow indicates the flight direction. (**c**) Wind profile along the flight route (FLEXPART interpolation based on ECMWF data) in the time interval of the NO_2 peak, namely from 12:03 to 12:16 UTC. Depicted is $v \cdot \sin(\beta)$, cf. red squares in (a).

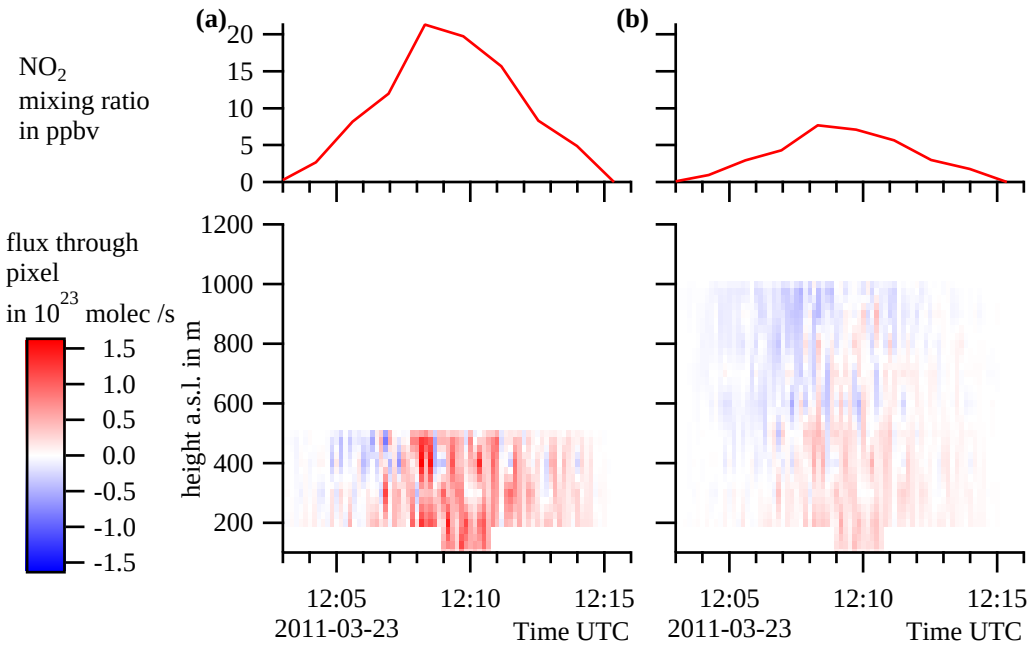

Figure 7.32.: Flux calculation using a twodimensional wind field (cf. Fig. 7.31c), assuming a box-shaped concentration profile, cf. analogous graph for Norilsk, Fig. 7.25 p. 155. The upper plume height is assumed to be 500 m a.s.l in (a) and 1000 m in (b); a ground height of 100 m a.s.l. is taken. The upper part depicts the mixing ratio within the plume as a result of the VCD divided by the plume's thickness (400 m for (a), 900 m for (b)) and converting this concentration into a mixing ratio (applying for a pressure of 10^5 Pa). In the lower part, the flux pixels contributing to the total flux are shown (red: flux from the left to the right side of the flight route; blue: flux from right to left).

Additional and larger uncertainties are caused by the wind direction and wind speed, which are depicted in Fig. 7.31: In (a) and (b), wind data are depicted, taken at noon time of 2011-03-23 by the 'Trappes' sounding station, which is situated ∼25 km south-west of Paris (coordinates: 2.00° E, 48.76° N). For the flux calculation essential is the red curve with the red squares in (a), which depicts the wind component perpendicular to the flight direction, namely $v \cdot \sin(\beta)$, cf. (7.3). Only in the lowermost kilometer, this quantity is positive, meaning a flux from the left to right side of the flight route. In higher altitudes, the wind is predominantly coming from east, thus crossing to flight route from right to left. A similar message is given in Fig. 7.31c, where the profile of $v \cdot \sin(\beta)$ is depicted along the flight route in the time interval of interest. The underlying wind data were retrieved using a FLEXPART interpolation (Version 8.2, *Stohl et al.* (2005)) based on 3 hourly $1° \times 1°$ ECMWF data.

Figure Fig. 7.32 depicts the retrieved flux for two box shaped concentration profiles with a ground height of 100 m a.s.l. and a top height of 500 m (a) and 1000 m (b). For (a), a total flux of $2.2 \cdot 10^{25}$ molecules per second is calculated; for (b) the result is only $1.3 \cdot 10^{24}$ – more than an order of magnitude less, caused by the change in the

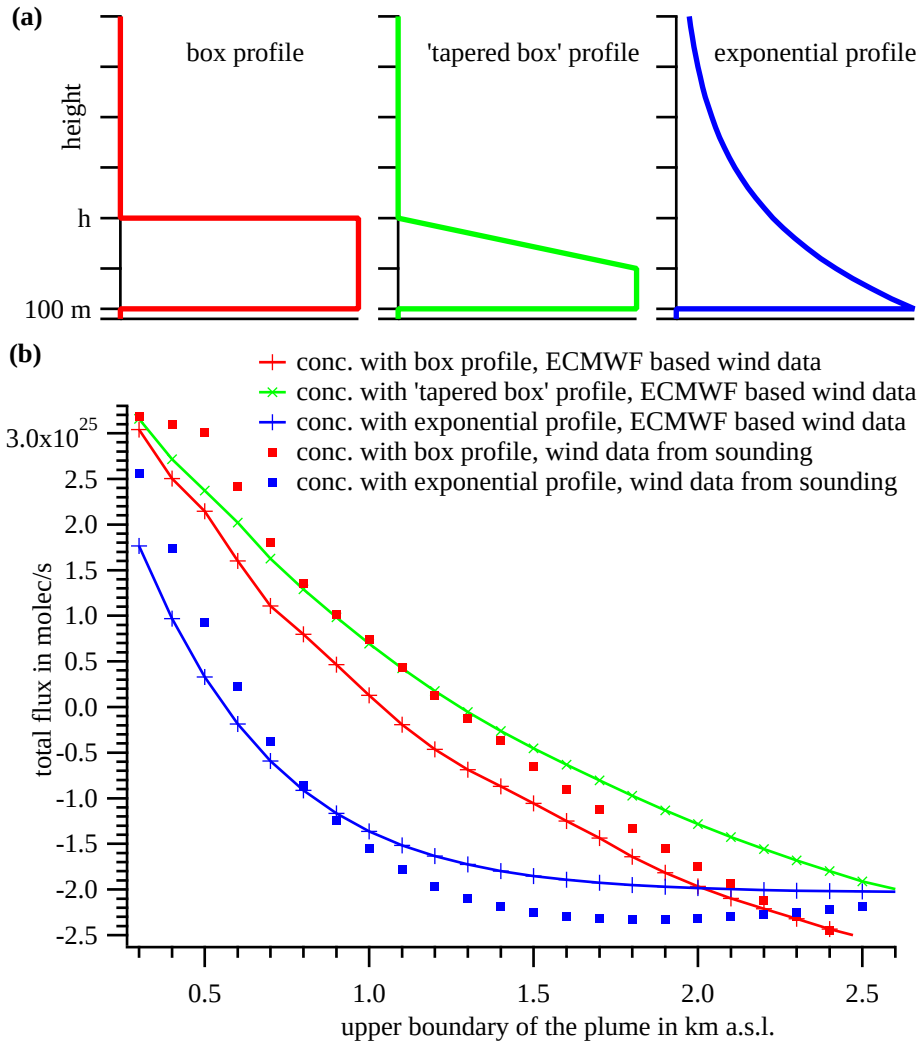

Figure 7.33.: Dependency of the retrieved flux on the plume height and the shape of the relative concentration profile. (**a**) Shapes of the assumed relative concentration profiles. Due to the gridded data for wind, Box-AMF and SCD, the profiles actually used for the calculation are not smooth but contain steps. (**b**) The calculated flux is plotted against the top height h of the plume. For the case of the exponential profile, the height in which the concentration is reduced to $1/e \approx 37\,\%$ of the maximum concentration is meant.

assumed prevailing wind direction with higher altitude. For the assumption of higher plume heights (more than ∼1 km), even 'negative' fluxes are calculated, as summarized in Fig. 7.33. For the lined curves, the twodimensional FLEXPART wind field is used, the squares result from the sounding based wind data. Both wind data have to be treated with caution: The FLEXPART model is based on ECMWF data with limited temporal and spatial resolution ($1° \times 1°$), especially the wind field in the lowermost altitudes contains significant small scale variations due to surface patterns which can not be resolved in the model. The wind measurement of the soundings only give punctual information, here for the 'Trappes' station which is about 20 km off from the observed maximum. Furthermore, the wind is given only for a few altitudes in lowermost kilometer, namely 168 m (close to ground), 302 m, 310 m, and 958 m a.s.l. At least, the time of the measurement (namely 12 UTC) concurs well with the CARIBIC overfly time.

A box profile is the simplest case for a calculation, but the real shape in unknown. Two other profiles (cf. Fig. 7.33a) were tested to demonstrate this dependency. Here, the 'tapered box' profile leads to higher fluxes than the box profile (for the same top height) because here, the lower part of the plume has a higher concentration, so the wind in the lower altitude is pronounced. Much lower fluxes (or negative fluxes already for low scale heights) result for the case of an exponential profile with scale height h, because here, also the strong easterly and southeasterly wind of higher altitudes contributes to the result.

For the Norilsk flight (Sect. 7.5), the wind crossed the flight route nearly perpendicular (cf. Fig. 7.21 p. 152), and the wind direction only changed moderately with hight, thus the factor $\sin(\beta)$ in the flux equation (7.3) is rather unproblematic. Conversely, for the case of Paris, the wind direction (and therefore $\sin(\beta)$) causes the largest uncertainties. A simple approach to estimate the predominant wind direction based on the DOAS measurement is to connect the center of Paris with the position of the observed maximum, see cyan-blue arrow in Fig. 7.28b. The direction of that line is 135°, which corresponds to a wind direction of 45°, just as estimated above (cf. Fig. 7.30a) based on the sounding data for low altitudes (cf. Fig. 7.31c). This indicates that the NO_2 is concentrated in the lowermost half kilometer. According to Fig. 7.33b, this corresponds to a flux of about $2 \cdot 10^{25}$ to $3 \cdot 10^{25}$ molec/s.

Further uncertainty factors

The start position of the arrow in Fig. 7.28b is the center of Paris (Ile de la Cité, 2.35° E, 48.85° N), assuming a more or less homogeneous distribution of the NO_x sources within the city of Paris. The main contributor to the NO_x emission is traffic in the city area and several highways. NO_x is predominantly emitted as NO and then in large part converted to NO_2 (cf. 'Leighton ratio', Sect. 2.3.2), so the total NO_x emission is higher than the measured NO_2. Furthermore, the lifetime of NO_x becomes relevant – the distance between the center of Paris and the position of the observed maximum is

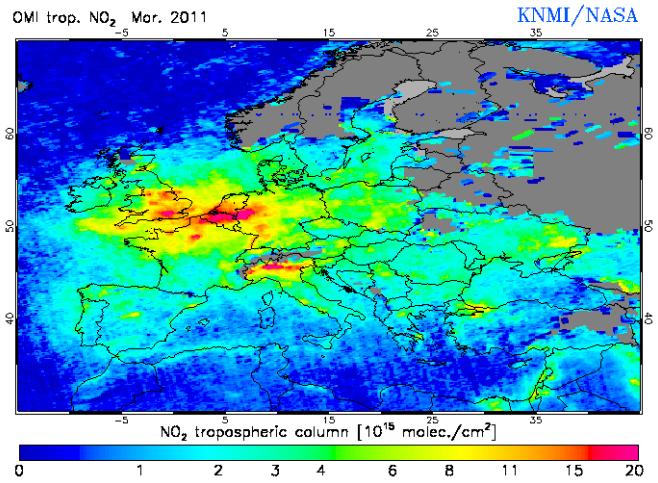

Figure 7.34.: Mean tropospheric NO_2 column for March 2011 from OMI satellite, DOMINO version 2.0, *K. F. Boersma* (2011) over Europe. (From Tropospheric Emission Monitoring Internet Service (TEMIS), "http://www.temis.nl/airpollution/no2col/no2regioomimonth_v2.php?Region=1&Year=2011&Month=03", accessed on 2013-04-12)

∼45 km, which corresponds to plume age of ∼2.5 hours for a wind speed of 5 m/s (cf. Fig. 7.31). The lifetime of NO_2, which is on the order of 10 hours (cf. *Shaiganfar*, 2012, p. 64; *Martin et al.*, 2003), depends on several factors, and the plume age has a large span due to the extended length of the observed peak and the large area of Paris: The closest distance between the flight route and Paris center is about 15 km, and the airport 'Orly Field' in the South of Paris is passed by the flight track by less than 5 km.

Paris is assumed to be the only source of the observed NO_2. Due to other cities and highways, this is not really the case, but the very 'broad scaled' background of far sources is subtracted as mentioned above (cf. Fig. 7.30b). Larger cities in the vicinity of Paris and north of the flight route are rare, Rouen and Le Havre for example with about 110 000 and 175 000 inhabitants[10] are already more than 100 km off the flight route; an observed NO_2 enhancement (∼12:20 UTC) probably originated by Reims (∼180 000 inhabitants[10]) is observed *after* the interval used for the flux calculation. However, Paris can not be distinguished from its various suburbs and smaller cities in direct vicinity like Versailles (∼90 000 inhabitants[10]) which is situated more or less between Paris and the observed NO_2 peak.

7.6.3. Comparison with other observations

With a population of over two million people in the administrative area and over 10 million people in the metropolitan area, Paris is one of the largest population centres in Europe[10] and belongs to the megacities investigated by the MEGAPOLI project ('**M**egacities: **E**missions, urban, regional and **G**lobal **A**tmospheric **POL**lution and cli-

[10]Source: "www.wikipedia.org"

mate effects, and **I**ntegrated tools for assessment and mitigation') with respect to emissions and air quality. Within this project, two measurement campaigns were performed in 2009 and 2010 by *Shaiganfar* (2012) using a mobile MAX-DOAS instrument installed on the roof of a car. This mobile observatory was driven around Paris several times. The retrieved flux depended on several factors like the enclosed area, time of day and season, with higher results in the winter campaign (Jan. and Feb. 2010) than in the summer campaign (July 2009). Like for the CARIBIC measurements, uncertainties due to the conversion from SCD to VCD (aeorsol), the wind field and the assumed relative concentration profile occurred. Exponential NO_2 profiles with scale heights between 100 m an 700 m were tested. For the case of 500 m scale height in summer and 300 m in winter, an average flux of about $4 \cdot 10^{25}$ molec/s in summer and $9 \cdot 10^{25}$ in winter were obtained, spreading from $2 \cdot 10^{25}$ molec/s to $13 \cdot 10^{25}$ molec/s for the single days of the campaigns, cf. *Shaiganfar* (2012, p. 81).

Figure 7.34 shows the tropospheric NO_2 column over Europe measured by the OMI satellite (cf. Sect. 7.5.6) in March 2011.[11] A clear maximum over Paris is observed, surrounded by enhanced NO_2 concentrations in the northern part of France due to other cities and the downdraft of Paris averaged over one month. Within the study of *Shaiganfar* (2012, p. 88, 91), a satellite based source estimation was performed using OMI data of 2009-07-16 and a similar approach as described in Sect. 7.5.5 (cf. (7.1) p. 159), resulting in $6.5 \cdot 10^{25}$ molec/s or $4.5 \cdot 10^{25}$ molec/s depending on the choice of the OMI data product version.

An alternative approach including a satellite based NO_2 lifetime estimate is described by *Beirle et al.* (2011). Using a modified version of that approach, an emission of 98 ± 47 mol/s was calculated based on OMI data from 2005 to 2009 (S. Beirle, pers. comm., 2013), which corresponds to $(5.9 \pm 2.8) \cdot 10^{25}$ molec/s.

A similar value, namely $\approx 5 \cdot 10^{25}$ molec/s, can be extracted from the EDGAR database (*EDGAR*, 2011) by integrating over the corresponding grids in the area of Paris, cf. *Shaiganfar* (2012, p. 81).

The flux estimate of $2 \cdot 10^{25}$ to $3 \cdot 10^{25}$ molec/s from the CARIBIC measurement is at the lower end of those other independent measurements. Nevertheless, given that we deal with a snapshot observation, this result is encouraging.

[11] Data for the day of measurement were neither available for OMI, SCIAMACHY nor GOME-2 at "www.temis.nl", accessed on 2013-04-12.

8. Network of DOAS Instruments in Passenger Aircraft

This chapter deals with the possible adaptation of DOAS instruments for other passenger aircraft. The expected benefits and needs of the installation of a DOAS based network are discussed.

8.1. Expected Benefits and Flight Hours

The first DOAS instrument onboard CARIBIC was in operation from 2005 to 2009, the current one has been flying since 2009. In those years, many events have been observed, cf. *Dix* (2007), *Dix et al.* (2009), *Heue et al.* (2010), *Heue et al.* (2011), *Walter et al.* (2012), although the system was onboard the aircraft for only a small fraction of time. The number of flight hours in the recent years allow a rough estimate about the potential increase of the measurement time when using a permanently installed system. The first regular flights since the renovation of the container and the installation of the new DOAS system took place in June 2010. Within 2.5 years (until December 2012), 112 flights (flights 297–408) took place, containing ≈1100 flight hours, which correspond to 440 hours per year. The annual number of flight hours of a commercial aircraft depends on the aircraft type and the usage (long distance or short distance flights). For assuming the aircraft to be flying roughly the half of the 8766 hours of a year (taking the time for loading and maintainance into account), this would mean, that a permanently installed instrument could measure 10 times longer than currently done within CARIBIC, or '4 Norilsk and 4 Paris events' each year and several BrO observations and deep convective clouds.

In this upscaling, the fraction of daylight time was assumed to be the same as for the CARIBIC flights. There, in 51 %, of the flight time, the SZA was below 80°, thus roughly the half of the time was suitable for DOAS measurements. This fraction is strongly dependent on the flight route. Another aspect is the steadiness of the instrument and the need for maintainance. In seven of the abovementioned 112 flights, no or only a few usable spectra were taken due to technical problems of the power supply for or within the the container or bugs of the measurement routine of the DOAS instrument. Furthermore, the fibre bundle for the upward looking instrument was broken during several flights (Sect. 6.1.1). In CARIBIC, there are several weeks between two flight sets,

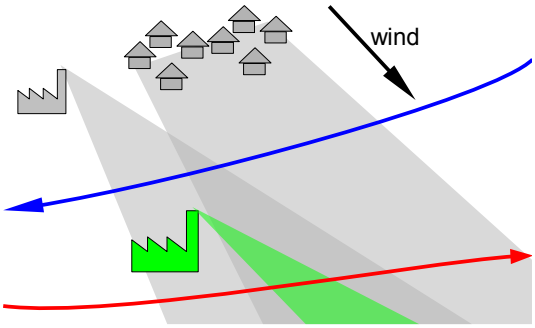

Figure 8.1.: The flux under the red flight route contains the plume of several sources. To retrieve the output of a single source (green) the background (gray) can be corrected by subtracting the flux under the blue flight route. (From *Walter et al.* (2012))

where problems of the container instrument can be issued, while the exchange of the fibres can only be done during a larger maintainance of the aircraft. For a permanently installed instrument, it is crucial to be both, robust and easy to exchange by a spare part in short time.

Having 10 times more spectra has the advantages to be able to investigate further megacities and large facilities and to have repeated measurements. Concerning the number of 'new' emission sources, it has to be countered that Norilsk is a facility with outstanding high SO_2 emissions, and also the NO_2 emission of Paris is reached only by a limited number of other megacities. However, also with CARIBIC, further cities were clearly observed, e.g. Tianjin (Sect. 7.1.1), but not under ideal circumstances (wind direction, clouds, flight route too close or too far from city). Here, the chances of good snapshots increase with a higher flight frequency.

Important is the possibility of repeated measurements, because major uncertainties in the flux estimations of Norilsk and Paris were (partly) of statistic kind like the uncertainties in the current wind field, cf. discussion in Sect. 7.5.4. Also the doubtful extrapolation from one single snapshot to an annual emission estimate can be overcome.

A further improvement would be the installation of DOAS instruments in a larger number of passenger aircraft as part of a network. This would increase the spatial and temporal coverage – more flight routes would be probed more often. Therewith, diurnal, weekly and seasonal variations of emissions could be observed. Especially the diurnal cycle in cities is a problem for satellite observations, because satellites with a sun-synchronous orbit overpass a city every day at the same time (e.g. during rush hours), so they may be biased.

Different instruments flying on the same route can be used to validate each other. Also satellite observations can be validated by such a network (and vice versa). The comparison of the data from these different platforms represents an application as well as a validation of radiative transfer models.

A network of DOAS instruments also allows to resolve sources that are downwind

other sources, as depicted in Fig. 8.1. There, the aircraft on the red flight route measures both, the emission of the green industrial plant as well as the emission of the city behind. By subtracting the flux retrieved by the aircraft on the blue flight route, the industrial plant can be isolated, if the temporal distance between both measurements is not too large.

8.2. Technical Issues, Adaptation in Aircraft

For designing a DOAS instrument for the usage in passenger aircrafts, several points have to be considered. In the following, some requirements are discussed.

8.2.1. Requirements

Weight and Mechanical Stability

Any load of an aircraft has to be lightweight in order to save energy. Therefore, DOAS instruments are well-suited, because their mass is typically quite low compared to other measurement techniques. The weight of the CARIBIC instrument with its three spectrographs is below 15 kg, including cooling, electronics, measurement computer and housing. Additional weight comes from the telescope block in the pylon ($\sim$0.5 kg) and the quartz fibres. The latter weight depends on the distance between the optics and the spectrograph. Such fibres are not necessary in every setup.

Probably the heaviest single part of the instrument is the body of the spectrograph, containing the mirrors, the grating and the detector. Typically (and so for the CARIBIC instrument), it consists of a quite solid milled out aluminium block and a lid. This provides mechanical stability against vibrations and pressure variations. The latter one can be avoided by allowing air exchange between the inside and outside of the spectrographs, but then, humidity and dust have to be kept in mind. Also the instrument's housing might be redundant or could be made lighter. In the end, the weight should be no significant problem.

Energy Consumption and Electromagnetic Compatibility

Being part of an aircraft, the instrument should save energy. Because the energy consumption of the current instrument is only around 50 W, this is not a crucial point. However, reducing the power consumption also reduces the heat production and therefore increases the fire safety. Furthermore, a lower heat production makes the temperature stabilisation and the cooling of the detector easier to handle. The spectrograph itself does not consume any energy, the detector only small amounts, so the computer and the electronics (read out, temperature control) would be the candidates for improvements. A further but small energy consumption would occur in the case of using a scanning device for Imaging DOAS.

As already experienced with the CARIBIC container, the electromagnetic compatibility of the instrument has to be guaranteed. Although a DOAS instrument mainly consists of standard electronic components, an EMC test has to be performed, and the threshold values are lower in avionics than in 'standard environments'. The clock generator of the computer and the read out electronics of the camera can be sources for electromagnetic emission. An appropriate EMC housing and a electromagnetic filter can solve that problem.

Maintainance

In the case of CARIBIC, the container and its components can be maintained after each set of flight. For a permanently installed DOAS network, the effort of maintainance has to be decrease as far as possible. The crew should not be bothered with additional work concerning the measurements. Therefore, the measurements have to be performed fully automatically, also a widely automated approach for the data transfer of the raw data to servers of the network is needed. The instrument has to work reliably for weeks without any service. If nevertheless the instrument has to be repaired, it is important to have a quick access to it. Usually the time schedule of the aircraft does not contain enough time for repairing the instrument onboard. Therefore, it should be possible to replace the instrument by an identical spare instrument and repairing it offline.

Costs

Like for any project, financial aspects are relevant for such a network. The main factors for the costs are the development and the building ot the instruments, the maintainance and the evaluation of the data. The development includes necessary adaptations inside the aircraft and at the shell. Hereby, the safety has to be guaranteed by performing extended tests and careful consideration of the regulations. Using aircraft of the same or similar type can help to minimize those costs. The most expensive parts of the instruments are the spectrographs (containing two mirrors and the grating) and the detector. At least for the costs for the assembly of the parts, there is space for reductions when producing a large number of identical devices. In ideal case, new models of aircraft would be directly equipped with remote sensing instruments, saving time for the installation. During operation, the data have to be transferred to a central computing facility (server), which can be done widely automatically without much effort. The expenses on the evaluation depend on the scientific questions and can be attributed to interested institutions (e.g. atmospheric research groups).

8.2.2. Position and Measurement Geometry

In the most basic version, the instrument only contains one viewing direction. For emission estimates, the nadir direction is best suited. For that purpose, a quartz window

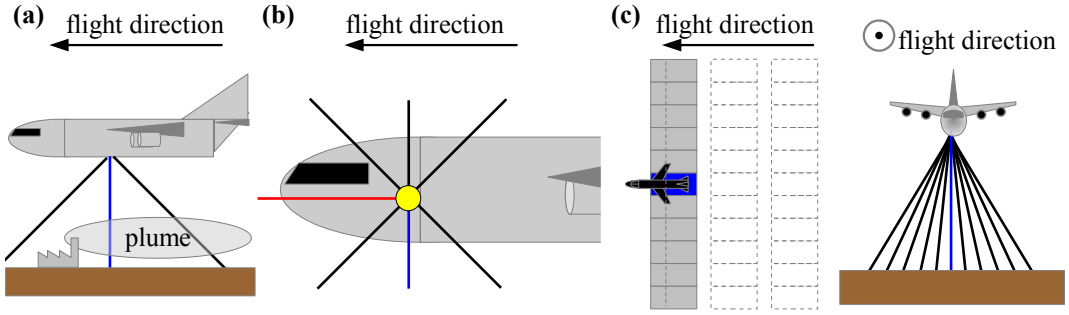

Figure 8.2.: Examples for measurement geometries. The blue line represents the nadir direction. (**a**) Slant forward, nadir and slant backward directions for informations about the vertical distribution of the plume; (**b**) Protruding part at the side of the aircraft (or towards the nose) for upward and frontward looking; (**c**) Imaging DOAS (several lines of sight perpendicular to the flight direction) for the retrieval of two-dimensional maps.

with a radius of a few millimetre at the bottom of the aircraft is sufficient. Several lines of sight can be realised either by a scanning device, several spectrographs or an imaging spectrograph. For the case of a scanning device, the different directions are recorded after each other, and a moving part is necessary, which might be error-prone considering the everyday usage.

In Fig. 8.2a, a slant foward and a slant backward viewing direction are added to the nadir direction, providing information about the vertical position of a plume. Under certain assumptions, a tomographic reconstraction of a plume is possible, cf. *Heue* (2005). With further elevation angles (MAX-DOAS, cf. Sect. 4.4), also vertical profiles of horizontally widespread layers can be obtained. A protruding part at the side of the aircraft also allows upward and frontward looking (limb) directions for enhanced sensitivity towards the stratosphere and the UTLS (Fig. 8.2b). A real-time analysis of the frontward looking direction (red line) can be used as an (additional) forewarning system for volcanic clouds based on the measurement of SO_2, cf. *Vogel et al.* (2011).[1] The installation at the bottom of the aircraft enables several downward viewing directions perpendicular to the flight route for Imaging-DOAS (Fig. 8.2c): In combination with the forward moving of the aircraft, two-dimensional SCD-fields (maps) are created, cf. *Heue et al.* (2008), *Walter* (2008), General (in preparation).

8.3. Data Analysis

In order to be able to efficiently use the produced data, their collection, storage and analysis has to be prepared before the first data are taken. There is a large variety of existing networks dealing with similar challenges, like radio soundings or ground based measurement stations. Very large datasets are produced by satellites. As the

[1] Whether the SO_2 signal can be used as indicator for volcanic ash, depends on the composition of the volcanic emission, cf. Sect. 7.2.

satellite community also uses DOAS or modified analysis methods, it can offer ideas for the implementation of an airborne DOAS network. Also the CARIBIC dataset shows examples of difficulties to deal with, especially with conventions changing in the course of time.

8.3.1. Requirements

In order to avoid inconsistencies within the dataset, each instrument has to use the same data format, and all raw data have to be stored and managed centrally. The server receives the raw data from all instruments, in best case in real-time, transmitted from the aircrafts to satellites or ground-based stations during flight. For the case of the CARIBIC DOAS instrument, one spectrum is taken roughly every 8 seconds by each spectrograph with a size of roughly 8 Kilobytes, which corresponds to a data rate of 1 Kilobyte per second and spectrograph, which is quite moderate. Additionally (for redundancy) or alternatively, the data can be stored by the instrument itself (as it is the case for the CARIBIC DOAS instrument) or another data storage device within the aircraft. The data have then to be transferred to the network server at the airport.

8.3.2. Additional Data

Beside the spectrum itself, additional information are necessary. The most important ones are time and coordinates. In CARIBIC, those data are offered by the ARINC bus system and stored by the Master computer (cf. Sect. 6.7.1). There, the altitude is not given directly, but in terms of pressure. Also the attitude (pitch, roll, yaw) of the aircraft is relevant because it has a direct influence on the viewing direction. Unstable temperatures cause problems at the DOAS analysis (cf. Sect. 6.4.2), therefore this parameter has also to be logged. The pressure surrounding (and inside) the instrument is relevant for the wavelength calibration (cf. Sect. 4.3.4). The AMF retrieval is influenced by the aerosol load in the atmosphere, therefore it would be ideal to have instruments for the remote observation of aerosols and clouds (e.g. an additional spectrograph with a wide wavelength range, reaching into IR). Otherwise, satellite data (e.g. from the MODIS instrument) or model data can be used. Furthermore, the DOAS-data themselves can be used for aerosol retrieval in case of a MAX-DOAS setup, cf. *Frieß et al.* (2006), *Yilmaz* (2012).

8.3.3. Data Products

The acquired spectra contain numbers representating the incoming radiation for several wavelengths. The result of the DOAS analysis are SCDs. Based on RTM, and with the help of assumptions about the relative concentrations, these can be converted to VCDs, to concentrations or mixing ratios, which are the preferred quantities for the most threedimensional atmospheric models. However, these steps contain uncertainties,

and it depends on the scientific question, which quantity is the most adequate one. Therefore, several Data Products are necessary. In the satellite community, the products are typically classified into several levels (Sect. 8.3.4).

Raw Data

Natively, the raw data themselves represent the first data product to be stored. While the other products can be deduced from the raw data and change with other settings of the algorithms or other analysis methods, the raw data represent a valuable spectral archive.

Corrected Raw Data

Often, the raw data contain several errors which can lead to wrong analysis results or crashes of the retrieval algorithm. Therefore, a slightly conditioned version of the raw data is usually created for the further analysis (cf. 'Level 1 data' in Sect. 8.3.4). For the case of CARIBIC DOAS, the time was the most obvious quantity which had to be corrected due to the problems of the computer clock (Sect. 6.5.2).

As the altitude offered by the ARINC bus system was based on the pressure, a more precise altitude information might be derived by adding information about the pressure profile based on weather observations. Also the longitude and latitude can significantly differ from the real coordinates, depending on whether GPS data or data based on a gyroscope are taken. The discrepancy of the latter one increases with the time since the last synchronisation (which is usually performed at the airport before starting). For a correction of the position data close to the destination airport cf. Sect. 5.4. The GPS data are more accurate, but they may contain gaps when the GPS signal is too low. So the gaps have to be filled by interpolation, if available with the help of the gyroscopic data. In case of sudden interruption of the power supply, log files and spectra files can not be stored correctly, leading to missing or corrupted files which can cause problems during the further analysis. A consistent way to handle the resulting gaps is needed for an undisturbed automated data evaluation.

The offset signal and the dark current of the instrument could also be corrected for in this data set, because this signals are an instrument feature and do not belong to the real signal. However, this correction is not straightforward. Instead of just subtracting the offset and the dark current signal (weighted by time and scan number), a more sophisticated correction might take account of the temperature dependence of those signals or use other spectra for the retrieval of those signals. This would lead to further versions of 'corrected raw data'. To avoid this, the offset and dark current corrections can be postponed to the next step, being included in the DOAS retrieval algorithm. Much the same applies for the wavelength calibration.

SCDs and VCDs

The SCDs are the direct result of the DOAS retrieval. At least for the nadir direction, the SCD can be directly compared to Satellite Observations to some extend, if the time of day (resulting in the SZA) coincides. However, already the SCDs can significantly depend on the settings of the DOAS retrieval (wavelength range, choice of literature cross sections, instrument function etc.).

The conversion of the SCDs to VCDs, which have a more handy physical meaning, introduces a variety of choices in terms of the transfer model and the needed assumptions about parameters like concentration profiles of aerosols and gases, the surface albedo and cloud condition. An imprecise approach is to use geometric AMF (Sect. 6.7.5), however, it is simple and straightforward, because for this calculation, only the SCD, the viewing direction and the SZA are needed. For individual case studies, different RTM can be tested with a variety of parameters. For operational retrievals, however, the complexity of the RTM has to be limited, in particular, only parameters can be taken into account, which are globally available or appreciable.

Concentrations and Fluxes

In Sect. 7.5, the calculation of the Norilsk mining facilities were calculated. That approach can be applied to other sources as well. While the settings for the radiative transfer, the extrapolation of the wind data and the choice of the used spectra were done manually for that single measurement, a more automated approach is necessary for the extension to other sources and repeated measurements. Also the conversion of the retrieved SCD to concentrations needs assumptions of the relative concentration profile. Therefore, additional information of measurements and models are needed, cf. Sect. 4.5.1. Vertical information of the measured species can also be obtained by MAX-DOAS measurements, using multiple viewing directions. Such measurements have been performed onboard research aircraft, as described in *Heue* (2005).

8.3.4. GOME-2 Satellite Products

Due to the almost permanent dataflow of satellites, a large experience about the storage and analysis of large spectral datasets has been developed in the satellite community. Because there are many satellites of several institutions, there is not one single concept; however, for the spectra and the retrieval of trace gases, the data are typically classified into different levels. Because similar levels could be used for an airborne DOAS network, the data product levels of the GOME-2 instrument onboard the METOP satellite are briefly described here, based on information given by *Callies et al.* (2004) and *EUMETSAT* (2011).

With *Level 0*, the raw data are denoted, which are send in packets by the satellite to the receiving ground stations via an X-band link with a data transfer rate of about

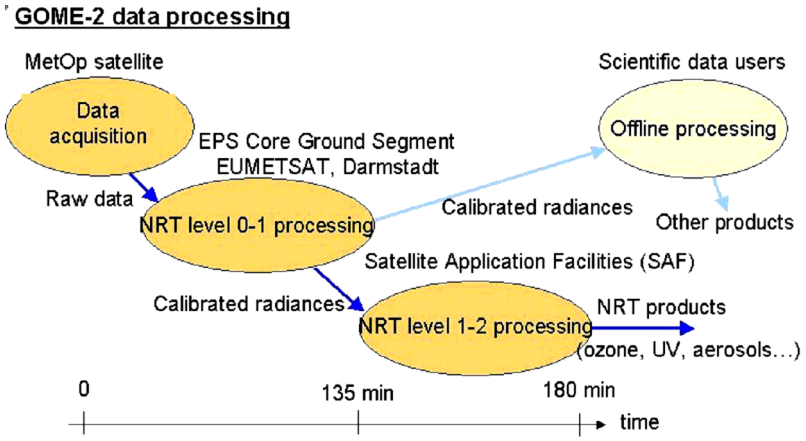

Figure 8.3.: Processing chain for GOME-2 data. (From *Callies et al.*, 2004)

400 kbit/s. This data are transmitted to a central Core Ground Segment (CGS) in Darmstadt (Germany), which is operated by EUMETSAT (**Eu**ropean Organisation for the Exploitation of **Met**eorological **Sat**ellites).

The Level 0 to *Level 1* (1a and 1b) processor is part of the EUMETSAT CGS. Here, several preprocessing steps are included like the calibration of the wavelength and the irradiances. Technical characteristics like the slit function of the spectrographs and the temperature dependency are considered. A dark current and an offset correction are applied based on dark measurements which are performed each orbit during the eclipse, when the earth is between the satellite and the sun. The Level 1b dataset furthermore includes time-stamps and geolocations for each spectrum as well as a straylight-correction. Also the effective cloud fraction and the cloud top pressure are calculated (*EUMETSAT*, 2011).

Level 2 data are meteorological or geophysical products like the Slant and Vertical Column Densities of trace gases. The calculation of the Level 2 products based on the Level 1b dataset is in charge of the 'Satellite Application Facility on Ozone & Atmospheric Chemistry Monitoring' (O3M SAF), a consortium consisting of several institutes and coordinated by the Finnish Meteorological Institute (FMI). The O3M SAF provides two operational Level 2 classes to end-users, namely near-real-time products and off-line products. The near-real-time (NRT) products are released within three hours after the measurement by the satellite, the off-line products within 15 days. Furthermore, experimental products can be disseminated.

Besides the processing by the O3M SAF, the level 1 data are spread to a larger number of institutes for further analysis and testing of different algorithms. Significant improvements of the retrieval algorithms can lead to a reanalysis of the level 2 product.

9. Summary

In this chapter, the experiences with the new DOAS instrument and the results presented in Chap. 7 are summarized and an outlook about open issues and future investigation is given.

9.1. Instrument

After some smaller problems in the beginning had been solved, the container instrument has been working reliably. Compared to the first DOAS instrument onboard CARIBIC, a higher sensitivity and the wavelength range of the instruments (286–423 nm) allowed to measure particularly BrO and SO_2 with higher precision (Sect. 7.2, 7.3, 7.5). Early problems with straylight could be solved by inserting blinds in the spectrographs (Sect. 6.3.4).

A rather simple PI-controller based routine included in the measurement procedure provides stable temperatures of the optical bench as long as the ambient temperature is not too far above or below the setpoint temperature (Sect. 6.4.3). Unfortunately, the cooling capacity of the Peltier elements and the connected electronics are not strong enough if the cargo compartment has notably high temperatures. In winter, also the reverse case occurred, where the ambient temperature was lower than the setpoint temperature for a large fraction at the beginning of the flight. For such cases, the possibility to heat would be desirable.

Malfunction occurred due to broken fibres. While at first, the small bend radius and the large temperature variability inside the CARIBIC pylon were supposed to be the most vulnerable part of the fibres, the experience with the recently broken fibres indicate that the distort of the last meters at the other end is more problematic, caused by the rolling-up of the fibres in the floor of the aircraft's cargo compartment after each set of flights. Therefore a coupling between the stationary and the flexible part of the fibre is intended, allowing to replace the flexible part in case of break, cf. Sect. 6.1.1.

A weak point of the instrument is the accessibility of the spectrographs for maintainance. Connected to each spectrograph is a bushing for fixing the fibre end against twisting. For the adjustment of these bushings, not only the outer housing of the instrument has to be opened, but also the spectrograph box (p. 94 Fig. 6.5d). Due to the narrow space and several thin cables within this box, this is always elaborate and involves the risk of damaging the cables. Therefore, a potential successor instrument

should allow an easier accessibility of the units, also with regard to the possibility of replacing parts in case of malfunction.

9.2. Results

Before the first regular flights, three special mission flights were performed to investigate the eruption of the Eyjafjallajökull volcano in spring 2010. In good agreement with satellite data, the first flight on 20 April 2010 showed no or only minor amounts of SO_2 in the early stage of the eruption, while for the second flight on 16 May 2012, SCDs up to $7 \cdot 10^{17}$ molec/cm^2 were found in the nadir direction and $9 \cdot 10^{17}$ molec/cm^2 in the $-10°$ direction; also BrO was detected, cf. Sect. 7.2. A detailed analysis including satellite comparison has been published by *Heue et al.* (2011).

Interesting insights into processes in deep convective clouds were found at flight 353 in August 2011, where nitrous acid and formaldehyde could be measured due to the strongly enhanced light path inside the clouds. The investigation of this event will be published soon by *Heue et al.* (2013); cf. *Dix* (2007) and *Dix et al.* (2009) for a similar observation by the first CARIBIC DOAS instrument.

During a flight from Frankfurt to Vancouver in April 2011, BrO was detected twice in all three viewing directions, with highest SCDs in the nadir direction. The first peak was found shortly before crossing the eastern coast of Greenland, the second one over Northern Canada (p. 137 Fig. 7.9). In the first case, it could not clearly be identified whether the enhancement was of stratospheric origin or whether tropospheric BrO was observed. In contrast to that, the second peak could be confidently attributed to tropospheric BrO – most probably due to a bromine explosion –, in good agreement with satellite data and an algorithm by *Sihler et al.* (2012) for discerning between tropospheric and stratospheric BrO. Because vertical distinctions based on satellite nadir observation are in principle challenging, such airborne observations represent a feasible way of validation. After BrO in the arctic spring had already been detected by the old DOAS instrument in 2009, this was the second time for CARIBIC to observe bromine activation events, therefore the chances are high for further arctic BrO observations depending on the choice of the flight routes.

In September 2012, SO_2 and NO_2 in the plume of a power plant were measured by the $+10°$ and the $-10°$ instruments, shortly before landing at Caracas (Sect. 7.4). Due to the temporal coincidence of the detection between both instruments, an alternative explanation, namely descending into horizontally homogeneously polluted boundary layer, could be excluded. Other potential sources could be excluded with the help of HYSPLIT backward trajectories.

One of the largest anthropogenic point sources of SO_2 worldwide was observed in October 2010, namely the huge industrial facilities of Norilsk Nickel. While the wind was coming from the north, the aircraft was flying westwards, just a few Kilometres to the south of the industrial plants, thus crossing the plume nearly perpendicular. This allowed a flux calculation and therefore an emission estimate, using wind data based on ECMWF and the assumption that the plume was evenly distributed throughout the lowermost 1.5 km. An emission rate of $3 \cdot 10^{26}$ molec/s was calculated, which corresponds to 30 kg/s of SO_2 or 1 Megaton per year. This amounts to nearly 1 % of the global anthropogenic SO_2 emission, being 120 Mt/yr in 2005 according to the EDGAR database (*EDGAR*, 2011).

Uncertainties were discussed in Sect. 7.5.4 and sensitivity studies were performed by using other assumptions about the albedo, aerosol scattering and the plume's profile. Thereby, also up to 60 % higher and 20 % lower values were obtained, cf. p. 158 Table 7.1. The main uncertainties are supposed to be caused by inaccuracies in the wind field, the ground albedo and thus the AMF.

The CARIBIC estimate is lower but within the same order of magnitude as the 1.685 ± 0.3 Mt/yr SO_2 reported by *Khokhar et al.* (2008) as average for the years 1996–2002, based on GOME data, cf. Sect. 7.5.5. It should be emphasized, that in Khokhar's study, not a flux calculation was performed. Instead, a calculation was used, in which the obtained emission is antiproportional to the lifetime τ of SO_2, cf. p. 159 (7.1). While that approach has the advantage of not depending on wind data, the large uncertainties in the lifetime τ is problematic (cf. p. 29), while τ is only of minor importance for the flux calculation (as long as τ is large compared to the time between emission and observation). OMI data of the day of the CARIBIC overpass showed a reasonable agreement with the CARIBIC result when using $\tau = 1$ day, namely 0.7 Mt/yr, cf. Sect. 7.5.6.

Because the estimates based on the CARIBIC and the OMI observations of that day are only a snapshot and therefore the extrapolation to one year to be treated with caution, a decreasing trend of Norilsk's emission can not be deduced based on this comparison. But the rather well agreements demonstrate the applicability of flux calculations using automated measurements from passenger aircraft.

A flux calculation was also performed for the downwind of the city of Paris in March 2011, observed during a flight from Bogota to Frankfurt, cf. Sect. 7.6. In contrast to the case of Norilsk, the plume did not cross the flight route perpendicularly, and the wind direction changed with increasing height. Therefore the calculated emission highly depended on the assumed vertical profile – for assuming a box profile of more than 1 km altitude even negative fluxes were calculated. More realistic plume heights lead to fluxes around $2 \cdot 10^{25}$ to $3 \cdot 10^{25}$ molec/s. These are within the range of results reported by *Shaiganfar* (2012), namely $2 \cdot 10^{25}$ to $13 \cdot 10^{25}$ molec/s.

In a reverse argumentation, assuming a flux of $2 \cdot 10^{25}$ molec/s or more, the combina-

tion of the CARIBIC observation and the wind field (based on ECMWF or a sounding station near Paris) could be used to constrain the height of the downwind plume of Paris to less than ∼400–600 m a.g.l. However, due to the large uncertainties in the wind field and the shape of the profile, this reverse argumentation is rather speculative.

9.3. Outlook

Considering the experiences with the instrument mentioned in Sect. 6 and 9.1, following issues may be considered for improvement.

- An increase of the light quantity is always desirable, which could be obtained by larger (higher) detectors. The DOAS housing still contains some free space, therefore slightly larger spectrographs would be possible for gaining a higher spectral resolution and potentially less straylight.
- A frequent problem is the temperature stabilisation. Therefore, special attention should be taken concerning the capacity of the cooling system.
- As mentioned in Sect. 6.6, several single scans are added into one spectrum. The exposure time is set depending on the light intensity during the previous spectrum. Due to the high speed of the aircraft, the light intensity can significantly change within the total acquisition time of a spectrum due to clouds or changes in the albedo. Therefore some of the scans of a spectrum can be oversaturated, leading to a DOAS fit of poor quality. To avoid this, such an adaptation or a saturation check should be implemented after each scan. Alternatively or additionally, a realtime measurement (e.g. by a photodiode) could be used to stop the acquisition as soon as enough light has been received (U. Platt, pers. comm., 2013).
- A mechanical coupling of the fibre cables would allow a quick replacement in case of a break in the upper part of the cable, cf. Sect. 9.1, Sect. 6.1.1.
- As mentioned in Sect. 9.1, a potential successor instrument should allow an easier accessibility of the units, also with regard to replacing parts in case of malfunction. Also a timely availability of spare parts should be taken into account, considering the monthly sequence of measurement flights.
- In Sect. 5.4, the impreciseness of the position data were addressed. Especially with regard to the nadir instrument, rather precise GPS data would be desirable.
- The video camera can help to identify clouds and changes in the surface albedo. However, the currently installed one has a rather poor contrast, a low resolution and another viewing direction than the DOAS instruments. Here, an additional

camera with nadir view would give additional information. For special events, it could even help to reconstruct the aircraft's position (cf. previous point) or the field of view of the nadir instrument.

- A permanent installation of a DOAS system onboard a passenger aircraft would yield a tenfold amount of spectra. In a network of several such instruments, the emissions of large cities and industrial plants could be monitored, cf. Chap. 8.

The existing spectral dataset recorded by both, the old and the new CARIBIC DOAS instruments, contains a large potential for further investigation, for example the only briefly presented events in Sect. 7.1. In this thesis, which focused on tropospheric events, stratospheric signals of NO_2 and O_3 were avoided by using a FRS close to the event. However, in combination with radiative transfer modeling, these stratospheric signals can be analyzed in a statistical way for creating a climatology of this substances. Therewith, satellite retrievals can be validated. Reversely, radiative transfer models can be tested, e.g. with the help of the O_4 data.

Because CARIBIC is an ongoing long-term project, many further interesting findings can be expected, and with the increasing timespan of the project, trend analyses based on the DOAS data should be investigated.

Bibliography

Ångström, A., The Albedo of Various Surfaces of Ground, *Geografiska Annaler*, *7*, pp. 323–342, doi:10.2307/519495, 1925.

Alicke, B., U. Platt, and J. Stutz, Impact of nitrous acid photolysis on the total hydroxyl radical budget during the Limitation of Oxidant Production/Pianura Padana Produzione di Ozono study in Milan, *Journal of Geophysical Research: Atmospheres*, *107*(D22), LOP 9–1–LOP 9–17, doi:10.1029/2000JD000075, 2002.

Anderson, L. G., J. A. Lanning, R. Barrell, J. Miyagishima, R. H. Jones, and P. Wolfe, Sources and sinks of formaldehyde and acetaldehyde: An analysis of Denver's ambient concentration data, *Atmospheric Environment*, *30*(12), 2113–2123, doi:10.1016/1352-2310(95)00175-1, 1996.

Andreae, M. O., Ocean-atmosphere interactions in the global biogeochemical sulfur cycle, *Marine Chemistry*, *30*(0), 1–29, doi:10.1016/0304-4203(90)90059-L, 1990.

Andreae, M. O., and P. Merlet, Emission of trace gases and aerosols from biomass burning, *Global Biogeochemical Cycles*, *15*(4), 955–966, doi:10.1029/2000GB001382, 2001.

Andreae, M. O., R. J. Ferek, F. Bermond, K. P. Byrd, R. T. Engstrom, S. Hardin, P. D. Houmere, F. LeMarrec, H. Raemdonck, and R. B. Chatfield, Dimethyl sulfide in the marine atmosphere, *Journal of Geophysical Research: Atmospheres*, *90*(D7), 12,891–12,900, doi:10.1029/JD090iD07p12891, 1985.

Arlander, D., D. Brüning, U. Schmidt, and D. Ehhalt, The tropospheric distribution of formaldehyde during TROPOZ II, *Journal of Atmospheric Chemistry*, *22*, 251–269, doi:10.1007/BF00696637, 1995.

Assonov, S. S., C. A. M. Brenninkmeijer, T. J. Schuck, and P. Taylor, Analysis of ^{13}C and ^{18}O isotope data of CO_2 in CARIBIC aircraft samples as tracers of upper troposphere/lower stratosphere mixing and the global carbon cycle, *Atmospheric Chemistry and Physics*, *10*(17), 8575–8599, doi:10.5194/acp-10-8575-2010, 2010.

ASTM, 2000 ASTM Standard Extraterrestrial Spectrum Reference E-490-00, doi:10.1520/E0490-00AR06, data from spreadsheet `http://rredc.nrel.gov/solar/spectra/am0/E490_00a_AM0.xls`, online accessed on 2013-05-17, 2000.

Atkinson, R., D. L. Baulch, R. A. Cox, J. N. Crowley, R. F. Hampson, R. G. Hynes, M. E. Jenkin, M. J. Rossi, and J. Troe, Evaluated kinetic and photochemical data for atmospheric chemistry: Volume I – gas phase reactions of O_x, HO_x, NO_x and SO_x species, *Atmospheric Chemistry and Physics*, *4*(6), 1461–1738, doi:10.5194/acp-4-1461-2004, 2004.

Atkinson, R., D. L. Baulch, R. A. Cox, J. N. Crowley, R. F. Hampson, R. G. Hynes, M. E. Jenkin, M. J. Rossi, and J. Troe, Evaluated kinetic and photochemical data for atmospheric chemistry: Volume III – gas phase reactions of inorganic halogens, *Atmospheric Chemistry and Physics*, *7*(4), 981–1191, doi:10.5194/acp-7-981-2007, 2007.

Baidar, S., H. Oetjen, S. Coburn, B. Dix, I. Ortega, R. Sinreich, and R. Volkamer, The CU Airborne MAX-DOAS instrument: vertical profiling of aerosol extinction and trace gases, *Atmospheric Measurement Techniques*, *6*(3), 719–739, doi:10.5194/amt-6-719-2013, 2013.

Baker, A. K., F. Slemr, and C. A. M. Brenninkmeijer, Analysis of non-methane hydrocarbons in air samples collected aboard the CARIBIC passenger aircraft, *Atmospheric Measurement Techniques*, *3*(1), 311–321, doi:10.5194/amt-3-311-2010, 2010.

Barnes, I., K. H. Becker, and I. Patroescu, The tropospheric oxidation of dimethyl sulfide: A new source of carbonyl sulfide, *Geophysical Research Letters*, *21*(22), 2389–2392, doi:10.1029/94GL02499, 1994.

Batenburg, A. M., T. J. Schuck, A. K. Baker, A. Zahn, C. A. M. Brenninkmeijer, and T. Röckmann, The stable isotopic composition of molecular hydrogen in the tropopause region probed by the CARIBIC aircraft, *Atmospheric Chemistry and Physics*, *12*(10), 4633–4646, doi:10.5194/acp-12-4633-2012, 2012.

Bates, T. S., R. J. Charlson, and R. H. Gammon, Evidence for the climatic role of marine biogenic sulphur, *Nature*, *329*(6137), 319–321, doi:10.1038/329319a0, 1987.

Becker, G. T., RighTime™ – A Real Time Clock Correcting Program for MS-DOS-Based Computer Systems, Air System Technologies, Inc, 14232 Marsh Lane, Suite 339, Dallas, TX, 75234-3899; `http://oai.dtic.mil/oai/oai?verb=getRecord&metadataPrefix=html&identifier=ADA502229`, 1992.

Beirle, S., K. F. Boersma, U. Platt, M. G. Lawrence, and T. Wagner, Megacity Emissions and Lifetimes of Nitrogen Oxides Probed from Space, *Science*, *333*(6050), 1737–1739, doi:10.1126/science.1207824, 2011.

Bethan, S., G. Vaughan, and S. J. Reid, A comparison of ozone and thermal tropopause heights and the impact of tropopause definition on quantifying the ozone content of the troposphere, *Quarterly Journal of the Royal Meteorological Society*, *122*(532), 929–944, doi:10.1002/qj.49712253207, 1996.

BIPM, *Le système international d'unités (SI)*, Bureau international des poids et mesures (BIPM), Sèvres Cedex, France, ISBN 978-92-822-2213-3; `http://www.bipm.org/utils/common/pdf/si_brochure_8.pdf`, 2006.

Blacksmith Instititute, The World's Worst Polluted Places – The Top Ten of The Dirty Thirty, `www.blacksmithinstitute.org`; `http://www.worstpolluted.org/`, 2007.

Bleck, R., Numerical Forecasting Experiments Based on the Conservation of Potential Vorticity on Isentropic Surfaces, *J. Appl. Meteor.*, *12*(5), 737–752, doi:10.1175/1520-0450(1973)012<0737:NFEBOT>2.0.CO;2, 1973.

Bobrowski, N., and U. Platt, SO_2/BrO ratios studied in five volcanic plumes, *Journal of Volcanology and Geothermal Research*, *166*(3-4), 147 – 160, doi:10.1016/j.jvolgeores.2007.07.003, 2007.

Bobrowski, N., G. Honninger, B. Galle, and U. Platt, Detection of bromine monoxide in a volcanic plume, *Nature*, *423*(6937), 273–276, doi:10.1038/nature01625, 2003.

Bobrowski, N., R. von Glasow, A. Aiuppa, S. Inguaggiato, I. Louban, O. W. Ibrahim, and U. Platt, Reactive halogen chemistry in volcanic plumes, *J. Geophys. Res.*, *112*(D6), D06,311, doi:10.1029/2006JD007206, 2007.

Bogumil, K., J. Orphal, T. Homann, S. Voigt, P. Spietz, O. C. Fleischmann, A. Vogel, M. Hartmann, H. Kromminga, H. Bovensmann, J. Frerick, and J. P. Burrows, Measurements of molecular absorption spectra with the SCIAMACHY pre-flight model: instrument characterization and reference data for atmospheric remote-sensing in the 230-2380 nm region, *Journal of Photochemistry and Photobiology A: Chemistry*, *157*(2-3), 167 – 184, doi: 10.1016/S1010-6030(03)00062-5, 2003.

Bohren, C., and B. Albrecht, *Atmospheric Thermodynamics: Elementary Physics and Chemistry*, Oxford University Press, Incorporated, New York, ISBN 978-0-521-89963-5, 1998.

Bozóki, Z., M. Szakáll, A. Mohácsi, G. Szabó, and Z. Bor, Diode laser based photoacoustic humidity sensors, *Sensors and Actuators B: Chemical*, *91*(1-3), 219–226, doi:10.1016/S0925-4005(03)00120-5, 2003.

Brasseur, G., *Atmospheric Chemistry and Global Change*, vol. 654, Oxford University Press New York, Oxford Oxfordshire, ISBN 0195105214, 1999.

Brasseur, G., and S. Solomon, *Aeronomy of the Middle Atmosphere*, no. 32 in Atmospheric and oceanographic sciences library ; 32 ; Atmospheric and oceanographic sciences library, 3., rev. and enlarged ed. ed., XII, 644 S. pp., Springer, Dordrecht, ISBN 1-4020-3284-6, 2005.

Brenninkmeijer, C. A. M., P. J. Crutzen, H. Fischer, H. Gusten, W. Hans, G. Heinrich, J. Heintzenberg, M. Hermann, T. Immelmann, D. Kersting, M. Maiss, M. Nolle, A. Pitscheider, H. Pohlkamp, D. Scharffe, K. Specht, and A. Wiedensohler, CARIBIC – Civil aircraft for global measurement of trace gases and aerosols in the tropopause region, *J. Atmos. Ocean. Technol.*, *16*(10), 1373–1383, doi:10.1175/1520-0426(1999)016<1373:CCAFGM>2.0.CO;2, 1999.

Brenninkmeijer, C. A. M., P. Crutzen, F. Boumard, T. Dauer, B. Dix, R. Ebinghaus, D. Filippi, H. Fischer, H. Franke, U. Frieß, J. Heintzenberg, F. Helleis, M. Hermann, H. H. Kock, C. Koeppel, J. Lelieveld, M. Leuenberger, B. G. Martinsson, S. Miemczyk, H. P. Moret, H. N. Nguyen, P. Nyfeler, D. Oram, D. O'Sullivan, S. Penkett, U. Platt, M. Pupek, M. Ramonet, B. Randa, M. Reichelt, T. S. Rhee, J. Rohwer, K. Rosenfeld, D. Scharffe, H. Schlager, U. Schumann, F. Slemr, D. Sprung, P. Stock, R. Thaler, F. Valentino, P. van Velthoven, A. Waibel, A. Wandel, K. Waschitschek, A. Wiedensohler, I. Xueref-Remy, A. Zahn, U. Zech, and H. Ziereis, Civil Aircraft for the regular investigation of the atmosphere based on an instrumented container: The new CARIBIC system, *Atmospheric Chemistry and Physics*, *7*(18), 4953–4976, doi:10.5194/acp-7-4953-2007, 2007.

Bröske, R., J. Kleffmann, and P. Wiesen, Heterogeneous conversion of NO_2 on secondary organic aerosol surfaces: A possible source of nitrous acid (HONO) in the atmosphere?, *Atmospheric Chemistry and Physics*, *3*(3), 469–474, doi:10.5194/acp-3-469-2003, 2003.

Brühl, C., J. Lelieveld, P. J. Crutzen, and H. Tost, The role of carbonyl sulphide as a source of stratospheric sulphate aerosol and its impact on climate, *Atmospheric Chemistry and Physics*, *12*(3), 1239–1253, doi:10.5194/acp-12-1239-2012, 2012.

Brunner, D., J. Staehelin, D. Jeker, H. Wernli, and U. Schumann, Nitrogen oxides and ozone in the tropopause region of the Northern Hemisphere: Measurements from commercial aircraft in 1995/1996 and 1997, *J. Geophys. Res.*, *106*(D21), 27,673–27,699, doi:10.1029/2001JD900239, 2001.

Budd, L., S. Griggs, D. Howarth, and S. Ison, A Fiasco of Volcanic Proportions? Eyjafjallajökull

and the Closure of European Airspace, *Mobilities*, *6*(1), 31–40, doi:10.1080/17450101.2011.532650, 2011.

Burrows, J. P., M. Weber, M. Buchwitz, V. Rozanov, A. Ladstätter-Weißenmayer, A. Richter, R. DeBeek, R. Hoogen, K. Bramstedt, K.-U. Eichmann, M. Eisinger, and D. Perner, The Global Ozone Monitoring Experiment (GOME): Mission Concept and First Scientific Results, *J. Atmos. Sci.*, *56*(2), 151–175, doi:10.1175/1520-0469(1999)056<0151:TGOMEG>2.0.CO;2, 1999.

Burrows, J. P., U. Platt, and P. Borrell, *The Remote Sensing of Tropospheric Composition from Space*, Physics of earth and space environments, XXXII, 549 S. pp., Springer, Berlin ; Heidelberg [u.a.], doi:10.1007/978-3-642-14791-3, ISBN 978-3-642-14790-6, 2011.

Bussemer, M., Der Ring-Effekt: Ursachen und Einfluß auf die spektroskopische Messung stratosphärischer Spurenstoffe, Diploma thesis, Institut für Umweltphysik, Universität Heidelberg, 1993.

Buxmann, J., 'Bromine and Chlorine Explosion' in a Simulated Atmosphere, Ph.D. thesis, Institut für Umweltphysik, Universität Heidelberg, urn:nbn:de:bsz:16-opus-136552, 2012.

Callies, J., E. Corpaccioli, M. Eisinger, A. Lefebvre, R. Munro, A. Perez-Albinana, B. Ricciarelli, L. Calamai, G. Gironi, R. Veratti, G. Otter, M. Eschen, and L. van Riel, GOME-2 ozone instrument onboard the European METOP satellites, *Proceedings of SPIE–the international society for optical engineering*, *5549*, doi:10.1117/12.557860, 2004.

Calvert, J. G., Hydrocarbon involvement in photochemical smog formation in Los Angeles atmosphere, *Environmental Science & Technology*, *10*(3), 256–262, doi:10.1021/es60114a003, 1976.

Carn, S. A., and T. M. Lopez, Opportunistic validation of sulfur dioxide in the Sarychev Peak volcanic eruption cloud, *Atmospheric Measurement Techniques*, *4*(9), 1705–1712, doi:10.5194/amt-4-1705-2011, 2011.

Carn, S. A., A. J. Krueger, N. A. Krotkov, and M. A. Gray, Fire at Iraqi sulfur plant emits SO_2 clouds detected by Earth Probe TOMS, *Geophys. Res. Lett.*, *31*(19), L19,105, doi:10.1029/2004GL020719, 2004.

Casadevall, T. J., Volcanic Hazards and Aviation Safety: Lessons of the Past Decade, 1993.

Chan, K. L., D. Pöhler, G. Kuhlmann, A. Hartl, U. Platt, and M. O. Wenig, NO_2 measurements in Hong Kong using LED based long path differential optical absorption spectroscopy, *Atmospheric Measurement Techniques*, *5*(5), 901–912, doi:10.5194/amt-5-901-2012, 2012.

Chapman, S., XXXV. On ozone and atomic oxygen in the upper atmosphere, *Philosophical Magazine Series 7*, *10*(64), 369–383, doi:10.1080/14786443009461588, 1930.

Charlson, R. J., J. E. Lovelock, M. O. Andreae, and S. G. Warren, Oceanic phytoplankton, atmospheric sulphur, cloud albedo and climate, *Nature*, *326*(6114), 655–661, doi:10.1038/326655a0, 1987.

Cheng, R. J., J. R. Hwu, J. T. Kim, and S. M. Leu, Deterioration of marble structures. The role of acid rain, *Analytical Chemistry*, *59*(2), 104A–106A, doi:10.1021/ac00129a002, 1987.

Chin, M., and D. J. Jacob, Anthropogenic and natural contributions to tropospheric sulfate: A global model analysis, *J. Geophys. Res.*, *101*(D13), 18,691–18,699, doi:10.1029/96JD01222, 1996.

Clemitshaw, K. C., Coupling between the Tropospheric Photochemistry of Nitrous Acid (HONO) and Nitric Acid (HNO_3), *Environ. Chem.*, *3*(1), 31–34, doi:10.1071/EN05073, 2006.

Clough, S. A., N. S. Grahame, and A. O'Neill, Potential vorticity in the stratosphere derived using data from satellites, *Quarterly Journal of the Royal Meteorological Society*, *111*(468), 335–358, doi:10.1002/qj.49711146805, 1985.

CLS, Airbus Industrie A340-500/600. Operations Manual FLT Crew Traning. Taxi, Takeoff, Climb, Cruise, Descand & Landing., `https://www.commerciallevel.com/misc/A346/CLS_A340_doc.zip`, 2006.

Cox, R. A., and D. Sheppard, Reactions of OH radicals with gaseous sulphur compounds, *Nature*, *284*(5754), 330–331, doi:10.1038/284330a0, 1980.

Crutzen, P., Albedo Enhancement by Stratospheric Sulfur Injections: A Contribution to Resolve a Policy Dilemma?, *Climatic Change*, *77*, 211–220, doi:10.1007/s10584-006-9101-y, 2006.

Crutzen, P. J., Ozone production rates in an oxygen-hydrogen-nitrogen oxide atmosphere, *Journal of Geophysical Research*, *76*(30), 7311–7327, doi:10.1029/JC076i030p07311, 1971.

Crutzen, P. J., The possible importance of CSO for the sulfate layer of the stratosphere, *Geophysical Research Letters*, *3*(2), 73–76, doi:10.1029/GL003i002p00073, 1976.

Cruz, C. N., and S. N. Pandis, The effect of organic coatings on the cloud condensation nuclei activation of inorganic atmospheric aerosol, *Journal of Geophysical Research: Atmospheres*, *103*(D11), 13,111–13,123, doi:10.1029/98JD00979, 1998.

Czerny, M., and A. F. Turner, Über den Astigmatismus bei Spiegelspektrometern, *Zeitschrift für Physik*, *61*, 792, doi:10.1007/BF01340206, 1930.

Demtröder, W., *Experimentalphysik 3: Atome, Moleküle und Festkörper*, 2nd edition 2000, corrected reprint 2004 ed., Springer, Berlin ; Heidelberg [u.a.], ISBN 3-540-66790-3, 2000.

Demtröder, W., *Experimentalphysik 2: Elektrizität und Optik*, 3., überarb. u. erw. aufl. ed., XIX, 482 S. pp., Springer, Berlin ; Heidelberg [u.a.], ISBN 978-3-540-20210-3, 2004.

Deutschmann, T., Atmospheric Radiative Transfer Modelling with Monte Carlo Methods, Diploma thesis, Institut für Umweltphysik, Universität Heidelberg, 2009.

Deutschmann, T., and T. Wagner, *TRACY-II manual 0.85*, Institut für Umweltphysik der Universität Heidelberg, `joseba.mpch-mainz.mpg.de/matr/tracy_II/manual.pdf`, 2007.

Deutschmann, T., S. Beirle, U. Frieß, M. Grzegorski, C. Kern, L. Kritten, U. Platt, C. Prados-Román, J. Puķīte, T. Wagner, B. Werner, and K. Pfeilsticker, The Monte Carlo atmospheric radiative transfer model McArtim: Introduction and validation of Jacobians and 3D features, *Journal of Quantitative Spectroscopy and Radiative Transfer*, *112*(6), 1119–1137, doi:10.1016/j.jqsrt.2010.12.009, 2011.

Diffey, B. L., Solar ultraviolet radiation effects on biological systems, *Physics in Medicine and Biology*, *36*(3), 299, doi:10.1088/0031-9155/36/3/001, 1991.

Dix, B., Spectroscopic Measurements of Atmospheric Trace Gases on Long-Distance Flights, Ph.D. thesis, Institut für Umweltphysik, Universität Heidelberg, urn:nbn:de:bsz:16-opus-81183, 2007.

Dix, B., C. A. M. Brenninkmeijer, U. Frieß, T. Wagner, and U. Platt, Airborne multi-axis DOAS measurements of atmospheric trace gases on CARIBIC long-distance flights, *Atmospheric Measurement Techniques*, *2*(2), 639–652, doi:10.5194/amt-2-639-2009, 2009.

Dobson, G. M. B., Forty Years' Research on Atmospheric Ozone at Oxford: a History, *Appl. Opt.*, *7*(3), 387–405, doi:10.1364/AO.7.000387, 1968.

Draxler, R. R., and G. D. Rolph, HYSPLIT (HYbrid Single-Particle Lagrangian Integrated Trajectory) Model, Access via NOAA ARL READY Website (http://ready.arl.noaa.gov/HYSPLIT.php). NOAA Air Resources Laboratory, Silver Spring, MD., 2011.

Dütsch, H., Vertical ozone distribution on a global scale, *pure and applied geophysics*, *116*(2-3), 511–529, doi:10.1007/BF01636904, 1978.

Dyroff, C., D. Fütterer, and A. Zahn, Compact diode-laser spectrometer ISOWAT for highly sensitive airborne measurements of water-isotope ratios, *Applied Physics B*, *98*, 537–548, doi:10.1007/s00340-009-3775-6, 2010.

EDGAR, Emission Database for Global Atmospheric Research, European Commission, Joint Research Centre (JRC)/Netherlands Environmental Assessment Agency (PBL). Emission Database for Global Atmospheric Research (EDGAR), release version 4.1. http://edgar.jrc.ec.europa.eu/, 2010., 2011.

Ertel, H., Ein neuer hydrodynamischer Erhaltungssatz, *Naturwissenschaften*, *30*, 543–544, doi:10.1007/BF01475602, 1942.

EUMETSAT, *GOME-2 Product Guide*, EUMETSAT, Darmstadt, Germany, Doc.No. EUM/OPS-EPS/MAN/07/0445; `http://www.eumetsat.int/groups/ops/documents/document/PDF_V2C_GOME_2_PRODUCTS_GUIDE.pdf`, 2011.

Fall, R., D. Albritton, F. Fehsenfeld, W. Kuster, and P. Goldan, Laboratory studies of some environmental variables controlling sulfur emissions from plants, *Journal of Atmospheric Chemistry*, *6*, 341–362, doi:10.1007/BF00051596, 1988.

Fan, S.-M., and D. J. Jacob, Surface ozone depletion in Arctic spring sustained by bromine reactions on aerosols, *Nature*, *359*(6395), 522–524, doi:10.1038/359522a0, 1992.

Fayt, C., and M. van Roozendael, WinDOAS 2.1 Software User Manual, Belgium Institute for Space Aeronomie (BIRA-IASB), `http://bro.aeronomie.be/WinDOAS-SUM-210b.pdf`, 2001.

Fick, A., Ueber Diffusion, *Annalen der Physik*, *170*(1), 59–86, doi:10.1002/andp.18551700105, 1855.

Fischer, H., F. G. Wienhold, P. Hoor, O. Bujok, C. Schiller, P. Siegmund, M. Ambaum, H. A. Scheeren, and J. Lelieveld, Tracer correlations in the northern high latitude lowermost stratosphere: Influence of cross-tropopause mass exchange, *Geophys. Res. Lett.*, *27*(1), 97–100, doi:10.1029/1999GL010879, 2000.

Fish, D. J., and R. L. Jones, Rotational Raman scattering and the ring effect in zenith-sky spectra, *Geophysical Research Letters*, *22*(7), 811–814, doi:10.1029/95GL00392, 1995.

Fitzenberger, R., H. Bösch, C. Camy-Peyret, M. P. Chipperfield, H. Harder, U. Platt, B.-M. Sinnhuber, T. Wagner, and K. Pfeilsticker, First profile measurements of tropospheric BrO, *Geophysical Research Letters*, *27*(18), 2921–2924, doi:10.1029/2000GL011531, 2000.

Flentje, H., H. Claude, T. Elste, S. Gilge, U. Köhler, C. Plass-Dülmer, W. Steinbrecht, W. Thomas, A. Werner, and W. Fricke, The Eyjafjallajökull eruption in April 2010 – detection of volcanic plume using in-situ measurements, ozone sondes and lidar-ceilometer profiles, *Atmospheric Chemistry and Physics*, *10*(20), 10,085–10,092, doi:10.5194/acp-10-10085-2010,

2010.

Fontaine, J.-P., F. Pointurier, X. Blanchard, and T. Taffary, Atmospheric xenon radioactive isotope monitoring, *Journal of Environmental Radioactivity*, *72*(1-2), 129–135, doi:10.1016/S0265-931X(03)00194-2, 2004.

Frieß, U., Spectroscopic measurements of atmospheric trace gases at neumayer-station, antarctica, Ph.D. thesis, Institut für Umweltphysik, Universität Heidelberg, urn:nbn:de:bsz:16-opus-17093, 2001.

Frieß, U., P. S. Monks, J. J. Remedios, A. Rozanov, R. Sinreich, T. Wagner, and U. Platt, MAX-DOAS O_4 measurements: A new technique to derive information on atmospheric aerosols: 2. Modeling studies, *Journal of Geophysical Research: Atmospheres*, *111*(D14), doi:10.1029/2005JD006618, 2006.

Gaines, S. E., and R. S. Hipskind, ASCII File Format Specification for Data Exchange, `http://espoarchive.nasa.gov/sites/default/files/archive/formatspec_2_0.pdf`, 2001.

Galle, B., M. Johansson, C. Rivera, Y. Zhang, M. Kihlman, C. Kern, T. Lehmann, U. Platt, S. Arellano, and S. Hidalgo, Network for Observation of Volcanic and Atmospheric Change (NOVAC) – A global network for volcanic gas monitoring: Network layout and instrument description, *J. Geophys. Res.*, *115*(D5), D05,304, doi:10.1029/2009JD011823, 2010.

Gerlach, T. M., Volcanic sources of tropospheric ozone-depleting trace gases, *Geochemistry, Geophysics, Geosystems*, *5*(9), n/a–n/a, doi:10.1029/2004GC000747, 2004.

Gettelman, A., P. Hoor, L. L. Pan, W. J. Randel, M. I. Hegglin, and T. Birner, The extratropical upper troposphere and lower stratosphere, *Rev. Geophys.*, *49*(3), RG3003, doi:10.1029/2011RG000355, 2011.

Glickman, T., *Glossary of meteorology*, American Meteorological Society, Boston, Mass., ISBN 978-1-878220-34-9; online version: `http://glossary.ametsoc.org/wiki/Main_Page`, 2000.

Graf, H.-F., J. Feichter, and B. Langmann, Volcanic sulfur emissions: Estimates of source strength and its contribution to the global sulfate distribution, *J. Geophys. Res.*, *102*(D9), 10,727–10,738, doi:10.1029/96JD03265, 1997.

Grainger, J. F., and J. Ring, Anomalous Fraunhofer Line Profiles, *Nature*, *193*(4817), 762–762, doi:10.1038/193762a0, 1962.

Greenblatt, G. D., J. J. Orlando, J. B. Burkholder, and A. R. Ravishankara, Absorption Measurements of Oxygen Between 330 and 1140 nm, *J. Geophys. Res.*, *95*(D11), 18,577–18,582, doi:10.1029/JD095iD11p18577, 1990.

Gudmundsson, M. T., R. Pedersen, K. Vogfjörd, B. Thorbjarnardóttir, S. Jakobsdóttir, and M. J. Roberts, Eruptions of Eyjafjallajökull Volcano, Iceland, *Eos Trans. AGU*, *91*(21), doi:10.1029/2010EO210002, 2010.

Guo, S., G. J. S. Bluth, W. I. Rose, I. M. Watson, and A. J. Prata, Re-evaluation of SO_2 release of the 15 June 1991 Pinatubo eruption using ultraviolet and infrared satellite sensors, *Geochemistry, Geophysics, Geosystems*, *5*(4), doi:10.1029/2003GC000654, 2004.

Hadley, G., Concerning the Cause of the General Trade-Winds, *Philosophical Transactions of the Royal Society of London*, *39*, 58–62, 1735.

Hamamatsu, *CCD area image sensor S10140/S10141 series*, Hamamatsu Photonics K.K., Solid State Division, `http://jp.hamamatsu.com/products/sensor-ssd/pd101/pd102/pd104/`

`S10141-1107S/index_en.html`, 2011.

Hansen, J., A. Lacis, R. Ruedy, and M. Sato, Potential climate impact of Mount Pinatubo eruption, *Geophysical Research Letters*, *19*(2), 215–218, doi:10.1029/91GL02788, 1992.

Hanst, P. L., N. W. Wong, and J. Bragin, A long-path infra-red study of Los Angeles smog, *Atmospheric Environment (1967)*, *16*(5), 969 – 981, doi:10.1016/0004-6981(82)90183-4, 1982.

Henyey, L. G., and J. L. Greenstein, Diffuse radiation in the Galaxy, *Astrophysical Journal*, *93*, 70–83, doi:10.1086/144246, 1941.

Hermann, M., and A. Wiedensohler, Counting efficiency of condensation particle counters at low-pressures with illustrative data from the upper troposphere, *Journal of Aerosol Science*, *32*(8), 975–991, doi:10.1016/S0021-8502(01)00037-4, 2001.

Heue, K.-P., Airborne Multi AXis DOAS instrument and meausrements of two-dimensional tropospheric trace gas distributions, Ph.D. thesis, Institut für Umweltphysik, Universität Heidelberg, urn:nbn:de:bsz:16-opus-59909, 2005.

Heue, K.-P., A. Richter, M. Bruns, J. P. Burrows, C. v. Friedeburg, U. Platt, I. Pundt, P. Wang, and T. Wagner, Validation of SCIAMACHY tropospheric NO_2-columns with AMAXDOAS measurements, *Atmospheric Chemistry and Physics*, *5*(4), 1039–1051, doi:10.5194/acp-5-1039-2005, 2005.

Heue, K.-P., T. Wagner, S. P. Broccardo, D. Walter, S. J. Piketh, K. E. Ross, S. Beirle, and U. Platt, Direct observation of two dimensional trace gas distributions with an airborne Imaging DOAS instrument, *Atmospheric Chemistry and Physics*, *8*(22), 6707–6717, doi:10.5194/acp-8-6707-2008, 2008.

Heue, K.-P., C. A. M. Brenninkmeijer, T. Wagner, K. Mies, B. Dix, U. Frieß, B. G. Martinsson, F. Slemr, and P. F. J. van Velthoven, Observations of the 2008 Kasatochi volcanic SO_2 plume by CARIBIC aircraft DOAS and the GOME-2 satellite, *Atmospheric Chemistry and Physics*, *10*(10), 4699–4713, doi:10.5194/acp-10-4699-2010, 2010.

Heue, K.-P., C. A. M. Brenninkmeijer, A. K. Baker, A. Rauthe-Schöch, D. Walter, T. Wagner, C. Hörmann, H. Sihler, B. Dix, U. Frieß, U. Platt, B. G. Martinsson, P. F. J. van Velthoven, A. Zahn, and R. Ebinghaus, SO_2 and BrO observation in the plume of the Eyjafjallajökull volcano 2010: CARIBIC and GOME-2 retrievals, *Atmospheric Chemistry and Physics*, *11*(6), 2973–2989, doi:10.5194/acp-11-2973-2011, 2011.

Heue, K.-P., H. Riede, D. Walter, C. A. M. Brenninkmeijer, U. Frieß, T. Wagner, U. Platt, A. Zahn, G. Stratmann, and H. Ziereis, CARIBIC DOAS observations of nitrous acid and formaldehyde in a large convective cloud, *in preparation for submission at Atmospheric Chemistry and Physics*, 2013.

Holton, J. R., P. H. Haynes, M. E. McIntyre, A. R. Douglass, R. B. Rood, and L. Pfister, Stratosphere-troposphere exchange, *Rev. Geophys.*, *33*(4), 403–439, doi:10.1029/95RG02097, 1995.

Hönninger, G., C. von Friedeburg, and U. Platt, Multi axis differential optical absorption spectroscopy (MAX-DOAS), *Atmospheric Chemistry and Physics*, *4*(1), 231–254, doi:10.5194/acp-4-231-2004, 2004.

Horbanski, M., D. Pöhler, T. Mahr, T. Wagner, and U. Platt, Application of DOAS Instruments for Trace Gas Measurements on Unmanned Aerial Systems, EGU General As-

sembly 2012, held 22-27 April, 2012 in Vienna, Austria., p.5949, Bibliographic Code: 2012EGUGA..14.5949H; http://adsabs.harvard.edu/abs/2012EGUGA..14.5949H, 2012.

Hörmann, C., Space-based Monitoring of Volcanic Emissions Using the GOME-2 Instrument, Ph.D. thesis, Institut für Umweltphysik, Universität Heidelberg, urn:nbn:de:bsz:16-heidok-145368, 2013.

IPCC, Climate Change 2007: The Physical Science Basis. Contribution of Working Group I to the Fourth Assessment Report of the Intergovernmental Panel on Climate Change, ISBN 978-0-521-88009-1; http://www.ipcc.ch/publications_and_data/publications_and_data_reports.shtml, 2007.

Jaenicke, R., Über die Dynamik atmosphärischer Aitkenteilchen, *Berichte der Bunsengesellschaft für physikalische Chemie*, *82*(11), 1198–1202, doi:10.1002/bbpc.19780821126, 1978.

Johnson, J. E., A. R. Bandy, D. C. Thornton, and T. S. Bates, Measurements of atmospheric carbonyl sulfide during the NASA Chemical Instrumentation Test and Evaluation project: Implications for the global COS budget, *Journal of Geophysical Research: Atmospheres*, *98*(D12), 23,443–23,448, doi:10.1029/92JD01911, 1993.

Johnston, P. V., Making UV/Vis cross-sections, reference Fraunhofer and synthetic spectra, *Unpublished Manuscript, NIWA, Lauder*, 1996.

Junge, C. E., C. W. Chagnon, and J. E. Manson, A World-wide Stratospheric Aerosol Layer, *Science*, *133*(3463), 1478–1479, doi:10.1126/science.133.3463.1478-a, 1961.

Jurgschat, M., Messung von Spurengasen in der freien Troposphäre mit der MAX-DOAS Methode auf der Umweltforschungsstation Schneefernerhaus, Diploma thesis, Universität zu Köln, Universität Heidelberg, 2011.

K. F. Boersma, R. J. v. d. A., R. Braak, Dutch OMI NO_2 (DOMINO) data product v2.0. HE5 data file user manual, http://www.temis.nl/docs/OMI_NO2_HE5_2.0_2011.pdf, 2011.

Kaiser, E. W., and C. H. Wu, A kinetic study of the gas phase formation and decomposition reactions of nitrous acid, *The Journal of Physical Chemistry*, *81*(18), 1701–1706, doi:10.1021/j100533a001, 1977.

Kesselmeier, J., Exchange of Short-Chain Oxygenated Volatile Organic Compounds (VOCs) between Plants and the Atmosphere: A Compilation of Field and Laboratory Studies, *Journal of Atmospheric Chemistry*, *39*, 219–233, doi:10.1023/A:1010632302076, 2001.

Khokhar, M. F., U. Platt, and T. Wagner, Temporal trends of anthropogenic SO_2 emitted by non-ferrous metal smelters in Peru and Russia estimated from Satellite observations, *Atmospheric Chemistry and Physics Discussions*, *8*(5), 17,393–17,422, doi:10.5194/acpd-8-17393-2008, 2008.

Khokhar, M. F. A., Retrieval and interpretation of tropospheric SO_2 from UV-VIS satellite instruments, Ph.D. thesis, Universität Leipzig, 2006.

Kiehl, J. T., and K. E. Trenberth, Earth's Annual Global Mean Energy Budget, *Bulletin of the American Meteorological Society*, *78*, 197–208, doi:10.1175/1520-0477(1997)078<0197:EAGMEB>2.0.CO;2, 1997.

Kleipool, Q. L., M. R. Dobber, J. F. de Haan, and P. F. Levelt, Earth surface reflectance climatology from 3 years of OMI data, *J. Geophys. Res.*, *113*(D18), D18,308, doi:10.1029/2008JD010290, 2008.

Koepke, P., M. Garhammer, M. Hess, and E.-P. Roeth, NO_2 photolysis frequencies in street canyons, *Atmospheric Chemistry and Physics*, *10*(15), 7457–7466, doi:10.5194/acp-10-7457-2010, 2010.

Kraus, S., DOASIS: A framework design for DOAS, Ph.D. thesis, Universität Mannheim in collaboration with the Institut für Umweltphysik of the Universität Heidelberg, `http://hci.iwr.uni-heidelberg.de/publications/dip/2006/Kraus_PhD2006.pdf`; also available as book, published by Shaker Verlag GmbH, Aachen, Germany, under ISBN 978-3-8322-5452-0., 2006.

Kromminga, H., J. Orphal, S. Voigt, and J. P. Burrows, Cross section of OClO at 233 K, `http://www.iup.uni-bremen.de/gruppen/molspec/net/OClO1cm1_233K.DAT`; Cross section file from IUP Bremen, references therein: H. Kromminga. Diploma Thesis. IUP. University of Bremen. 1999; H. Kromminga. S. Voigt. J. Orphal. J. P. Burrows: "UV-Visible FT Spectra of OClO at Atmospheric Temperatures" (Proceedings of the 1st European Symposium on Atmospheric Measurements from Space. ESA Special Publication. 1999).

Kuebbeler, M., U. Lohmann, and J. Feichter, Effects of stratospheric sulfate aerosol geoengineering on cirrus clouds, *Geophysical Research Letters*, *39*(23), n/a–n/a, doi:10.1029/2012GL053797, 2012.

Kurucz, R. L., I. Furenlid, J. Brault, and L. Testerman, *Solar flux atlas from 296 to 1300 nm*, no. 1 in National Solar Observatory atlas ; 1 ; National Solar Observatory - Sacramento Peak <Sunspot, NM>: National Solar Observatory atlas, 239 S. pp., National Solar Observatory, Sunspot, NM, 1984.

Leder, G. N., A. Follesdal, A. L. Gade, O. Mestad, and B. Ostbo, Recommendation of February 16, 2009, on the exclusion of the company Norilsk Nickel, Council on Ethics – Norwegian Government Pension Fund Global, `http://www.regjeringen.no/pages/2267887/Recommendation%20-%20%20Final.pdf`, 2009.

Lee, D., I. Köhler, E. Grobler, F. Rohrer, R. Sausen, L. Gallardo-Klenner, J. Olivier, F. Dentener, and A. Bouwman, Estimations of global NO_x emissions and their uncertainties, *Atmospheric Environment*, *31*(12), 1735–1749, doi:10.1016/S1352-2310(96)00327-5, 1997.

Lefohn, A. S., J. D. Husar, and R. B. Husar, Estimating historical anthropogenic global sulfur emission patterns for the period 1850-1990, *Atmospheric Environment*, *33*(21), 3435–3444, doi:10.1016/S1352-2310(99)00112-0, 1999.

Leighton, P. A., *Photochemistry of air pollution*, no. 9 in Physical chemistry ; 9 ; Physical chemistry, IX, 300 S. pp., Academic Press, New York [u.a.], 1961.

Lelieveld, J., C. Brühl, P. Jöckel, B. Steil, P. J. Crutzen, H. Fischer, M. A. Giorgetta, P. Hoor, M. G. Lawrence, R. Sausen, and H. Tost, Stratospheric dryness: model simulations and satellite observations, *Atmospheric Chemistry and Physics*, *7*(5), 1313–1332, doi:10.5194/acp-7-1313-2007, 2007.

Leser, H., G. Hönninger, and U. Platt, MAX-DOAS measurements of BrO and NO_2 in the marine boundary layer, *Geophysical Research Letters*, *30*(10), n/a–n/a, doi:10.1029/2002GL015811, 2003.

Levasseur, M., M. Gosselin, and S. Michaud, A new source of dimethylsulfide (DMS) for the arctic atmosphere: ice diatoms, *Marine Biology*, *121*, 381–387, doi:10.1007/BF00346748, 1994.

Levelt, P., G. van den Oord, M. Dobber, A. Malkki, H. Visser, J. de Vries, P. Stammes, J. Lun-

dell, and H. Saari, The ozone monitoring instrument, *IEEE Transactions on Geoscience and Remote Sensing*, *44*(5), 1093–1101, doi:10.1109/TGRS.2006.872333, 2006.

Li, S.-M., Equilibrium of particle nitrite with gas phase HONO: Tropospheric measurements in the high Arctic during polar sunrise, *Journal of Geophysical Research: Atmospheres*, *99*(D12), 25,469–25,478, doi:10.1029/94JD00620, 1994.

LI-COR, *LI-6262 CO_2/H_2O Analyzer: Operating and Service Manual*, LI-COR inc., Lincoln, Nebraska, 1996.

Lohberger, F., G. Hönninger, and U. Platt, Ground-Based Imaging Differential Optical Absorption Spectroscopy of Atmospheric Gases, *Appl. Opt.*, *43*(24), 4711–4717, doi:10.1364/AO.43.004711, 2004.

Lovelock, J. E., r. J. Maggs, and R. A. Rasmussen, Atmospheric Dimethyl Sulphide and the Natural Sulphur Cycle, *Nature*, *237*(5356), 452–453, doi:10.1038/237452a0, 1972.

Marbach, T., S. Beirle, U. Platt, P. Hoor, F. Wittrock, A. Richter, M. Vrekoussis, M. Grzegorski, J. P. Burrows, and T. Wagner, Satellite measurements of formaldehyde linked to shipping emissions, *Atmospheric Chemistry and Physics*, *9*(21), 8223–8234, doi:10.5194/acp-9-8223-2009, 2009.

Marquardt, D., An Algorithm for Least-Squares Estimation of Nonlinear Parameters, *Journal of the Society for Industrial and Applied Mathematics*, *11*(2), 431–441, doi:10.1137/0111030, 1963.

Martin, R. V., D. J. Jacob, K. Chance, T. P. Kurosu, P. I. Palmer, and M. J. Evans, Global inventory of nitrogen oxide emissions constrained by space-based observations of NO_2 columns, *Journal of Geophysical Research: Atmospheres*, *108*(D17), n/a–n/a, doi:10.1029/2003JD003453, 2003.

McConnell, J. C., G. S. Henderson, L. Barrie, J. Bottenheim, H. Niki, C. H. Langford, and E. M. J. Templeton, Photochemical bromine production implicated in Arctic boundary-layer ozone depletion, *Nature*, *355*(6356), 150–152, doi:10.1038/355150a0, 1992.

Mebel, A. M., M. C. Lin, and C. F. Melius, Rate Constant of the HONO + HONO -> H_2O + NO + NO_2 Reaction from ab Initio MO and TST Calculations, *The Journal of Physical Chemistry A*, *102*(10), 1803–1807, doi:10.1021/jp973449w, 1998.

Melamed, M. L., S. Solomon, J. S. Daniel, A. O. Langford, R. W. Portmann, T. B. Ryerson, D. K. Nicks, Jr., and S. A. McKeen, Measuring reactive nitrogen emissions from point sources using visible spectroscopy from aircraft, *J. Environ. Monit.*, *5*, doi:10.1039/B204220G, 2003.

Meller, R., and G. K. Moortgat, Temperature dependence of the absorption cross sections of formaldehyde between 223 and 323 K in the wavelength range 225–375 nm, *Journal of Geophysical Research: Atmospheres*, *105*(D6), 7089–7101, doi:10.1029/1999JD901074, 2000.

Merten, A., Neues Design von Langpfad-DOAS-Instrumenten basierend auf Faseroptiken und Anwendung der Untersuchung der urbanen Atmosphäre, Ph.D. thesis, Institut für Umweltphysik, Universität Heidelberg, urn:nbn:de:bsz:16-opus-84994, 2008.

Mettendorf, K. U., Aufbau und Einsatz eines Multibeam Instrumentes zur DOAS-tomographischen Messung zweidimensionaler Konzentrationsverteilungen, Ph.D. thesis, Institut für Umweltphysik, Universität Heidelberg, urn:nbn:de:bsz:16-opus-59914, 2005.

Mie, G., Beiträge zur Optik trüber Medien, speziell kolloidaler Metallösungen, *Annalen der*

Physik, *330*(3), 377–445, doi:10.1002/andp.19083300302, 1908.

Miller, J. A., and C. T. Bowman, Mechanism and modeling of nitrogen chemistry in combustion, *Progress in Energy and Combustion Science*, *15*(4), 287–338, doi:10.1016/0360-1285(89)90017-8, 1989.

MMC, Webpage of the Open Joint Stock Company "Mining and Metallurgical Company "Norilsk Nickel", `http://www.nornik.ru/en/`, 2012.

Mu, Y., C. Geng, M. Wang, H. Wu, X. Zhang, and G. Jiang, Photochemical production of carbonyl sulfide in precipitation, *Journal of Geophysical Research: Atmospheres*, *109*(D13), doi:10.1029/2003JD004206, 2004.

Munro, R., M. Eisinger, C. Anderson, J. Callies, E. Corpaccioli, R. Lang, A. Lefebvre, Y. Livschitz, and A. Albiñana, GOME-2 on MetOp, in *Proc. The 2006 EUMETSAT Meteorological Satellite Conference, Helsinki, Finland, EUMETSAT*, 2006.

Nic, M., J. Jirat, B. Kosata, and A. Jenkins, Compendium of Chemical Terminology (Gold Book), doi:10.1351/goldbook, XML on-line corrected version: http://goldbook.iupac.org (2006-) created by M. Nic, J. Jirat, B. Kosata; updates compiled by A. Jenkins. ISBN 0-9678550-9-8. pdf-Version 2.3.2, 2012-08-19. Cf. book version: (IUPAC. Compendium of Chemical Terminology, 2nd ed. (the "Gold Book"). Compiled by A. D. McNaught and A. Wilkinson. Blackwell Scientific Publications, Oxford), 2012.

Niwa, Y., T. Machida, Y. Sawa, H. Matsueda, T. J. Schuck, C. A. M. Brenninkmeijer, R. Imasu, and M. Satoh, Imposing strong constraints on tropical terrestrial CO_2 fluxes using passenger aircraft based measurements, *J. Geophys. Res.*, *117*(D11), D11,303, doi:10.1029/2012JD017474, 2012.

Norilsk Nickel, M., Commitment to Environmental Protection; MMC Norilsk Nickel Annual Report 2009 Chapter 8, `http://www.nornik.ru/en/investor/report/annual/year2009/`, 2009.

O'Keefe, A., J. J. Scherer, and J. B. Paul, cw Integrated cavity output spectroscopy, *Chemical Physics Letters*, *307*(5-6), 343 – 349, doi:10.1016/S0009-2614(99)00547-3, 1999.

Palmer, C., and E. Loewen, *Diffraction grating handbook*, 5. ed. ed., Thermo RGL, Rochester, NY, 2002.

Pan, L. L., W. J. Randel, B. L. Gary, M. J. Mahoney, and E. J. Hintsa, Definitions and sharpness of the extratropical tropopause: A trace gas perspective, *J. Geophys. Res.*, *109*(D23), D23,103, doi:10.1029/2004JD004982, 2004.

Perner, D., and U. Platt, Detection of nitrous acid in the atmosphere by differential optical absorption, *Geophys. Res. Lett.*, *6*(12), 917–920, doi:10.1029/GL006i012p00917, 1979.

Peters, E., F. Wittrock, K. Großmann, U. Frieß, A. Richter, and J. P. Burrows, Formaldehyde and nitrogen dioxide over the remote western Pacific Ocean: SCIAMACHY and GOME-2 validation using ship-based MAX-DOAS observations, *Atmospheric Chemistry and Physics*, *12*(22), 11,179–11,197, doi:10.5194/acp-12-11179-2012, 2012.

Petersen, G. N., A short meteorological overview of the Eyjafjallajökull eruption 14 April–23 May 2010, *Weather*, *65*(8), 203–207, doi:10.1002/wea.634, 2010.

Platt, U., and G. Hönninger, The role of halogen species in the troposphere, *Chemosphere*, *52*(2), 325 – 338, doi:10.1016/S0045-6535(03)00216-9, 2003.

Platt, U., and C. Janssen, Observation and role of the free radicals NO_3, ClO, BrO and IO in the troposphere, *Faraday Discuss.*, *100*, 175–198, doi:10.1039/FD9950000175, 1995.

Platt, U., and J. Stutz, *Differential Optical Absorption Spectroscopy*, Physics of Earth and Space Environments, XV, 597 S. pp., Springer, Berlin; Heidelberg, ISBN 978-3-540-21193-8, 2008.

Platt, U., D. Perner, and H. W. Pätz, Simultaneous Measurement of Atmospheric CH_2O, O_3, and NO_2 by Differential Optical Absorption, *J. Geophys. Res.*, *84*(C10), 6329–6335, doi:10.1029/JC084iC10p06329, 1979.

Platt, U., D. Perner, G. W. Harris, A. M. Winer, and J. N. Pitts, Observations of nitrous acid in an urban atmosphere by differential optical absorption, *Nature*, *285*(5763), 312–314, doi:10.1038/285312a0, 1980.

Platt, U., W. Allan, and D. Lowe, Hemispheric average Cl atom concentration from $^{13}C/^{12}C$ ratios in atmospheric methane, *Atmospheric Chemistry and Physics*, *4*(9/10), 2393–2399, doi:10.5194/acp-4-2393-2004, 2004.

Platt, U., J. Meinen, D. Pöhler, and T. Leisner, Broadband Cavity Enhanced Differential Optical Absorption Spectroscopy (CE-DOAS) – applicability and corrections, *Atmospheric Measurement Techniques*, *2*(2), 713–723, doi:10.5194/amt-2-713-2009, 2009.

Pöhler, D., Determination of two dimensional trace gas distributions using tomographic LP-DOAS measurements in the city of Heidelberg, Germany, urn:nbn:de:bsz:16-opus-109961, 2010.

Prados-Roman, C., A. Butz, T. Deutschmann, M. Dorf, L. Kritten, A. Minikin, U. Platt, H. Schlager, H. Sihler, N. Theys, M. Van Roozendael, T. Wagner, and K. Pfeilsticker, Airborne DOAS limb measurements of tropospheric trace gas profiles: case studies on the profile retrieval of O_4 and BrO, *Atmospheric Measurement Techniques*, *4*(6), 1241–1260, doi:10.5194/amt-4-1241-2011, 2011.

Prata, A., and A. Tupper, Aviation hazards from volcanoes: the state of the science, *Natural Hazards*, *51*, 239–244, doi:10.1007/s11069-009-9415-y, 2009.

Pundt, I., J.-P. Pommereau, M. P. Chipperfield, M. Van Roozendael, and F. Goutail, Climatology of the stratospheric BrO vertical distribution by balloon-borne UV-visible spectrometry, *Journal of Geophysical Research: Atmospheres*, *107*(D24), ACH 23–1–ACH 23–14, doi:10.1029/2002JD002230, 2002.

Pyle, D. M., P. D. Beattie, and G. J. S. Bluth, Sulphur emissions to the stratosphere from explosive volcanic eruptions, *Bulletin of Volcanology*, *57*, 663–671, doi:10.1007/s004450050119, 1996.

Raman, C., A new radiation, *Indian Journal of Physics*, *2*, 387–398, `http://hdl.handle.net/2289/2135`, 1928.

Ramanathan, V., P. J. Crutzen, J. T. Kiehl, and D. Rosenfeld, Aerosols, Climate, and the Hydrological Cycle, *Science*, *294*(5549), 2119–2124, doi:10.1126/science.1064034, 2001.

Rapp, G., Building, Monumental, and Statuary Materials, in *Archaeomineralogy*, Natural Science in Archaeology, pp. 247–280, Springer Berlin Heidelberg, doi:10.1007/978-3-540-78594-1_11, ISBN 978-3-540-78593-4, 2009.

Rauthe-Schöch, A., A. Weigelt, M. Hermann, B. G. Martinsson, A. K. Baker, K.-P. Heue, C. A. M. Brenninkmeijer, A. Zahn, D. Scharffe, S. Eckhardt, A. Stohl, and P. F. J. van

Velthoven, CARIBIC aircraft measurements of Eyjafjallajökull volcanic clouds in April/May 2010, *Atmospheric Chemistry and Physics*, *12*(2), 879–902, doi:10.5194/acp-12-879-2012, 2012.

Ravishankara, A. R., Heterogeneous and Multiphase Chemistry in the Troposphere, *Science*, *276*(5315), 1058–1065, doi:10.1126/science.276.5315.1058, 1997.

Richter, A., Absorptionsspektroskopische Messungen atmosphärischer Spurengase über Bremen, 53° N, Ph.D. thesis, Universität Bremen, `http://www.iup.uni-bremen.de/doas/paper/diss_97_richter.zip`, 1997.

Roedel, W., *Physik unserer Umwelt: Die Atmosphäre*, 3., überarb. und aktualisierte Aufl. ed., XV, 498 S. pp., Springer, Berlin; Heidelberg, ISBN 3-540-67180-3, 2000.

Roedel, W., and T. Wagner, *Physik unserer Umwelt: Die Atmosphäre*, SpringerLink: Bücher, Springer Berlin Heidelberg, Berlin, Heidelberg, doi:10.1007/978-3-642-15729-5, ISBN 978-3-642-15729-5, 2011.

Sakamaki, F., S. Hatakeyama, and H. Akimoto, Formation of nitrous acid and nitric oxide in the heterogeneous dark reaction of nitrogen dioxide and water vapor in a smog chamber, *International Journal of Chemical Kinetics*, *15*(10), 1013–1029, doi:10.1002/kin.550151006, 1983.

Sandoval-Soto, L., M. Stanimirov, M. von Hobe, V. Schmitt, J. Valdes, A. Wild, and J. Kesselmeier, Global uptake of carbonyl sulfide (COS) by terrestrial vegetation: Estimates corrected by deposition velocities normalized to the uptake of carbon dioxide (CO_2), *Biogeosciences*, *2*(2), 125–132, doi:10.5194/bg-2-125-2005, 2005.

Scharffe, D., F. Slemr, C. A. M. Brenninkmeijer, and A. Zahn, Carbon monoxide measurements onboard the CARIBIC passenger aircraft using UV resonance fluorescence, *Atmospheric Measurement Techniques*, *5*(7), 1753–1760, doi:10.5194/amt-5-1753-2012, 2012.

Scheele, M. P., P. C. Siegmund, and P. F. J. van Velthoven, Sensitivity of trajectories to data resolution and its dependence on the starting point: In or outside a tropopause fold, *Meteorological Applications*, *3*(3), 267–273, doi:10.1002/met.5060030308, 1996.

Schimang, R., A. Folkers, J. Kleffmann, E. Kleist, M. Miebach, and J. Wildt, Uptake of gaseous nitrous acid (HONO) by several plant species, *Atmospheric Environment*, *40*(7), 1324 – 1335, doi:10.1016/j.atmosenv.2005.10.028, 2006.

Schuck, T. J., C. A. M. Brenninkmeijer, F. Slemr, I. Xueref-Remy, and A. Zahn, Greenhouse gas analysis of air samples collected onboard the CARIBIC passenger aircraft, *Atmospheric Measurement Techniques*, *2*(2), 449–464, doi:10.5194/amt-2-449-2009, 2009.

Schuck, T. J., C. A. M. Brenninkmeijer, A. K. Baker, F. Slemr, P. F. J. van Velthoven, and A. Zahn, Greenhouse gas relationships in the Indian summer monsoon plume measured by the CARIBIC passenger aircraft, *Atmospheric Chemistry and Physics*, *10*(8), 3965–3984, doi:10.5194/acp-10-3965-2010, 2010.

Schumann, U., B. Weinzierl, O. Reitebuch, H. Schlager, A. Minikin, C. Forster, R. Baumann, T. Sailer, K. Graf, H. Mannstein, C. Voigt, S. Rahm, R. Simmet, M. Scheibe, M. Lichtenstern, P. Stock, H. Rüba, D. Schäuble, A. Tafferner, M. Rautenhaus, T. Gerz, H. Ziereis, M. Krautstrunk, C. Mallaun, J.-F. Gayet, K. Lieke, K. Kandler, M. Ebert, S. Weinbruch, A. Stohl, J. Gasteiger, S. Groß, V. Freudenthaler, M. Wiegner, A. Ansmann, M. Tesche, H. Olafsson, and K. Sturm, Airborne observations of the Eyjafjalla volcano ash cloud over

Europe during air space closure in April and May 2010, *Atmospheric Chemistry and Physics*, *11*(5), 2245–2279, doi:10.5194/acp-11-2245-2011, 2011.

Seco, R., J. Peñuelas, and I. Filella, Short-chain oxygenated VOCs: Emission and uptake by plants and atmospheric sources, sinks, and concentrations, *Atmospheric Environment*, *41*(12), 2477 – 2499, doi:10.1016/j.atmosenv.2006.11.029, 2007.

Seinfeld, J. H., and S. N. Pandis, *Atmospheric chemistry and physics*, 2. ed. ed., XXVIII, 1203 S. pp., Wiley, Hoboken, NJ, ISBN 0-471-72018-6, 2006.

Shaiganfar, R., Estimation of NO_x Emissions from megacities using mobile MAX-DOAS and satellite observations, Ph.D. thesis, Universität Heidelberg, urn:nbn:de:bsz:16-heidok-142018, 2012.

Sihler, H., Halogen Activation in the Polar Troposphere, Ph.D. thesis, Institut für Umweltphysik, Universität Heidelberg, urn:nbn:de:bsz:16-opus-136630, 2012.

Sihler, H., U. Platt, S. Beirle, T. Marbach, S. Kühl, S. Dörner, J. Verschaeve, U. Frieß, D. Pöhler, L. Vogel, R. Sander, and T. Wagner, Tropospheric BrO column densities in the Arctic derived from satellite: retrieval and comparison to ground-based measurements, *Atmospheric Measurement Techniques*, *5*(11), 2779–2807, doi:10.5194/amt-5-2779-2012, 2012.

Sillman, S., J. A. Logan, and S. C. Wofsy, The sensitivity of ozone to nitrogen oxides and hydrocarbons in regional ozone episodes, *Journal of Geophysical Research: Atmospheres*, *95*(D2), 1837–1851, doi:10.1029/JD095iD02p01837, 1990.

Simpson, W. R., R. von Glasow, K. Riedel, P. Anderson, P. Ariya, J. Bottenheim, J. Burrows, L. J. Carpenter, U. Frieß, M. E. Goodsite, D. Heard, M. Hutterli, H.-W. Jacobi, L. Kaleschke, B. Neff, J. Plane, U. Platt, A. Richter, H. Roscoe, R. Sander, P. Shepson, J. Sodeau, A. Steffen, T. Wagner, and E. Wolff, Halogens and their role in polar boundary-layer ozone depletion, *Atmospheric Chemistry and Physics*, *7*(16), 4375–4418, doi:10.5194/acp-7-4375-2007, 2007.

Slemr, F., R. Ebinghaus, C. A. M. Brenninkmeijer, M. Hermann, H. H. Kock, B. G. Martinsson, T. Schuck, D. Sprung, P. van Velthoven, A. Zahn, and H. Ziereis, Gaseous mercury distribution in the upper troposphere and lower stratosphere observed onboard the CARIBIC passenger aircraft, *Atmospheric Chemistry and Physics*, *9*(6), 1957–1969, doi:10.5194/acp-9-1957-2009, 2009.

Sliney, D. H., Radiometric quantities and units used in photobiology and photochemistry: recommendations of the Commission Internationale de L'Eclairage (International Commission on Illumination), *Photochemistry and photobiology*, *83*(2), 425–432, doi:10.1562/2006-11-14-RA-1081, 2007.

Smagorinsky, J., General circulation experiments with the primitive equations, *Mon. Wea. Rev.*, *91*(3), 99–164, doi:10.1175/1520-0493(1963)091<0099:GCEWTP>2.3.CO;2, 1963.

Smith, S. J., H. Pitcher, T. Wigley, R. Andres, E. Conception, and J. Lurz, Historical Sulfur Dioxide Emissions 1850-2000: Methods and Results, doi:10.2172/15020102, JGCRI Report, PNNL-14537, 2004.

Solomon, S., A. L. Schmeltekopf, and R. W. Sanders, On the interpretation of zenith sky absorption measurements, *Journal of Geophysical Research: Atmospheres*, *92*(D7), 8311–8319, doi:10.1029/JD092iD07p08311, 1987.

Spengler, J., and K. Sexton, Indoor air pollution: a public health perspective, *Science*,

221(4605), 9–17, doi:10.1126/science.6857273, 1983.

Sprung, D., and A. Zahn, Acetone in the upper troposphere/lowermost stratosphere measured by the CARIBIC passenger aircraft: Distribution, seasonal cycle, and variability, *J. Geophys. Res.*, *115*(D16), D16,301, doi:10.1029/2009JD012099, 2010.

Steffen, W., J. Grinevald, P. Crutzen, and J. McNeill, The Anthropocene: conceptual and historical perspectives, *Philosophical Transactions of the Royal Society A: Mathematical, Physical and Engineering Sciences*, *369*(1938), 842–867, doi:10.1098/rsta.2010.0327, 2011.

Stevenson, D. S., C. E. Johnson, E. J. Highwood, V. Gauci, W. J. Collins, and R. G. Derwent, Atmospheric impact of the 1783-1784 Laki eruption: Part I Chemistry modelling, *Atmospheric Chemistry and Physics*, *3*(3), 487–507, doi:10.5194/acp-3-487-2003, 2003.

Stockwell, W. R., and J. G. Calver, The mechanism of the HO-SO_2 reaction, *Atmospheric Environment*, *17*(11), 2231–2235, doi:10.1016/0004-6981(83)90220-2, 1983.

Stohl, A., C. Forster, A. Frank, P. Seibert, and G. Wotawa, Technical note: The Lagrangian particle dispersion model FLEXPART version 6.2, *Atmospheric Chemistry and Physics*, *5*(9), 2461–2474, doi:10.5194/acp-5-2461-2005, 2005.

Stull, R. B. (Ed.), *An Introduction to Boundary Layer Meteorology*, Kluwer Academic Publishers, Dordrecht, Boston, London, 1988.

Stutz, J., and U. Platt, Numerical analysis and estimation of the statistical error of differential optical absorption spectroscopy measurements with least-squares methods, *Appl. Opt.*, *35*(30), 6041–6053, doi:10.1364/AO.35.006041, 1996.

Stutz, J., E. S. Kim, U. Platt, P. Bruno, C. Perrino, and A. Febo, UV-visible absorption cross sections of nitrous acid, *J. Geophys. Res.*, *105*(D11), 14,585–14,592, doi:10.1029/2000JD900003, 2000.

Stutz, J., B. Alicke, and A. Neftel, Nitrous acid formation in the urban atmosphere: Gradient measurements of NO_2 and HONO over grass in Milan, Italy, *Journal of Geophysical Research: Atmospheres*, *107*(D22), LOP 5–1–LOP 5–15, doi:10.1029/2001JD000390, 2002.

Su, H., Y. Cheng, R. Oswald, T. Behrendt, I. Trebs, F. X. Meixner, M. O. Andreae, P. Cheng, Y. Zhang, and U. Pöschl, Soil Nitrite as a Source of Atmospheric HONO and OH Radicals, *Science*, *333*(6049), 1616–1618, doi:10.1126/science.1207687, 2011.

Sverdrup, H., P. Warfvinge, and D. Britt, Assessing the potential for forest effects due to soil acidification in Maryland, *Water, Air, and Soil Pollution*, *87*(1-4), 245–265, doi:10.1007/BF00696840, 1996.

Talukdar, R. K., C. A. Longfellow, M. K. Gilles, and A. R. Ravishankara, Quantum yields of $O(^1D)$ in the photolysis of ozone between 289 and 329 nm as a function of temperature, *Geophysical Research Letters*, *25*(2), 143–146, doi:10.1029/97GL03354, 1998.

Taylor, P. E., R. C. Flagan, R. Valenta, and M. Glovsky, Release of allergens as respirable aerosols: A link between grass pollen and asthma, *Journal of Allergy and Clinical Immunology*, *109*(1), 51–56, doi:10.1067/mai.2002.120759, 2002.

Theuwissen, A., Influence of terrestrial cosmic rays on the reliability of CCD image sensors, in *Electron Devices Meeting, 2005. IEDM Technical Digest. IEEE International*, pp. 811 –814, doi:10.1109/IEDM.2005.1609479, 2005.

Thomas, H. E., and A. J. Prata, Sulphur dioxide as a volcanic ash proxy during the April–

May 2010 eruption of Eyjafjallajökull Volcano, Iceland, *Atmospheric Chemistry and Physics*, *11*(14), 6871–6880, doi:10.5194/acp-11-6871-2011, 2011.

Trainer, M., B. A. Ridley, M. P. Buhr, G. Kok, J. Walega, G. Hübler, D. D. Parrish, and F. C. Fehsenfeld, Regional ozone and urban plumes in the southeastern United States: Birmingham, a case study, *J. Geophys. Res.*, *100*(D9), 18,823–18,834, doi:10.1029/95JD01641, 1995.

Vandaele, A. C., C. Hermans, P. C. Simon, M. Roozendael, J. M. Guilmot, M. Carleer, and R. Colin, Fourier transform measurement of NO_2 absorption cross-section in the visible range at room temperature, *Journal of Atmospheric Chemistry*, *25*, 289–305, doi:10.1007/BF00053797, 1996.

Vogel, L., B. Galle, C. Kern, H. Delgado Granados, V. Conde, P. Norman, S. Arellano, O. Landgren, P. Lübcke, J. M. Alvarez Nieves, L. Cárdenas Gonzáles, and U. Platt, Early in-flight detection of SO_2 via Differential Optical Absorption Spectroscopy: a feasible aviation safety measure to prevent potential encounters with volcanic plumes, *Atmospheric Measurement Techniques*, *4*(9), 1785–1804, doi:10.5194/amt-4-1785-2011, 2011.

Voigt, C., J. Schreiner, A. Kohlmann, P. Zink, K. Mauersberger, N. Larsen, T. Deshler, C. Kröger, J. Rosen, A. Adriani, F. Cairo, G. D. Donfrancesco, M. Viterbini, J. Ovarlez, H. Ovarlez, C. David, and A. Dörnbrack, Nitric Acid Trihydrate (NAT) in Polar Stratospheric Clouds, *Science*, *290*(5497), 1756–1758, doi:10.1126/science.290.5497.1756, 2000.

Voigt, S., J. Orphal, K. Bogumil, and J. P. Burrows, The temperature dependence (203–293 K) of the absorption cross sections of O_3 in the 230–850 nm region measured by Fourier-transform spectroscopy, *Journal of Photochemistry and Photobiology A: Chemistry*, *143*(1), 1–9, doi:10.1016/S1010-6030(01)00480-4, 2001.

von Glasow, R., Atmospheric chemistry in volcanic plumes, *Proceedings of the National Academy of Sciences*, *107*(15), 6594–6599, doi:10.1073/pnas.0913164107, 2010.

von Glasow, R., R. Sander, A. Bott, and P. J. Crutzen, Modeling halogen chemistry in the marine boundary layer 2. Interactions with sulfur and the cloud-covered MBL, *J. Geophys. Res.*, *107*(D17), doi:10.1029/2001JD000943, 2002.

von Glasow, R., R. von Kuhlmann, M. G. Lawrence, U. Platt, and P. J. Crutzen, Impact of reactive bromine chemistry in the troposphere, *Atmospheric Chemistry and Physics*, *4*(11/12), 2481–2497, doi:10.5194/acp-4-2481-2004, 2004.

von Smoluchowski, M., Zur kinetischen Theorie der Brownschen Molekularbewegung und der Suspensionen, *Annalen der Physik*, *326*(14), 756–780, doi:10.1002/andp.19063261405, 1906.

Wagner, T., Satellite Observations of Atmospheric Halogen Oxides, Ph.D. thesis, Institut für Umweltphysik, Universität Heidelberg, urn:nbn:de:bsz:16-opus-5397, 1999.

Wagner, T., and U. Platt, Satellite mapping of enhanced BrO concentrations in the troposphere, *Nature*, *395*, 486–490, doi:10.1038/26723, 1998.

Wagner, T., S. Beirle, and T. Deutschmann, Three-dimensional simulation of the Ring effect in observations of scattered sun light using Monte Carlo radiative transfer models, *Atmospheric Measurement Techniques*, *2*(1), 113–124, doi:10.5194/amt-2-113-2009, 2009.

Walter, D., Flugzeugmessungen von Spurengasverteilungen mittels abbildender Differentieller Optischer Absorptionsspektroskopie im südafrikanischen Highveld, Diploma thesis, Institut für Umweltphysik, Universität Heidelberg, 2008.

Walter, D., K.-P. Heue, A. Rauthe-Schöch, C. A. M. Brenninkmeijer, L. N. Lamsal, N. A. Krotkov, and U. Platt, Flux calculation using CARIBIC DOAS aircraft measurements: SO_2 emission of norilsk, *J. Geophys. Res.*, *117*(D11), D11,305, doi:10.1029/2011JD017335, 2012.

Wang, P., A. Richter, M. Bruns, J. P. Burrows, R. Scheele, W. Junkermann, K.-P. Heue, T. Wagner, U. Platt, and I. Pundt, Airborne multi-axis DOAS measurements of tropospheric SO_2 plumes in the Po-valley, Italy, *Atmospheric Chemistry and Physics*, *6*(2), 329–338, doi:10.5194/acp-6-329-2006, 2006.

Wang, T., T. F. Cheung, Y. S. Li, X. M. Yu, and D. R. Blake, Emission characteristics of CO, NO_x, SO_2 and indications of biomass burning observed at a rural site in eastern China, *Journal of Geophysical Research: Atmospheres*, *107*(D12), ACH 9–1–ACH 9–10, doi:10.1029/2001JD000724, 2002.

Warneck, P., and J. Williams, *The atmospheric chemist's companion*, IX, 436 S. pp., Springer, Dordrecht; Heidelberg, doi:10.1007/978-94-007-2275-0, ISBN 978-94-007-2274-3, 2012.

Watts, S. F., The mass budgets of carbonyl sulfide, dimethyl sulfide, carbon disulfide and hydrogen sulfide, *Atmospheric Environment*, *34*(5), 761–779, doi:10.1016/S1352-2310(99)00342-8, 2000.

Wayne, R., G. Poulet, P. Biggs, J. Burrows, R. Cox, P. Crutzen, G. Hayman, M. Jenkin, G. L. Bras, G. Moortgat, U. Platt, and R. Schindler, Halogen oxides: Radicals, sources and reservoirs in the laboratory and in the atmosphere, *Atmospheric Environment*, *29*(20), 2677 – 2881, doi:10.1016/1352-2310(95)98124-Q, 1995.

Weller, R., O. Schrems, A. Boddenberg, S. Gäb, and M. Gautrois, Meridional distribution of hydroperoxides and formaldehyde in the marine boundary layer of the Atlantic (48°N-35°S) measured during the Albatross campaign, *Journal of Geophysical Research: Atmospheres*, *105*(D11), 14,401–14,412, doi:10.1029/1999JD901145, 2000.

Wennberg, P., Atmospheric chemistry: Bromine explosion, *Nature*, *397*(6717), 299–301, doi:10.1038/16805, 1999.

White, J. U., Long Optical Paths of Large Aperture, *J. Opt. Soc. Am.*, *32*(5), 285–285, doi:10.1364/JOSA.32.000285, 1942.

White, W. H., J. A. Anderson, D. L. Blumenthal, R. B. Husar, N. V. Gillani, J. D. Husar, and J. Wilson, W. E., Formation and Transport of Secondary Air Pollutants: Ozone and Aerosols in the St. Louis Urban Plume, *Science*, *194*(4261), pp. 187–189, `http://www.jstor.org/stable/1742680`, 1976.

Wilmouth, D. M., T. F. Hanisco, N. M. Donahue, and J. G. Anderson, Fourier Transform Ultraviolet Spectroscopy of the A $2\pi 3/2$ <- X $2\pi 3/2$ Transition of BrO, *The Journal of Physical Chemistry A*, *103*(45), 8935–8945, doi:10.1021/jp991651o, 1999.

Yakovlev, A., I. Plekhanova, S. Kudryashov, and R. Aimaletdinov, Assessment and Regulation of the Ecological State of Soils in the Impact Zone of Mining and Metallurgical Enterprises of Norilsk Nickel Company, *Eurasian Soil Science*, *41*, 648–659, doi:10.1134/S1064229308060100, 2008.

Yilmaz, S., Retrieval of Atmospheric Aerosol and Trace Gas Vertical Profiles using Multi-Axis Differential Optical Absorption Spectroscopy, urn:nbn:de:bsz:16-opus-131285, 2012.

Zahn, A., C. A. M. Brenninkmeijer, and P. F. J. van Velthoven, Passenger aircraft project

CARIBIC 1997–2002, Part I: the extratropical chemical tropopause, *Atmospheric Chemistry and Physics Discussions*, *4*(1), 1091–1117, doi:10.5194/acpd-4-1091-2004, 2004.

Zahn, A., J. Weppner, H. Widmann, K. Schlote-Holubek, B. Burger, T. Kühner, and H. Franke, A fast and precise chemiluminescence ozone detector for eddy flux and airborne application, *Atmospheric Measurement Techniques*, *5*(2), 363–375, doi:10.5194/amt-5-363-2012, 2012.

Zdeňka, K., M. Vladimír, L. Karel, and D. Pavel, Urban Air Pollution by Nanoparticles in Ostrava Region, *Journal of Physics: Conference Series*, *429*(1), 012,005, doi:10.1088/1742-6596/429/1/012005, 2013.

Ziereis, H., H. Schlager, P. Schulte, P. F. J. van Velthoven, and F. Slemr, Distributions of NO, NO_x, and NO_y in the upper troposphere and lower stratosphere between 28° and 61°N during POLINAT 2, *J. Geophys. Res.*, *105*(D3), 3653–3664, doi:10.1029/1999JD900870, 2000.

Zwinkels, J. C., E. Ikonen, N. P. Fox, G. Ulm, and M. L. Rastello, Photometry, radiometry and 'the candela': evolution in the classical and quantum world, *Metrologia*, *47*(5), R15, doi:10.1088/0026-1394/47/5/R01, 2010.

A. Flight Overview

A.1. List of Flights

The following table lists all CARIBIC flights from flight 297 (June 2010) to flight 416 (February 2013). The sets of flights (SoF, in most cases consisting of 4 single flights) are grouped by horizontal lines. The table contains the following columns:

Fnr	CARIBIC flight number
From	start airport (airport abbreviations are listed on p. 225)
To	destination airport
Start	start time (take-off, given in UTC)
Landing	landing time (touch-down, given in UTC)
A, B, C	light received by spectrograph A, B, C
Tof	time of flight (from start to landing), given in hours
Light	time of flight during daylight (when SZA was smaller than 80° and the DOAS instrument was working), given in hours
Fract	fraction of time with SZA $< 80°$ and DOAS working

The last two columns are based on the ARINC data stored by the Master computer (cf. Sect. 5.3 p. 82); due to missing data, they contain some inaccuracy. Notes about the problems during SoF 317, 385, 387 and 409 are given in Sect. A p. 209

Fnr	From	To	Start	Landing	A	B	C	Tof	Light	Fract
297	FRA	CCS	2010-06-22 09:50	2010-06-22 19:38		B	C	9.8	9.7	99 %
298	CCS	FRA	2010-06-22 21:45	2010-06-23 07:18		B	C	9.6	1.9	19 %
299	FRA	KIX	2010-06-23 12:30	2010-06-23 23:10		B	C	10.7	6.5	61 %
300	KIX	FRA	2010-06-24 01:47	2010-06-24 13:28		B	C	11.7	11.6	99 %
301	FRA	CCS	2010-07-27 09:52	2010-07-27 19:31		B	C	9.7	9.6	99 %
302	CCS	FRA	2010-07-27 22:36	2010-07-28 07:52		B	C	9.3	1.6	17 %
303	FRA	KIX	2010-07-28 12:20	2010-07-28 23:12		B	C	10.9	4.6	42 %
304	KIX	FRA	2010-07-29 01:07	2010-07-29 12:51		B	C	11.7	11.7	99 %
305	FRA	CCS	2010-08-25 10:08	2010-08-25 20:20		B	C	10.2	10.1	99 %
306	CCS	FRA	2010-08-25 23:08	2010-08-26 08:06		B	C	9.0	1.5	16 %
307	FRA	KIX	2010-08-26 12:29	2010-08-26 23:10		B	C	10.7	3.7	35 %
308	KIX	FRA	2010-08-27 01:22	2010-08-27 13:17		B	C	11.9	11.8	99 %
309	FRA	CCS	2010-09-22 10:14	2010-09-22 19:35		B	C	9.3	9.3	99 %
310	CCS	FRA	2010-09-22 22:11	2010-09-23 07:32		B	C	9.3	0.7	8 %
311	FRA	KIX	2010-09-23 12:21	2010-09-23 22:58		B	C	10.6	3.0	28 %

312	KIX	FRA	2010-09-24 01:03	2010-09-24 12:48	B C	11.8	11.7	100 %
313	FRA	CCS	2010-10-20 10:39	2010-10-20 20:28	B C	9.8	9.8	99 %
314	CCS	FRA	2010-10-20 22:42	2010-10-21 08:10	B C	9.5	0.7	7 %
315	FRA	KIX	2010-10-21 12:40	2010-10-21 23:11	B C	10.5	1.9	18 %
316	KIX	FRA	2010-10-22 01:08	2010-10-22 12:57	B C	11.8	8.7	73 %
317	FRA	JNB	2010-11-14 23:07	2010-11-15 09:17	- - -	10.2		
318	JNB	FRA	2010-11-15 17:50	2010-11-16 04:25	- - -	10.6		
319	FRA	BOG	2010-11-16 15:08	2010-11-17 02:09	- - -	11.0		
320	BOG	FRA	2010-11-17 04:18	2010-11-17 14:34	- - -	10.3		
321	FRA	CPT	2010-12-12 22:21	2010-12-13 09:15	B C	10.9	3.8	35 %
322	CPT	FRA	2010-12-13 17:19	2010-12-14 04:25	B C	11.1	0.0	0 %
323	FRA	BOG	2010-12-14 14:17	2010-12-15 01:40	B C	11.4	0.0	0 %
324	BOG	FRA	2010-12-15 03:58	2010-12-15 14:19	B C	10.4	3.4	32 %
325	FRA	JNB	2011-01-18 21:53	2011-01-19 08:01	A B C	10.1	2.8	28 %
326	JNB	FRA	2011-01-19 18:28	2011-01-20 04:46	A B C	10.3	0.0	0 %
327	FRA	BOG	2011-01-20 13:11	2011-01-21 00:22	A B C	11.2	6.9	62 %
328	BOG	FRA	2011-01-21 03:10	2011-01-21 13:45	A B C	10.6	3.1	29 %
329	FRA	CPT	2011-02-24 22:31	2011-02-25 09:12	A B C	10.7	3.4	32 %
330	CPT	FRA	2011-02-25 17:23	2011-02-26 04:20	A B C	10.9	0.0	0 %
331	FRA	KIX	2011-02-26 13:30	2011-02-27 00:38	A B C	11.1	3.1	28 %
332	KIX	FRA	2011-02-27 02:36	2011-02-27 14:41	A B C	12.1	12.0	99 %
333	FRA	CPT	2011-03-20 22:06	2011-03-21 09:02	A B C	10.9	3.3	30 %
334	CPT	FRA	2011-03-21 17:15	2011-03-22 04:34	A B C	11.3	0.0	0 %
335	FRA	BOG	2011-03-22 12:45	2011-03-22 23:57	A B C	11.2	9.1	81 %
336	BOG	FRA	2011-03-23 03:07	2011-03-23 12:59	A B C	9.9	4.1	42 %
337	FRA	CCS	2011-04-18 09:46	2011-04-18 19:37	A B C	9.8	9.8	99 %
338	CCS	FRA	2011-04-18 21:56	2011-04-19 07:25	A B C	9.5	1.1	11 %
339	FRA	YVR	2011-04-19 12:09	2011-04-19 21:44	A B C	9.6	9.5	99 %
340	YVR	FRA	2011-04-19 23:46	2011-04-20 09:03	A B C	9.3	3.8	41 %
341	FRA	CCS	2011-05-16 10:00	2011-05-16 19:49	A B C	9.8	9.8	99 %
342	CCS	FRA	2011-05-16 21:54	2011-05-17 07:27	A B C	9.6	1.6	17 %
343	FRA	YVR	2011-05-17 12:04	2011-05-17 21:44	A B C	9.7	9.6	99 %
344	YVR	FRA	2011-05-17 23:45	2011-05-18 09:22	A B C	9.6	4.5	47 %
345	FRA	YVR	2011-06-15 11:56	2011-06-15 21:23	A B C	9.5	9.4	99 %
346	YVR	FRA	2011-06-15 23:32	2011-06-16 09:01	A B C	9.5	6.8	72 %
347	FRA	BOG	2011-06-16 13:04	2011-06-17 00:10	A B C	11.1	9.1	82 %
348	BOG	FRA	2011-06-17 03:32	2011-06-17 13:43	A B C	10.2	4.9	48 %
349	FRA	CCS	2011-07-20 09:54	2011-07-20 19:48	A B C	9.9	9.8	99 %
350	CCS	FRA	2011-07-20 22:03	2011-07-21 07:34	A B C	9.5	1.6	16 %
351	FRA	YVR	2011-07-21 11:48	2011-07-21 21:24	A B C	9.6	9.5	99 %
352	YVR	FRA	2011-07-21 23:31	2011-07-22 08:56	A B C	9.4	6.1	65 %
353	FRA	CCS	2011-08-16 09:47	2011-08-16 19:33	A B C	9.8	9.7	99 %
354	CCS	FRA	2011-08-16 22:02	2011-08-17 07:05	A B C	9.0	1.0	11 %

355	FRA	YVR	2011-08-17 12:04	2011-08-17 21:49	A B C	9.8	9.6	99 %
356	YVR	FRA	2011-08-18 00:06	2011-08-18 09:27	A B C	9.4	3.7	40 %
357	FRA	CCS	2011-09-20 09:56	2011-09-20 19:43	B C	9.8	9.7	99 %
358	CCS	FRA	2011-09-20 22:15	2011-09-21 07:38	B C	9.4	0.8	9 %
359	FRA	YVR	2011-09-21 11:48	2011-09-21 21:33	B C	9.8	9.7	99 %
360	YVR	FRA	2011-09-21 23:38	2011-09-22 08:27	B C	8.8	2.2	24 %
361	FRA	CCS	2011-10-24 09:56	2011-10-24 19:38	B C	9.7	9.6	99 %
362	CCS	FRA	2011-10-24 21:57	2011-10-25 07:18	B C	9.4	0.0	0 %
363	FRA	YVR	2011-10-25 12:02	2011-10-25 21:29	B C	9.5	5.3	56 %
364	YVR	FRA	2011-10-25 23:36	2011-10-26 09:26	B C	9.8	1.3	13 %
365	FRA	MAA	2011-11-15 09:40	2011-11-15 18:21	B C	8.7	2.9	33 %
366	MAA	FRA	2011-11-15 20:30	2011-11-16 06:02	B C	9.5	0.0	0 %
367	FRA	CCS	2011-11-16 10:20	2011-11-16 19:54	B C	9.6	9.5	99 %
368	CCS	FRA	2011-11-16 22:32	2011-11-17 07:53	B C	9.4	0.0	0 %
369	FRA	MAA	2011-12-15 09:37	2011-12-15 18:11	B C	8.6	2.5	30 %
370	MAA	FRA	2011-12-15 20:30	2011-12-16 06:18	B C	9.8	0.0	0 %
371	FRA	CCS	2011-12-16 10:18	2011-12-16 20:24	B C	10.1	10.0	99 %
372	CCS	FRA	2011-12-16 22:59	2011-12-17 07:48	B C	8.8	0.0	0 %
373	FRA	MAA	2012-01-16 09:42	2012-01-16 18:10	B C	8.5	3.5	42 %
374	MAA	FRA	2012-01-16 20:27	2012-01-17 05:59	B C	9.5	0.0	0 %
375	FRA	CCS	2012-01-17 10:14	2012-01-17 20:29	B C	10.3	10.2	99 %
376	CCS	FRA	2012-01-17 22:31	2012-01-18 07:37	B C	9.1	0.0	0 %
377	FRA	MAA	2012-03-06 09:33	2012-03-06 17:56	B C	8.4	4.1	48 %
378	MAA	FRA	2012-03-06 20:21	2012-03-07 06:16	B C	9.9	0.0	0 %
379	FRA	CCS	2012-03-07 10:06	2012-03-07 19:57	B C	9.9	9.8	99 %
380	CCS	FRA	2012-03-07 22:24	2012-03-08 07:37	B C	9.2	0.4	4 %
381	FRA	CCS	2012-03-27 10:18	2012-03-27 20:25	B C	10.1	10.0	99 %
382	CCS	FRA	2012-03-28 01:02	2012-03-28 10:10	B C	9.1	2.2	24 %
383	FRA	ICN	2012-03-28 16:41	2012-03-29 02:35	B C	9.9	2.8	28 %
384	ICN	FRA	2012-03-29 05:16	2012-03-29 16:19	B C	11.0	10.9	99 %
385	FRA	YVR	2012-04-25 11:34	2012-04-25 21:22	B C	9.8	9.7	99 %
386	YVR	FRA	2012-04-25 23:26	2012-04-26 08:37	B C	9.2	3.8	41 %
387	FRA	ICN	2012-05-22 16:32	2012-05-23 02:20	B	9.8		
388	ICN	FRA	2012-05-23 05:35	2012-05-23 16:52	B	11.3		
389	FRA	CCS	2012-08-07 10:05	2012-08-07 20:09	A B C	10.1	9.8	97 %
390	CCS	FRA	2012-08-07 22:31	2012-08-08 07:24	A B C	8.9	1.2	14 %
391	FRA	YVR	2012-08-08 11:26	2012-08-08 21:21	A B C	9.9	9.8	99 %
392	YVR	FRA	2012-08-08 23:27	2012-08-09 08:45	A B C	9.3	4.5	49 %
393	FRA	CCS	2012-09-18 10:01	2012-09-18 19:56	A B C	9.9	9.8	99 %
394	CCS	FRA	2012-09-18 22:36	2012-09-19 07:56	A B C	9.3	1.0	11 %
395	FRA	YVR	2012-09-19 11:26	2012-09-19 20:56	A B C	9.5	9.4	99 %
396	YVR	FRA	2012-09-19 23:22	2012-09-20 08:38	A B C	9.3	2.4	26 %
397	FRA	CCS	2012-10-16 10:01	2012-10-16 19:47	A B C	9.8	9.7	99 %

398	CCS	FRA	2012-10-16 22:25	2012-10-17 07:48	A B C	9.4	0.5	6 %
399	FRA	YVR	2012-10-17 11:45	2012-10-17 21:31	A B C	9.8	5.9	61 %
400	YVR	FRA	2012-10-17 23:33	2012-10-18 08:49	A B C	9.3	1.3	14 %
401	FRA	BKK	2012-11-21 21:35	2012-11-22 07:51	A B C	10.3	4.6	45 %
402	BKK	KUL	2012-11-22 09:31	2012-11-22 11:17	A B C	1.8	0.5	30 %
403	KUL	BKK	2012-11-22 13:13	2012-11-22 14:54	A B C	1.7	0.0	0 %
404	BKK	FRA	2012-11-22 17:10	2012-11-23 04:39	A B C	11.5	0.0	0 %
405	FRA	BKK	2012-12-12 21:42	2012-12-13 07:44	A B C	10.0	4.3	43 %
406	BKK	KUL	2012-12-13 09:46	2012-12-13 11:36	A B C	1.8	0.3	15 %
407	KUL	BKK	2012-12-13 13:27	2012-12-13 15:03	A B C	1.6	0.0	0 %
408	BKK	FRA	2012-12-13 17:15	2012-12-14 04:52	A B C	11.6	0.0	0 %
409	FRA	BKK	2013-01-23 21:29	2013-01-24 07:27	A B C	10.0	4.1	42 %
410	BKK	KUL	2013-01-24 10:00	2013-01-24 11:00	- - -	1.8		
411	KUL	BKK	2013-01-24 13:00	2013-01-24 14:00	- - -	1.8		
412	BKK	FRA	2013-01-24 16:00	2013-01-24 17:00	- - -	1.8		
413	FRA	BKK	2013-02-20 21:22	2013-02-21 07:28	A B C	10.1	4.4	44 %
414	BKK	KUL	2013-02-21 09:30	2013-02-21 11:25	A B C	1.9	1.4	75 %
415	KUL	BKK	2013-02-21 13:16	2013-02-21 14:59	A B C	1.7	0.0	0 %
416	BKK	FRA	2013-02-21 17:13	2013-02-22 04:43	A B C	11.5	0.0	0 %

A.2. Overview Graphs

The following pages contain overview graphs over the DOAS results of the CARIBIC set of flights (SoF), from SoF 297 (i.e. the first regular flight set of the new DOAS instrument, taken place in June 2010) until SoF 413 (February 2013).

The black horizontal bars on top of each graph indicate the time spans of the single flights. In several cases, parts of the flights are cropped off because of missing or poor DOAS data due to lack of sunlight. Time gaps within the x-axes are indicated by grey vertical bars. With the change in the SZA, also the stratospheric light paths strongly changes, which leads to high SCDs of ozone and NO_2. In order to be able to depict smaller features, the scaling of the y-axis was chosen such, that those high SCD at high SZA are cut off.

The SZA is depicted in the lowermost parts of the graphs (black line) together with the averaged number of counts per seconds. The other lines show the SCDs of NO_2, BrO, SO_2 and O_3 in molec/cm^2 and the oxygen dimer O_4 in molec^2/cm^5, also the fit coefficient for the Ring spectrum is included.

Red lines belong to spectrograph A, green lines to spectrograph B and blue lines to spectrograph C. Therefore they correspond to the directions +10° (upwards), −10° (downwards) and −82° (nadir), with the exception of SoF 393, where A and B have been exchanged (cf. Sect. 6.8 p. 123). Because the +10° fibre was broken during several

SoF (cf. Sect. 6.1.1 p. 90), only some of the graphs contains red lines.

No DOAS data and therefore no graph exists for SoF 317 because of a failure of the DOAS instrument. SoF 387 and SoF 389 only contain two flights each; for the latter one, no graph is given, because no light was received by the +10° and the −82° direction. During SoF 409, the CARIBIC container only got power for the first flight.

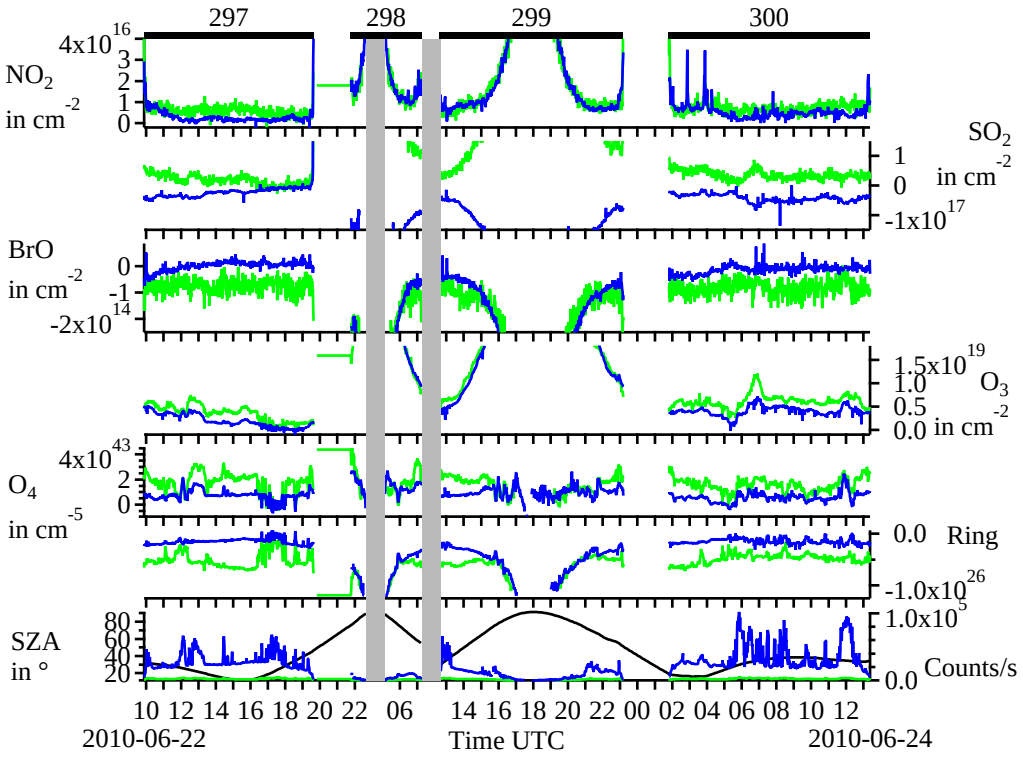

Figure A.1.: Set of flights 297–300 (June 2010).
SoF 297: FRA → CCS → FRA → KIX → FRA
red: Spec A (+10°), green: Spec B (−10°), blue: Spec B (−82°)

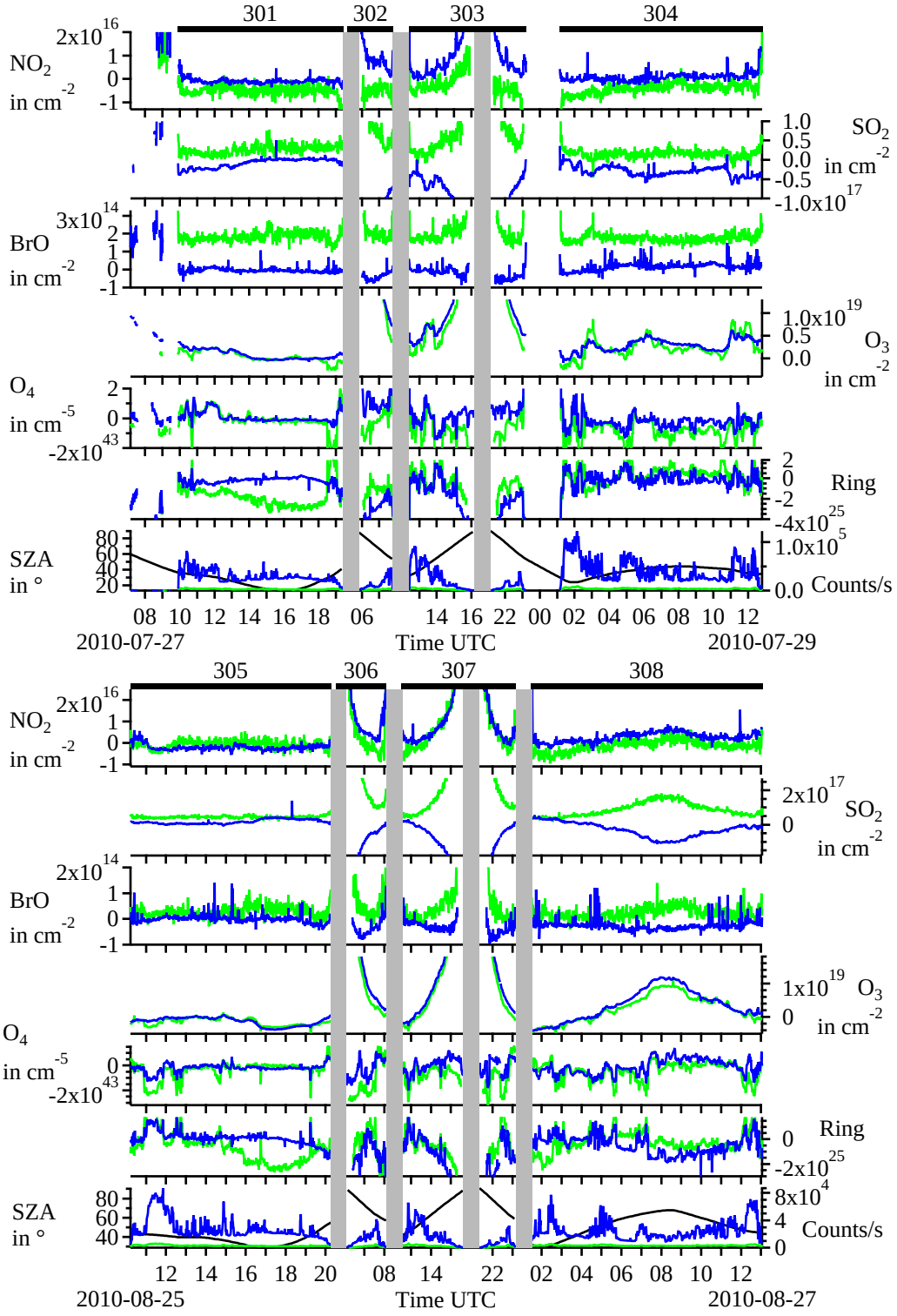

Figure A.2.: Set of flights 301–304 (July 2010) and 305–308 (August 2010).
SoF 301: FRA → CCS → FRA → KIX → FRA
SoF 305: FRA → CCS → FRA → KIX → FRA
red: Spec A (+10°), green: Spec B (−10°), blue: Spec B (−82°)

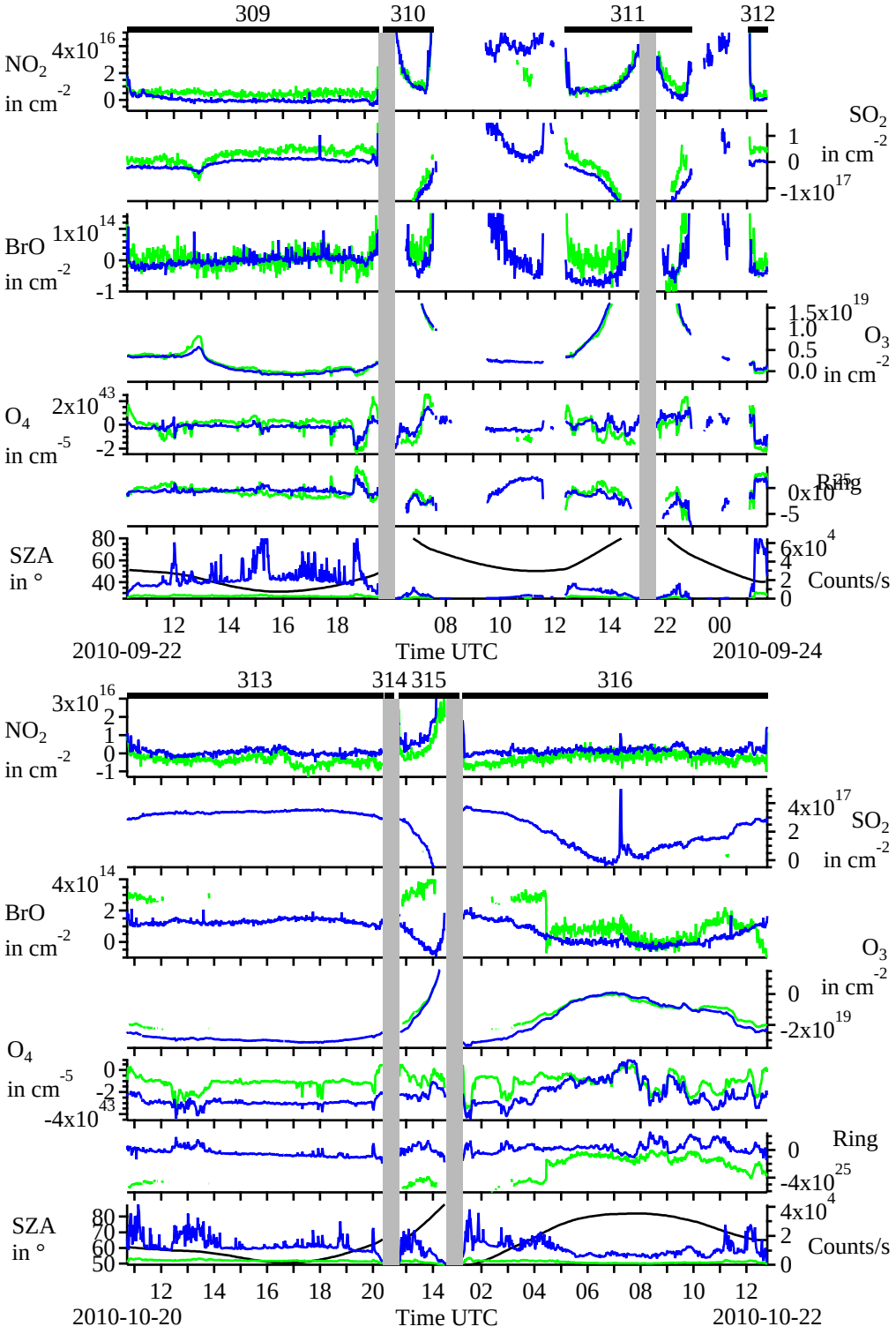

Figure A.3.: Set of flights 309–312 (September 2010) and 313–316 (October 2010).
SoF 309: FRA → CCS → FRA → KIX → FRA
SoF 313: FRA → CCS → FRA → KIX → FRA
red: Spec A (+10°), green: Spec B (−10°), blue: Spec B (−82°)

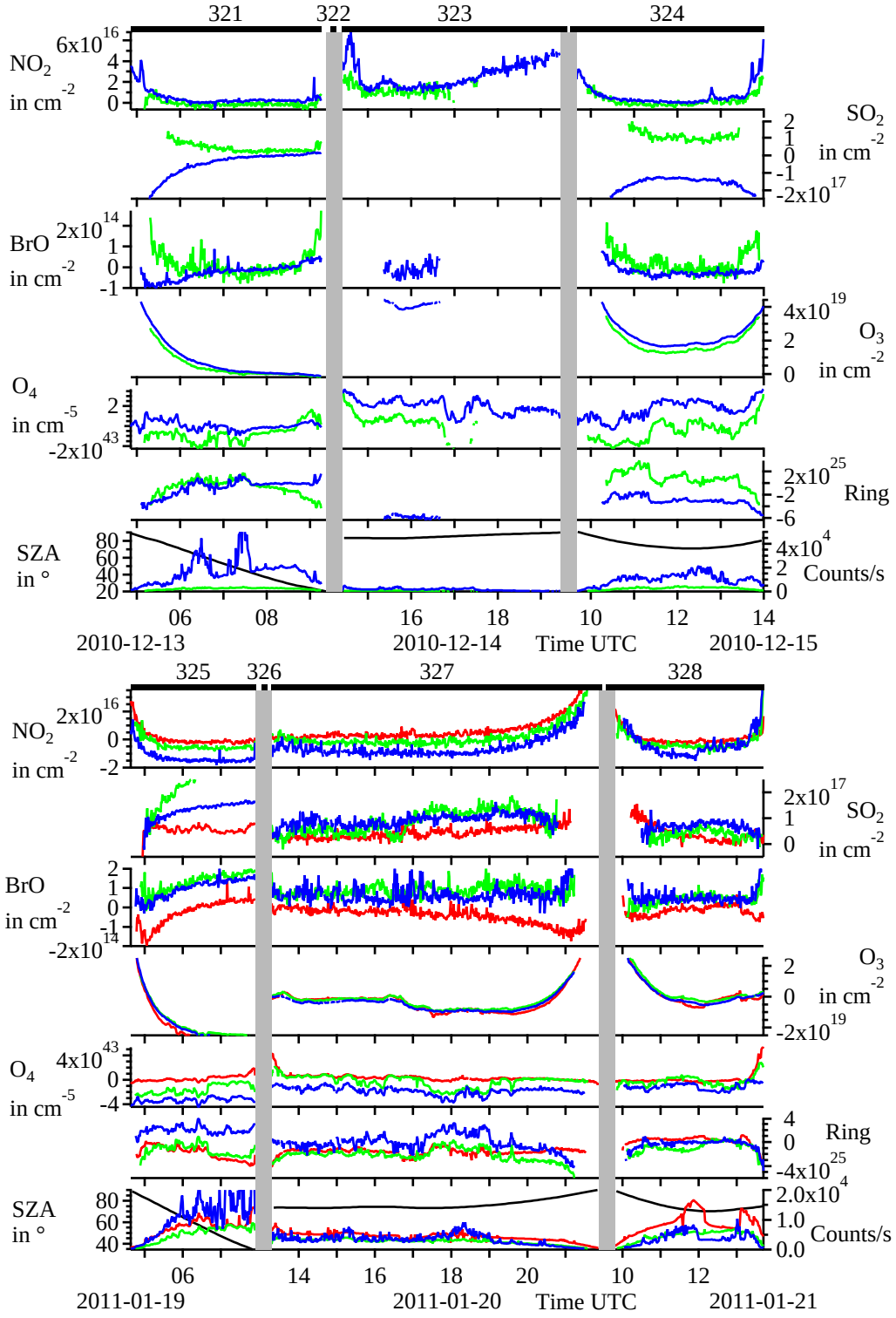

Figure A.4.: Set of flights 321–324 (December 2010) and 325–328 (January 2011).
SoF 321: FRA → CPT → FRA → BOG → FRA
SoF 325: FRA → JNB → FRA → BOG → FRA
red: Spec A (+10°), green: Spec B (−10°), blue: Spec B (−82°)

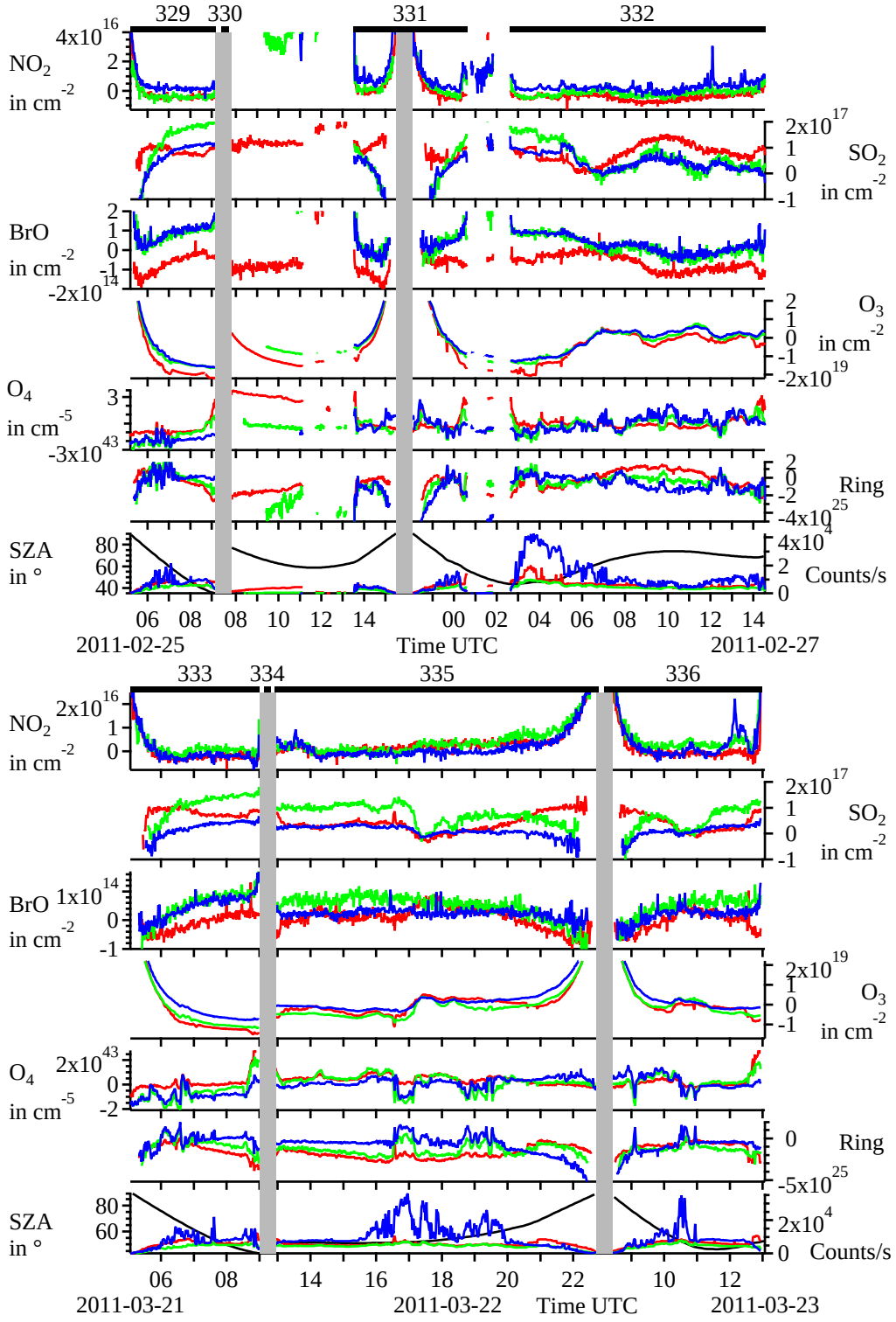

Figure A.5.: Set of flights 329–332 (February 2011) and 333–336 (March 2011).
SoF 329: FRA → CPT → FRA → KIX → FRA
SoF 333: FRA → CPT → FRA → BOG → FRA
red: Spec A (+10°), green: Spec B (−10°), blue: Spec B (−82°)

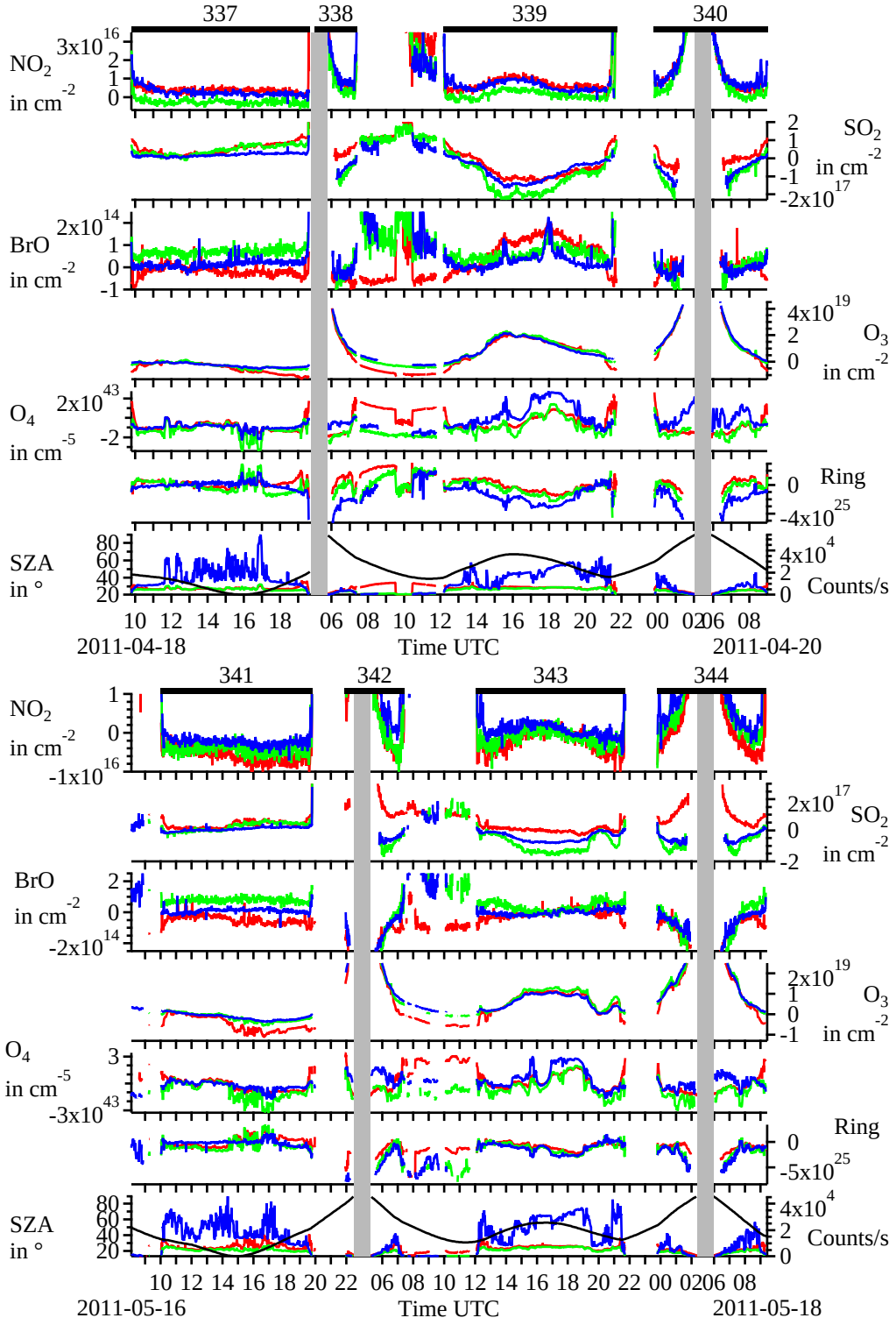

Figure A.6.: Set of flights 337–340 (April 2011) and 341–344 (May 2011).
SoF 337: FRA → CCS → FRA → YVR → FRA
SoF 341: FRA → CCS → FRA → YVR → FRA
red: Spec A (+10°), green: Spec B (−10°), blue: Spec B (−82°)

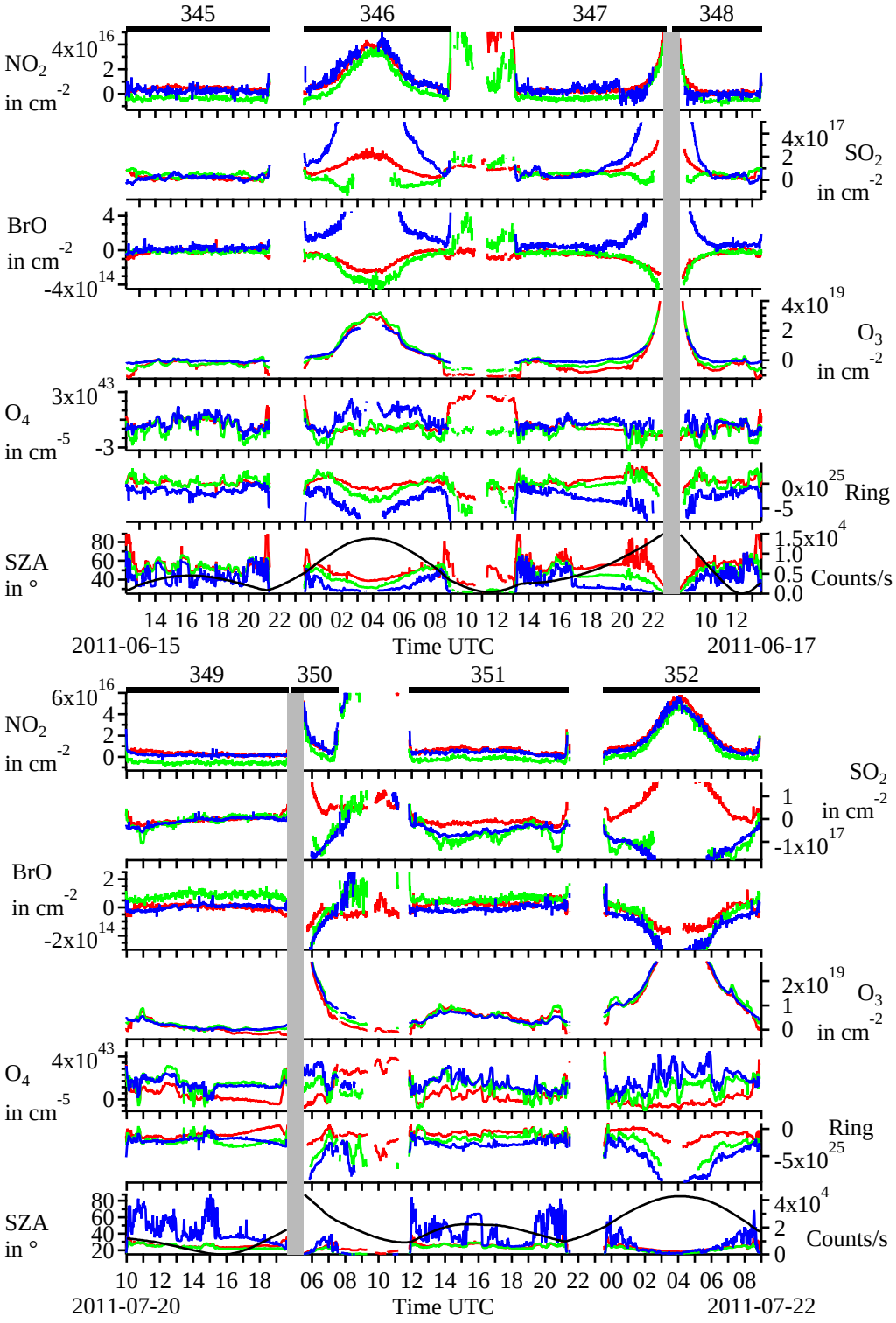

Figure A.7.: Set of flights 345–348 (June 2011) and 349–352 (July 2011).
SoF 345: FRA → YVR → FRA → BOG → FRA
SoF 349: FRA → CCS → FRA → YVR → FRA
red: Spec A (+10°), green: Spec B (−10°), blue: Spec B (−82°)

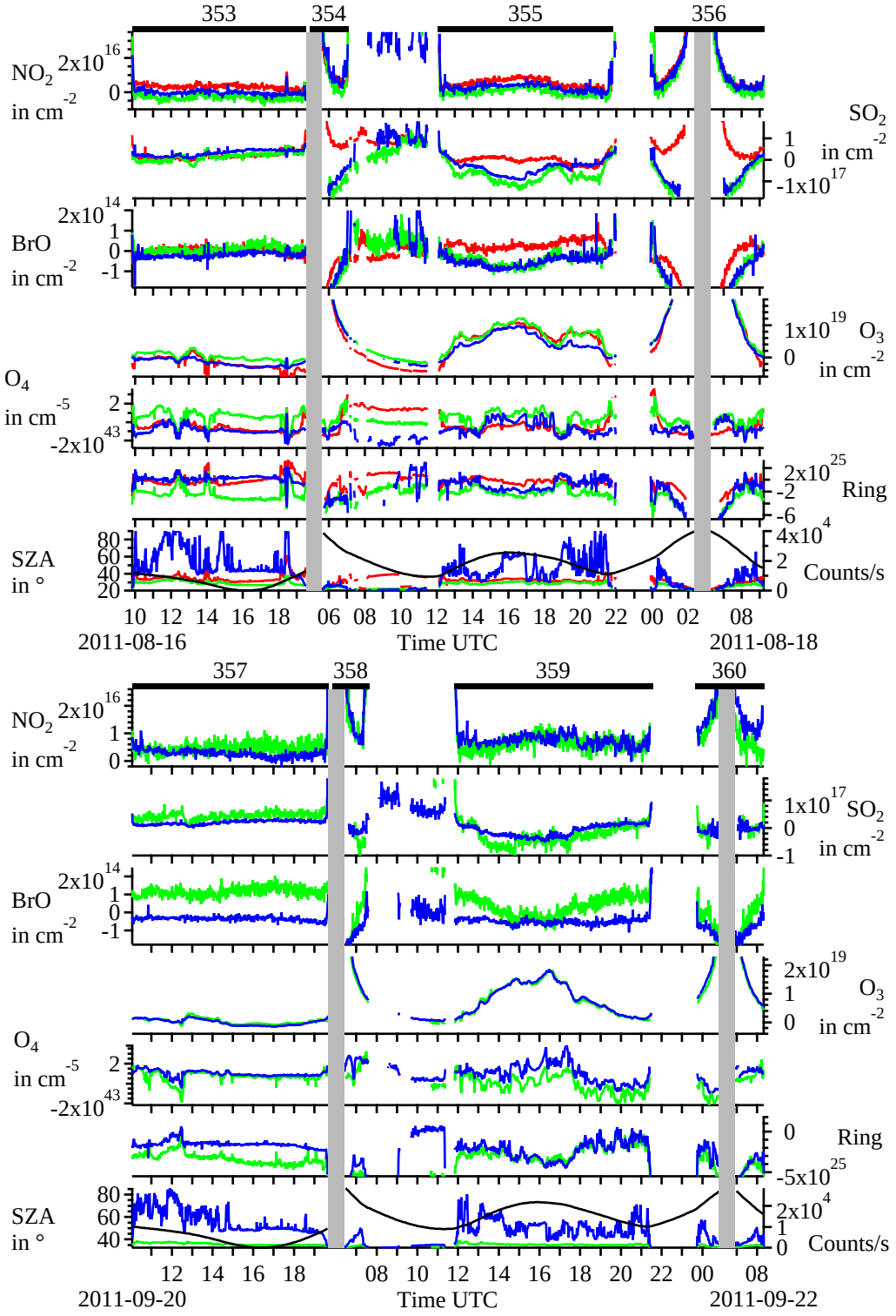

Figure A.8.: Set of flights 353–356 (August 2011) and 357–360 (September 2011).
SoF 353: FRA → CCS → FRA → YVR → FRA
SoF 357: FRA → CCS → FRA → YVR → FRA
red: Spec A (+10°), green: Spec B (−10°), blue: Spec B (−82°)

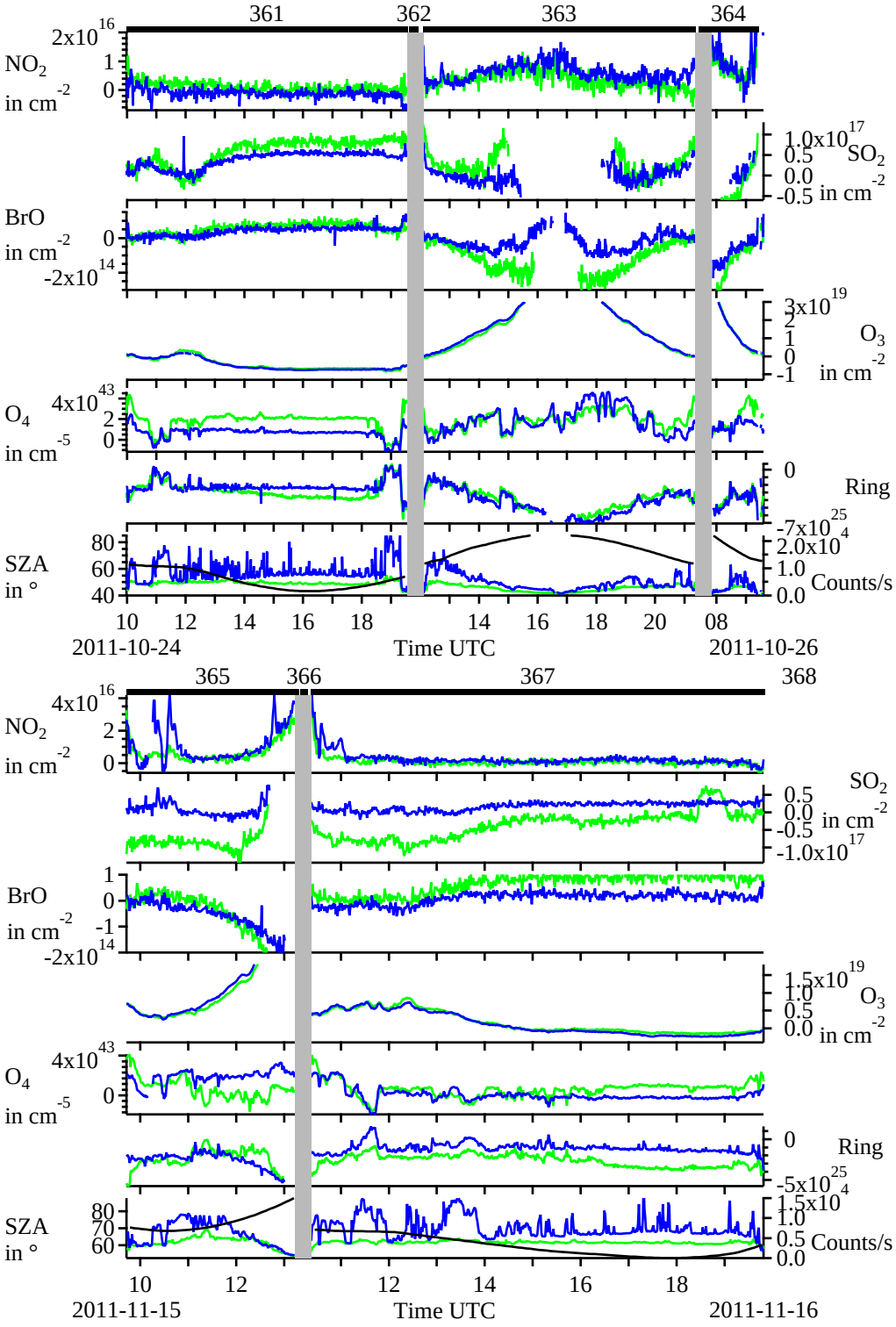

Figure A.9.: Set of flights 361–364 (October 2011) and 365–368 (November 2011).
SoF 361: FRA → CCS → FRA → YVR → FRA
SoF 365: FRA → MAA → FRA → CCS → FRA
red: Spec A (+10°), green: Spec B (−10°), blue: Spec B (−82°)

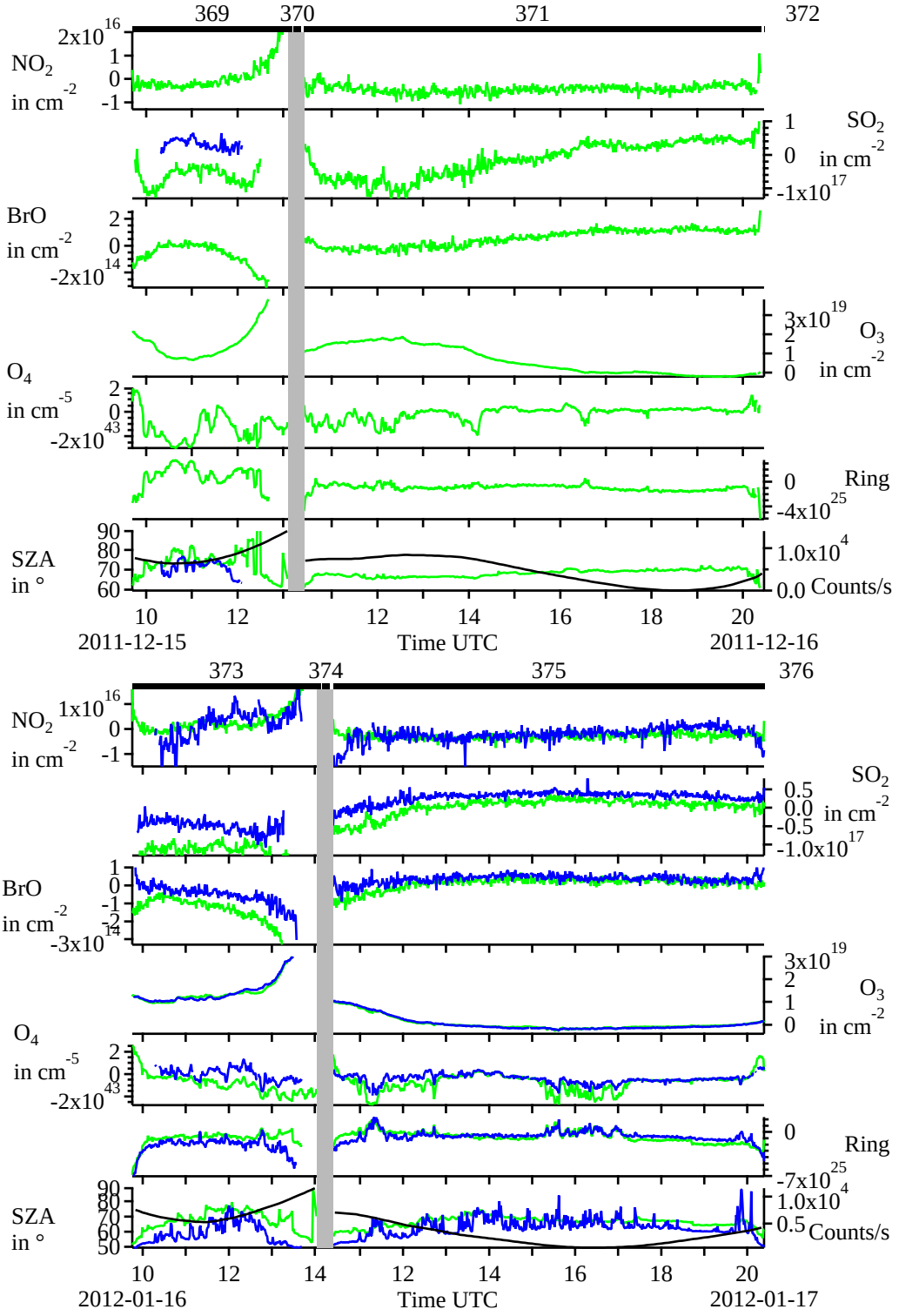

Figure A.10.: Set of flights 369–372 (December 2011) and 373–376 (January 2012).
SoF 369: FRA → MAA → FRA → CCS → FRA
SoF 373: FRA → MAA → FRA → CCS → FRA
red: Spec A (+10°), green: Spec B (−10°), blue: Spec B (−82°)

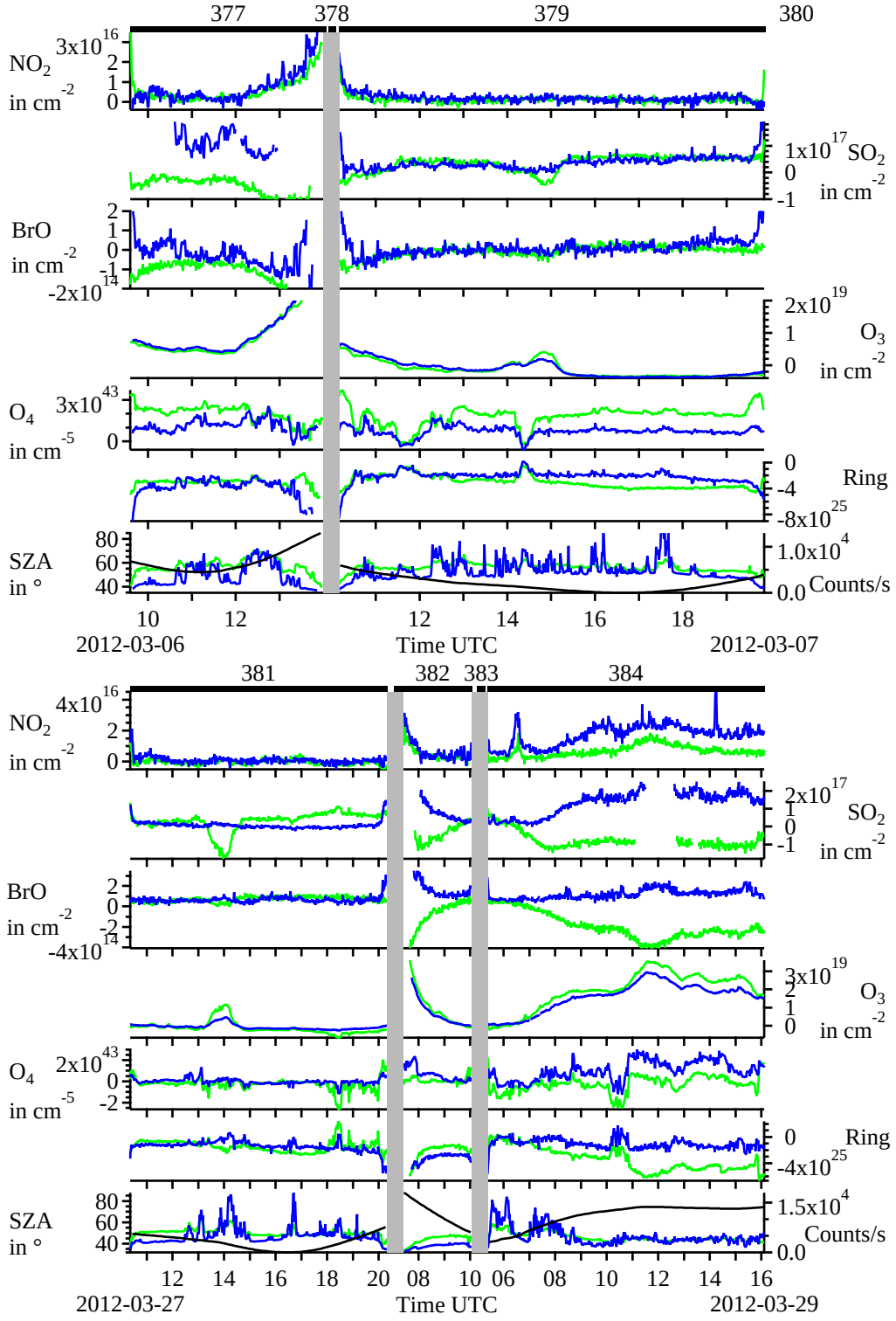

Figure A.11.: Set of flights 377–380 (March 2012) and 381–384 (March 2012).
SoF 377: FRA → MAA → FRA → CCS → FRA
SoF 381: FRA → CCS → FRA → ICN → FRA
red: Spec A (+10°), green: Spec B (−10°), blue: Spec B (−82°)

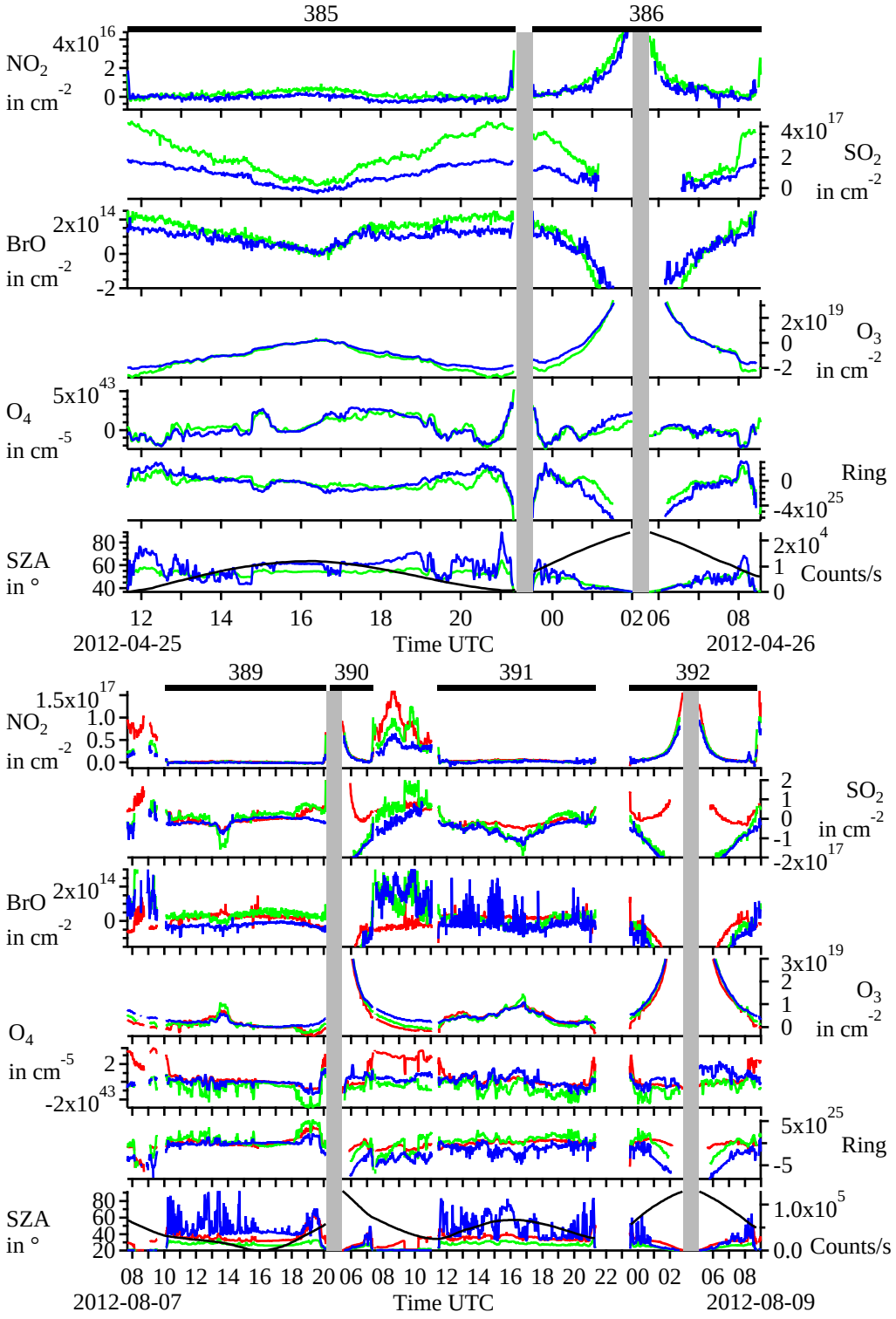

Figure A.12.: Set of flights 385–386 (April 2012) and 389–392 (August 2012).
SoF 385: FRA → YVR → FRA
SoF 389: FRA → CCS → FRA → YVR → FRA
red: Spec A (+10°), green: Spec B (−10°), blue: Spec B (−82°)

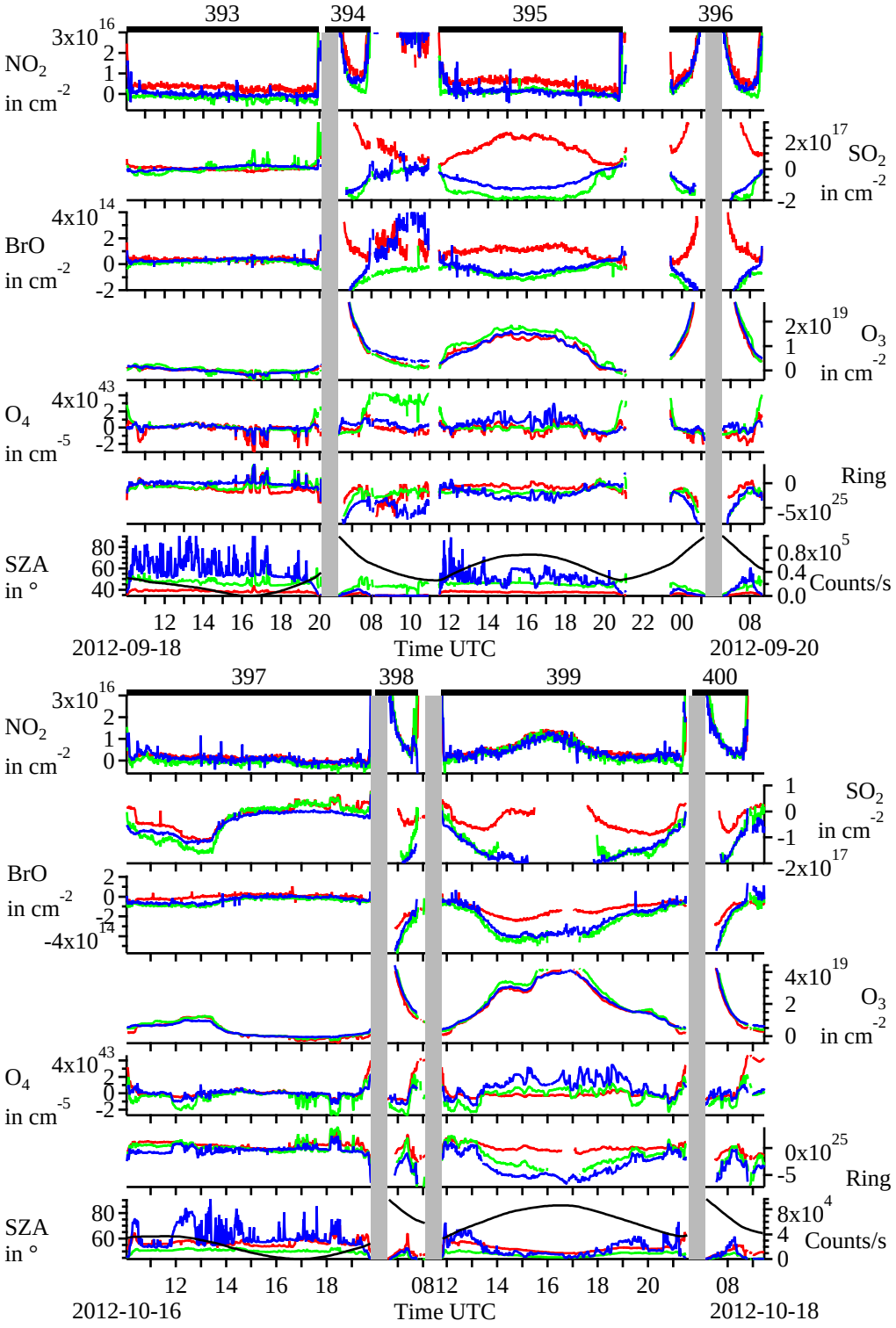

Figure A.13.: Set of flights 393–396 (September 2012) and 397–400 (October 2012).
SoF 393: FRA → CCS → FRA → YVR → FRA
SoF 397: FRA → CCS → FRA → YVR → FRA
red: Spec A (+10°), green: Spec B (−10°), blue: Spec B (−82°)

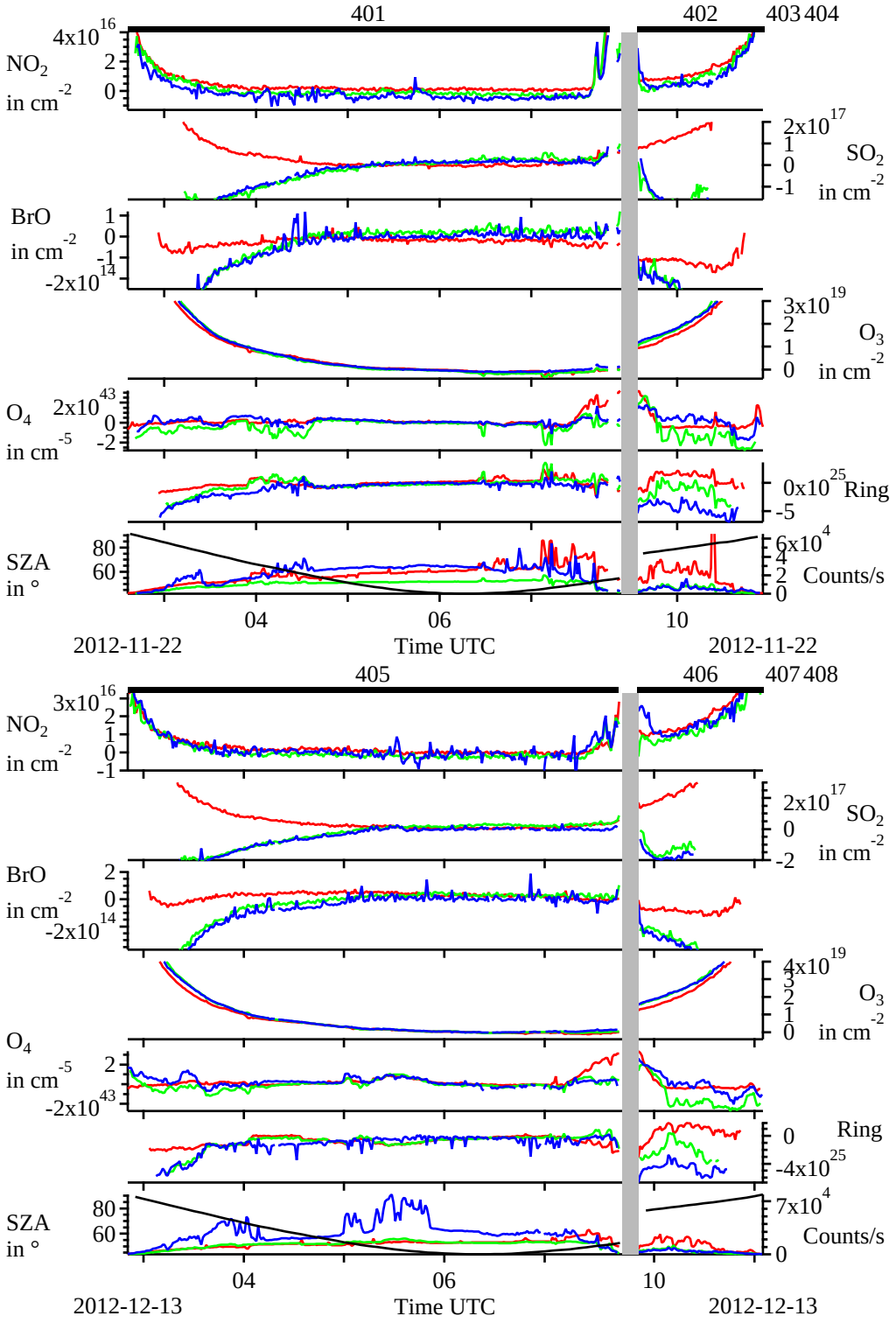

Figure A.14.: Set of flights 401–404 (November 2012) and 405–408 (December 2012).
SoF 401: FRA → BKK → KUL → BKK → FRA
SoF 405: FRA → BKK → KUL → BKK → FRA
red: Spec A (+10°), green: Spec B (−10°), blue: Spec B (−82°)

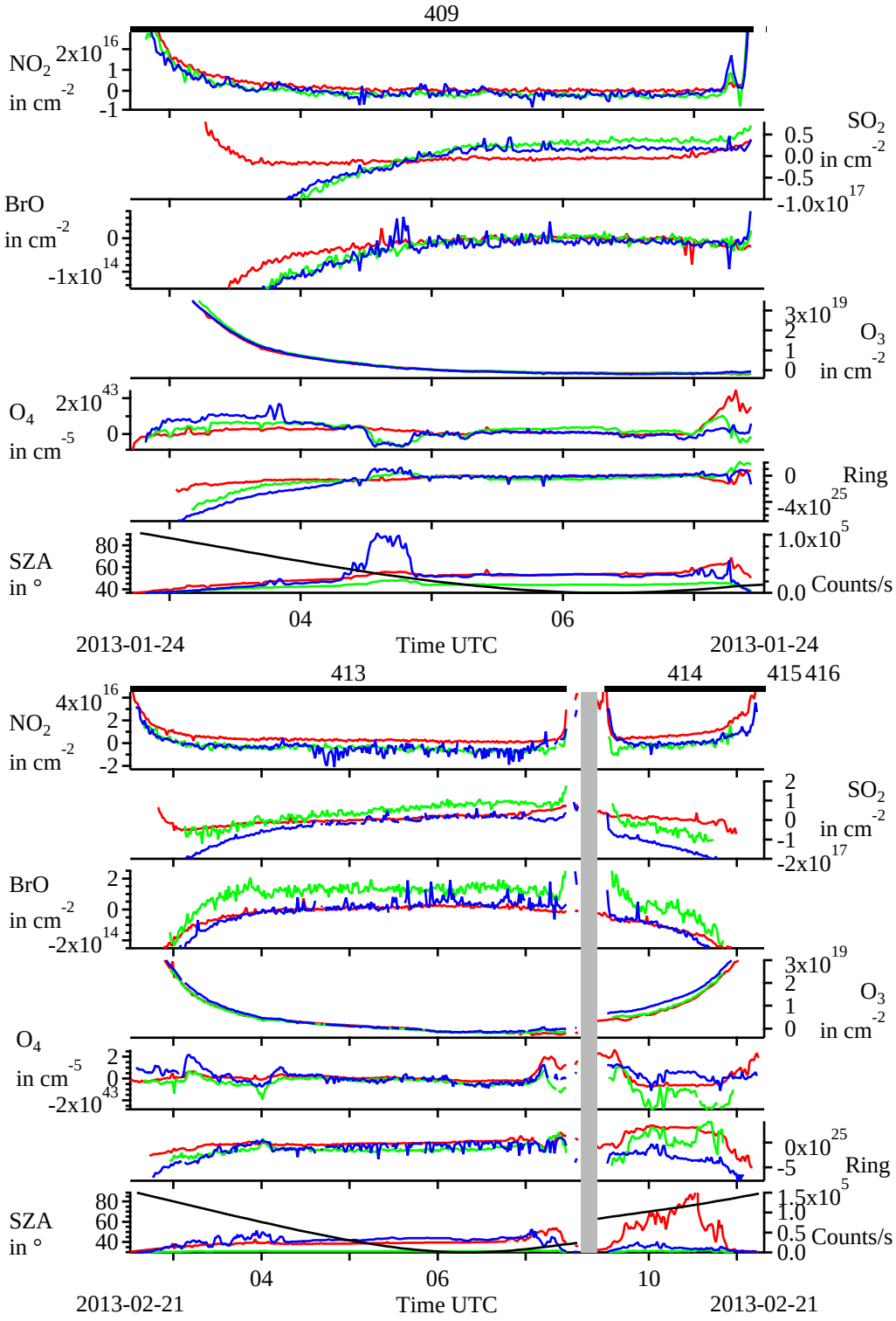

Figure A.15.: Set of flights 409 (January 2013) and 413–416 (February 2013).
SoF 409: FRA → BKK
SoF 413: FRA → BKK → KUL → BKK → FRA
red: Spec A (+10°), green: Spec B (−10°), blue: Spec B (−82°)

B. Symbols, Terms and Acronyms

The following table contains the destination airports of CARIBIC since 2010. The first column contains the IATA codes ('International Air Transport Association airport code') of the airports.

IATA	Lon	Lat	Place, Country (Name)
BKK	100.75	13.68	Bangkok, Thailand ('Suvarnabhumi Airport')
BOG	-74.14	4.70	Bogota, Colombia ('El Dorado International Airport')
CCS	-66.99	10.60	Caracas, Venezuela ('Simón Bolívar International Airport of Maiquetia')
CPT	18.60	-33.96	Cape Town, South Africa ('Cape Town International Airport')
FRA	8.54	50.03	Frankfurt, Germany ('Frankfurt am Main Airport')
ICN	126.45	37.47	Incheon/Seoul, South Korea ('Incheon International Airport')
JNB	28.24	-26.12	Johannesburg, South Africa ('O. R. Tambo International Airport')
KIX	135.24	34.43	Osaka, Japan ('Kansai International Airport')
KUL	101.71	2.75	Sepang, Malaysia ('Kuala Lumpur International Airport')
MAA	80.18	12.99	Chennai, India ('Chennai International Airport')
YVR	-123.18	49.20	Richmond/Vancouver, Canada ('Vancouver International Airport')

In the following, symbols, terms and acronyms used within this thesis are listed.

$\propto$	proportional to
$\sim$	on the order of, very roughly
$\approx$	approximately
$\simeq$	approximation (DOAS fit)
№	numero sign, used for numbering gases (→ p. 47), instruments (→ p. 79), events (→ p. 128) or scenarios (→ p. 158)
α_λ	→ 'absorptivity'
Γ	adiabatic lapse rate, the negative temperature gradient in a neutral atmosphere → p. 7, 10
ϵ_L	→ 'emissivity'
θ	solar zenith angle SZA, → p. 50 or Celsius temperature, i.e. $\theta/°\mathrm{C} = T/\mathrm{K} - 273.15\,°\mathrm{C}$, → p. 114
λ	wavelength
Λ	position on the detector, corresponds to wavelength λ → p. 59, 98
σ	cross section for absorption or scattering, e.g. σ_Rayleigh for Rayleigh scattering (→ p. 35). In Chap. 4, σ' and σ'' denote the narrowband and broadband structure of σ → p. 48

τ	optical density (→ p. 47) or lifetime of a gas (e.g. of SO_2 → p. 29)
[ ]	e.g. $[NO_2]$: concentration of NO_2 → p. 18
ABL	'Atmospheric Boundary Layer', also 'Planetary Boundary Layer' → p. 12
absorptivity	spectral absorptivity α_λ describing the fraction of light being absorbed by the surface of a body. → p. 39
ACD	apparent column density → p. 53, 55
ADC	analog-to-digital converter → p. 111
AMF	air mass factor, symbol A, cf. 'Box-AMF' → p. 50
a.g.l.	above ground level
ARINC data	data provided by the aircraft to the CARIBIC Master computer, containing time, position, flight phase etc. → p. 82
ARINC time	part of the ARINC data, supposed to be identic to UTC → p. 82, 119
a.s.l.	above sea level
attitude	also 'flight dynamics', the orientation of an aircraft. It can be described by the quantities 'pitch', 'roll', 'yaw'. These parameters are included in the ARINC data. → p. 82
BrO	bromine monoxide → p. 21, 136
Box-AMF	box air mass factor, symbol A_j, cf. 'AMF' → p. 54
c	light speed, in vacuum: $c = 299\,792\,458$ m/s
c, c_k, c_j	number concentration of a species, i.e. the number of molecules per volume; SI unit: $1/m^3$ → p. 5, 47, 54, 71ff
CARIBIC	Civil Aircraft for the Regular Investigation of the atmosphere Based on an Instrument Container, "www.caribic.de" or "www.caribic-atmospheric.com" → p. 75
CARIBIC time	reference time for all CARIBIC instruments. In ideal case and for practical purpose virtually identical to UTC; for most flights identical to Master time → p. 119
CCB	Container Connector Bracket → p. 77
CCD	charge-coupled device → p. 111
CCN	cloud condensation nuclei → p. 17
CTE	charge transfer efficiency → p. 111
DOAS	Differential Optical Absorption Spectroscopy → p. 46
DOASIS	'DOAS Intelligent System', DOAS analysis progam → p. 59, *Kraus* (2006)
e	Euler's number, $e = \exp(1) \approx 2.71828$
emissivity	also 'spectral emission coefficient', ϵ_λ, describing the fraction of light being emitted by a body with respect to the emission of a black body. → p. 40
eV	electron Volt, an energy unit; $1\,eV \approx 1.6022 \cdot 10^{-19}$ Joule
exposure time	Acquisition time for one scan of a spectrum → p. 109
EMC	Electromagnetic compatibility → p. 116
EUMETSAT	European Organisation for the Exploitation of Meteorological Satellites → p. 180

FRS	Fraunhofer Reference Spectrum → p. 56
GOME	Global Ozone Monitoring Experiment, onboard ERS-2 satellite → p. 159
GOME-2	Second Global Ozone Monitoring Experiment, onboard MetOp-A satellite → p. 141
h, $\hbar$	Planck constant, reduced Planck constant; $2 \cdot \pi \cdot \hbar = \mathrm{h} \approx 6.62607 \cdot 10^{-34} \mathrm{J} \cdot \mathrm{s}$
H_S	spectrograph function, converts $I(\lambda)$ to $I^*(\Lambda)$, i.e. $I^*(\Lambda) = (I * H_\mathrm{S})(\lambda)$ → (4.41) p. 61
H_D	detector function, converts $I^*(\Lambda)$ to $I^\times(n)$ → (4.43) p. 61
H_DS	instrument function (a combination of H_S and H_D) → p. 62, 99
HCHO	formaldehyde → p. 20
HONO	nitrous acid → p. 19
HYSPLIT	'Hybrid Single Particle Lagrangian Integrated Trajectory Model' → (*Draxler and Rolph*, 2011)
$\bar{I}_\mathrm{rad}$, $\bar{I}_\mathrm{irr}$, $\bar{I}_\mathrm{int}$, $\bar{I}_\mathrm{flux}$	integrated radiance, irradiance, intensity, flux → p. 31
I_rad, I_irr, I_int, I_flux	spectral radiance, irradiance, intensity, flux → p. 31
I	(spectral) intensity or similar quantity; used in cases where the distinction between radiance, irradiance, intensity and flux is not crucial. In combination with the subscript '*' or '×', the irradiance at the detector or the measured digital signal is denoted, see below. In Sect. 6.4.3, 'I' is used for a completely different quantity.
I_0	spectrum of the light source (in this work, I_FRS was used instead of I_0) → p. 43, 47
I_FRS	Fraunhofer reference spectrum → p. 56
$I^*(\Lambda)$	irradiance impinging on the detector at position Λ → p. 59
$I^\times(n)$	number of counts in a digital spectrum at channel n → p. 59
$I^{\times[\mathrm{d}]}$	dark current contribution of the spectrum $I^\times$ → p. 62, 112, 120
$I^{\times[\mathrm{o}]}$	offset signal contribution of the spectrum $I^\times$ → p. 62, 112, 120
$I^{\times[\mathrm{real}]}$	contribution of the 'real light' to spectrum $I^\times$, without offset and dark current signal and without straylight → p. 62, 120
$I^{\times[\mathrm{s}]}$	straylight contribution of the spectrum $I^\times$ → p. 62, 65, 102
IAGOS	'In-service Aircraft for a Global Observing System', an airborne research project including MOZAIC and CARIBIC → "www.iagos.org")
ICB	Inlet Connector Bracket → p. 77
instrument function	→ 'H_DS'
IR	infrared radiation, i.e. radiation with $\lambda \gtrsim 800\,\mathrm{nm}$
ITCZ	Inner Tropical Convergence Zone → p. 12
IUP	Institute for Environmental Physics, Heidelberg University, Heidelberg, Germany, "www.iup.uni-heidelberg.de"
j	index used for counting heights or height intervals
J	flux of a species through a surface → p. 71

k	index used for denoting (gaseous) species, e.g. σ_k for the cross section and c_k for the concentration of gas № k → p. 41, 47
k_B	Boltzmann constant, $k_B \approx 1.3806 \cdot 10^{-23}$J/K
landing time	ending time of a flight; more precisely the time when the aircraft's wheels get ground contact. Also denoted as 'weight on wheels' or 'touch-down'. Cf. 'take-off time'
M	in chemical reaction equations used to represent a catalyst which has to be involved in the reaction in order to fulfil the required conservation of momentum and energy. → p. 18
Master computer	central controller of the CARIBIC container → p. 80, 83, 119
Master time	original time of the Master computer → p. 119
meridional	a flow, average, or functional variation taken in a direction northerly or southerly; as opposed to zonal. → p. 13
molec/cm^2	unit used for SCDs and VCDs, i.e. a number concentration integrated along a path. Sometimes, 'molec' is omitted: $1\,\text{molec/cm}^2 = 1\,\text{cm}^{-2}$
MPIC	Max Planck Institute for Chemistry, Mainz, Germany, "www.mpic.de"
Mt	Megaton; $1\,\text{Mt} = 1\,\text{Tg} = 10^9\,\text{kg}$
n	integer number, e.g. channel of the detector or a spectrum. Typically $n \in 1, \ldots, N$ → p. 59
NO	nitric oxide, also 'nitrogen oxide', 'nitrogen monoxide' → p. 17
NO_2	nitrogen dioxide → p. 17
NO_x	nitrogen oxides NO and NO_2 → p. 17
O_3	ozone → p. 23
O_4	oxygen dimer, also 'tetraoxygen', 'oxozone', with concentration proportional to the square of the O_2 concentration → p. 130, 139, *Greenblatt et al.* (1990), *Platt and Stutz* (2008, p. 589) and references therein
OMI	Ozone Monitoring Instrument → p. 159
OMT	'omt – optische messtechnik gmbh', Ulm, Germany, "www.omt-instruments.com"
OPC	Optical Particle Counter → p. 80, 132
p	pressure (→ p. 4) or coefficients of a polynomial (→ p. 48)
PBL	Planetary Boundary Layer → 'ABL'
PI	'Proportional Integral controller', a mechanical device or a algorithm to fix a certain quantity (e.g. the temperature T) by adjusting another quantity (e.g. the cooling current) → p. 114
pitch	angle of the aircraft relative to the horizon (nose to tail) → 'attitude'
ppb, ppbv	parts per billion (volume): 10^{-9}
ppm, ppmv	parts per million (volume): 10^{-6}
ppt, pptv	parts per trillion (volume): 10^{-12}
Q	source strength of an emission source → p. 71, 155, 166
RMS	Root Mean Square → p. 50

roll	angle of the aircraft relative to the horizon (wing to wing) → 'attitude'
RTE	Radiative Transfer Equation → p. 41
RTM	Radiative Transfer Model → p. 53
S	Slant Column Density (SCD) → p. 47
SAA	solar azimuth angle
SCD	slant column density, symbol S → p. 47
SCIAMACHI	'Scanning Imaging Absorption Spectrometer for Atmospheric CHartographY', a spectrometer onboard the ENVISAT satellite (2002–2012)
set of flights	→ 'SoF'
SI	Systeme Internationale d'unités – International System of Units. → *BIPM* (2006)
SO_2	sulphur dioxide → p. 26
SoF	'Set of Flights'; a set of typically four consecutive measurement flights. For example, SoF 297 was the first regular mission of the new instrument, consisting of the CARIBIC flights 297–300. The CARIBIC container is installed before a SoF in the cargo compartment of the aircraft, where it stays until the end of the SoF. → Appendix A
spectral absorption, emission coefficient	→ 'absorptivitiy', 'emissivity', p. 39
sr	steradian, a dimensionless SI unit for indicating solid angles, $1\,\mathrm{sr} = 1\,\mathrm{m}^2/\mathrm{m}^2 = 1$, e.g. a hemisphere has a solid angle of $1/2 \cdot 4\pi\,\mathrm{sr} = 2\pi$; → p. 31
SZA	Solar Zentith Angle, symbol θ → p. 50
take-off time	start time of a flight, when the aircraft looses ground contact.
T	thermodynamic temperature (also called 'absolute temperature'), SI unit $1\,\mathrm{K} = 1\,\mathrm{Kelvin}$
UTC	Coordinated Universal Time, formerly 'GMT' for 'Greenwich Mean Time'. Unless otherwise mentioned, all times reported in this thesis are given in UTC. To be precise, the (known) CARIBIC time instead of the (ideal) UTC is given in the context of CARIBIC measurement results, but the difference to UTC is negligible. → p. 119
UTLS	Upper Troposphere and Lower Stratosphere → p. 8
UV	ultraviolet radiation, i.e. radiation with $\lambda \lesssim 400\,\mathrm{nm}$
visible light	light visible for humans, i.e. radiation with $400\,\mathrm{nm} \lesssim \lambda \lesssim 800\,\mathrm{nm}$
VCD, V	vertical column density (VCD), symbol V → p. 50
VOC	'Volatile organic compound', "defined by the World Health Organization (WHO) as any organic compound having a saturation vapor pressure at 30 °C greater than 102 kPa" (*Warneck and Williams*, 2012, p. 431). For VOCs except methane, the term 'NMVOC' is used. → p. 20
yaw	angle of the aircraft relative to the flight direction (nose to tail) caused by side wind → 'attitude'

Danksagung

Hiermit möchte ich mich bei all denen bedanken, die mich im Laufe der vergangen vier Jahre begleitet und bei meiner Arbeit unterstützt haben. Dabei möchte ich mich ganz besonders bedanken bei

- meinem Doktorvater Prof. Dr. Ulrich Platt für die Betreuung dieser Arbeit sowie seine wertvollen Anregungen. In zahlreichen Gruppensitzungen im IUP haben mich sein großer Wissensschatz und Erfahrungsreichtum beeindruckt; motiviert haben mich sein Optimismus und sein Ideenreichtum.

- meinem Chef Dr. Carl Brenninkmeijer für die Ermöglichung und Betreuung dieser Arbeit in seiner Arbeitsgruppe und seinem einzigartigen Projekt CARIBIC. Vorbildlich sind seine Begeisterung und sein Werben für die Wissenschaft im Allgemeinen und CARIBIC im Speziellen.

- meinem DOAS-Kollegen und Mentor Dr. Klaus-Peter Heue für die tatkräftige Unterstützung in allen Belangen meiner Arbeit. Auf seine Hilfe und seinen Rat konnte ich mich stets verlassen, ob bei Tätigkeiten am Instrument, der Auswertung und Interpretation unserer Messungen oder das Korrekturlesen meiner Doktorarbeit. Ein herzliches Dankeschön für die freundschaftliche Zusammenarbeit seit meiner Diplomarbeit.

- Prof. Dr. Thomas Wagner für die sofortige Bereitschaft, sich als Zweitgutachter mit der Lektüre dieser Arbeit zu befassen.

- Prof. Dr. Iring Bender und Prof. Dr. Peter Glässel für ihre Bereiterklärung, als Prüfer an meiner Disputation teilzunehmen.

- Prof. Dr. Jos Lelieveld für die Ermöglichung der Arbeit in seiner Abteilung sowie allen Mitarbeitern des MPICs für das angenehme Arbeitsklima im Institut.

- Angela Baker, Emma Leedham, Carl Brenninkmeijer und Klaus-Peter Heue für das Korr~~f~~ekturlesen meines Papers und meiner Doktorarbeit.

- Den Co-Autoren meines Papers, Klaus-Peter Heue, Armin Rauthe-Schöch, Carl Brenninkmeier, Lok Lamsal, Nickolay Krotkov und Ulrich Platt, für die gute Zusammenarbeit.

- Armin Rauthe-Schöch, Steffen Dörner, Christoph Hörmann und Holger Sihler für die Bereitstellung von Winddaten und Satellitendaten (SO_2 und BrO) sowie Reza Shaiganfar für Messdaten seiner Paris-Kampagne.
- Elmar Uherek und Agnes Heinemann für die Betreuung im Rahmen der IMPRS sowie Jasmin Vishvanath for improving my English.
- Dieter Scharffe, Stefan Weber, Claus Koeppel, Martin Körner und Frank Helleis sowie den Werkstätten am IUP und am MPIC für ihren Einsatz am CARIBIC-Container, die Bereitstellung der Daten, ihre Hilfe beim DOAS-Instrument, den Fasern und sonstigen technischen Angelegenheiten.
- Johannes Lampel, Stefan Schmitt und Moritz Jurgschat für die Unterstützung bei der Behebung des Streulichtproblems unserer Spektrographen.
- Udo Frieß, Barbara Dix und Klaus-Peter Heue für die Vorarbeit bei Planung und Realisierung von 'DOAS onboard CARIBIC' sowie für die Hilfe bzgl. der Messsoftware.
- allen Kollegen der Luftchemie-Gruppe am IUP, ebenso Thomas Wagner und seiner Satellitengruppe am MPIC für die Möglichkeit des Gedankenaustausches.
- allen Mitarbeitern des CARIBIC-Teams für die große Hilfsbereitschaft und angenehme Atmosphäre, stellvertretend seien hierbei unsere 'Pensionäre' Franz Slemr und Tanja Schuck erwähnt.
- Nicole Bobrowski für eine erlebnisreiche Messkampagne im herrlichen Sizilien. Ganz besonders beeindruckt hat mich der Blick in den Krater des Etna.
- meinen Zimmerkollegen Senchao Lai, Taku Umezawa, Klaus-Peter Heue, Hella Riede und Sergey Gromov für zahlreiche Diskussionen zu und jenseits von Themen unserer Wissenschaft, sowie für unseren stetigen Einsatz für die Gewährleistung unserer Arbeitsproduktivität (Kaffee kochen).
- Christoph Brühl und Claus Koeppel für die gemeinsame Erkundung der regionalen Natur und Kultur.
- meinen Freunden und Verwandten, insbesondere meinen Eltern Franziska und Willy Walter sowie meinen Geschwistern Berna, Verena, Markus und Willibald, für die Ermöglichung meines Studiums, den Rückhalt und die Unterstützung.

Bereichernd, Kraft spendend und unterhaltsam waren auch Gespräche und Erlebnisse bei Kaffeepausen, auf den Fluren, in der Mensa oder in der Freizeit mit meinen Kollegen und Freunden.

Euch allen: Vielen herzlichen Dank!